eman ta zabal zazu

Universidad del País Vasco
Euskal Herriko Unibertsitatea
The University of the Basque Country

Spectroscopic analysis of atoms and molecules

Doctorate in Physics of Nanostructures and Advanced Materials
by

Alison Crawford Uranga

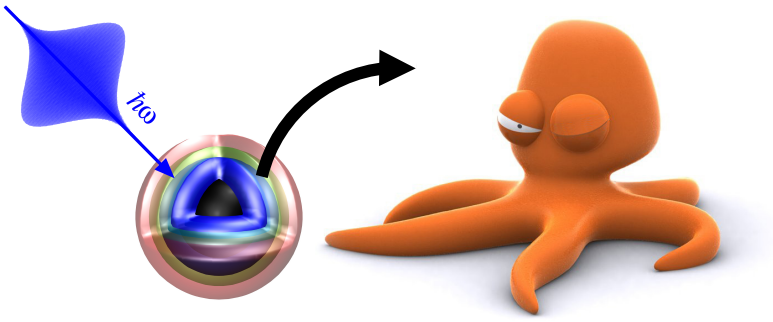

Supervisors:
Prof. **Stefan Kurth**
Prof. **Angel Rubio**

25th of May 2015

Acknowledgements

I would like to thank the Donostia International Physics Centre and the Departamento de Educación, Universidades e Investigación del Gobierno Vasco (Ref. BFI-2011-26) for the financial support to carry out this thesis as well as my supervisors, collaborators and the Nano-Bio Spectroscopy Group.

Resumen

En esta tesis he analizado la respuesta espectroscópica de varios átomos y moléculas a un campo electromagnético externo. Entender teóricamente dicha respuesta para moléculas es incluso más complejo que para átomos porque además del movimiento electrónico hay que tener también en cuenta el movimiento nuclear.

Debido a los avances experimentales en el campo de la óptica, hoy en día es posible seguir en vivo la respuesta nuclear y electrónica de estos átomos y moléculas expuestos a un campo electromagnético externo. El control del movimiento nuclear nos sirve, por ejemplo, para observar y controlar la formación y rotura de enlaces en moléculas. El control del movimiento electrónico nos permite, por ejemplo, fabricar aparatos cuyo funcionamiento está basado en el movimiento electrónico. Por tanto, necesitamos desarrollar teorías que complementen a los resultados experimentales para poder interpretarlos.

El movimiento electrónico tiene lugar en la escala de attosegundos a varios femtosegundos, mientras que el movimiento nuclear tiene lugar en la escala de cientos de femtosegundos a picosegundos.

Para que seamos capaces de resolver estas escalas de tiempo, necesitamos generar y controlar láseres muy energéticos y de duración muy corta. La fuerte y rápida interacción de estos láseres con un átomo o molécula es no-lineal y por tanto se requieren técnicas teóricas que sean capaces de lidiar con estos efectos no-lineales.

En el capítulo introductorio de esta tesis, he descrito en mayor detalle el desarrollo de las técnicas tanto experimentales como teóricas en el campo de la espectroscopía de átomos y moléculas.

Resolver la ecuación de Schrödinger tratando tanto la parte electrónica como nuclear de manera cuántica es una tarea muy compleja pero posible para moléculas de pocos electrones tales como H_2^+ y H_2, ya que están compuestas por uno y dos electrones, respectivamente. Por tanto, necesitamos utilizar métodos teóricos que nos permitan simplificar este problema y que a la vez sean precisos. Para la mayor parte de las moléculas hay que usar aproximaciones tanto para la parte nuclear como electrónica. Para la parte nuclear se suelen utilizar aproximaciones clásicas como la aproximación de Born-Oppenheimer (BOA) y la de dinámica de Ehrenfest (ED). En la BOA el movimiento nuclear se fija mientras que en ED la parte nuclear se mueve de manera clásica. Para los electrones se usa frecuentemente la teoría del funcional de la densidad (DFT) y la teoría del funcional de la densidad dependiente del tiempo (TDDFT) que corresponde a la extensión temporal de DFT.

Las aproximaciones clásicas son precisas si la masa de la parte nuclear de una molécula es pesada. Si este es el caso, la parte nuclear se mueve mucho más despacio que la parte

electrónica ante una perturbación externa. Para analizar la precisión de estas aproximaciones nucleares he obtenido el espectro lineal de excitación de las moléculas de H_2^+ y H_2. Como he mencionado más arriba, para estas moléculas podemos resolver tanto la parte electrónica como nuclear de manera cuántica mediante la ecuación de Schrödinger. Por tanto, para determinar la validez de las aproximaciones clásicas he obtenido el espectro lineal de excitación de estas dos moléculas de dos maneras. He tratado tanto la parte nuclear como la electrónica de manera cuántica o he tratado la parte electrónica de manera cuántica mientras que la nuclear de manera clásica usando la BOA y la ED.

Como la validez de las aproximaciones clásicas depende de la masa de la parte nuclear, he obtenido el espectro de excitación lineal tratando la parte nuclear y electrónica de manera cuántica para diferentes masas nucleares. Los efectos cuánticos de la parte nuclear deberían ser más importantes conforme la masa de la parte nuclear se reduce hacia el límite de la masa electrónica. En este caso he analizado la respuesta lineal de estas moléculas bajo un campo externo débil. Los movimientos nucleares no deberían ser fuertemente apreciables bajo este campo débil porque las escalas de tiempo en las que se mueven requieren de campos externos más fuertes.

Las aproximaciones de DFT y TDDFT son mucho más simples que la ecuación de Schrödinger porque para interpretar las propiedades del sistema se pueden utilizar funcionales de la densidad en vez de la compleja función de onda. Adicionalmente el problema se facilita porque se utilizan las funciones de onda no interactuantes de Kohn y Sham donde los efectos complicados de interacción se incluyen en los funcionales de intercambio y correlación. La forma en la que aproximemos estos funcionales de intercambio y correlación determinará el rendimiento de TDDFT. Además TDDFT es una técnica con la que se puede interpretar con una buena precisión en general los efectos no-lineales que surgen debido a la interacción de un láser fuerte y corto con un átomo o molécula.

Como TDDFT se puede utilizar para moléculas sometidas a campos externos fuertes, he utilizado esta teoría para estudiar la ionización de átomos de argón y neón expuestos a un láser de electrones libres y para estudiar la ionización de una molécula de etileno expuesta a un sistema compuesto de un láser bomba y sonda. El láser bomba se utiliza para crear en la molécula un estado excitado no estacionario. Después se utiliza un láser sonda que monitoriza la evolución de este estado excitado con el tiempo tras ser la molécula ionizada por el láser sonda. Los láseres usados aquí para estos átomos y moléculas son fuertes y su energía es suficiente para ionizar sus electrones.

En el caso de los átomos de neón y argón he estudiado la ionización tanto individual como total de sus electrones. Para ello he utilizado las funciones de onda no interactuantes de Kohn y Sham y la densidad electrónica. Los resultados obtenidos con TDDFT los he comparado a los mismos obtenidos a través de otro método teórico perturbativo conocido como teoría perturbativa de bajo orden (LOPT). Dicha comparación se ha realizado en una zona de actuación perturbativa donde este método funciona. Comparamos nuestros resultados obtenidos con TDDFT a los obtenidos con LOPT porque con este método ya

se han obtenido buenos resultados en comparación con datos experimentales para argón y neón. TDDFT ofrece la posibilidad de tratar efectos no-perturbativos pero se pensaba que no funcionaba porque falló para describir la doble ionización de un átomo de helio. Como veremos más adelante, en el capítulo de resultados, TDDFT sí funciona para neón y argón, por lo que se abre la posibilidad de analizar la ionización de éstos y otros átomos además de la ionización de moléculas más complejas usando TDDFT en una zona de actuación no-perturbativa.

En el caso de etileno he estudiado la evolución de sus orbitales moleculares con el tiempo tras ser expuesto a un láser bomba y sonda. Para ello, primero excito la transición de interés de π_z a π_z^* con un láser bomba y luego sigo la evolución de dicha transición tras ionizar la molécula con un láser sonda. He analizado la energía cinética en el espectro de fotoemisión y la distribución angular de los electrones ionizados. He comparado tanto el espectro de fotoemisión como la distribución angular de los orbitales de etileno fijando la parte nuclear con BOA y permitiendo el movimiento de la parte nuclear de manera clásica con ED. Así, he podido estudiar el efecto de movimiento de la parte nuclear en el espectro de fotoemisión y en la distribución angular de los orbitales moleculares de etileno. Como veremos más adelante, en el capítulo de resultados, se pueden observar fuertes cambios nucleares cuando se fija la ocupación del estado excitado π_z^* sin usar un láser bomba. De lo contrario, el láser bomba favorece la desocupación de dicho estado y su ocupación debe ser suficiente para que el láser sonda pueda resolver los cambios debidos al movimiento nuclear.

El capítulo teórico de esta tesis está compuesto de dos bloques principales. En el primer bloque introduzco como resolver el problema nuclear y electrónico de manera cuántica con la ecuación de Schrödinger. Esto sólo es factible para moléculas de pocos electrones como H_2^+ y H_2. Esta parte contiene el desarrollo teórico de las aproximaciones clásicas BOA y ED. Además he incluido una sección en la que explico teóricamente como obtengo el espectro de excitación lineal para las moléculas de H_2^+ y H_2 tratando la parte electrónica de manera cuántica y la parte nuclear de manera tanto cuántica como clásica con la BOA y ED. En el segundo bloque introduzco como resolver el problema de muchos electrones de manera cuántica usando DFT y TDDFT. Para la parte nuclear se utiliza la BOA o la ED. Aquí he incluido un análisis de la ionización de átomos de neón y argón y la molécula de etileno utilizando TDDFT. Para argón y neón he seguido la evolución en el tiempo de la carga electrónica del sistema que se ioniza. Al ionizarse los átomos, pierden carga electrónica. La ionización total se puede determinar a través de la densidad electrónica. Sin embargo, para obtener las ionizaciones individuales utilizamos las funciones de onda no interactuantes de Kohn y Sham. Para obtener el espectro de fotoemisión resuelto en el tiempo y las distribuciones fotoangulares para etileno con TDDFT he dividido el espacio computacional total de la molécula en una parte interactuante en espacio real y en una parte no interactuante en espacio impulsivo que están conectados por un espacio de absorción.

El capítulo de resultados y discusión de esta tesis contiene una sección con los resultados del espectro de excitación lineal de H_2^+ y H_2, una sección con los resultados de ionización total e individual de los electrones de los átomos de neón y argón y una última sección donde se muestra la evolución de los orbitales moleculares de etileno expuesto a un sistema láser bomba y sonda en el espectro de fotoemisión resuelto en el tiempo y las distribuciones fotoangulares. Cada una de estas secciones contiene una subsección con los detalles numéricos y el procedimiento que he llevado a cabo para resolver las ecuaciones del capítulo teórico, una subsección con los resultados obtenidos y una subsección con las conclusiones específicas.

El último capítulo de esta tesis contiene las conlusiones más generales para cada uno de estos proyectos, además de posible trabajo que todavía se puede realizar y cosas que nos falta por entender en más profundidad.

En el caso de H_2^+ y H_2, he comparado el espectro de excitación lineal que obtenemos para un tratamiento de la parte nuclear y electrónica de manera cuántica con el que obtenemos mediante un tratamiento de la parte electrónica de manera cuántica y nuclear de manera clásica. Un tratamiento totalmente cuántico en general no es posible y por tanto se usan la BOA y ED como aproximaciones clásicas para la mayoría de las moléculas. Dichas aproximaciones están formuladas de manera que su validez depende de que la masa nuclear sea pesada. Por tanto, es de esperar que el espectro lineal con parte nuclear cuántica sólo se equipare totalmente al de parte nuclear clásica cuando la masa nuclear sea muy pesada. Por esta razón nuestro análisis de dicho espectro lineal se ha hecho para moléculas del tipo de H_2^+ y H_2 de diferentes masas nucleares. He encontrado que el espectro apenas varía si utilizamos para la parte nuclear la BOA o la ED. Por ello he comparado el espectro de la parte nuclear cuántica con el obtenido con la BOA para la parte nuclear clásica. Como es de esperar he encontrado que para masas nucleares pesadas, las características del espectro lineal cuántico se equiparan al clásico usando la BOA. Sin embargo, conforme disminuye la masa nuclear y se hace más ligera podemos apreciar diferencias entre el espectro lineal cuántico y el clásico con BOA. En particular, los picos se ensanchan, se hacen más asimétricos y nuevas contribuciones aparecen en el espectro. Dichas contribuciones parece que surgen de una división de los picos de BOA clásicos en dos contribuciones separadas, una para mayores energías y otra para menores. Estos efectos cuánticos son sobre todo apreciables para la molécula de H_2^+ pero son más débiles para el caso de la molécula de H_2. Por ello he realizado un análisis más en detalle para la molécula de H_2^+. La división de los picos nos sugiere que puede ser debido a una hibridación entre dos niveles y por ello he usado un modelo de dos niveles para interpretar estos resultados. Además como estos nuevos efectos son mayores o menores dependiendo de la masa nuclear, he construido un modelo de dos niveles en función de la masa nuclear. Estas diferencias entre el espectro lineal cuántico y clásico nos sugieren que la naturaleza cuántica de la parte nuclear puede jugar un papel muy importante en la descripción lineal de procesos de absorción, especialmente para moléculas ligeras.

En este caso las aproximaciones clásicas no son suficientes para interpretar los procesos de absorción lineales. Con dicho modelo he analizado cuantitativamente tanto el ensanchamiento como la energía de los picos en el espectro lineal cuántico para la molécula de un electrón H_2^+ y diferentes masas nucleares. Con un modelo tan simple como el de dos niveles, he podido ajustar con una buena precisión el comportamiento de tanto el ensanchamiento como los cambios energéticos de los picos observados en el espectro lineal cuántico. Todavía nos falta entender la razón física por la cual dicho modelo funciona tan bien, además de porqué los efectos del movimiento nuclear cuántico son mucho más fuertes para una molécula de H_2^+ que para una molécula de H_2. Como sí es predecible, estos efectos son más importantes para masas nucleares ligeras. Por otra parte he deducido que las aproximaciones clásicas de BOA y ED, que son tan ampliamente usadas, pueden fallar incluso en la respuesta lineal. Esto es importante porque los movimientos nucleares se mueven en escalas de tiempo para las cuales se necesitan láseres más fuertes que en la zona de actuación lineal.

Por otra parte, he analizado la ionización de átomos de neón y argón utilizando TDDFT. Como estos átomos están compuestos de bastantes electrones, usamos TDDFT. En particular, he analizado tanto la contribución total de estos electrones que se ioniza como la contribución individual de cada uno de los electrones que se ioniza. Dichos átomos están expuestos a un láser de electrones libres en la zona de actuación perturbativa. Aunque TDDFT se puede usar en la zona no-perturbativa, realizamos nuestro análisis en la zona perturbativa. Esto es debido a que vamos a comparar nuestros resultados obtenidos con TDDFT a los mismos obtenidos con un método perturbativo conocido como teoría perturbativa de bajo orden (LOPT). Por tanto, LOPT sólo funciona en la zona de actuación perturbativa. LOPT ya se ha utilizado para analizar tanto la ionización individual como total de los electrones de neón y argón. Los resultados teóricos de LOPT se han comparado con los experimentales previamente y se ha encontrado un buen acuerdo entre ambos. Aunque se pensaba que TDDFT no funcionaba bien para describir la ionización de átomos, como sucedió en el caso de la doble ionización de helio, he encontrado que sí funciona bien para neón y argón comparando nuestros resultados con los de LOPT. TDDFT además de poder usarse en la zona de actuación no-perturbativa es un método simple porque resolvemos el problema con las funciones de onda no interactuantes de Kohn y Sham. Como los efectos interactuantes se introducen en el funcional de intercambio y correlación, la precisión de TDDFT dependerá de cómo aproximemos este funcional de intercambio y correlación. Los dos efectos importantes para describir de manera precisa dichos funcionales son la forma asimptótica de su potencial y su dependencia con el tiempo. En esta tesis he usado funcionales adiabáticos por lo que hemos obviado la dependencia del tiempo. Sin embargo, sí he analizado el efecto de la forma asimptótica. Para ello he obtenido los resultados de ionización tanto individual como total de neón y argón usando cuatro diferentes funcionales, de los cuales dos tienen la correcta forma asimptótica y dos no la tienen. Como es de esperar, los resultados obtenidos son

mejores cuando se utiliza una forma correcta asimptótica con TDDFT en comparación con los resultados de LOPT. Por tanto, hemos observado que una descripción correcta del comportamiento asimptótico es crucial para obtener unos buenos resultados de ionización con TDDFT. Este efecto lo hemos podido observar tanto para la contribución total de electrones ionizada como para las contribuciones ionizadas individuales de cada electrón. Aunque la precisión de TDDFT es buena, LOPT es un poco mejor en comparación con los resultados experimentales que existen para neón y argón. Aunque ya obtenemos un buen acuerdo entre LOPT y TDDFT se podría intentar mejorar lo que hemos obtenido con TDDFT. Una posible opción que no he barajado en esta tesis es utilizar funcionales de intercambio y correlación que tengan memoria. Aunque LOPT y TDDFT están formulados de una manera teórica totalmente diferente, el acuerdo entre los dos nos sugiere que ambos métodos pueden proveernos una interpretación física correcta de la ionización de estos dos átomos. Con este proyecto hemos descubierto que al contrario de lo que se pensaba por el caso de helio, TDDFT resulta ser un método no-perturbativo que puede proveer muy buenos resultados de ionización y puede ser utilizado para interpretar resultados en la zona de acuación no-lineal en la cual LOPT no se puede utilizar.

Finalmente, he analizado la evolución de los orbitales moleculares de una molécula de etileno expuesta a un sistema de láser bomba y sonda. Dicha molécula está compuesta por muchos electrones por lo que usamos TDDFT. Para la parte nuclear que está ausente para los átomos de neón y argón he utilizado las aproximaciones clásicas de BOA y ED. El etileno contiene un enlace doble entre sus dos carbonos y cuatro enlaces simples entre carbono e hidrógeno. El enlace doble es rígido por lo que debería de ser difícil observar tanto elongaciones como rotaciones de dicho enlace. Sin embargo los enlaces de carbono e hidrógeno son simples y dichos átomos son además ligeros por lo que en este caso los movimientos nucleares deberían ser más importantes. En este caso he analizado cómo los movimientos nucleares afectan a los orbitales moleculares de etileno. Para ello he excitado la transición de interés de π_z a π_z^* mediante un sistema bomba creando un estado no estacionario en la molécula. La evolución de este estado se sigue tras aplicar un láser sonda que ioniza la molécula. He observado la energía cinética en el espectro de fotoemisión y la distribución fotoangular de los electrones ionizados. Para analizar el efecto de los movimientos nucleares en el espectro de fotoemisión y en la distribución angular he incluido el movimiento nuclear clásico mediante ED o no lo he incluido fijando la parte nuclear con la BOA. Con el espectro de fotoemisión y la distribución fotoangular somos capaces de resolver tanto los movimientos electrónicos como nucleares por lo que la técnica espectroscópica de bomba y sonda es apropiada para este análisis. He observado que el efecto de los movimientos nucleares es inapreciable cuando se utiliza un láser bomba para excitar a la molécula del estado π_z al π_z^*. Para que se observen los efectos nucleares, la ocupación del estado excitado π_z^* debe ser suficiente para que la sonda pueda resolver los efectos nucleares. El problema es que el láser bomba aparte de ocupar dicho estado con la excitación del estado π_z también es capaz de inducir la desocupación

de dicho estado. Desde un punto de vista experimental esto podría interpretarse como la dificultad de controlar la evolución de una reacción química desde los reactivos hasta los productos. Si fijamos artificialmente la ocupación del estado π_z^* sin usar la bomba, conseguimos que la ocupación del estado π_z^* se mantenga constante sin ninguna pérdida para poder observar claramente los efectos nucleares. Esto es algo que podemos hacer fácilmente teóricamente pero no experimentalmente. Así se pueden observar cambios en el espectro de fotoemisión y en la distribución angular que están causados por los efectos nucleares de gran elongación y torsión que experimenta la molécula de etileno. En el espectro de fotoemisión resuelto en el tiempo he observado que las energías cinéticas de los orbitales moleculares de etileno cambian con el tiempo. Estos cambios son más pronunciados para los orbitales que están más fuertemente afectados por la elongación y torsión de la molécula. Para interpretar estos cambios observados nos hemos basado en la simetría de los orbitales que podemos observar de las distribuciones fotoangulares. Experimentalmente, esto es una tarea difícil porque es difícil controlar la orientación de una molécula dando lugar a distribuciones angulares asimétricas. Sin embargo, teóricamente podemos controlar este aspecto fácilmente. Con este proyecto hemos sido capaces de observar fuertes cambios en el espectro de fotoemisión y en la distribución fotoangular de una molécula de etileno debido a su gran elongación y torsión nuclear. Un análisis teórico nos ha permitido controlar con mucha más facilidad que de manera experimental tanto la orientación como la ocupación de los estados de la molécula de etileno. Esto ha sido clave para poder intepretar los efectos nucleares. En primer lugar nuestro estudio se ha basado en la simetría de los orbitales para lo cual necesitamos controlar la orientación de las moléculas. En segundo lugar, hemos tenido que controlar la ocupación del estado excitado π_z^* para que su ocupación sea suficiente para que la sonda sea capaz de resolver los cambios inducidos por el movimiento nuclear. Hemos podido observar cambios nucleares tan grandes que incluso puede que sea posible, con esta técnica de TDDFT utilizada aquí, estudiar procesos más interesantes como la disociación de moléculas.

Contents

List of Figures

List of Tables

CHAPTER 1

Introduction and motivations

Spectroscopy deals with the response of a system to an electromagnetic pulse. In this thesis I have focused on the spectroscopic response of several atoms and molecules.

The motion of electrons and nuclei in atoms and molecules can only be directly observed and controlled using electromagnetic pulses whose duration is comparable to the time scales on which their wavefunctions evolve. According to Heisenberg's uncertainty principle [1], this time scale is the inverse of the energy of the vibrational and electronic transitions for molecules and of the energy of the electronic transitions for atoms. Vibrational energy transitions occur on a time scale of picoseconds to hundreds of femtoseconds, whereas electron energy transitions occur on a time scale of attoseconds to tens of femtoseconds.

Control of nuclear scale motion is important to follow the formation and breakage of bonds [2], whereas with electronic scale motion we can follow electron migration in molecular electronics [3] and the damage and repair mechanisms of DNA [4, 5].

Progress in ultrafast optics has allowed the generation and control of intense electromagnetic pulses comprising merely a few field oscillation cycles [6]. The experimental tools and techniques for the observation and control of nuclear dynamics with femtosecond time resolution [7] and electron dynamics with attosecond time resolution [8, 9, 10] have only recently become available.

Electromagnetic pulses were initially produced by the mode locking technique [11]. This technique is based on the constructive interference of the phase-modulated modes in the resonant cavity of the laser, giving rise to short bursts of electromagnetic pulses. To shorten the duration of the pulse to the femtosecond and attosecond time scale, the phase of the cavity modes has to be locked over a large bandwidth. Optical pulse compression based on the interplay between self-phase modulation induced by the optical Kerr effect and negative group delay dispersion is the key concept [12, 13] for light pulse generation in the few cycle regime. Currently, it is most efficiently implemented in mirror dispersion controlled Kerr Lens mode locked (KLM) Ti:sapphire laser oscillators [14, 15]. To shorten the duration of the pulses the bandwidth of the laser is increased with a hollow-fibre waveguide [16, 17, 18, 19] and subsequently compressed by chirped-mirrors [20], prisms [21] or optical parametric amplifiers [22].

Ultrashort pulses can be produced from high harmonic generation [23, 24] and free electron lasers [25].

High order harmonics are generated when the atom or molecule is subject to an external source that is strong enough to ionise an electron. The ionised electron can then return to the parent ion it has left behind and recombine with it emitting a photon [26, 27, 28, 29]. The produced high harmonic generation can be used as a train [10, 30] and an isolated single-cycle [31, 32, 33] attosecond source. The conversion efficiency of high harmonic generation can be increased using ultrashort pulses. Using ultrashort pulses the phase shift between the driving fundamental source and the harmonic waves can be controlled as has been predicted theoretically [34]. As mentioned previously, ultrashort pulses are obtained by increasing the bandwidth of the laser by guiding it through hollow waveguides [16, 19, 35, 36, 37, 38].

X-rays were discovered by Röntgen in 1895 [39]. The idea of using a free electron laser to produce X-rays was first proposed by Madey [40] and it was first operated by Deacon et al. [41]. The current free electron lasers are based on the the Self Amplified Spontaneous Emission (SASE) technique [42, 43, 44, 45]. A bunch of accelerated electrons is introduced into an undulator. This undulator region contains a series of periodic magnets which accelerate the incoming electrons along the transverse direction, giving rise to the emission of electromagnetic radiation [46]. When the electron along the transverse direction and the magnetic field in the undulator are in phase [47], the electron transfers energy to the electromagnetic radiation. Choosing a proper phase shift between the two is the basic principle of a free electron laser to amplify the emitted radiation [48]. Once this phase matching mechanism is lost for a certain undulator length, the amplifying process is saturated and then reversed. Therefore, determining the undulator length is essential for the efficiency of free electrons lasers [49, 50, 51]. The SASE technique is currently implemented in the ultraviolet (UV) to soft x-ray regime [52, 53] and the hard x-ray regime [54, 55]. Free electron lasers have been used to study the photoionisation of atoms such as neon [56], argon [57] and xenon [58, 59].

The response of an atom or molecule to an external electromagnetic pulse will depend on the energy, intensity and duration of the pulse.

When the photon energy does not equal or exceed the ionisation potential of the electrons in atoms and molecules, ionisation will only be possible via multiphoton ionisation if the laser is relatively intense. Multiphoton ionisation can proceed via sequential ionisation [60, 61] where the system needs to absorb more than a single photon to get ionised. Otherwise, if the laser is not very intense and the incoming photon matches the energy difference between the initial and final bound state, an electron will only be excited.

When the photon energy does equal or exceed the ionisation potential of the electrons in atoms and molecules, a bound electron will escape from the system via tunnelling or above the barrier classically. Tunnelling has been observed experimentally in real time [62].

After tunnelling, the ionised electron will be driven by the electric field of the electromagnetic pulse and once the electric field reverses its sign, the electron will return to

the parent ion it left behind to recombine releasing energy. This three step semiclassical description [63] has been extended using quantum mechanical models based on quantum orbits and the saddle point method [64, 65].

The ionised electron can recombine with the parent ion in several ways. It can recombine with the parent ion and emit a photon or it can scatter elastically and inelastically.

The recombination process can lead to the emission of energy in the form of a photon. This process is responsible for the high-order harmonic generation mentioned above.

The electron can scatter elastically, as predicted theoretically [66], leading to Above Threshold Ionisation (ATI) [67], for example, which was first discovered by Agostini [68]. Here atoms absorb a larger number of photons than those required for ionisation. The ATI spectrum contains a series of peaks equally separated by the frequency of the incoming field. Due to rescattering, the photoelectron ATI spectrum will extend over a large energy plateau region with a maximal classical energy of ten times the ponderomotive energy U_p [69] and rings will appear in the ATI photoelectron angular distributions [70]. ATI has been observed for noble gas atoms [71], using multichannel quantum defect theory with the R-matrix technique [72].

The electron can also scatter inelastically transferring energy to the ion. Non-sequential ionisation is due to this process. According to Fittinghoff's non-sequential model [73], the returning electron can excite "shake-up" or ionise "shake-off" another electron due to screening. In Watson's model [74], the ejected electron induces a change in the potential of the electrons left behind. Non-sequential ionisation is only possible due to electron correlation [75, 76, 77, 78, 79]. Non-sequential ionisation has been studied mainly for noble gas atoms such as helium [74, 80, 81, 82], neon [83, 84], argon [85, 86], xenon [87, 88], as well as diatomic hydrogen [89], deuterium [90] and nitrogen and oxygen molecules [91].

Photoemission spectroscopy has been established as a key method to study the electronic and vibrational response of atoms and molecules to strong light sources [92]. It is based on the application of the photoelectric effect first observed by Hertz [93] and then explained by Einstein [94]. When light is incident on a material with a certain frequency ω, a bound initial electron can absorb a photon and escape to vacuum from the material with a maximum kinetic energy $E_k = h\omega - E_b$, where E_b is the binding energy of the material.

The macroscopic photocurrent of the emitted electrons produced from the photoelectric effect is related to the microscopic photoionisation differential cross section [95]. Here, the cross section is expressed in terms of the electron's kinetic energy and angular ejection distribution as a function of the laser's energy and polarisation. To develop a theoretical description of the photoemission process, one has to calculate the probability for an optical excitation between the ground state and one of the possible final vacuum states. This can be approximated using Fermi's Golden Rule from scattering theory [96].

To photoionise an electron a monochromatic beam is focused on the sample emitting electrons. Depending on the frequency of the incoming beam we can ionise valence and

core electrons. This monochromatic beam is generated from an Aluminium or Magnesium anode in the X-ray regime for the core electrons and a gas-discharged lamp [97] in the UV regime for the valence electrons. The emitted electrons are collected via the 2D velocity map imaging [98] technique in an electrostatic analyser where their kinetic energy and angular distribution is measured in microchannel plate detectors [99]. The whole setup is under vacuum conditions so that the photoelectrons emitted are not affected by their interaction with the background atmosphere.

In time resolved photoemission spectroscopy a pump is used to resonantly create an excited non-stationary wave packet, whose evolution is monitored as a function of time by means of a delayed probe pulse [100, 101]. The spectroscopic technique used in pump probe setups is called attosecond streaking spectroscopy [102, 103]. The idea behind the pump probe setup was first employed by Toepler [104], who varied electrically the delay time between a spark generating a shock wave and a second spark which acted as a flash light source to visualise the evolution of the shock wave.

A time resolved pump probe setup can be used, for example, to monitor the evolution of vibrational wavepacket motion [105, 106, 107], ultrafast internal conversions [108], inner shell Auger relaxations [109], internal relaxations after the ionisation of an electron [110], the buildup of fano resonances [111], intersystem crossings from a singlet to a triplet state [112, 113], intramolecular vibrational relaxations [114], intramolecular proton transfers [115], dissociations [116, 117, 118, 119, 120, 121, 122], the emission time of the electron [123], the time delay in the emission of different electrons [124], the tunnelling delay time [125] and the time taken in double ionisation [126].

The angular distribution of the emitted photoelectrons can be described using the asymmetry parameter [127], which measures the forward to backscattered photoemission from the sample. The backscattered photoemission is strongly dependent on the initial orientation of the molecule with respect to the laser polarisation [128, 129] leading to asymmetries in the photoangular distribution. Several experiments have been performed by initially fixing the orientation of the molecule [130, 131, 132, 133, 134]. However, fixing the orientation is a complex task experimentally [121, 135]. With a theoretical approach this is not an issue, as we can choose and fix the orientation of the molecule.

The angular resolved pump probe setup can be used to image the orbitals [136, 137], the molecular structure [138, 139] and the nuclear wavefunctions [140] via the diffraction patterns obtained from the interference of the forward and backscattered emitted contributions [141, 142, 143].

Understanding theoretically the response of a molecule or an atom to an external electromagnetic source is becoming more important now that femtosecond and attosecond sources are available. Modelling these time-dependent processes becomes unfeasible with the time-dependent Schrödinger equation (TDSE) as the system studied becomes realistic, i.e., systems in 3D that contain many electrons and nuclei [144]. Most work using the TDSE has been done for the one electron H_2^+ and H_3^{2+} molecules [145], the one electron

H atom [144] the two electron He atom [146, 147, 148] and the two electron molecule H_2 [149, 150]. By reducing the dimensionality of the TDSE, we can simplify the problem and still gain some insight to understand the more complex problem. However, a computationally inexpensive electronic structure theory method which can model excited state dynamics for more complex systems is necessary.

For molecules this response becomes even more complicated because we also have to take into account the motion of the nuclei which is absent in atoms. The nuclei in molecules are usually treated in terms of adiabatic potential energy surfaces with the Born-Oppenheimer approximation (BOA) [151]. Within this approximation, we assume that the electrons move along a potential energy surface for fixed nuclear positions. An improvement to the fixed nuclei BOA scheme is to use an Ehrenfest dynamics (ED) scheme [152] where all the possible excited trajectories of the nuclei are described by Newtonian classical methods along an averaged potential energy surface. The coupling between electrons and nuclei can lead to the formation of avoided crossings and conical intersections between the adiabatic potential energy surfaces [153]. This non-adiabatic coupling effect is neglected within the BOA [154]. This term should only be neglected when the nuclei move slowly and when the energy difference between the adiabatic potential energy surfaces is large.

Depending on the strength of the interaction between the atom or molecule to an external electromagnetic source, the ionisation of the electrons in atoms and molecules can be understood from a perturbative or a non-perturbative theory. A theoretical interpretation of the perturbative and non-perturbative regimes was first introduced by Keldysh [155]. Such interpretation is based on the ponderomotive energy U_p, i.e., the average kinetic energy of the ejected electron driven by the laser field.

If not very intense long pulses are used, electron ionisation can be understood in a perturbative way. The peak intensity must be within the validity of Perturbation Theory, for which the ponderomotive energy U_p, must be significantly smaller than the photon frequency [156]. The pulse duration should be long enough so that complete ionisation does not take place before the laser pulse reaches its maximum [157]. In the perturbative regime several models have been proposed in terms of collective excitations [158, 159], the isolated core excitation method [160, 161] and lowest-order perturbation theory (LOPT) [162]. Within LOPT, the overall ionisation process is broken up into steps whose time evolution is described in terms of transition probabilities per unit time or rate equations.

To observe strong non-perturbative behaviour at very high intensities, we need ultrashort intense laser pulses towards the x-ray regime [163, 164]. If the intense laser is not short enough, atoms and molecules may ionise completely before the laser pulse reaches its maximum [157]. A possible theoretical approach is to use the single active electron (SAE) approximation [27], where only the electron that is ionised interacts via an effective Hartree-Fock potential with the parent ion left behind [165]. This method has worked

very well for noble gas atoms such as argon [166] and helium [167] because they have a very high ionisation potential to eject more than a single electron simultaneously. However, it tends to fail when the other electrons play a role in the ionisation process [168].

Time-dependent density functional theory (TDDFT) [169, 170] is an inexpensive electronic structure method where the properties of the system can be determined by using density functionals instead of the wavefunction itself due to their one to one mapping [169]. The TDDFT problem is solved in a non-interacting way including all the many-body effects in the exchange-correlation functional. The performance of TDDFT depends on how this exchange-correlation functional is approximated. With TDDFT we can capture the high degree of non-linearity due to non-perturbative phenomena such as electron correlation that arises with ultrashort and intense pulses.

However, with TDDFT there are difficulties to properly describe excited states which have double- and higher-excitation characters. This is because within the adiabatic TDDFT approximation, the excitation energies have a single-excitation character [171]. To overcome these limitations several TDDFT theories based on multicomponent [172], constrained configuration interaction [173] and Bethe-Salpeter methods [174] have been implemented. Moreover, TDDFT underestimates excitation energies in charge transfer reactions [175]. This is especially the case for long-range charge transfer excitations, where non-local effects are stronger [176]. This is because the electrostatic attraction between charge transfer states originates from the non-local Hartree-Fock exchange potential. Non-locality is not described accurately with adiabatic TDDFT. These charge transfer underestimation errors can generate a series of spurious low lying charge transfer states [177] and spurious crossings [175] which may have a profound effect on the excited state dynamics. TDDFT also fails to describe the non-perturbative non-sequential "knee" effect [178] shown experimentally for helium [179]. Here, the double ionisation curve of helium follows a non-sequential mechanism for lower intensities until the singly ionised species has saturated. From then onwards, it follows a sequential mechanism. This experimental "knee" effect can be described accurately including the derivative discontinuity with an exact exchange-correlation potential [180, 181].

The failure of TDDFT to describe charge transfer excitations and excitation energies is attributed to the incorrect asymptotic behaviour and locality of the exchange-correlation potential of the adiabatic functionals used. The time-dependent exchange-correlation functionals are constructed adiabatically from the ground state functionals, neglecting their time-dependent evolution. This approximation is only reasonable if the system begins in a ground state where the external time dependence is very slow, which is not the case for strong non-perturbative phenomena. The incorrect asymptotic behaviour can be improved by introducing a long range separation into the exchange component of the functional [182]. The non-locality can be included using hybrid functionals which are constructed using the non-local Hartee-Fock exchange potential [183].

In this thesis I have investigated theoretically various aspects of the spectroscopic response of several atoms and molecules to an external source.

In Chapter 2, I first introduce the theoretical approaches used to study the spectroscopic response of atoms and molecules. A full quantum description of the coupled electron-nuclear response of molecules to an external electromagnetic source described in Sec. 2.1 is unfeasible in most cases except for few-electron molecules such as the H_2^+ and H_2 model molecules. For the nuclei the Born-Oppenheimer approximation (BOA) and Ehrenfest dynamics (ED) classical approximations for fixed and moving nuclei, respectively, are typically used. In particular, to test the validity of these classical approaches I have theoretically studied the linear excitation spectra from quantum versus classical nuclei for the H_2^+ and H_2 model molecules in Sec. 2.2. For these molecules I have studied the effects of quantum-nuclear motion on the linear excitation spectra. This analysis has been performed as a function of the nuclear mass because we expect the classical approaches to gradually break down as the nuclear mass decreases. For many-electron atoms and molecules, one usually solves the approximated many-electron problem by means of density functional theory (DFT) and its time-dependent extension time-dependent density functional theory (TDDFT) as explained in Sec. 2.3. For many-electron molecules the motion of the nuclei is treated classically with either the BOA or ED. In particular, I have studied the photoionisation of neon and argon atoms and of an ethylene molecule by means of TDDFT in Sec. 2.4. TDDFT is a theoretical method which allows us to interpret in a simple and accurate way the non-perturbative response of these systems. To ionise the electrons for the neon and argon atoms a free electron laser has been used experimentally. The argon and neon individual and total photoionisation yields are here obtained theoretically using the TDDFT non-interacting density and the Kohn-Sham (KS) wavefunctions. As the performance of TDDFT depends on the local and asymptotic behaviour of the exchange-correlation functional used, I have used several TDDFT exchange-correlation functionals. To ionise the electrons for ethylene a pump probe setup has been used. The photoemission spectra and angular distributions are theoretically obtained using a TDDFT scheme where space is partitioned in a real and momentum space region separated by an absorbing boundary region.

In Chapter 3, I then show and analyse the results obtained for each of the atoms and molecules mentioned in the previous paragraph. Each of these sections contains a subsection with the computational details and procedure needed to perform our calculations, a subsection where the results are shown and analysed and a final subsection with the conclusions for each project. In Sec. 3.1 I first show the results obtained for the linear excitation spectra of the H_2^+ and H_2 molecules with quantum and classical nuclei and quantum electrons. From this analysis I have investigated the effects of quantum nuclear motion on the excitation linear spectra and I have checked the validity of the classical approaches. Then I show the results for the individual and total photoionisation yields

of neon and argon atoms subject to free electron lasers in Sec. 3.2 using a TDDFT approach based on the KS wavefunctions. Here I have checked the accuracy of TDDFT to describe these yields by comparing our results to the ones obtained from a lowest-order perturbation theory (LOPT) perturbative method in the perturbative regime. Finally, an analysis of the photoemission spectra and angular distributions for the molecular orbitals of an ethylene molecule subject to a pump probe setup is given in Sec. 3.3. The evolution of these molecular orbitals is followed including (ED) or not (BOA) the nuclear motion to check the effects of classical nuclear motion on the photoemission spectra and angular distributions.

Finally, in Chapter 4, I summarise the main conclusions of this thesis and possible future work that can be carried out from it. At the very end of the thesis, after the bibliography, I have included some Appendices for further details on the H_2^+ and H_2 molecules, to which the reader can refer to. Specifically, I provide the static accuracy of the BOA in Appendix A, the centre of mass transformation in Appendix B, the ED Hamiltonians in Appendix C, and a derivation of the Hellmann-Feynman theorem in Appendix D.

CHAPTER 2

Theoretical background

In this chapter I first discuss the full quantum electron-nuclear problem in Sec. 2.1. Here I introduce the Born-Oppenheimer approximation (BOA) and Ehrenfest dynamics (ED) classical approximations to treat the nuclei. Solving the full quantum problem is computationally very demanding and is only feasible for one and two electron molecules such as H_2^+ and H_2. For most systems, the BOA and ED approximations are used. To test the accuracy of these classical approximations, I have compared the linear response spectra obtained from both a quantum and classical nuclear treatment for quantum electrons for H_2^+ and H_2. In Sec. 2.2 I have introduced the theoretical details to obtain the photoexcitation linear response spectra of the H_2^+ and H_2 diatomic molecules.

In Sec. 2.3 I focus on solving the electronic problem only for many electron systems, by means of density functional theory (DFT) and its time-dependent extension time-dependent density functional theory (TDDFT). For many-electron molecules, the nuclear motion is typically included via the BOA and ED classical approaches. TDDFT has been used to analyse the photoionisation of neon and argon atoms and the ethylene molecule in Sec. 2.4. To photoionise these systems I expose them to ultrashort intense sources giving rise to non-perturbative phenomena. TDDFT is a theoretical method which allows us to interpret in a simple and accurate way the non-perturbative response of these systems.

2.1. Approaches to the full quantum electron-nuclear problem

The quantum mechanical dynamics of a many-body system composed of a collection of N nuclei and n electrons is governed by the total electron-nuclear time-dependent Hamiltonian (atomic units a.u. are used throughout this thesis unless stated otherwise) which can be written as

$$\hat{H}(t) = \hat{T}_I + \hat{T}_e + \hat{V}_{II} + \hat{V}_{Ie} + \hat{V}_{ee} + \hat{V}_{ext}(t), \tag{2.1}$$

where the kinetic energy operator of the nuclei is

$$\hat{T}_I = \sum_{\alpha=1}^{N} -\frac{1}{2M_\alpha}\nabla_\alpha^2, \tag{2.2}$$

with the mass M_α of nucleus α and the electronic kinetic energy operator is

$$\hat{T}_e = \sum_{i=1}^{n} -\frac{1}{2}\nabla_i^2. \tag{2.3}$$

The interaction between the nuclei is given by

$$\hat{V}_{II} = \frac{1}{2}\sum_{\substack{\alpha,\beta=1 \\ \alpha\neq\beta}}^{N} \frac{Z_\alpha Z_\beta}{|\mathbf{R}_\alpha - \mathbf{R}_\beta|}, \tag{2.4}$$

where Z_α is the atomic number of nucleus α and $\mathbf{R}_\alpha$ its coordinate. Similarly, the electron-electron repulsion is

$$\hat{V}_{ee} = \frac{1}{2}\sum_{\substack{i,j=1 \\ i\neq j}}^{n} \frac{1}{|\mathbf{r}_i - \mathbf{r}_j|}, \tag{2.5}$$

where $\mathbf{r}_i$ and $\mathbf{r}_j$ are the coordinates of electrons i and j. The attractive interaction between the electrons and nuclei is

$$\hat{V}_{Ie} = -\sum_{\alpha=1}^{N}\sum_{i=1}^{n} \frac{Z_\alpha}{|\mathbf{r}_i - \mathbf{R}_\alpha|}. \tag{2.6}$$

Finally, $\hat{V}_{ext}(t)$ describes the interaction of the system of electrons and nuclei with an external electromagnetic time-dependent field. Throughout this thesis $\hat{V}_{ext}(t)$ will describe laser fields in the dipole approximation as explained in more detail in Sec. 2.4.1. The exact form I have used for $\hat{V}_{ext}(t)$ will be given in Sec. 2.4.1.

The time-dependent Schrödinger equation (TDSE) for the full quantum mechanical description of the combined electronic and nuclear system then reads

$$\begin{aligned} &i\frac{\partial}{\partial t}\psi(\mathbf{R}_1 S_1, \mathbf{R}_2 S_2, ...\mathbf{R}_N S_N; \mathbf{r}_1 s_1, \mathbf{r}_2 s_2 ... \mathbf{r}_n s_n, t) \\ &= \hat{H}(t)\psi(\mathbf{R}_1 S_1, \mathbf{R}_2 S_2, ...\mathbf{R}_N S_N; \mathbf{r}_1 s_1, \mathbf{r}_2 s_2 ... \mathbf{r}_n s_n, t), \end{aligned} \tag{2.7}$$

where ψ is the many body time-dependent electron-nuclear wavefunction which depends on the nuclear and electronic coordinates defined previously and on the spin coordinates S_α and s_i of nuclei α and electron i, respectively.

For time-independent problems ($\hat{V}_{ext}(t) = 0$), the general solution of the time-dependent Schrödinger equation can be written as

$$\psi = \sum_k c_k \exp(-i\varepsilon_k t)\psi_k(\mathbf{R}_1 S_1, \mathbf{R}_2 S_2, ...\mathbf{R}_N S_N; \mathbf{r}_1 s_1, \mathbf{r}_2 s_2 ... \mathbf{r}_n s_n), \tag{2.8}$$

where ε_k and ψ_k are the k^{th} eigenvalue and eigenstate of the electron-nuclear stationary Schrödinger equation

$$\begin{aligned}\hat{H}\psi_k &= \hat{H}\psi_k(\mathbf{R}_1 S_1, \mathbf{R}_2 S_2, ...\mathbf{R}_N S_N; \mathbf{r}_1 s_1, \mathbf{r}_2 s_2 ...\mathbf{r}_n s_n) \\ &= \varepsilon_k \psi_k(\mathbf{R}_1 S_1, \mathbf{R}_2 S_2, ...\mathbf{R}_N S_N; \mathbf{r}_1 s_1, \mathbf{r}_2 s_2 ...\mathbf{r}_n s_n),\end{aligned} \tag{2.9}$$

with

$$\hat{H} = \hat{T}_I + \hat{T}_e + \hat{V}_{II} + \hat{V}_{Ie} + \hat{V}_{ee}. \tag{2.10}$$

Solving the quantum electron-nuclear many body problem is computationally very demanding and becomes unfeasible in most cases, except for one and two-electron systems, such as the model systems studied in Sec. 2.2. In particular, the resources required to solve the quantum 3D electron-nuclear many-body problem scale exponentially with the number of electronic $3n$ and nuclear $3N$ coordinates in the system. This makes the solution of this problem very difficult when n and N are large. Thus, in Secs. 2.1.1 and 2.1.2 I introduce widely used approximations for the nuclei to computationally simplify this problem.

2.1.1. The Born-Oppenheimer approximation. The Born-Oppenheimer approximation (BOA) [151] is used in the vast majority of electronic structure calculations. Within the BOA, the total electronic-nuclear wavefunction ψ is assumed to be separable into a nuclear χ and electronic φ part. As the electrons move much faster than the nuclei due to their typically much smaller mass, we assume that the kinetic energy of the nuclei does not cause the excitation of the electrons to another electronic state, i.e., the adiabatic approximation. In other words, the motion of the electrons is not affected by the motion of the nuclei. Such an approximation is valid as long as the ratio of vibrational to electronic energies, E_{vib} to E_{elec}, which goes as the root of the electron-nuclear mass ratio, i.e., $E_{vib}/E_{elec} \approx \sqrt{m_e/M}$, is small [151] (see Appendix A for details).

Assuming this separability into an electronic problem only in φ and a nuclear problem only in χ, we make a product ansatz for the solution ψ_k of the electron-nuclear stationary Schrödinger equation, Eq. 2.9, as

$$\begin{aligned}&\psi_k(\mathbf{R}_1 S_1, \mathbf{R}_2 S_2, ...\mathbf{R}_N S_N; \mathbf{r}_1 s_1, \mathbf{r}_2 s_2 ...\mathbf{r}_n s_n) \\ &= \chi(\mathbf{R}_1 S_1, \mathbf{R}_2 S_2, ...\mathbf{R}_N S_N)\varphi^{(\mathbf{R}_1, \mathbf{R}_2, ...\mathbf{R}_N)}(\mathbf{r}_1 s_1, \mathbf{r}_2 s_2 ...\mathbf{r}_n s_n),\end{aligned} \tag{2.11}$$

where χ depends on the nuclear coordinates only and φ depends on both the electronic coordinates and on the nuclear coordinates which, however, only enter in the electronic wavefunctions as parameters.

In the first step of the BOA procedure one solves the "frozen-nuclei" Schrödinger equation for the electronic wavefunction φ

$$\begin{aligned}&\hat{H}_e(\mathbf{R},\mathbf{r})\varphi_i^{(\mathbf{R}_1,\mathbf{R}_2,...\mathbf{R}_N)}(\mathbf{r}_1 s_1,\mathbf{r}_2 s_2...\mathbf{r}_n s_n)\\&=\varepsilon_i(\mathbf{R}_1,\mathbf{R}_2,...\mathbf{R}_N)\varphi_i^{(\mathbf{R}_1,\mathbf{R}_2,...\mathbf{R}_N)}(\mathbf{r}_1 s_1,\mathbf{r}_2 s_2...\mathbf{r}_n s_n),\end{aligned} \tag{2.12}$$

where the nuclear coordinates $\mathbf{R}_\alpha$ are fixed classically as parameters. Here

$$\hat{H}_e=\hat{T}_e+\hat{V}_{Ie}+\hat{V}_{ee}+\hat{V}_{II}. \tag{2.13}$$

The corresponding eigenvalues give the i^{th} potential energy surfaces $\varepsilon_i(\mathbf{R}_1,\mathbf{R}_2,...\mathbf{R}_N)$ (PESs). The PES's are representations of the electronic energy of the system as a function of the positions of the nuclei. Note that we neglect the effect of the kinetic energy of the nuclei $\hat{T}_I=0$ from Eq. 2.10, although the electrons still feel the static field of the nuclei ($\hat{V}_{eI},\hat{V}_{II}\neq 0$).

In the second step of the BOA procedure, the nuclear kinetic energy ($\hat{T}_I\neq 0$) is reintroduced by adding its contribution to the PESs obtained from the "frozen-nuclei" Schrödinger equation

$$\begin{aligned}&\hat{H}_I^i\chi_{i,j}(\mathbf{R}_1 S_1,\mathbf{R}_2 S_2,...\mathbf{R}_N S_N)\\&=\varepsilon_{i,j}\chi_{i,j}(\mathbf{R}_1 S_1,\mathbf{R}_2 S_2,...\mathbf{R}_N S_N),\end{aligned} \tag{2.14}$$

where

$$\hat{H}_I^i=\sum_{\alpha=1}^{N}-\frac{1}{2M_\alpha}\nabla_\alpha^2+\varepsilon_i(\mathbf{R}_1,\mathbf{R}_2,...\mathbf{R}_N), \tag{2.15}$$

and the nuclear excitations j depend on the excited i electronic PES.

From Eqs. 2.12 and 2.13 the electronic "frozen-nuclei" Schrödinger equation in the BOA is given by

$$\begin{aligned}\hat{H}_e\psi_n=&\chi\sum_{i=1}^{n}\left(-\frac{1}{2}\nabla_i^2\varphi\right)+\chi(\hat{V}_{Ie}+\hat{V}_{ee}+\hat{V}_{II})\varphi\\&=\chi\left[\left(\sum_{i=1}^{n}\left(-\frac{1}{2}\nabla_i^2\right)+\hat{V}_{Ie}+\hat{V}_{ee}+\hat{V}_{II}\right)\varphi\right]=\varepsilon_i(\mathbf{R}_1,\mathbf{R}_2,...\mathbf{R}_N)\psi_n.\end{aligned} \tag{2.16}$$

For the full electron-nuclear coupled problem we insert Eqs. 2.10 and 2.11 into Eq. 2.9 to obtain

$$
\begin{aligned}
\hat{H}\psi_n = &\sum_{\alpha=1}^{N}\left(-\frac{1}{2M_\alpha}\nabla_\alpha^2\chi\right)\varphi + \sum_{\alpha=1}^{N}\left(-\frac{2}{2M_\alpha}\nabla_\alpha\chi\cdot\nabla_\alpha\varphi\right) + \chi\sum_{\alpha=1}^{N}\left(-\frac{1}{2M_\alpha}\nabla_\alpha^2\varphi\right)\\
&+\chi\sum_{i=1}^{n}\left(-\frac{1}{2}\nabla_i^2\varphi\right) + \chi(\hat{V}_{Ie}+\hat{V}_{ee}+\hat{V}_{II})\varphi\\
&=\chi\left[\left(\sum_{i=1}^{n}\left(-\frac{1}{2}\nabla_i^2\right)+\hat{V}_{Ie}+\hat{V}_{ee}+\hat{V}_{II}\right)\varphi\right]\\
&+\sum_{\alpha=1}^{N}\left(-\frac{1}{2M_\alpha}\nabla_\alpha^2\chi\right)\varphi\\
&+\sum_{\alpha=1}^{N}\left(-\frac{1}{M_\alpha}\nabla_\alpha\chi\cdot\nabla_\alpha\varphi\right)+\chi\sum_{\alpha=1}^{N}\left(-\frac{1}{2M_\alpha}\nabla_\alpha^2\varphi\right) = E_n\psi_n.
\end{aligned}
\tag{2.17}
$$

Comparing the full quantum electron-nuclear Eq. 2.17 to the BOA Eqs. 2.15 and 2.16, we realise that the last two terms in Eq. 2.17 are neglected in the BOA. The kinetic energy of the nuclei is not affecting the electronic part φ, i.e., the BOA amounts to the assumption that $\nabla_\alpha\varphi \approx 0$.

The factorisation in Eq. 2.11 of the full electron-nuclear wavefunction can be made exact, both for static [184] and time-dependent situations [185], and is not intrinsic to BOA. In this case, however, the equations for which we obtain the solution of χ and φ, have a more complicated form.

2.1.2. Ehrenfest dynamics. Within the Ehrenfest dynamics (ED) scheme the electrons evolve according to the time-dependent Schrödinger equation (TDSE)

$$
i\frac{\partial}{\partial t}\varphi(\mathbf{R}_\alpha(t),\mathbf{r},t) = \hat{H}_e(\mathbf{R}_\alpha(t),t)\varphi(\mathbf{R}_\alpha(t),\mathbf{r},t),
\tag{2.18}
$$

which parametrically depends on the time-dependent coordinates $R_\alpha(t)$ of the nuclei.

The nuclei, in turn, evolve according to the following dynamic equation from Newton's second equation of motion

$$
\mathbf{F}_{ED}(\mathbf{R}_\alpha(t)) = M_\alpha\frac{d^2\mathbf{R}_\alpha(t)}{dt^2} = -\left\langle\varphi_i(\mathbf{r},\mathbf{R}_\alpha,t)\left|\nabla_\alpha H_e(\mathbf{R}_\alpha,\mathbf{r})\right|\varphi_i(\mathbf{r},\mathbf{R}_\alpha,t)\right\rangle.
\tag{2.19}
$$

The Ehrenfest electron-nuclear scheme consists of the time propagation of the coupled equations Eqs. 2.18 and 2.19.

2.2. Linear excitation spectra of H_2^+ and H_2 with quantum versus classical nuclei

As mentioned in Sec. 2.1, solving the full quantum time-dependent Schrödinger equation (TDSE) is computationally very demanding and the Born-Oppenheimer approximation (BOA) and Ehrenfest dynamics (ED) classical approaches are widely used to treat the nuclei. H_2^+ and H_2 are one and two electron diatomic molecules for which solving the TDSE is feasible, allowing us to test the validity of the classical approaches.

The aim of this project is to compare the linear response spectra obtained from both a quantum and classical nuclear treatment for quantum electrons. In the perturbative linear regime, the quantum nuclear changes induced by the external electromagnetic source should not be very strong and the classical approaches should be able to describe the spectra accurately. However, for light molecules such as H_2^+ and H_2, non-adiabatic couplings between the nuclei and electrons may be important and the classical approaches may not be able to describe the spectra accurately.

As the classical approximations rely on the fact that the ratio $E_{vib}/E_{elec} \approx \sqrt{m_e/M}$ is small (see Appendix A), I quantify their accuracy by fictitiously varying the nuclear mass M of our molecules for the quantum electron-nuclear problem [186]. As the nuclei's mass M increases, the quantum results should be consistent with the classical nuclear results.

I model these molecules in 1D and in the centre of mass coordinates [187], so that the numerical computational effort to carry out the calculations is largely reduced. The $3n$ electron and $3N$ nuclear coordinate problem in 3D is reduced to a n and N coordinate problem in 1D. Within the centre of mass transformation the centre of mass motion is exactly separated out (see Appendix B), thus further reducing the number of coordinates.

To model in 1D the interactions between any type of particles I use the so called "Soft Coulomb interaction", which for particles i and j with charges Z_i and Z_j has the general form

$$V_{int}(x_i - x_j) = \frac{Z_i Z_j}{\sqrt{(x_i - x_j)^2 + \Delta^2}}, \tag{2.20}$$

where Δ is the Soft Coulomb parameter [188]. The reason for using this modified interaction is that the bare Coulomb interaction is singular in 1D. This may lead to physically pathological features such as, e.g., an infinite ground state energy of the 1D H atom as $\Delta \to 0$.

2.2.1. Initial configurations. In Fig. 2.1 I show four and three possible configurations that I have tested for the H_2^+ and H_2 molecules, as a function of the Soft Coulomb parameter between the nuclei Δ_{II}, the electrons Δ_{ee} and the nuclei and electrons Δ_{Ie}. As the most probable electron-proton separation in a hydrogen atom is the Bohr radius a_0, I have tested Soft Coulomb parameter values within this distance range.

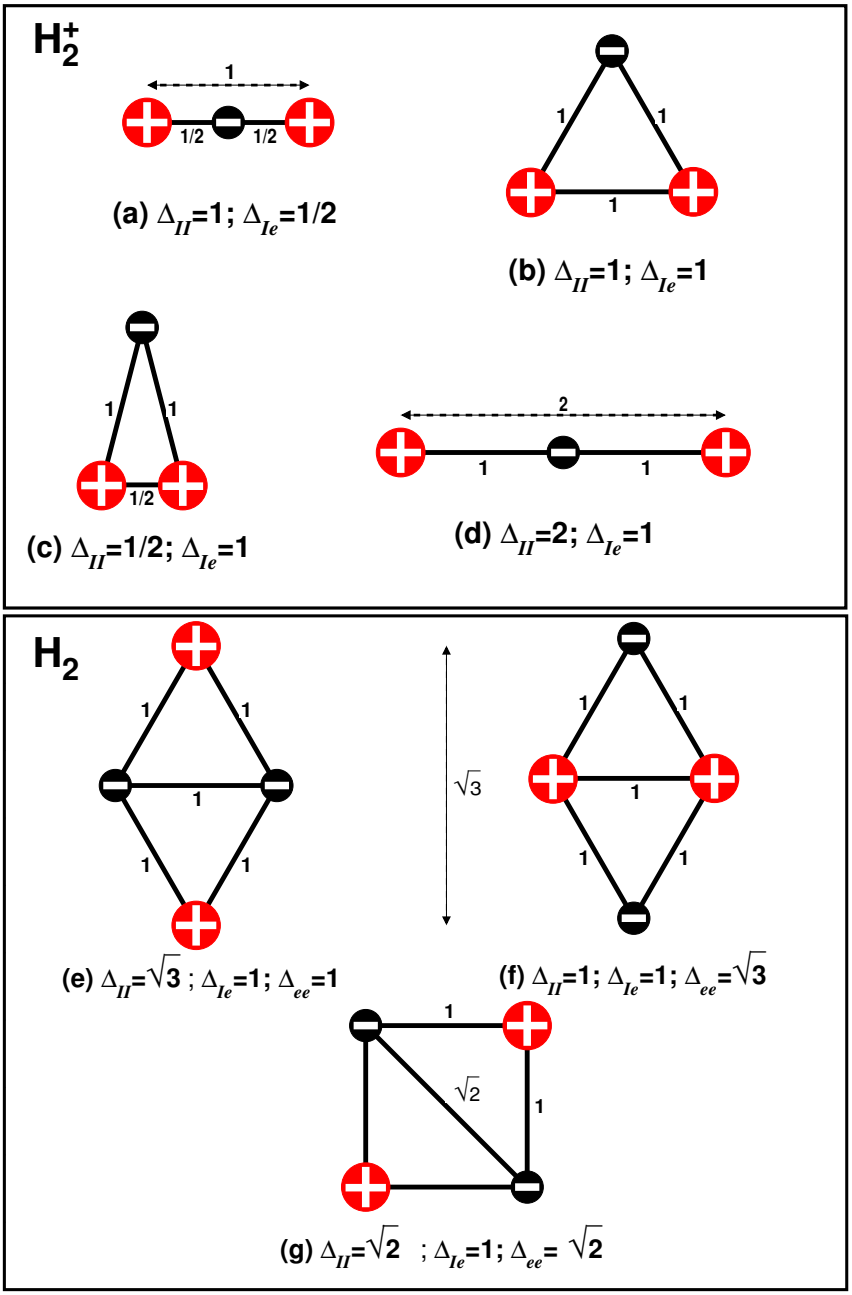

FIGURE 2.1. Schematic representation of the (a–d) H_2^+ and (e–g) H_2 geometries for the nuclear–nuclear separation Δ_{II}, nuclear–electron separation Δ_{Ie}, and electron–electron separation Δ_{ee} for each configuration. Protons are shown in red and electrons in black.

All the configurations I have analysed are symmetric under exchange of identical particles (see Sec. 2.2.3). One such configuration has been used previously [189] to study the dynamics of a one-dimensional H_2 model molecule in strong laser fields by means of quantum nuclei.

2.2.2. Hamiltonians in the centre of mass. The classical energies of the one-dimensional homonuclear H_2^+ and H_2 molecules in 1D are given by

$$\begin{aligned} E_{H_2^+} = &\frac{1}{2}MV_1^2 + \frac{1}{2}MV_2^2 + \frac{1}{2}\tilde{v}^2 - \frac{1}{\sqrt{(\tilde{x}-X_1)^2+\Delta_{Ie}^2}} \\ &- \frac{1}{\sqrt{(X_2-\tilde{x})^2+\Delta_{Ie}^2}} + \frac{1}{\sqrt{(X_2-X_1)^2+\Delta_{II}^2}}, \end{aligned} \tag{2.21}$$

and

$$\begin{aligned} E_{H_2} = &\frac{1}{2}MV_1^2 + \frac{1}{2}MV_2^2 + \frac{1}{2}v_1^2 + \frac{1}{2}v_2^2 \\ &- \frac{1}{\sqrt{(x_1-X_1)^2+\Delta_{Ie}^2}} - \frac{1}{\sqrt{(X_2-x_2)^2+\Delta_{Ie}^2}} \\ &- \frac{1}{\sqrt{(x_2-X_1)^2+\Delta_{Ie}^2}} - \frac{1}{\sqrt{(X_2-x_1)^2+\Delta_{Ie}^2}} \\ &+ \frac{1}{\sqrt{(X_2-X_1)^2+\Delta_{II}^2}} + \frac{1}{\sqrt{(x_2-x_1)^2+\Delta_{ee}^2}}, \end{aligned} \tag{2.22}$$

respectively. Here, M is the nuclear mass; V_1, V_2, X_1 and X_2 are the proton velocities and positions for both molecules; $\tilde{v}$ and $\tilde{x}$ are the electron velocity and position for H_2^+ and v_1, v_2, x_1, x_2 are the electron velocities and positions for H_2.

The first three and four terms of Eqs. 2.21 and 2.22 are the kinetic energies of the electrons and nuclei and molecules explained above. The remaining terms correspond to the attractive and repulsive electrostatic potential energy terms between such electrons and nuclei.

In the centre of mass, the spatial configuration of any molecule does not change if the particle positions are translated uniformly. This reduces our three- and four-body coordinate problems for the H_2^+ and H_2 molecules into two- and three-body ones, respectively.

We rewrite the classical energy in Eq. 2.21 and 2.22 in terms of the centre-of-mass transformation (see Appendix B) to obtain the following two-body (X,$\tilde{\xi}$) and three-body (X,x,ξ) internal Hamiltonians in the centre of mass frame

$$\begin{aligned}\hat{H}(X,\tilde{\xi})_{H_2^+} = &-\frac{1}{M}\frac{\partial^2}{\partial X^2} - \frac{2M+1}{4M}\frac{\partial^2}{\partial \tilde{\xi}^2} - \frac{1}{\sqrt{\left(\frac{X}{2}+\tilde{\xi}\right)^2+\Delta_{Ie}^2}} \\ &- \frac{1}{\sqrt{\left(\frac{X}{2}-\tilde{\xi}\right)^2+\Delta_{Ie}^2}} + \frac{1}{\sqrt{X^2+\Delta_{II}^2}},\end{aligned} \tag{2.23}$$

and

$$\begin{aligned}\hat{H}(X,x,\xi)_{H_2} = &-\frac{1}{M}\frac{\partial^2}{\partial X^2} - \frac{\partial^2}{\partial x^2} - \frac{1+M}{4M}\frac{\partial^2}{\partial \xi^2} \\ &- \frac{1}{\sqrt{\left(\frac{X}{2}-\frac{x}{2}+\xi\right)^2+\Delta_{Ie}^2}} - \frac{1}{\sqrt{\left(\frac{X}{2}-\frac{x}{2}-\xi\right)^2+\Delta_{Ie}^2}} \\ &- \frac{1}{\sqrt{\left(\frac{X}{2}+\frac{x}{2}+\xi\right)^2+\Delta_{Ie}^2}} - \frac{1}{\sqrt{\left(\frac{X}{2}+\frac{x}{2}-\xi\right)^2+\Delta_{Ie}^2}} \\ &+ \frac{1}{\sqrt{x^2+\Delta_{ee}^2}} + \frac{1}{\sqrt{X^2+\Delta_{II}^2}},\end{aligned} \tag{2.24}$$

for the H_2^+ and H_2 molecules, respectively, after removing the centre of mass term. Here the internal coordinates are given by

$$\tilde{\xi} = \tilde{x} - \frac{X_1+X_2}{2}; \xi = \frac{x_1+x_2}{2} - \frac{X_1+X_2}{2}; x = x_2 - x_1; X = X_2 - X_1. \tag{2.25}$$

2.2.3. Symmetries of the wavefunctions. Both electrons and protons are fermions. Due to the Pauli exclusion principle, the wavefunction of a system of two or more identical fermions must be antisymmetric with respect to exchange of any pair of identical fermions.

Since in the H_2^+ molecules there are one electron and two protons, the antisymmetry of the many-body wavefunction must be enforced for the protons only as

$$\psi_{H_2^+}(X_1S_1, X_2S_2, \tilde{x}\tilde{s}) = -\psi_{H_2^+}(X_2S_2, X_1S_1, \tilde{x}\tilde{s}). \tag{2.26}$$

For the H_2 molecule there are two electrons and two protons, therefore, the antisymmetry of the many-body wavefunction must be enforced both for the protons and the electrons as

$$\psi_{H_2}(X_1S_1, X_2S_2, x_1s_1, x_2s_2) = -\psi_{H_2}(X_2S_2, X_1S_1, x_1s_1, x_2s_2), \tag{2.27}$$

and

$$\psi_{H_2}(X_1S_1, X_2S_2, x_1s_1, x_2s_2) = -\psi_{H_2}(X_1S_1, X_2S_2, x_2s_2, x_1s_1), \tag{2.28}$$

respectively.

For two identical particles the many-body wavefunction can be factorised into a spin and spatial part as

$$\psi_{H_2^+}(X_1 S_1, X_2 S_2, \tilde{x}\tilde{s}) = \psi_{H_2^+}(X_1 X_2, \tilde{x})|\tilde{s}m\rangle_e |S\,M\rangle_n, \tag{2.29}$$

for H_2^+ and

$$\psi_{H_2}(X_1 S_1, X_2 S_2, x_1 s_1, x_2 s_2) = \psi_{H_2}(X_1 X_2, x_1 x_2)|sm\rangle_e |S\,M\rangle_n, \tag{2.30}$$

for H_2 where the subscripts "e" and "n" refer to electronic and nuclear spin coordinates, respectively. For spin $\frac{1}{2}$ fermions, the single particle spin basis functions are denoted as $|\uparrow\rangle_\gamma, |\downarrow\rangle_\gamma$ with $\gamma \in \{e, n\}$.

For H_2^+ we only have a single electron with a spin of $\frac{1}{2}$. This unpaired electron can be orientated $|\uparrow\rangle_\gamma, |\downarrow\rangle_\gamma$, so that we have two resulting spin states for $\frac{1}{2}$ and $-\frac{1}{2}$, i.e a doublet. For H_2^+ we have a pair of protons with a spin of $\frac{1}{2}$ which can combine in different ways. The single possible combination of these spin states that leads to a total spin quantum number value equal to zero is called a singlet state. The three possible combinations of these spin states that lead to a total spin quantum number value equal to one are called triplet states. For H_2 we have a pair of both protons and electrons. Therefore, in this case we can obtain triplets and singlets for both the electrons and protons.

The singlet state is given by

$$\left.\begin{aligned} |0,0\rangle_\gamma = \tfrac{1}{\sqrt{2}}(|\uparrow,\downarrow\rangle_\gamma - |\downarrow,\uparrow\rangle_\gamma) \end{aligned}\right\} S = 0 \text{ (singlet)}, \tag{2.31}$$

while the three triplet states are

$$\left.\begin{aligned} |1,-1\rangle_\gamma &= |\downarrow,\downarrow\rangle_\gamma \\ |1,0\rangle_\gamma &= \tfrac{1}{\sqrt{2}}(|\uparrow,\downarrow\rangle_\gamma + |\downarrow,\uparrow\rangle_\gamma) \\ |1,1\rangle_\gamma &= |\uparrow,\uparrow\rangle_\gamma \end{aligned}\right\} S = 1 \text{ (triplet)}. \tag{2.32}$$

If the particles are exchanged, the singlet state changes sign (antisymmetric) while the sign of the triplet state remains unchanged (symmetric). Therefore, in order to have a total antisymmetric many-body wavefunction, the spatial part of the nuclear and electronic wavefunction must be antisymmetric for the triplet state and symmetric for the singlet state.

As a consequence, I will only be concerned with the spatial part of the wavefunction, the spin part already being separated off due to the exchange symmetry of the many-body wavefunction.

The antisymmetry in the nuclear coordinates requires that the spatial part in the centre of mass frame of the H_2^+ wavefunction in the nuclear singlet state in 1D is

$$\psi_{H_2^+}(X, \tilde{\xi}) = \psi_{H_2^+}(-X, \tilde{\xi}), \tag{2.33}$$

and similarly for the H_2 molecule

$$\psi_{H_2}(X, x, \xi) = \psi_{H_2}(-X, x, \xi). \tag{2.34}$$

For H_2, the antisymmetry in the electronic coordinates requires that the spatial part in the centre of mass frame of the H_2 wavefunction in the electronic singlet state in 1D is

$$\psi_{H_2}(X, x, \xi) = \psi_{H_2}(X, -x, \xi). \tag{2.35}$$

Similarly, in the nuclear triplet state we have with respect to the antisymmetry of the nuclear coordinates

$$\psi_{H_2^+}(X, \tilde{\xi}) = -\psi_{H_2^+}(-X, \tilde{\xi}), \tag{2.36}$$

for H_2^+ and

$$\psi_{H_2}(X, x, \xi) = -\psi_{H_2}(-X, x, \xi), \tag{2.37}$$

for H_2 and for the electronic triplet state the antisymmetry in the electronic coordinates

$$\psi_{H_2}(X, x, \xi) = -\psi_{H_2}(X, -x, \xi), \tag{2.38}$$

for H_2.

2.2.4. Born-Oppenheimer approximation in the one-dimensional centre of mass. Within the Born-Oppenheimer approximation (BOA) in the centre of mass in 1D, Eq. 2.11 becomes

$$\psi(X, \tilde{\xi}) = \psi_{i,j}(X, \tilde{\xi}) = \chi_{i,j}(X)\varphi_i(X, \tilde{\xi}), \tag{2.39}$$

for H_2^+ and

$$\psi(X, x, \xi) = \psi_{i,j}(X, x, \xi) = \chi_{i,j}(X)\varphi_i(X, x, \xi), \tag{2.40}$$

for H_2 where $\varphi_i(X, \tilde{\xi})$ and $\varphi_i(X, x, \xi)$ are the i^{th} eigenfunctions of the "frozen nuclear" (X is fixed as a parameter) Schrödinger equations

$$\hat{H}_e(X, \tilde{\xi})\varphi_i(X, \tilde{\xi}) = \varepsilon_i(X)\varphi_i(X, \tilde{\xi}), \tag{2.41}$$

and

$$\hat{H}_e(X, x, \xi)\varphi_i(X, x, \xi) = \varepsilon_i(X)\varphi_i(X, x, \xi), \tag{2.42}$$

from which we solve for the electronic eigenstates at fixed internuclear distances X to obtain the potential energy surfaces (PES) $\varepsilon_i(X)$.

Here, we have defined the electronic "frozen nuclear" BOA Hamiltonian for H_2^+ as

$$\hat{H}_e(X,\tilde{\xi}) = -\frac{2M+1}{4M}\frac{\partial^2}{\partial\tilde{\xi}^2} - \frac{1}{\sqrt{\left(\frac{X}{2}+\tilde{\xi}\right)^2+\Delta_{Ie}^2}} - \frac{1}{\sqrt{\left(\frac{X}{2}-\tilde{\xi}\right)^2+\Delta_{Ie}^2}} + \frac{1}{\sqrt{X^2+\Delta_{II}^2}}, \quad (2.43)$$

and for H_2 as

$$\begin{aligned}\hat{H}_e(X,x,\xi) = &-\frac{\partial^2}{\partial x^2} - \frac{1+M}{4M}\frac{\partial^2}{\partial\xi^2} - \frac{1}{\sqrt{\left(\frac{X}{2}-\frac{x}{2}+\xi\right)^2+\Delta_{Ie}^2}} \\ &- \frac{1}{\sqrt{\left(\frac{X}{2}-\frac{x}{2}-\xi\right)^2+\Delta_{Ie}^2}} - \frac{1}{\sqrt{\left(\frac{X}{2}+\frac{x}{2}+\xi\right)^2+\Delta_{Ie}^2}} \\ &- \frac{1}{\sqrt{\left(\frac{X}{2}+\frac{x}{2}-\xi\right)^2+\Delta_{Ie}^2}} + \frac{1}{\sqrt{X^2+\Delta_{II}^2}} + \frac{1}{\sqrt{x^2+\Delta_{ee}^2}},\end{aligned} \quad (2.44)$$

and $\chi_{i,j}(X)$ is the j^{th} eigenfunction of the effective nuclear Schrödinger equation

$$\hat{H}_I^i(X)\chi_{i,j}(X) = \varepsilon_{i,j}\chi_{i,j}(X), \quad (2.45)$$

where for both molecules

$$\hat{H}_I^i(X) = -\frac{1}{M}\frac{\partial^2}{\partial X^2} + \varepsilon_i(X). \quad (2.46)$$

2.2.5. Modelling the time-dependent linear response spectra for H_2^+ and H_2. To obtain the linear response photoexcitation spectra I apply an initial external impulsive perturbation, or "kick" [190]

$$\begin{aligned}\mathcal{K}(H_2^+) &= \exp\left(iK(X_1+X_2-\tilde{x})\right), \\ \mathcal{K}(H_2) &= \exp\left(iK(X_1+X_2-x_1-x_2)\right),\end{aligned} \quad (2.47)$$

to the ground state wavefunctions ψ_{gs} of our H_2^+ and H_2 molecules, respectively, for the fixed classical nuclear Born-Oppenheimer approximation (BOA) and quantum nuclear approaches. K is a measure of the strength of the kick. I employ a converged kick strength of $K = 0.001$, for which the linear response spectra does not change if it is decreased further.

Using the centre of mass coordinates defined in Appendix B, the terms in Eq. 2.47 become

$$\begin{aligned}\mathcal{K}(H_2^+) &= \exp\left(iK\left(\tilde{X}_{CM_2} - \frac{2M+2}{2M+1}\tilde{\xi}\right)\right), \\ \mathcal{K}(H_2) &= \exp(-iK2\xi),\end{aligned} \quad (2.48)$$

where $\tilde{X}_{CM_2}$ is the global centre of mass coordinate for H_2^+, ξ is the separation between the nuclear and electronic centres of mass for H_2 and $\tilde{\xi}$ the separation between the electron and the centre of mass of the nuclei for H_2^+. The external perturbative kick $\mathcal{K}$ will only induce polarisation on the coordinates ξ and $\tilde{\xi}$ defined for H_2^+ and H_2 in Eqs. B.10 and B.33 for the fixed classical BOA and quantum nuclear methods.

In linear response for small K, we expand Eq. 2.48 in terms of K, neglecting higher order terms

$$\begin{aligned}\mathcal{K}(H_2^+) &\approx 1 + iK\left(\tilde{X}_{CM_2} - \frac{2M+2}{2M+1}\tilde{\xi}\right) + O(K^2),\\ \mathcal{K}(H_2) &\approx 1 - iK2\xi + O(K^2).\end{aligned} \tag{2.49}$$

Note that for the first term in Eq. 2.49, $\frac{2M+2}{2M+1}\tilde{\xi} \approx \tilde{\xi}$ when $M \gg 1$, for H_2^+.

For the Ehrenfest dynamics (ED) approach one should follow the same procedure, but using

$$\begin{aligned}\mathcal{K}(H_2^+) &= \exp\left(iK(-\tilde{x})\right),\\ \mathcal{K}(H_2) &= \exp(iK(-x_1 - x_2)).\end{aligned} \tag{2.50}$$

Here I do not use the centre of mass transformation coordinates, as during the time propagation the ions X are not fixed, but evolve as parameters according to Eq. 2.19. The electron is kicked relative to the centre of mass of the nuclei for the H_2^+ molecule, as is the case for the fixed BOA and quantum nuclear approaches. The two electrons are kicked relative to their distance to the nuclei for the H_2 molecule. For the fixed classical BOA and quantum nuclei I kicked the centre of mass of the electrons relative to the centre of mass of the nuclei. However, the linear response absorption spectra does not depend on uniform translations of the nuclei and electrons, so the different kicking effect can be disregarded. The reader can refer to Appendix C to find the ED modelling details.

I apply the enforced time-reversal symmetry evolution operator [191] to propagate our equations after this external perturbation has been applied to the ground state wavefunction. This operator is given by

$$U(t+\Delta t, t) = \exp\left(-i\frac{\Delta t}{2}H(t+\Delta t)\right)\exp\left(-i\frac{\Delta t}{2}H(t)\right), \tag{2.51}$$

and the kicked initial state I propagate is

$$\psi(t) = U(t+\Delta t, t)\psi(t=0) = U(t+\Delta t, t)\mathcal{K}\psi_{gs} = \exp(-i\Delta t H_0)\mathcal{K}\psi_{gs}, \tag{2.52}$$

where ψ_{gs} is the ground state eigenstate of the time independent Hamiltonian $H_0 = H(t+\Delta t) = H(t)$ of Eqs. 2.23 and 2.24 and Eqs. 2.43 and 2.44 for H_2^+ and H_2 , for the quantum and classical BOA problems respectively. For the ED problem, the Hamiltonians are

shown in Appendix C. As explained in the previous paragraph, the ED Hamiltonians are equivalent to the BOA ones.

Introducing the applied external field kick contribution $\mathcal{K}$ given in Eq. 2.49 and the static equation for ψ_{gs} given in Eq. 2.8 into Eq. 2.52 we get

$$|\psi(t)\rangle \approx \exp(-i\varepsilon_{gs}t)|\psi_{gs}\rangle - iK\sum_k \exp(-i\varepsilon_k t)\left\langle \psi_k \left| \frac{2M+2}{2M+1}\hat{\tilde{\xi}} \right| \psi_{gs} \right\rangle |\psi_k\rangle, \tag{2.53}$$

for the H_2^+ molecule and

$$|\psi(t)\rangle \approx \exp(-i\varepsilon_{gs}t)|\psi_{gs}\rangle - iK\sum_k \exp(-i\varepsilon_k t)\left\langle \psi_k \left| 2\hat{\xi} \right| \psi_{gs} \right\rangle |\psi_k\rangle, \tag{2.54}$$

for the H_2 molecule, using the completeness relation $\sum_k |\psi_k\rangle\langle\psi_k| = \mathbb{1}$.

The "kick" $\mathcal{K}$ is applied to the ground state wavefunction ψ_{gs} and it introduces excited state wavefunctions ψ_k. All the final states I have after this "kick" are then propagated in time via Eq. 2.51. The initial ground state ψ_{gs} is even in the $\tilde{\xi}$ and ξ coordinates. From Eqs. 2.53 and 2.54, we see that only the even ψ_{gs} to odd ψ_k dipole moment matrix elements are non-zero by parity, since $\hat{\tilde{\xi}}$ and $\hat{\xi}$ are odd operators.

When an external "kick" is applied, a dipole moment is induced in the molecule which will oscillate back and forth with time. The dipole moment is a measure of the charge separation induced due to the application of the "kick" between an initial and a final electronic state. The expectation value of the dipole moment $d(t)$ at time t is

$$d(t) = \langle\psi(t)|\hat{\tilde{\xi}}|\psi(t)\rangle, \tag{2.55}$$

for H_2^+ and

$$d(t) = \langle\psi(t)|\hat{\xi}|\psi(t)\rangle, \tag{2.56}$$

for H_2.

Eq. 2.55 can be written as

$$
\begin{aligned}
d(t) \approx & \left[\langle\psi_{gs}|\exp(i\varepsilon_{gs}t) + iK\sum_k \exp(i\varepsilon_k t)\left\langle\psi_{gs}\left|\frac{2M+2}{2M+1}\hat{\xi}\right|\psi_k\right\rangle\langle\psi_k|\right] \\
& \times \frac{2M+2}{2M+1}\hat{\xi}\left[\exp(-i\varepsilon_{gs}t)|\psi_{gs}\rangle - iK\sum_k \exp(-i\varepsilon_k t)\left\langle\psi_k\left|\frac{2M+2}{2M+1}\hat{\xi}\right|\psi_{gs}\right\rangle|\psi_k\rangle\right] \\
\approx & -iK\sum_k \exp(i(\varepsilon_{gs}-\varepsilon_k)t)\left\langle\psi_{gs}\left|\frac{2M+2}{2M+1}\hat{\xi}\right|\psi_k\right\rangle\left\langle\psi_k\left|\frac{2M+2}{2M+1}\hat{\xi}\right|\psi_{gs}\right\rangle \\
& + iK\sum_k \exp(i(\varepsilon_k-\varepsilon_{gs})t)\left\langle\psi_k\left|\frac{2M+2}{2M+1}\hat{\xi}\right|\psi_{gs}\right\rangle\left\langle\psi_{gs}\left|\frac{2M+2}{2M+1}\hat{\xi}\right|\psi_k\right\rangle \\
\approx & + iK\sum_k \left[\exp(i(\varepsilon_k-\varepsilon_{gs})t)\left|\left\langle\psi_k\left|\frac{2M+2}{2M+1}\hat{\xi}\right|\psi_{gs}\right\rangle\right|^2\right. \\
& \left. - \exp(i(\varepsilon_{gs}-\varepsilon_k)t)\left|\left\langle\psi_{gs}\left|\frac{2M+2}{2M+1}\hat{\xi}\right|\psi_k\right\rangle\right|^2\right] \\
\approx & + iK\sum_k [\cos(\omega_k t) + i\sin(\omega_k t) - \cos(\omega_k t) + i\sin(\omega_k t)] \\
& \times \left|\left\langle\psi_k\left|\frac{2M+2}{2M+1}\hat{\xi}\right|\psi_{gs}\right\rangle\right|^2 \approx -2K\frac{2M+2}{2M+1}\sum_k \sin\omega_k t\left|\left\langle\psi_k\left|\hat{\xi}\right|\psi_{gs}\right\rangle\right|^2,
\end{aligned}
\tag{2.57}
$$

for the H_2^+ molecule using Eq. 2.53, the Euler formula $\exp(i\omega_k t) = \cos(\omega_k t) + i\sin(\omega_k t)$ and $\omega_k \equiv (\varepsilon_k - \varepsilon_{gs})$. Note that $d(t)$ depends linearly on K.

Following the same procedure for the H_2 molecule and using Eq. 2.54 we find that the dipole moment is

$$
d(t) \approx -4K\sum_k \sin\omega_k t\left|\left\langle\psi_k\left|\hat{\xi}\right|\psi_{gs}\right\rangle\right|^2. \tag{2.58}
$$

Within ED the final dipole moments are

$$
d(t) \approx 2K\sum_k \sin\omega_k t\left|\left\langle\psi_k\left|\hat{x}\right|\psi_{gs}\right\rangle\right|^2, \tag{2.59}
$$

for the H_2^+ molecule and

$$
d(t) \approx 2K\sum_k \sin\omega_k t\left|\left\langle\psi_k\left|(\hat{x}_1+\hat{x}_2)\right|\psi_{gs}\right\rangle\right|^2, \tag{2.60}
$$

for the H_2 molecule.

The optical photoabsorption cross section spectra σ_{abs} is obtained by performing a discrete Fourier transform of $d(t)$ [192]. More precisely,

$$\sigma_{abs} = 4\pi\alpha\omega \mathrm{Im}\left[\frac{1}{K}\sum_{t=0}^{T}\Delta t \exp(-i\omega t) f\left(\frac{t}{T}\right)[d(t) - d(0)]\right], \tag{2.61}$$

where

$$f\left(\frac{t}{T}\right) = \exp\left(-25\left(\frac{t}{T}\right)^2\right), \tag{2.62}$$

is a Gaussian damping applied to improve the resolution of the photoabsorption peaks, ω is the frequency of the oscillations of $d(t)$, α is the fine structure constant, T is the total propagation time, and Δt is the time step.

2.3. Density functional theory approach to the many-electron problem

In most electronic structure calculations, one typically neglects the nuclear motion and starts from the Born-Oppenheimer approximation (BOA) using fixed nuclear coordinates. However, even if we neglect the nuclear part, the solution of the problem of many interacting electrons (Eq. 2.12 in the static case or Eq. 2.18 in the time-dependent case) is highly non-trivial and can in practice only be done for fairly small electron number systems. Density functional theory (DFT) offers an alternative approach to the many-electron problem, both for static and time-dependent situations.

2.3.1. Static density functional theory. Density functional theory (DFT) is an electronic quantum mechanical theory which allows us to describe the many-body electronic problem directly in terms of the electronic ground state density without the need of calculating the many-body wavefunction.

The Hamiltonian of n interacting electrons moving in an arbitrary static external potential $\hat{V}_{ext}$ is

$$\hat{H} = \hat{T}_e + \hat{V}_{ee} + \hat{V}_{ext}, \tag{2.63}$$

where $\hat{T}_e$ and $\hat{V}_{ee}$ were defined in Eqs. 2.3 and 2.5, and the operator of the external potential is

$$\hat{V}_{ext} = \sum_{i=1}^{n} V_{ext}(\mathbf{r}_i). \tag{2.64}$$

The many-electron Schrödinger equation for the electronic ground state $\varphi(\mathbf{r}_1 \cdots \mathbf{r}_n)$ is

$$\hat{H}\varphi(\mathbf{r}_1 \cdots \mathbf{r}_n) = E\varphi(\mathbf{r}_1 \cdots \mathbf{r}_n), \tag{2.65}$$

and the electronic ground state density $\rho(\mathbf{r})$ is defined as

$$\rho(\mathbf{r}) = n \int d^3\mathbf{r}_2 ... d^3\mathbf{r}_n |\varphi(\mathbf{r}, \mathbf{r}_2 ... \mathbf{r}_n)|^2. \tag{2.66}$$

All observable properties of a many-body system are determined by the external potential $\hat{V}_{ext}$ because the other two terms in Eq. 2.63 are only density dependent. The central theorem of static DFT, the Hohenberg-Kohn (HK) theorem [193], states that there is a one to one correspondence between external potentials $V_{ext}(\mathbf{r})$ and ground state densities $\rho(\mathbf{r})$. Two external potentials, V_{ext} and V'_{ext}, which differ by more than an arbitrary additive constant, $V'_{ext} \neq V_{ext} + const.$, lead to different ground state densities. The Schrödinger equations for the ground states of these two external potentials are

$$\begin{aligned} \hat{H}\varphi &= (\hat{T}_e + \hat{V}_{ee} + \hat{V}_{ext})\varphi = E\varphi, \\ \hat{H}'\varphi' &= (\hat{T}_e + \hat{V}_{ee} + \hat{V}'_{ext})\varphi' = E'\varphi'. \end{aligned} \tag{2.67}$$

The proof of the HK theorem is by *reductio and absurdum*. We assume that the different potentials $\hat{V}_{ext}, \hat{V}'_{ext}$ lead to the same ground state density ($\rho(\mathbf{r}) = \rho'(\mathbf{r})$) and show that this leads to a contradiction. We assume that the ground states of $\hat{H}$ and $\hat{H}'$ are non-degenerate. Then, by virtue of the Rayleigh-Ritz variational principle we can write for the ground state energy E of $\hat{H}$

$$\begin{aligned} E &= \langle\varphi|\hat{H}|\varphi\rangle < \langle\varphi'|\hat{H}|\varphi'\rangle = \langle\varphi'|\hat{H}' + \hat{V}_{ext} - \hat{V}'_{ext}|\varphi'\rangle \\ &= \langle\varphi'|\hat{H}'|\varphi'\rangle + \langle\varphi'|\hat{V}_{ext} - \hat{V}'_{ext}|\varphi'\rangle = E' + \langle\varphi'|\hat{V}_{ext} - \hat{V}'_{ext}|\varphi'\rangle \\ &= E' + \int d^3\mathbf{r}\rho'(\mathbf{r})(V_{ext}(\mathbf{r}) - V'_{ext}(\mathbf{r})). \end{aligned} \tag{2.68}$$

Similarly, we obtain for the ground state energy E' of $\hat{H}'$

$$\begin{aligned} E' &= \langle\varphi'|\hat{H}'|\varphi'\rangle < \langle\varphi|\hat{H}'|\varphi\rangle = \langle\varphi|\hat{H} + \hat{V}'_{ext} - \hat{V}_{ext}|\varphi\rangle \\ &= \langle\varphi|\hat{H}|\varphi\rangle + \langle\varphi|\hat{V}'_{ext} - \hat{V}_{ext}|\varphi\rangle = E + \langle\varphi|\hat{V}'_{ext} - \hat{V}_{ext}|\varphi\rangle \\ &= E + \int d^3\mathbf{r}\rho(\mathbf{r})(V'_{ext}(\mathbf{r}) - V_{ext}(\mathbf{r})). \end{aligned} \tag{2.69}$$

Adding Eqs. 2.68 and 2.69 while assuming that the ground state densities are equal, ($\rho(\mathbf{r}) = \rho'(\mathbf{r})$), we find that $E + E' < E' + E$ which is a contradiction. Therefore, the ground state densities corresponding to two different external potentials differ. The ground state density uniquely determines the external potential, which via the many electron Schrödinger equation 2.65 determines the eigenstates of the system.

This then means that the expectation value of any quantum mechanical operator, such as the ones in Eq. 2.63 with respect to the ground state or any other eigenstate of $\hat{H}$, is an explicit functional of the ground state density alone.

For a given fixed external potential $\hat{V}_{ext}(\mathbf{r})$, we can now write the ground state energy as a functional of the density, i.e.,

$$E_{V_{ext}}[\rho] = \langle\varphi[\rho]|\hat{T} + \hat{V}_{ee}|\varphi[\rho]\rangle + \langle\varphi[\rho]|\hat{V}_{ext}|\varphi[\rho]\rangle = F_{HK}[\rho] + \int d^3\mathbf{r} V_{ext}(\mathbf{r})\rho(\mathbf{r}), \quad (2.70)$$

where we have defined the HK functional

$$F_{HK}[\rho] = \langle\varphi[\rho]|\hat{T} + \hat{V}_{ee}|\varphi[\rho]\rangle, \quad (2.71)$$

which is minimised in the sense that it does not depend on V_{ext}. The second statement of the HK theorem is a density variational principle which states that the ground state density $\rho_0(\mathbf{r})$ corresponding to the given V_{ext} can be obtained from

$$\left.\frac{\delta E_{V_{ext}}[\rho]}{\delta\rho(\mathbf{r})}\right|_{\rho=\rho_0(\mathbf{r})} = 0. \quad (2.72)$$

The HK proof goes through for any interaction $\hat{V}_{ee}$, in particular also for the non-interacting case $\hat{V}_{ee} = 0$. The total energy of n non-interacting electrons in an external potential $V_S(\mathbf{r})$ can then be written as

$$E^S_{V_S}[\rho] = T_S[\rho] + \int d^3\mathbf{r} V_S(\mathbf{r})\rho(\mathbf{r}), \quad (2.73)$$

where the non-interacting kinetic energy can be written explicitly in terms of non-interacting single-particle orbitals $\phi_i(\mathbf{r})$

$$T_S[\rho] = \sum_i^n \int d\mathbf{r}^3 \phi_i^*(\mathbf{r})\left(-\frac{\nabla^2}{2}\right)\phi_i(\mathbf{r}). \quad (2.74)$$

For non-interacting electrons, the density variational principle

$$\left.\frac{\delta E^S_{V_S}}{\delta\rho(\mathbf{r})}\right|_{\rho_0(\mathbf{r})} = \left.\frac{\delta T_S}{\delta\rho(\mathbf{r})}\right|_{\rho_0(\mathbf{r})} + V_S(\mathbf{r}) = 0, \quad (2.75)$$

is equivalent to solving the single-particle Schrödinger equation

$$\left[-\frac{\nabla^2}{2} + V_S(\mathbf{r})\right]\phi_i(\mathbf{r}) = \varepsilon_i\phi_i(\mathbf{r}), \quad (2.76)$$

and to calculating the ground state density from the n non-interacting single-particle orbitals

$$\rho_0(\mathbf{r}) = \sum_{i=1}^n |\phi_i(\mathbf{r})|^2. \quad (2.77)$$

This observation can be used to derive the Kohn-Sham (KS) scheme [194]. To this end we rewrite the energy functional of the interacting system in Eq. 2.70 by addition and subtraction as

$$E_{V_{ext}}[\rho] = T_S[\rho] + E_H[\rho] + E_{xc}[\rho] + \int d^3\mathbf{r} V_{ext}(\mathbf{r})\rho(\mathbf{r}), \tag{2.78}$$

where we have defined the classical electrostatic Hartree energy as

$$E_H[\rho] = \frac{1}{2}\int\int d^3\mathbf{r} d^3\mathbf{r}' \frac{\rho(\mathbf{r})\rho(\mathbf{r}')}{|\mathbf{r}-\mathbf{r}'|}, \tag{2.79}$$

and the exchange-correlation (xc) energy is

$$E_{xc}[\rho] = F_{HK}[\rho] - T_S[\rho] - E_H[\rho]. \tag{2.80}$$

From Eq. 2.75, the density variational principle in Eq. 2.72 becomes

$$0 = \left.\frac{\delta E^S_{V_{ext}}}{\delta\rho(\mathbf{r})}\right|_{\rho_0(\mathbf{r})} = \left.\frac{\delta T_S}{\delta\rho(\mathbf{r})}\right|_{\rho_0(\mathbf{r})} + V_S(\mathbf{r}). \tag{2.81}$$

From Eqs. 2.78 and 2.81, the effective potential is

$$V_S[\rho](\mathbf{r}) = V_{ext}(\mathbf{r}) + V_H[\rho_0](\mathbf{r}) + V_{xc}[\rho_0](\mathbf{r}), \tag{2.82}$$

where the Hartree potential is given by

$$V_H[\rho](\mathbf{r}) = \frac{\delta E_H[\rho]}{\delta\rho(\mathbf{r})} = \int d^3\mathbf{r}' \frac{\rho(\mathbf{r}')}{|\mathbf{r}-\mathbf{r}'|}, \tag{2.83}$$

and the xc potential is

$$V_{xc}[\rho](\mathbf{r}) = \frac{\delta E_{xc}[\rho]}{\delta\rho(\mathbf{r})}. \tag{2.84}$$

This means that we can obtain the ground state density of the interacting system in Eq. 2.81 through a self-consistent solution of the effective non-interacting problem of Eq. 2.76 with V_S given by Eq. 2.82.

Here we have assumed that the ground state density of the interacting system can also be represented as the ground state density of a non-interacting system.

While KS DFT is formally exact, in practice one has to employ an approximation for the unknown xc energy $E_{xc}[\rho]$ given in Eq. 2.80. The quality of a DFT calculation is determined by how well this exchange-correlation energy is approximated. To test this we can approximate Eq. 2.80 by using different density functionals.

2.3.1.1. *Functionals.* The simplest density functional used to approximate the exchange correlation energy is the Local Density Approximation (LDA) functional, which is based on the homogeneous electron gas. In the homogeneous electron gas the electronic density is constant over space and it is compensated by a uniform background density. Within the Kohn-Sham (KS) non-interacting scheme, $V_S(\mathbf{r}) = 0$ due to symmetry. The non-interacting kinetic energy per electron for a homogeneous electron gas is given by

$$t_s^{\text{unif}}[\rho] = \frac{3}{10}\left(3\pi^2\rho\right)^{2/3}. \tag{2.85}$$

The exchange energy per electron of the uniform electron gas is

$$e_x^{\text{unif}}[\rho] = -\frac{3}{4\pi}\left(3\pi^2\rho\right)^{1/3}. \tag{2.86}$$

The analytical form of the correlation energy per electron of the uniform electron gas $e_c^{\text{unif}}[\rho]$ is not known exactly. It is only known exactly for certain density limits through quantum Monte Carlo calculations. Therefore one uses Monte Carlo parametrisations to construct an analytical fit for the correlation energy. In particular, in this thesis I have used the parametrisation of Perdew and Wang [195] to obtain the correlation energy per electron of the uniform electron gas

$$e_c^{\text{unif}}[r_s,\zeta] = e_c^{\text{unif}}(r_s,0) + \alpha_c(r_s)\frac{f(\zeta)}{f''(0)}(1-\zeta^4) + [e_c^{\text{unif}}(r_s,1) - e_c^{\text{unif}}(r_s,0)]f(\zeta)\zeta^4, \tag{2.87}$$

where

$$f(\zeta) = \frac{[(1+\zeta)^{\frac{4}{3}} + (1-\zeta)^{\frac{4}{3}} - 2]}{2^{\frac{4}{3}} - 2}, \tag{2.88}$$

$$r_s = \left[\frac{3}{4\pi(\rho_\uparrow + \rho_\downarrow)}\right]^{\frac{1}{3}}, \tag{2.89}$$

$$\rho = \rho_\uparrow + \rho_\downarrow = \frac{3}{4\pi r_s^3}, \tag{2.90}$$

$$\zeta = \frac{\rho_\uparrow - \rho_\downarrow}{\rho_\uparrow + \rho_\downarrow}, \tag{2.91}$$

where $\rho_\uparrow$ and $\rho_\downarrow$ are the up- and down-spin electron ground state densities.

Here $e_c^{\text{unif}}(r_s,0)$, $e_c^{\text{unif}}(r_s,1)$ and $\alpha_c(r_s)$ are obtained with $f(0)$=0, $f(1)$=1 and $f''(0)$=1.709921 by fitting the analytical form

$$G(r_s,\alpha_1,\beta_1,\beta_2,\beta_3,\beta_4,p) = -2A(1+\alpha_1 r_s) \times \ln\left[1+\frac{1}{2A\left(\beta_1 r_s^{\frac{1}{2}}+\beta_2 r_s+\beta_3 r_s^{\frac{3}{2}}+\beta_4 r_s^{p+1}\right)}\right]. \tag{2.92}$$

To construct the LDA functional the LDA exchange energy functional is obtained from

$$E_x^{\mathrm{LDA}}[\rho] = \int d^3\mathbf{r} e_x^{\mathrm{unif}}[\rho(\mathbf{r})]\rho(\mathbf{r}), \tag{2.93}$$

and the LDA correlation energy functional from

$$E_c^{\mathrm{LDA}}[\rho] = \int d^3\mathbf{r} e_c^{\mathrm{unif}}[\rho(\mathbf{r})]\rho(\mathbf{r}). \tag{2.94}$$

Then the exchange-correlation LDA functional is given by

$$E_{xc}^{\mathrm{LDA}} = E_x^{\mathrm{LDA}} + E_c^{\mathrm{LDA}}. \tag{2.95}$$

Another LDA based functional I use in this thesis is the corrected-exchange-density [196] extension of LDA (CXD-LDA). Here, the exchange-correlation density $\rho_{xc}(\mathbf{r})$ is given by

$$\rho_{xc}(\mathbf{r}) = -\frac{1}{4\pi}\nabla^2 V_{xc}[\rho(\mathbf{r})], \tag{2.96}$$

where $\rho_{xc}(\mathbf{r})$ is corrected by using

$$\rho_{xc}^{\mathrm{corr}}(\mathbf{r}) = \rho_{xc}(\mathbf{r}) + \frac{1}{|q_{xc}(\eta_0)|}\Delta\rho_{xc}(\mathbf{r},\eta_0), \tag{2.97}$$

where the exchange-correlation charge is

$$q_{xc}(\eta) = \int d^3\mathbf{r}\left(\rho_{xc}[\rho(\mathbf{r})] + \Delta\rho_{xc}[\rho(\mathbf{r},\eta)]\right), \tag{2.98}$$

and the exchange-correlation density correction is

$$\Delta\rho_{xc}[\rho(\mathbf{r},\eta)] = \begin{cases} 0 & \text{if } \rho(\mathbf{r}) \geq \eta \\ -\rho_{xc}[\rho(\mathbf{r})] & \text{if } \rho(\mathbf{r}) < \eta \end{cases}. \tag{2.99}$$

Here $\eta_0 = min_{\eta\leq\eta_m}|q_{xc}(\eta)+1|$ is an optimised value for which we fulfil the following conditions for which the charge is closest to -1

$$\begin{array}{ll} \rho_{xc}(\mathbf{r}) = 0 & (|\mathbf{r}| \to \infty) \\ \int d^3\mathbf{r}\rho_{xc}[\rho(\mathbf{r})] = -1 & \end{array}, \tag{2.100}$$

where η_m is the smallest value where $q_{xc}(\eta)$ has a minimum.

As the LDA and CXD-LDA functionals are based on the homogeneous electron gas, they solely depend on the value of the electronic density at each point in space. Therefore, we only expect them to work for systems where the density varies slowly over space. To account for density inhomogeneities, Generalised Gradient Approximation (GGA) functionals have been constructed, which also account for derivatives of the density. One corrects the LDA based exchange-correlation energy with terms that depend on $\nabla\rho$ as

$$E_{xc}^{\mathrm{GGA}}[\rho] = E_{xc}^{\mathrm{LDA}}[\rho] + \int d^3\mathbf{r} f[\rho, \nabla\rho]. \tag{2.101}$$

In particular, in this thesis I have used the PBE [197] and LB94 [198] forms of the generalised gradient approximations (GGA).

For PBE the exchange energy functional is given by

$$E_x = \int d^3\mathbf{r}\rho e_x^{\mathrm{unif}}[\rho]F_x(s), \tag{2.102}$$

where $e_x^{\mathrm{unif}}[\rho]$ is defined in Eq. 2.86 and

$$F_x(s) = 1 + \kappa - \frac{\kappa}{\left(1 + \frac{\mu s^2}{\kappa}\right)}, \tag{2.103}$$

with κ=0.804 and μ=0.21951.

The PBE correlation energy functional is given by

$$E_c[\rho(r)] = \int d^3\mathbf{r}\rho[e_c^{\mathrm{unif}}(r_s, \zeta) + H(r_s, \zeta, t)], \tag{2.104}$$

where $e_c^{\mathrm{unif}}(r_s, \zeta)$ is defined in Eq. 2.87 and the density gradient contribution H is

$$H = \left(\frac{e^2}{a_0}\right)\gamma\phi(\zeta)^3 \ln\left[1 + \frac{\beta}{\gamma}t^2\left(\frac{1 + At^2}{1 + At^2 + A^2t^4}\right)\right], \tag{2.105}$$

with γ=0.031091, β=0.066725, $t = \frac{|\nabla\rho(r)|}{2\phi k_s\rho(r)}$ is the dimensionless density gradient, $k_s = \sqrt{\frac{4k_F}{\pi a_0}}$ is the Thomas Fermi screening wave number,

$$\phi(\zeta) = \frac{\left[(1+\zeta)^{\frac{2}{3}} + (1-\zeta)^{\frac{2}{3}}\right]}{2}, \tag{2.106}$$

is the spin scaling factor and

$$A = \frac{\beta}{\gamma}\left[\exp\left(-\frac{e_c^{unif}(r_s, \zeta)}{\gamma\phi(\zeta)^3}\right) - 1\right]^{-1}. \tag{2.107}$$

For LB94 the exchange-correlation potential is given by

$$V_{xc} = -\rho(r)^{\frac{1}{3}}\beta\frac{x^2}{1+3\beta x\sinh^{-1}(x)}, \tag{2.108}$$

where $x = \frac{|\nabla\rho(r)|}{\rho(r)^{\frac{4}{3}}}$ is the dimensionless density gradient and β=0.05.

Note that LB94 and CXD-LDA are not energy functionals, but models for the exchange correlation potential V_{xc}. In these cases, the exchange-correlation potentials do not result from functional derivatives of particular exchange-correlation energy functionals.

2.3.2. Time-dependent density functional theory. Time-dependent density functional theory (TDDFT) [199] is the time extension of density functional theory (DFT) (see Sec. 2.3.1) to study the dynamic response of systems in the presence of time-dependent external fields.

As in DFT, it has been proven by Runge-Gross (RG) that all physical properties of an interacting many-electron system can be determined from its time-dependent density [169]. Moreover, the interacting system is also mapped onto an auxiliary, non-interacting time-dependent Kohn-Sham (TDKS) system with the time-dependent corresponding density of Eq. 2.77 $\rho(\mathbf{r},t) = \sum_{i=1}^{n}|\phi_i(\mathbf{r},t)|^2$, where $\phi_i(\mathbf{r},t)$ are single-particle KS orbitals satisfying the TDKS equations

$$\begin{aligned} i\frac{\partial}{\partial t}\phi_i(\mathbf{r},t) = \quad & \Big[-\frac{\nabla^2}{2} + \hat{V}_{ext}(t) + \hat{V}_H[\rho](\mathbf{r},t) \\ & + \hat{V}_{xc}[\rho](\mathbf{r},t)\Big]\phi_i(\mathbf{r},t), \quad i = 1,\ldots,n, \end{aligned} \tag{2.109}$$

where the analogue time-dependent potential terms that were described in Sec. 2.3.1 have been used. Now the external field in Eq. 2.64 contains a time-dependent laser field term.

The exact expression used for $\hat{V}_{ext}(t)$ is given in Secs. 2.4.1 for the systems analysed with TDDFT.

In TDDFT we employ the adiabatic extension of the DFT functionals to the time-dependent case. By adiabatic we mean that the density at time t is plugged into a ground state (gs) density functional

$$V_{xc}^{\text{adia}}(\mathbf{r},t) = V_{xc}^{\text{gs}}[\rho(\mathbf{r},t)], \tag{2.110}$$

neglecting its time dependent evolution. This approximation is reasonable if the system begins in a ground state where the external time dependence is very slow.

2.4. Photoionisation of neon, argon and ethylene by means of time-dependent density functional theory

Due to the recent advances in the development of intense ultrashort lasers, it is now experimentally possible to study the strong field photoionisation of systems exposed to

such sources. In particular I have studied the response of neon and argon atoms which are subject to a free electron laser source and of an ethylene molecule subject to a pump probe setup. To understand the non-perturbative phenomena that arises due to a very strong interaction between these systems and the electromagnetic source I use time-dependent density functional theory (TDDFT).

Recently, Lambropoulos et al. have used a perturbative method in terms of rate equations known as lowest-order perturbation theory (LOPT) [200] to study the photoionisation of neon and argon atoms exposed to intense free electron laser sources. They have found a very good agreement with experiment [201, 202] in the perturbative regime. TDDFT was unable to describe non-perturbative phenomena such as the non-sequential double photoionisation "knee" found experimentally for helium, without including the derivative discontinuity. In this section I show how I obtain the individual and total photoionisation yields using a TDDFT approach suggested by Ullrich [203]. As the performance of TDDFT depends on the local and asymptotic behaviour of the exchange-correlation functional used, I have used several exchange-correlation functionals. The ionisation yields I obtain with TDDFT will then be compared to the accurate ones obtained from LOPT in the perturbative regime.

To photoionise ethylene I use a pump probe setup. With a pump I first excite ethylene's π_z to π_z^* transition which I then follow with a delayed probe pulse which ionises the molecule. For the many-electron ethylene molecule we also have to include the nuclear motion which is absent for the neon and argon atoms. The nuclear motion is included via the Born-Oppenheimer approximation (BOA) and Ehrenfest dynamics (ED) classical approaches. Pump probe spectroscopy can be used to monitor both electron and nuclear dynamics. Here, I have used TDDFT to model the pump-probe dynamics of ethylene. The time resolved photoemission spectra and photoangular distributions have been obtained using the TDDFT approach suggested by De Giovannini et al. [204]. I perform an analysis of the angular and time resolved distribution of ethylene's molecular orbitals using both the classical BOA and ED approaches to check the effect of nuclear motion. The strong probe I use to ionise ethylene can trigger non-perturbative effects. Moreover, the analysis of the photoemission spectra and angular distributions is performed once the probe is applied. The probe is applied after the ethylene molecule is already out of equilibrium due to the excitation introduced by the pump. Therefore, the analysis is performed from the response of an ethylene molecule which is already driven out of equilibrium initially due to a pump. TDDFT can be used non-perturbatively in out of equilibrium situations including electron correlation effects. Therefore it is desirable to describe the dynamic evolution of the molecular orbitals of ethylene in terms of TDDFT.

2.4.1. Laser field. To analyse the photoionisation yields for argon and neon I expose them to the following external potential in our time-dependent Kohn-Sham (TDKS) Eq. 2.109

$$\hat{V}_{\text{ext}}(t) = Af(t)\sin(\omega t)\mathbf{r}\cdot\boldsymbol{\alpha} - \sum_{\alpha=1}^{N}\frac{Z_\alpha}{|\mathbf{r}-\mathbf{R}_\alpha|}, \tag{2.111}$$

where the nuclei are treated as Born-Oppenheimer approximation (BOA) classical fixed particles and the atom free electron laser (FEL) interaction is written in the dipole approximation, i.e., proportional to $\mathbf{r}$. Here $\boldsymbol{\alpha}$ is the polarisation, ω the frequency and A the field amplitude of the sinusoidal laser. For ultraviolet (UV) to X-ray laser fields, the length scales range from 10 to 0.1 nm. As the typical size of an atom has a length scale of the order of 0.1 nm, the dipole approximation simplified model is valid. The length scale limit of an atom gives an upper photon frequency limit to the validity of the dipole approximation. The pulse envelope is of Gaussian shape $f(t) = \exp\left[-(t-t_0)^2/2\tau_0^2\right]$, with peak value centred at t_0 and full width at half maximum (FWHM) peak width given by $2\sqrt{\ln 2}\tau_0$.

To propagate Eq. 2.109 I use an enforced time-reversal symmetry based propagator, Eq. 2.51.

For an ethylene molecule exposed to a pump and probe laser, I use the following external potential to solve the TDKS Eq. 2.109

$$\hat{V}_{\text{ext}}(\mathbf{r},\mathbf{R}_\alpha(t),t) = \mathbf{r}\cdot\mathbf{E}(t) - \sum_\alpha \mathbf{R}_\alpha(t)\cdot\mathbf{E}(t) - \sum_{\alpha=1}^{N}\frac{Z_\alpha}{|\mathbf{r}-\mathbf{R}_\alpha(t)|}. \tag{2.112}$$

The first two terms describe the interaction of the electrons and the nuclei with the pump and probe laser fields where $\mathbf{E}(t)$ is the electric field associated to the lasers in the dipole approximation as in Eq. 2.111. The laser parameters given below for ethylene have been adapted from Ref. [205].

I employ an UV pump laser of energy $\omega_{Pu} = 0.326$ Ha, with a 15 cycle trapezoidal shape (3 cycle ramp), and an intensity $I = 1.67\times10^{11}$ W/cm^2 polarised along the x-axis. The probe is an extreme ultraviolet (XUV) laser of energy $\omega_{pr} = 1.8$ Ha, with a 40 cycle trapezoidal shape (8 cycle ramp), and an intensity of $I = 1.02\times10^{11}$ W/cm^2 polarised along the z-axis.

The last term in Eq. 2.112 corresponds to the motion of the nuclei moving according to Ehrenfest Dynamics (ED). Note that when the nuclei are treated as fixed BOA particles the second term in Eq. 2.112 vanishes and $\mathbf{R}_\alpha(t)$ becomes $\mathbf{R}_\alpha$ in the third term.

2.4.2. Time-dependent density functional theory functionals. For neon and argon I consider four different exchange-correlation(xc) potential approximations: the local-density approximation [195] (LDA), PBE [197] and LB94 [198] forms of the generalised gradient approximations (GGA), and the corrected-exchange-density [196] extension of LDA (CXD-LDA). The analytical form of these xc functionals is given in Sec. 2.3.1.1. These functionals are used in the static density functional theory (DFT) calculation of the

initial ground state and their adiabatic extensions are then used in the time propagation of the time-dependent Kohn-Sham (TDKS) equations.

A characterising property of both LB94 and CXD-LDA is the correct asymptotic decay of the xc potential, $V_{xc} \sim -1/r$, following the Coulomb potential for large distances r from the electrons to the nuclear core. In contrast, both LDA and PBE decay exponentially. The high-lying unoccupied KS bound states, close to the ionisation threshold, are thus expected to be more accurately described by the LB94 and CXD-LDA functionals.

The xc functional I use for the ethylene molecule is the well known Local Density Approximation (LDA) coupled to an Average Density Self Interaction Correction (ADSIC) [206, 207] for the ground state and its adiabatic extension for time-dependent density functional theory (TDDFT). Here, one subtracts from the LDA energy functional, the self interaction of every electron with itself in the molecule. I assume that indistinguishable electrons are represented by equal single-particle densities. This means that the density of each electron is given by the one-particle fraction of the total spin-density $\rho_i(t) = \frac{\rho_{\sigma_i}(t)}{n_{\sigma_i}}$ where σ_i is the spin of state i and n_{σ_i} the number of electrons with spin $\sigma_i \in \uparrow, \downarrow$.

$$E^{\mathrm{ADSIC}}[\rho(t)] = E^{\mathrm{LDA}}[\rho(t)] - \left(n_\uparrow (E_H + E_{xc}) \left[\frac{\rho_\uparrow(t)}{n_\uparrow} \right] + n_\downarrow (E_H + E_{xc}) \left[\frac{\rho_\downarrow(t)}{n_\downarrow} \right] \right). \tag{2.113}$$

The choice of ADSIC is motivated by its correct asymptotic behaviour of the corresponding xc potential in the ground state. In other words, for a large distance r from the molecule, $V_{xc} \sim -1/r$. The high-lying unoccupied KS bound states close to the ionisation threshold are thus described more accurately than with an exponentially decaying xc potential. This gives a bound $\pi_z \rightarrow \pi_z^*$ transition, which is not the case for standard xc-functionals with the wrong asymptotic behaviour. Moreover, I obtain an accurate ionisation potential and carbon-carbon (C–C) bond-length by comparison to experimental values (see beginning of Sec. 3.3.2.1). The (C–C) bond-length has been obtained by molecular force minimisation. Force minimisation can only be achieved using energy density functionals, i.e, xc potentials which can be obtained as functional derivatives of an xc energy functional. In particular I employ the method of steepest descent

$$\mathbf{R}_{k+1} = \mathbf{R}_k - s \nabla F(\mathbf{R}_k), \tag{2.114}$$

where $\mathbf{R}_k$ and $\mathbf{R}_{k+1}$ correspond to the initial and final coordinates of each atom of the molecule before and after force minimisation, respectively. $-\nabla F(\mathbf{R}_k)$ is the negative of the gradient of the force for the initial coordinates and s is the step size between $\mathbf{R}_k$ and $\mathbf{R}_{k+1}$. As $\nabla F(\mathbf{R}_k) \sim 0$, I converge towards the minimum force where the atoms are in their equilibrium configuration, $\mathbf{R}_{k+1} \approx \mathbf{R}_k$ and the minimisation process ends. The force $F(\mathbf{R}_k)$ is obtained by minimising the ground state energy as a function of the coordinate $\mathbf{R}_k$.

The combination of LDA and ADSIC has been successfully employed in conditions similar to the ones described in this work [208, 209].

2.4.3. Absorbing boundary. Continuum unbound delocalised states play a central role in the photoionisation of atoms and molecules. To obtain the correct distribution of the ejected electrons in the continuum one would need accurate wavefunctions in a large space domain to account for the spreading of these delocalised states. Knowledge of the whole space is not feasible computationally as we are limited to a simulation box of a certain width (see Sec. 3.2.1). Due to this limitation, ionised electrons can bounce off the edges of the simulating box and return to the atom, which is unphysical. This would lead to smaller ionisation yields than expected. Therefore, it is convenient to insert at the edges of the box an absorbing boundary region to avoid unphysical reflections. The quality of the absorbing boundary region is measured by the amount of reflections it can remove.

As the absorbing boundary method for the neon and argon atoms, I use a complex absorbing potential (CAP) [210, 211]. This method consists of adding to the Hamiltonian H_0 a spherically symmetric negative imaginary potential which is non-zero but small close to the boundaries of the simulating box. This potential $V_{\mathrm{CAP}}(\mathbf{r})$, acting at a certain distance $\mathbf{R}_{\mathrm{CAP}}$ from the centre of the spherical box of radius $\mathbf{R}$ is

$$V_{\mathrm{CAP}}(r) = -i\eta \begin{cases} 0 & \text{if } |\mathbf{r}| < |\mathbf{R}_{\mathrm{CAP}}| \\ \sin^2\left(\frac{\pi|\mathbf{r}-\mathbf{R}_{\mathrm{CAP}}|}{2|\mathbf{R}-\mathbf{R}_{\mathrm{CAP}}|}\right) & \text{if } |\mathbf{R}_{\mathrm{CAP}}| \leq |\mathbf{r}| \leq |\mathbf{R}| \end{cases} . \tag{2.115}$$

Time propagation with this modified Hamiltonian by means of the time propagator with $\Delta t \to 0$

$$U_{\mathrm{CAP}}(t + \Delta t, t) = \exp(iH\Delta t) = \exp\left(i[H_0 + V_{\mathrm{CAP}}(r)]\Delta t\right), \tag{2.116}$$

results in wavepacket absorption at the boundaries to avoid wavepacket reflection due to exponential damping. In order to obtain a damped exponential contribution, the values η of the imaginary part of the added potential must be negative. Characterising and controlling the reflection properties of the absorber is important to accurately describe continuum states. The amount of induced exponential damping depends on the kinetic energy of the absorbed wavepacket, on the width of the absorbing boundary region and on the negative value of the added potential. Taking into account these effects we can obtain a reflection error plot [212]. The kinetic energy of each outgoing electron, $E_k = \hbar\omega - E_b$, is determined by the photon energy $\hbar\omega$ of the incoming laser and its binding energy E_b. The width of the absorbing boundary region $\mathbf{R}_{\mathrm{CAP}}$ is limited by the size of the simulating box $\mathbf{R}$ we can numerically solve. The negative value of the added complex absorbing potential is then chosen to give the least possible reflections for the photon energy and simulating box size used.

The absorbing boundary method used for ethylene is given in Sec. 2.4.7.

2.4.4. Pseudopotentials. The strong nuclear Coulomb potential and many highly localised core electron wavefunctions are computationally very hard to describe with the grid-based non-localised `Octopus` code [213, 214, 215] used in this thesis. Since both the core and valence wavefunctions are eigenstates of the Hamiltonian, they must all be mutually orthogonal. To maintain this orthogonality, the valence states must oscillate rapidly in the core region where the core states are highly localised. As core excitations are only expected to play a relevant role for very high intensity laser pulses, it is reasonable to consider the core electrons as rigid frozen particles together with the nucleus. Therefore it is convenient to replace the strong Coulomb nuclear plus core potential by a weaker pseudopotential and replace the highly oscillating valence wavefunctions by smoother pseudowavefunctions in the core region.

For neon I freeze the two 1s core electrons and for argon I freeze the two 1s, two 2s, and six 2p core electrons. The number of initial unfrozen valence electrons for both atoms is $n = 8$. The pump and probe lasers that I use for ethylene cannot ionise its $1s$ core electrons as their energies are ~10.29 Ha. Therefore, I freeze the two tightly bound $1s$ core electrons in an LDA pseudopotential (see Secs. 2.3.1.1 and 2.4.2) generated for the neutral configuration.

The pseudopotentials used for neon and argon have been generated within the Troullier-Martins scheme [216] as distributed in the `APE` code [217] and then used in the `Octopus` code [213, 214, 215]. The pseudopotential for ethylene has been generated within the Troullier-Martins scheme [216] as distributed in the `Octopus` code [213, 214, 215].

The pseudowavefunction chosen for the valence electrons is described by means of the Troullier-Martins scheme and is parametrised according to

$$R_l^{\mathrm{PP}}(r) = \begin{cases} R_{nl}^{\mathrm{AE}}(r) & \text{if } r > r_c \\ r^l \exp(p(r)) & \text{if } r < r_c \end{cases}, \tag{2.117}$$

and

$$V_l^{\mathrm{PP}}(r) = \begin{cases} V_{nl}^{\mathrm{AE}}(r) & \text{if } r > r_c \\ \varepsilon_{nl} + \frac{l+1}{r} p'(r) + \frac{p''(r)+[p'(r)]^2}{2} & \text{if } r < r_c \end{cases}, \tag{2.118}$$

where n and l are the principal and angular quantum numbers, $R_{nl}^{\mathrm{AE}}(r)$, $R_l^{\mathrm{PP}}(r)$ and $V_{nl}^{\mathrm{AE}}(r)$, $V_l^{\mathrm{PP}}(r)$ are the all electron and pseudo wavefunctions and potentials, r_c a cutoff radius and

$$p(r) = c_0 + c_2 r^2 + c_4 r^4 + c_6 r^6 + c_8 r^8 + c_{10} r^{10} + c_{12} r^{12}. \tag{2.119}$$

Here $p'(r)$ and $p''(r)$ correspond to the first and second derivative of $p(r)$. The coefficients c of the function $p(r)$ are then adjusted to fulfil the following requirements beyond the cutoff radius r_c [218]: the parametrised calculation gives pseudowavefunctions and eigenvalues that have to match that of the valence electrons for the all electron calculation. The integrated density obtained from the pseudo and all electron wavefunction must

be identical. The pseudowavefunctions must be nodeless. The logarithmic derivative of the pseudowavefunction has the same behaviour as that of the all electron wavefunction.

The transferability of the pseudopotential is determined by the quality of the parametrisation for the chosen cutoff radius. The smaller the value of this cutoff radius, the calculation with pseudopotentials will be more transferable to the all electron one but also more expensive computationally.

2.4.5. Ehrenfest dynamics for ethylene. For the neon and argon atoms I do not have to model the nuclear part because we do not have vibrational degrees of freedom. However, this is not the case for ethylene.

The motion of the nuclei α for ethylene within the time-dependent density functional theory (TDDFT) framework is determined by the electronic density gradient through Newton's second equation of motion. For a conservative force that is a function of the position of the nuclei only, Newton's second equation of motion can be written as

$$F(\mathbf{R}_\alpha(t), t) = M_\alpha \frac{d^2\mathbf{R}_\alpha(t)}{dt^2} = -\nabla_\alpha V(\mathbf{R}_\alpha(t), t), \tag{2.120}$$

where $V(\mathbf{R}_\alpha(t), t)$ is the total potential acting on the nuclei only

$$V(\mathbf{R}_\alpha(t), t) = V_{ext}[\rho(t)] + V_{II}(\mathbf{R}_\alpha(t)), \tag{2.121}$$

where $V_{II}(\mathbf{R}_\alpha(t))$ is defined in Eq. 2.4 and the contribution of the external potential can be written explicitly in terms of the density

$$V_{ext}[\rho(t)] = \int d\mathbf{r}^3\, V_{ext}(\mathbf{r}, \mathbf{R}_\alpha(t), t)\, \rho(\mathbf{r}, t), \tag{2.122}$$

where $V_{ext}(\mathbf{r}, \mathbf{R}_\alpha(t), t)$ is defined in Eq. 2.112. Note that the first term in Eq. 2.112, which describes the interaction of the electrons with the pump and probe laser fields, disappears once you apply the gradient for the nuclei α in Eq. 2.120.

Inserting Eq. 2.122 into Eq. 2.121, we can write Eq. 2.120 as

$$M_\alpha \frac{d^2\mathbf{R}_\alpha(t)}{dt^2} = -\nabla_\alpha \left[\int d\mathbf{r}^3\, V_{ext}(\mathbf{r}, \mathbf{R}_\alpha(t), t)\, \rho(\mathbf{r}, t) + \frac{1}{2} \sum_{\substack{\alpha,\beta=1 \\ \alpha\neq\beta}}^{N} \frac{Z_\alpha Z_\beta}{|\mathbf{R}_\alpha - \mathbf{R}_\beta|} \right]. \tag{2.123}$$

The electron plus nuclear scheme consists of the time propagation of the coupled time-dependent Kohn-Sham (TDKS) Eq. 2.109 with Eq. 2.112 and the Ehrenfest Eq. 2.123. The TDKS equations are propagated via an enforced time reversal symmetry propagator, Eq. 2.51, and the nuclei via a velocity Verlet algorithm using

$$\begin{aligned}
\mathbf{R}_\alpha(t+\Delta t) &= \mathbf{R}_\alpha(t) + \mathbf{v}_\alpha(t)\Delta t + \frac{1}{2}\mathbf{a}_\alpha(t)\Delta t^2, \\
\mathbf{a}_\alpha(t+\Delta t) &= -\frac{1}{M_\alpha}\nabla_\alpha V\left(\mathbf{R}_\alpha(t+\Delta t)\right), \\
\mathbf{v}_\alpha(t+\Delta t) &= \mathbf{v}_\alpha(t) + \frac{1}{2}\mathbf{a}_\alpha(t)\Delta t + \frac{1}{2}\mathbf{a}_\alpha(t+\Delta t)\Delta t.
\end{aligned} \tag{2.124}$$

A random initial velocity v consistent with a Boltzmann distribution function $f(v)$ at a specific temperature T is assigned to each nucleus with mass M_α

$$f(v) = 4\pi\left[\frac{M_\alpha}{2\pi k_B T}\right]^{\frac{2}{3}} v^2 \exp\left(-\frac{mv^2}{2k_B T}\right), \tag{2.125}$$

where k_B is the Boltzmann constant.

2.4.6. Modelling the time-dependent density functional theory total and individual yields for neon and argon. In order to estimate the total ionic yields with time-dependent density functional theory (TDDFT), I follow the time evolution of the electronic charge remaining in a given interacting volume V around the atom. The evolution of the total electronic charge with time is obtained from the electronic density.

Our simulating volume has an interacting region where the time-dependent Kohn-Sham (TDKS) equations are solved in real space and an absorbing boundary region where the ionised electrons are collected via damping. This absorbing region ensures that no electron can reflect back to the atom by bouncing back from the borders of our interacting volume. The norm of the Kohn-Sham (KS) orbital for each electron inside the interacting volume $N_i(t) = \int_V \mathrm{d}\mathbf{r}\,|\phi_i(\mathbf{r},t)|^2$ decreases in time during the application of a laser pulse due to the ionisation of the electrons into the absorbing region. The total number of escaped electrons at time t is given by

$$N_{\mathrm{esc}}(t) = N_0 - N(t), \tag{2.126}$$

where N_0 is the initial number of non-frozen valence electrons and $N(t) = \sum_i N_i(t) = \int_V \mathrm{d}\mathbf{r}\,\rho(\mathbf{r},t)$, is the total number of remaining electrons in the interacting volume at a given time. The total ionisation yield is the long time limit of Eq. 2.126: $N_{\mathrm{esc}} = N_{\mathrm{esc}}(t\to\infty)$ to allow enough time for the electrons in lower-energy eigenstates to ionise. We stop our simulation when we see that the variation of $N_{\mathrm{esc}}(t)$ becomes negligible with time.

To calculate the TDDFT individual ionisation probabilities $P^{+q}(t)$ for an atom, i.e., the probability to produce an ion in a positively q-charged state ($q = 1,\ldots,N_0$), I employ the approach based on the TDKS orbitals described in [203]. In this approach, as the explicit time-dependent density functional for these probabilities is unknown, these are calculated from the KS single-electron orbital densities instead of the total density

$$\sum_{q=1}^{N_0} P^{+q}(t) = \sum_{i=1}^{N_0} \Big[(N_0 - q) N_j(t) + q \bar{N}_j(t) \Big], \tag{2.127}$$

where q is the charge of the species, N_0 the total number of non frozen valence electrons and

$$N_j(t) = \int_V d^3\mathbf{r} |\varphi_i(\mathbf{r}, t)|^2, \tag{2.128}$$

$$\bar{N}_j(t) = \int_{V_{\mathrm{CAP}}} d^3\mathbf{r} |\varphi_i(\mathbf{r}, t)|^2, \tag{2.129}$$

are the number of bound and continuum electrons in the real space interacting V and complex absorbing potential V_{CAP} region, respectively.

To obtain the individual ionic channels, we need to assume that the KS wavefunction is a good approximation to the many-body one. At the exact level of theory this assumption is certainly not valid. However, we may still view this assumption as a zeroth order approximation whose quality can be assessed on the basis of its success in recapturing results from different approaches and experimental data. The total yield is the only quantity that is rigorously correct since it is directly derived from the total electronic density and not the single particle KS orbitals.

2.4.7. Modelling the photoelectron spectra and the photoangular distribution for ethylene. In experimental setups photoelectrons travel long distances before being detected with a given momentum $\mathbf{p}$ and position $\mathbf{r}$ in phase space $(\mathbf{r}, \mathbf{p})$. The ejected electrons that are far away will feel a very weak or no interaction with the nuclear core and electrons that they have left behind. These ejected electrons will therefore travel as free particles driven by the laser and can be described in momentum space by plane waves whose solutions are Volkov states. Therefore, it is advantageous to describe the dynamics of the ejected free electrons analytically by plane waves in momentum space instead of numerically by propagating the time-dependent Kohn-Sham (TDKS) equations in real space. Moreover, as free electrons are very delocalised, extending over the whole space, it is convenient to represent them in momentum instead of in real space to accurately describe their wavefunctions. It is then reasonable to divide our simulation box into an inner region A and an outer region B for which we use different basis representations in the numerics [204]. In region A we solve the TDKS equation for the electrons plus either Born-Oppenheimer approximation (BOA) frozen or moving nuclei according to Ehrenfest dynamics (ED) using a grid basis set. In region B, the photoelectrons are recorded in momentum space as free particles using a plane wave basis set.

To access the kinetic energy $P(E)$ and angular resolved $P(E,\theta)$ photoelectron spectrum which we want to visualise, the knowledge of the momentum resolved photoelectron spectrum $\mathcal{P}(\mathbf{p})$ is required. $P(E)$ and $P(E,\theta)$ are given by

$$P(E) = \int_0^{4\pi} d\Omega \mathcal{P}(\mathbf{p}), \tag{2.130}$$

and

$$P(E,\theta) = \int_0^{2\pi} d\theta \mathcal{P}(\mathbf{p}), \tag{2.131}$$

where

$$\mathcal{P}(\mathbf{p}) = \lim_{t\to\infty} \int_B d\mathbf{R} w(\mathbf{R},\mathbf{p},t). \tag{2.132}$$

Note that the $\mathcal{P}(\mathbf{p})$ is only evaluated within region B and for $t \to \infty$ to ensure that all slow core outgoing photoelectrons have enough time to reach the detector region. It is only evaluated within region B because the probability of finding an ionised electron in region A for $t \to \infty$ is nearly zero.

The Wigner transform $w(\mathbf{R},\mathbf{p},t)$ is the classical link compatible with quantum mechanics that we can use to obtain $\mathcal{P}(\mathbf{p})$. From this we can extract the observables $P(E)$ and $P(E,\theta)$ of interest. The Wigner transform is defined as

$$w(\mathbf{R},\mathbf{p},t) = \int \frac{d\mathbf{s}}{2\pi^{\frac{d}{2}}} \exp(i\mathbf{p}\cdot\mathbf{s}) \rho\left(\mathbf{R}+\frac{\mathbf{s}}{2}, \mathbf{R}-\frac{\mathbf{s}}{2}, t\right), \tag{2.133}$$

where the coordinates are

$$\mathbf{R} = \frac{\mathbf{r}+\mathbf{r}'}{2}; \mathbf{s} = \mathbf{r}-\mathbf{r}', \tag{2.134}$$

and the full one-body density matrix is

$$\rho(\mathbf{r},\mathbf{r}',t) = \int d\mathbf{r}_2 \cdots d\mathbf{r}_n \psi(\mathbf{r},\mathbf{r}_2\cdots\mathbf{r}_n,t)\psi^*(\mathbf{r}',\mathbf{r}_2\cdots\mathbf{r}_n,t). \tag{2.135}$$

Evaluating numerically the full one-body density matrix in the whole space is unfeasible. To overcome this limitation, we use time-dependent density functional theory (TDDFT), where the one-body Kohn-Sham (KS) density matrix is given by the sum over all i occupied single-particle KS orbitals $\phi_i(\mathbf{r})$. Here we assume that the one-body KS density matrix is a good approximation to the fully interacting one. In Eq. 2.132 $\mathcal{P}(\mathbf{p})$ is only evaluated within region B. Therefore, this assumption can be safely used in region B because the outgoing electrons, far from the interacting region A, can be treated as non-interacting particles. From now on, we will also drop the time dependence of the orbitals because we take Eq. 2.132 in the limit of $t \to \infty$. The one-body KS density matrix is

$$\rho_{KS}(\mathbf{r},\mathbf{r}') = \sum_{i}^{occ} \phi_i(\mathbf{r})\phi_i(\mathbf{r}'), \tag{2.136}$$

where each orbital ϕ_i is decomposed according to the geometrical partition in regions A and B

$$\phi_i(\mathbf{r}) = \phi_{A,i}(\mathbf{r}) + \phi_{B,i}(\mathbf{r}), \tag{2.137}$$

where $\phi_{A,i}(\mathbf{r})$ is the part of the wave function describing states localised in A and $\phi_{B,i}(\mathbf{r})$ is the ionised contribution measured at the detector in B.

Introducing Eq. 2.137 into Eq. 2.136, we find that the one-body KS density matrix in terms of the single-particle KS orbitals in regions A and B is given by

$$\begin{aligned}\rho_{KS}(\mathbf{r},\mathbf{r}') = \sum_{i=1}^{occ} [&\phi_{A,i}(\mathbf{r})\phi^*_{A,i}(\mathbf{r}') + \phi_{A,i}(\mathbf{r})\phi^*_{B,i}(\mathbf{r}') \\ &+ \phi_{B,i}(\mathbf{r})\phi^*_{A,i}(\mathbf{r}') + \phi_{B,i}(\mathbf{r})\phi^*_{B,i}(\mathbf{r}')].\end{aligned} \tag{2.138}$$

Thus, inserting Eq. 2.138 into Eq. 2.133, Eq. 2.132 becomes

$$\mathcal{P}(\mathbf{p}) \approx \sum_{i=1}^{occ} |\tilde{\phi}_{B,i}(\mathbf{p}, t \to \infty)|, \tag{2.139}$$

where $\tilde{\phi}_{B,i}(\mathbf{p}, t \to \infty)$ is the Fourier transform of $\phi_{B,i}(\mathbf{r}, t \to \infty)$. As we are evaluating Eq. 2.132 only in region B, we drop the first term and neglect the small contribution from the mixed terms which involve both regions A and B in Eq. 2.138. The approximation sign in Eq. 2.139 is due to the fact that we neglect these mixed overlap integrals.

The momentum resolved photoelectron spectrum $\mathcal{P}(\mathbf{p})$ in Eq. 2.139 is obtained as a sum of the Fourier components of each orbital in the detector region B. Continuum states in region B can only be described accurately if the whole of space is considered because they are delocalised. However, we are computationally limited to a simulation box of a certain width. To overcome this limitation, we use a Mask Method (MM) $M(\mathbf{r})$ absorbing potential, which connects regions A and B

$$M(\mathbf{r}) = \begin{cases} 1 & \text{if } |\mathbf{r}| < |\mathbf{R}_A| \\ 1 - \sin\left(\frac{|\mathbf{r}-\mathbf{R}_A|\pi}{2|\mathbf{R}_B-\mathbf{R}_A|}\right) & \text{if } |\mathbf{R}_A| \le |\mathbf{r}| \le |\mathbf{R}_B| \\ 0 & \text{if } |\mathbf{r}| > |\mathbf{R}_B| \end{cases} . \tag{2.140}$$

Here $|\mathbf{R}_A|$ corresponds to the width of the box in region A before entering the MM region. $|\mathbf{R}_A|$ should be wide enough to accurately contain the localised bound wavefunctions in real space. $|\mathbf{R}_B$ - $\mathbf{R}_A|$ corresponds to the distance that the electrons need to travel to get into B once they are ejected from A. This distance is the MM region width which connects region A to region B. As the ejected electron gets further from the ion it has

left behind, $M(\mathbf{r})$ should gradually decrease to zero. In region B, once the electron is far enough to be driven freely by the laser field, $M(\mathbf{r})$=0 so that no outgoing electron in B can return to A.

To follow the evolution of the KS orbitals at each time step in regions A and B separately, we use $M(\mathbf{r})$

$$\phi_i(\mathbf{r},t) = \phi_{A,i}(\mathbf{r},t) + \phi_{B,i}(\mathbf{r},t) = M(\mathbf{r},t)\phi_i(\mathbf{r},t) + [1 - M(\mathbf{r})]\phi_i(\mathbf{r},t). \tag{2.141}$$

Note that for $M(\mathbf{r})$=0 we are only left with $\phi_{B,i}(\mathbf{r},t)$ whereas for $M(\mathbf{r})$=1 we are only left with $\phi_{A,i}(\mathbf{r},t)$.

Time propagation of Eq. 2.141 is given by

$$\begin{aligned}\phi_i(\mathbf{r},t+\Delta t) =& U(t',t)\phi_i(\mathbf{r},t) = \phi_{A,i}(\mathbf{r},t') + \phi_{B,i}(\mathbf{r},t') \\ &= U(t',t)M(\mathbf{r})\left(\phi_{A,i}(\mathbf{r},t) + \phi_{B,i}(\mathbf{r},t)\right) \\ &+ U(t',t)[1 - M(\mathbf{r})]\left(\phi_{A,i}(\mathbf{r},t) + \phi_{B,i}(\mathbf{r},t)\right),\end{aligned} \tag{2.142}$$

where $U(t',t)$ is the time propagator. The two pieces of wavefunctions $\phi_{A,i}(\mathbf{r},t)$ and $\phi_{B,i}(\mathbf{r},t)$ can separately be propagated using different methods. In region A we numerically propagate them in real space and in region B we propagate them analytically in momentum space. In region A we use an enforced time-reversal symmetry based propagator, Eq. 2.51, and in region B we use the Volkov time propagator, which written in the velocity gauge is

$$U_V(t+\Delta t,t) = \exp\left(-i\int_t^{t+\Delta t} d\tau \frac{1}{2}\left[\mathbf{p} - \mathbf{A}(\tau)\right]^2\right), \tag{2.143}$$

where $\mathbf{A}(\tau)$ is the vector potential, τ the time ordering operator and $\mathbf{p}$ is the momentum of the free electron.

The Volkov states propagator is known analytically. It can be obtained from the time-dependent Schrödinger equation (TDSE) of a free electron in the presence of a laser pulse in real space which in the velocity gauge is given by

$$i\frac{d}{dt}\phi(\mathbf{r},t) = \frac{1}{2}\left[-i\nabla - \mathbf{A}(\tau)\right]^2\phi(\mathbf{r},t), \tag{2.144}$$

and can be written in momentum space as

$$i\frac{d}{dt}\phi(\mathbf{p},t) = \frac{1}{2}\left[\mathbf{p} - \mathbf{A}(\tau)\right]^2\phi(\mathbf{p},t), \tag{2.145}$$

where

$$\phi(\mathbf{p},t) = \phi(\mathbf{p},0)\exp\left(-i\int_t^{t+\Delta t} d\tau \frac{1}{2}\left[\mathbf{p} - \mathbf{A}(\tau)\right]^2\right). \tag{2.146}$$

From Eq. 2.142, $\phi_{A,i}(\mathbf{r}, t')$ in real space is

$$\phi_{A,i}(\mathbf{r}, t') = M(\mathbf{r})U(t', t)\phi_{A,i}(\mathbf{r}, t) + \int \frac{d\mathbf{p}\exp(i\mathbf{p}\cdot\mathbf{r})}{2\pi^{\frac{d}{2}}} M(\mathbf{r})U_V(t', t)\tilde{\phi}_{B,i}(\mathbf{p}, t). \tag{2.147}$$

Here the first term corresponds to the time evolution of the real space components localised in A. The second term corresponds to the real components of B that can return to A.

From Eq. 2.142, $\tilde{\phi}_{B,i}(\mathbf{p}, t')$ in momentum space is

$$\begin{aligned}\tilde{\phi}_{B,i}(\mathbf{p}, t') = &\int \frac{d\mathbf{r}\exp(-i\mathbf{p}\cdot\mathbf{r})}{2\pi^{\frac{d}{2}}}[1 - M(\mathbf{r})]U(t', t)\phi_{A,i}(\mathbf{r}, t) + U_V(t', t)\tilde{\phi}_{B,i}(\mathbf{p}, t) + \\ &- \int \frac{d\mathbf{r}\exp(-i\mathbf{p}\cdot\mathbf{r})}{2\pi^{\frac{d}{2}}} \int \frac{d\mathbf{p}\exp(i\mathbf{p}\cdot\mathbf{r})}{2\pi^{\frac{d}{2}}} M(\mathbf{r})U_V(t', t)\tilde{\phi}_{B,i}(\mathbf{p}, t).\end{aligned} \tag{2.148}$$

The first term corresponds to the outgoing real space components from region A that are collected in momentum space in B. The second contribution corresponds to the momentum plane wave components that are already in region B and evolve according to the Volkov time propagator $U_V(t', t)$. The third contribution corresponds to the Fourier components of B that can return to A.

All the components localised in real space in Eqs. 2.147 and 2.148 are evaluated with spatial integrals and the components localised in momentum space are evaluated with momentum integrals. Therefore, all these integrals are evaluated within the small localised MM region, without requiring the knowledge of the whole space which is much easier computationally.

If we use an optimal width for the MM region we can neglect the terms that include unphysical reflections from B to A in Eq. 2.148, and we find that Eq. 2.139 contains the following terms

$$\tilde{\phi}_{B,i}(\mathbf{p}, t') = \int \frac{d\mathbf{r}\exp(-i\mathbf{p}\cdot\mathbf{r})}{2\pi^{\frac{d}{2}}}[1 - M(\mathbf{r})]U(t', t)\phi_{A,i}(\mathbf{r}, t) + U_V(t', t)\tilde{\phi}_{B,i}(\mathbf{p}, t). \tag{2.149}$$

CHAPTER 3

Results and Discussion

In this chapter I show and discuss the main results obtained from the three projects in this thesis. For each project I have included a section with the computational details and procedure that I have used to solve the equations given in the theoretical chapter. After the results and discussion section I have added a short summary with the main conclusions for each project.

3.1. Linear excitation spectra of H_2^+ and H_2[1]

The aim of this project is to compare the linear response spectra obtained from both a quantum and classical nuclear treatment for quantum electrons. This is done for the H_2^+ and H_2 molecules because solving the full quantum problem is feasible. The analysis of the spectra is performed for different nuclear masses because the classical approximations are valid for heavy nuclear masses. I find that quantum nuclear motion becomes important in the linear regime for light molecules where the coupling between the nuclei and the electrons needs to be taken into account. This effect is more noteworthy for the H_2^+ molecule than for the H_2 molecule. I propose a two level model that can describe quantitatively the changes induced on the linear excitation spectra due to the quantum nuclear motion as a function of the nuclear mass.

3.1.1. Computational details and procedure. To perform all the numerical calculations described in this thesis I have used the real space electronic structure code `Octopus` [213, 214, 215]. The wavefunctions are discretised on a grid in real space by means of a finite difference method.

I discretise the configuration space of our H_2^+ and H_2 molecules, i.e., all the electronic and nuclear coordinates for both molecules. Within the 1D centre of mass I have for the H_2^+ type molecules two coordinates X and $\tilde{\xi}$ and for the H_2 molecule I have three X, x and ξ. As explained in Sec. 2.2.3, with the `Octopus` code [213, 214, 215] I only treat the spatial part of the wavefunction, as the spin part can be separated off due to the exchange symmetry of the many-body wavefunction.

[1] This section is largely an adaptation of the work by A. Crawford-Uranga, D. J. Mowbray and D. M. Cardamone; *Quantum-ionic features in the absorption spectra of homonuclear diatomic molecules*; Phys. Rev. A **91**, 033410 (2015); DOI:10.1103/PhysRevA.91.033410. As such, the reported work includes collaboration with the rest of the authors of the article.

I use a finite set of values (i.e. a so-called grid) for coordinate values of b in the box intervals $box_{int} \in [-b, b]$ which are discretised as:

$$b_j = -b + j\Delta b \text{ for } b = 0, 1, 2...N_b, \tag{3.1}$$

by using N_b equispaced points. The spacing between two adjacent points in the b direction is $\Delta b = \frac{2b}{N_b}$. The total simulation box size will be given by $2b$ from $-b$ to b.

Convergence is achieved when a decrease in Δb and an increase in b does not change the static and time propagation observables I analyse.

For H_2^+, ground state convergence is achieved for $L_X = L_\xi = 10a_0$, $\Delta X = 0.05a_0$ and $\Delta\xi = 0.1a_0$. To obtain the potential energy surfaces (PES) I have used $L_\xi = 100a_0$ and $\Delta_\xi = 0.1a_0$. The convergence of the quantum nuclei optical spectra requires $L_X = 30a_0$, $L_\xi = 80a_0$, $\Delta X = 0.01a_0$ and $\Delta\xi = 0.5a_0$ (except for the M_μ case where I have used $L_X = 100a_0$, $L_\xi = 80a_0$, $\Delta X = 0.03a_0$ and $\Delta\xi = 0.5a_0$). Finally, for the Ehrenfest dynamics (ED) and Born-Oppenheimer approximation (BOA) optical spectra I have used $L_\xi = 500a_0$ and $\Delta\xi = 0.1a_0$.

For the H_2 type molecules, ground state convergence is achieved for $L_X = L_\xi = L_x = 10a_0$, $\Delta X = 0.07a_0$, $\Delta\xi = 0.2a_0$ and $\Delta x = 0.5a_0$. To obtain the PESs I have used $L_\xi = L_x = 40a_0$ and $\Delta_\xi = \Delta_x = 0.2a_0$. The convergence of the quantum nuclei optical spectra requires $L_X = 10a_0$, $L_x = 80a_0$, $L_\xi = 35a_0$, $\Delta X = 0.07a_0$, $\Delta x = 0.5a_0$ and $\Delta\xi = 0.6a_0$. Finally, for the ED and BOA optical spectra I have used $L_\xi = L_x = 200a_0$, $\Delta\xi = \Delta x = 0.5a_0$.

Within the BOA and ED, the X coordinate does not need to be discretised quantum mechanically. It is classically either fixed as a parameter in BOA or it changes according to the dynamic equations in ED. As a consequence, the two and three variable bare Coulomb quantum nuclei problems confined to 1D trajectories for the H_2^+ and H_2 molecules respectively, become one and two variable BOA and ED problems, which are easier to compute numerically providing a more attractive alternative.

The quantum nuclear eigenvalues in the 1D centre of mass are obtained by inserting Eqs. 2.23 and 2.24 into Eq. 2.9 for the H_2^+ and H_2 molecules, respectively.

To obtain the BOA eigenvalues in the 1D centre of mass frame I first calculate the PESs solving Eqs. 2.41 and 2.42 using Eqs. 2.43 and 2.44 for H_2^+ and H_2, respectively. To obtain the ED eigenvalues in 1D I solve Eqs. C.1 and C.3 using Eq. 2.9 for H_2^+ and H_2, respectively. To include the BOA nuclear eigenvalues to the PES I do not compute Eqs. 2.14 and 2.15. One can obtain the eigenvalues from these equations, but as we are interested in configurations around the nuclear equilibrium, the harmonic approximation is reasonable. Around the minimum of the PES of the electronic ground state, the BOA is expected to be accurate and the exact eigenvalues of the electron-nuclear problem can be interpreted in terms of the harmonic nuclear vibrational levels for the electronic ground state PES (the BOA picture).

To calculate the "frozen nuclei" BOA and quantum nuclei photoabsorption spectra from Eq. 2.61, I initially "kick" the ground state wavefunctions of our molecules and propagate them to obtain the dipole moments, Eqs. 2.57 and 2.58 within fixed BOA and quantum nuclei, and Eqs. 2.59 and 2.60 within ED for the H_2^+ and H_2 molecules, respectively. Here, for ψ_{gs} the quantum nuclear Hamiltonians are given in Eqs. 2.23 and 2.24, the "frozen-nuclei" BOA Hamiltonians are given in Eqs. 2.43 and 2.44 and the ED Hamiltonians in Eqs. C.1 and C.3 for the H_2^+ and H_2 molecules, respectively. The total propagation time to obtain the spectra is $T = 1000$ and $\Delta t = 0.01$ is the time step.

3.1.2. Results.

3.1.2.1. *Ground state potential energy surfaces.* In this section I show how the ground state potential energy surface (PES) changes as a function of the initial configuration of the H_2^+ and H_2 molecules in 1D. Then I compare the overall shape and optimal internuclear separation of these PES to the same obtained for both molecules in 3D.

In Fig. 3.1, I show how the H_2^+ and H_2 Born-Oppenheimer approximation (BOA) ground state PES changes as a function of the shifted nuclear separation $\sqrt{X^2 + \Delta_{II}^2}$ for each configuration shown in Fig. 2.1. I use this shifted nuclear separation to include the internuclear Soft Coulomb parameter Δ_{II} I use in our configurations.

Species	Δ_{II} (a_0)	Δ_{Ie} (a_0)	Δ_{ee} (a_0)	$E_0(X_{eq})$ (eV)	$\sqrt{X_{eq}^2 + \Delta_{II}^2}$ (Å)
H_2^+	1	0.5	—	-45.757	0.5627
	0.5	1	—	-21.431	1.3510
	1	1	—	-21.969	1.2697
	2	1	—	26.759	1.0584
H_2	$\sqrt{3}$	1	1	-45.193	0.9166
	1	1	$\sqrt{3}$	-44.790	0.9004
	$\sqrt{2}$	1	$\sqrt{2}$	-45.856	0.8241

TABLE 3.1. H_2^+ and H_2 ground state potential energy surface fitted ground state energies $E_0(X_{eq})$ and positions $\sqrt{X_{eq}^2 + \Delta_{II}^2}$ obtained from a harmonic fit around X_{eq} for the configurations shown in Fig. 2.1.

The PES fitted minimum energies at X_{eq}, $E_0(X_{eq})$ and positions $\sqrt{X_{eq}^2 + \Delta_{II}^2}$ are shown in Table 3.1 for the H_2^+ and H_2 molecules with the configurations shown in Figs. 2.1 a) and b). The data for X_{eq} and $E_0(X_{eq})$ in Table 3.1 has been obtained from a harmonic fit around $E_0(X_{eq})$. I fit the ground state PES around its minimum energy at the internuclear equilibrium distance X_{eq} using a harmonic approximation $E_{gs}(X_{eq}) + \frac{1}{2}k(X - X_{eq})^2$, where $k = \omega^2\mu_p$ is the harmonic constant, ω is the harmonic oscillator vibrational frequency and μ_p is defined in Eq. B.16. From ω, I obtain the ground state electron-nuclei eigenvalue

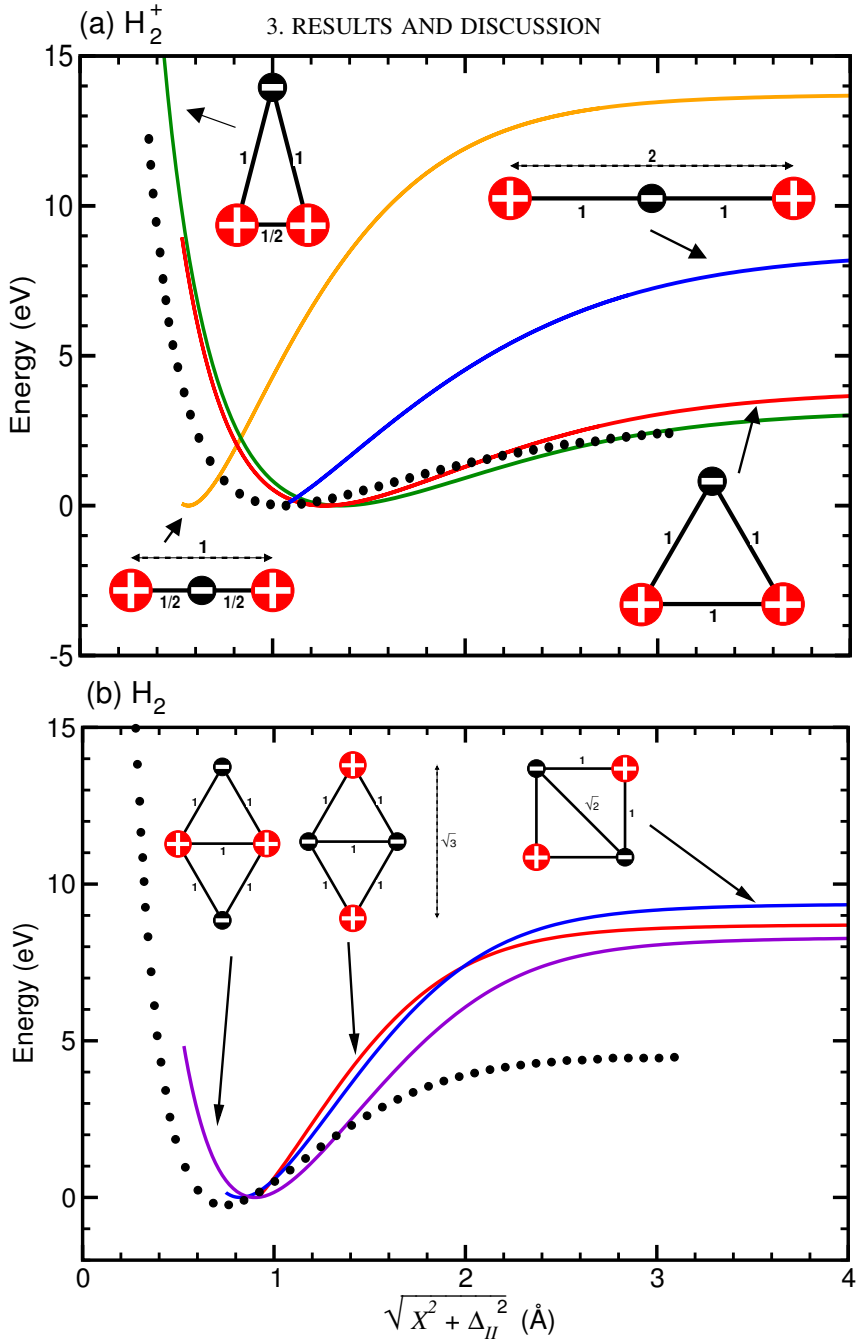

FIGURE 3.1. Born-Oppenheimer approximation one-dimensional ground state potential energy surfaces relative to $E_0(X_{eq})$ in eV, versus $\sqrt{X^2 + \Delta_{II}^2}$ in Å for (a) H_2^+ and (b) H_2 molecules for the Δ_{II}, Δ_{ee} and Δ_{Ie} configurations given in Fig. 2.1 shown here as insets. The Born-Oppenheimer approximation three-dimensional ground state potential energy surfaces (dotted lines) have been taken from Ref. [219].

of a harmonic oscillator $\varepsilon_{gs} = E_{gs}(X_{eq}) + \frac{1}{2}\hbar\omega$ in the BOA PES picture, where $\frac{\hbar\omega}{2}$ is the zero-point energy and $E_{gs}(X_{eq})$ is the energy of the PES at X_{eq}.

The ground state PESs [dotted black lines in Figs. 3.1 a) and b) and taken from Ref. [219]] have been obtained by solving the stationary Schrödinger equation in 3D using basis sets. The experimental bond lengths of H_2^+ and H_2 are $2a_0$ [220] and $\sqrt{2}a_0$ [219], respectively.

The overall shape of these 3D PES is reproduced by our configurations b) (red PES) and c) (green PES) from Fig. 2.1 a) for H_2^+ and the 1D PES in Fig. 3.1 a). The 3D ground state PES equilibrium distance is best reproduced by configuration d) from Fig. 2.1 a) for H_2^+ and the 1D PES in Fig. 3.1 a).

None of the configurations from Fig. 2.1 b) for H_2 and the 1D PES are able to reproduce the overall shape or equilibrium distance of the 3D PES in Fig. 3.1 b).

The nuclei sometimes feel a strong internuclear attraction and repulsion for larger and small X, respectively, depending on the initial configuration as shown in Figs. 3.1 a) and b). For the strongly repulsive configurations for small X, the nuclei want to be farther apart because the repulsion between the nuclei is stronger than the attraction between the nuclei and electrons. For the strongly attractive configurations for larger X, the nuclei want to be closer together because the repulsion between the nuclei is weaker than the attraction between the nuclei and electrons.

The even state and odd state subsequent PES's are degenerate for large X for both H_2^+ and H_2 molecules. Due to the exchange symmetry with respect to the X nuclear coordinate from X to $-X$ in the Hamiltonians for both molecules, the nuclear eigenfunctions have a given parity as explained in Sec. 2.2.3. The X and $-X$ components of the nuclear wavefunction overlap to give rise to bonding and antibonding contributions. The bonding contribution corresponds to an even singlet state and the antibonding to an odd triplet state. This overlap becomes negligible for large X and thus the singlet and triplet states become degenerate. For H_2^+ all excited PES's are unbound. This means that all excitation energies from the even state to the subsequent odd PES's at X_{eq}, are larger than the energy required from X_{eq} to large X of the even initial PES. For configuration a) in Fig. 2.1 a), we see that a lot of energy is required for large X in Fig. 3.1 a). Therefore, we expect that the excitation energies required for this configuration will be larger than any of the other configurations analysed for H_2^+. This will be shown in the spectra in Sec. 3.1.2.2 and Fig. 3.3 d).

For H_2^+, when $\Delta_{Ie} = 1a_0$, the PES becomes less repulsive for small X as Δ_{II} increases. When $\Delta_{Ie} = 0.5a_0$, the PES becomes strongly attractive for larger X.

For H_2, when $\Delta_{II} = \Delta_{ee} = \sqrt{2}a_0$, configuration g) (blue PES) from Fig. 2.1 b) the PES becomes more attractive than the other configurations for larger X as shown in Fig. 3.1 b). When $\Delta_{ee} = \sqrt{3}$, the PES becomes more repulsive than the other configurations for small X.

3.1.2.2. *Linear response photoabsorption spectra.* In this section I obtain the linear photoabsorption spectra from a classical (either fixing the nuclei at X_{eq} with the Born-Oppenheimer approximation (BOA) or allowing them to move according to Ehrenfest dynamics (ED) from X_{eq}) versus quantum perspective and for several configurations for the H_2^+ and H_2 molecules.

In Figs. 3.2 a) and b) I compare the H_2^+ and H_2 optical spectra I obtain by classically fixing the ions at X_{eq} with the ones where the nuclei evolve according to ED in time from X_{eq}.

The energy of the peaks in the photoabsorption spectra is given by the transition energy between the electronic ground and excited corresponding state for each peak at X_{eq}. In Figs. 3.2 a) and b) the mass M_{H} is the proton to electron mass ratio $\frac{M_{\mathrm{p}}}{m_{\mathrm{e}}}$ corresponding mass for a H atom, and M_{p} is the mass of the proton.

Essentially, including the classical movement of the nuclei with ED hardly changes the spectra as compared to fixing the nuclei via the BOA. However, when I allow the nuclei to move according to ED, a new small peak appears before the first electronic excitation for both molecules. For H_2^+ this new peak appears at $\sim$ 1 eV and for H_2 at $\sim$ 12 eV.

As shown in Sec. 2.1.2, in the ED approach the nuclear coordinates are coupled to the electronic coordinates and are updated at each time step. For this reason, in Fig. 3.2, I show that the time-dependent effects of the classical nuclear motion within ED have an impact on the spectra.

The H_2^+ peak for small energies corresponds to the frequency of the nuclear zero point motion for a harmonic oscillator around X_{eq} for H_2^+, which vanishes for large masses ($M_{\mathrm{p}} \times 10^4$). For large masses M_α, the nuclei will hardly move around X_{eq}. Consequently $\omega = \sqrt{\frac{k}{\mu_p}}$ and the zero point energy $\frac{\hbar\omega}{2}$ are small.

The inset of Fig. 3.2 a) illustrates the time-dependent effects of nuclear motion. The increasing difference $\Delta d(24\mathrm{fs}) \sim 0.7\mathrm{mD}$ between the ED and BOA dipole moments demonstrates that the nuclei move with time. Within the ED approach there is a shift of the global centre of mass of the molecule as it propagates. However, within the BOA approach the global centre of mass of the molecule is constant in time. This effect may lead to the appearance of the additional ED peak for H_2 at 12 eV [see Fig. 3.2 b)]. Due to this peak, the ED and fixed BOA nuclear spectra do not overlap completely. This peak does not vanish for large M, as is the case for the zero point energy peak for H_2^+.

Due to the minor differences between the ED versus BOA classical spectra in Figs. 3.2 a) and b), I will from now on compare the BOA classical spectra only to the quantum nuclear one. This is because for the fixed nuclei BOA method I only have to deal with the electrons computationally.

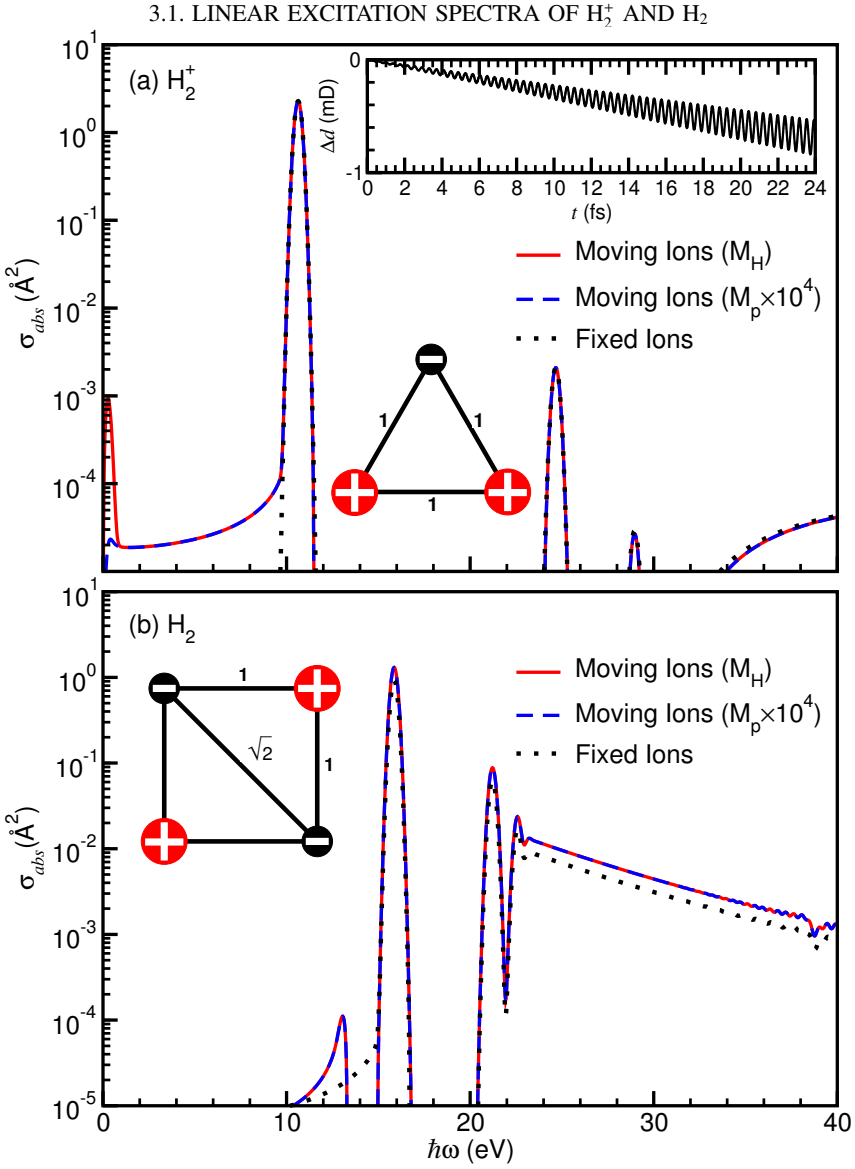

FIGURE 3.2. Optical spectra for the (a) H_2^+ and (b) H_2 molecules obtained by classically fixing the nuclei to their equilibrium positions X_{eq} (Born-Oppenheimer approximation) and evolving the nuclei (Ehrenfest dynamics) from X_{eq} for masses M_H and $M_p \times 10^4$ with nuclear and electronic separations (a) $\Delta_{II} = 1a_0$ (b) $\Delta_{II} = \Delta_{ee} = \sqrt{2}a_0$ and electron-nuclear separations (a,b) $\Delta_{Ie} = 1a_0$ shown as insets. The evolution of the difference in dipole moment Δd between Ehrenfest dynamics and Born-Oppenheimer approximation for M_H in milliDebye (mD) is shown as an inset of (a).

In Fig. 3.3, I show how a quantum mechanical treatment of the nuclei affects the optical absorption spectra for H_2^+ and H_2 molecules in the configurations of Δ_{II}, Δ_{ee} and Δ_{Ie} shown in Fig. 2.1.

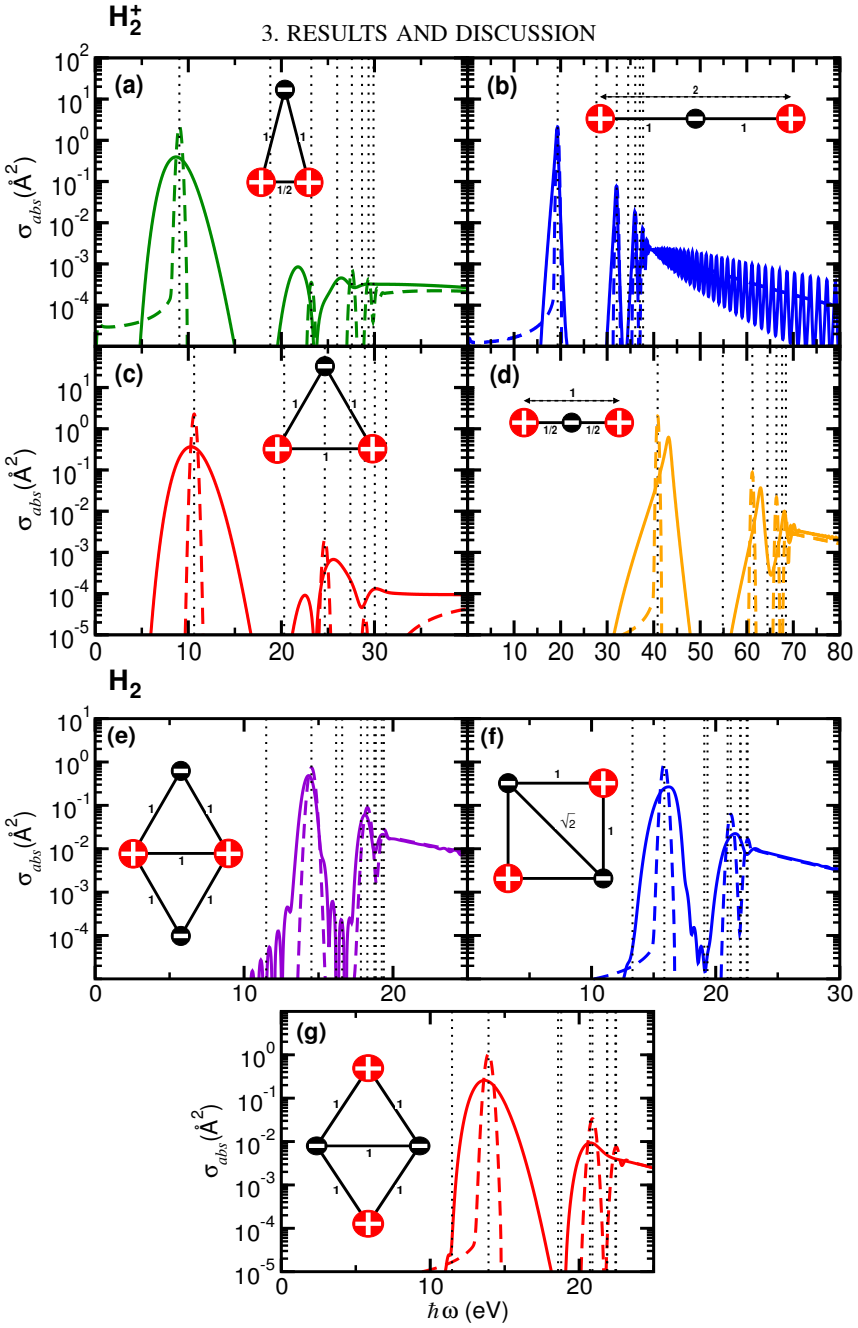

FIGURE 3.3. Absorption spectra obtained from a classical Born-Oppenheimer approximation (dashed lines) or a quantum mechanical (solid lines) treatment of the nuclei of an (a–d) H_2^+ molecule with configurations (a) $\Delta_{II} = \frac{1}{2}a_0; \Delta_{Ie} = 1a_0$ (green), (b) $\Delta_{II} = 2a_0; \Delta_{Ie} = 1a_0$ (blue), (c) $\Delta_{II} = 1a_0; \Delta_{Ie} = 1a_0$ (red), and (d) $\Delta_{II} = 1a_0; \Delta_{Ie} = \frac{1}{2}a_0$ (orange) or an (e–h) H_2 molecule with configurations (e) $\Delta_{II} = 1a_0; \Delta_{Ie} = 1a_0; \Delta_{ee} = \frac{1}{3}a_0$ (violet), (f) $\Delta_{II} = \sqrt{2}a_0; \Delta_{Ie} = 1a_0; \Delta_{ee} = \sqrt{2}a_0$ (blue), (g) $\Delta_{II} = \sqrt{3}a_0; \Delta_{Ie} = 1a_0; \Delta_{ee} = 1a_0$ (red), shown as insets. Dotted vertical lines denote the energies ε_i of the unoccupied electronic levels $\varphi_i^{X_{eq}}(\xi)$ relative to the ground state energy ε_0 for each configuration fixed at X_{eq}.

To ensure that the optical spectra I obtain is only affected by the external perturbation K, I symmetrise our initial wavefunction by imposing

$$\psi_{symm}(X,\xi) = \frac{\psi(X,\xi) + \psi(-X,\xi)}{\sqrt{2}}. \tag{3.2}$$

Thus, I always excite from a ground state which is symmetric in the nuclear coordinate. In Fig. 3.9, I show that symmetrising the wavefunction does not change the calculated optical absorption spectrum. This means that we already obtain a nearly symmetric ground state starting configuration from the stationary Schrödinger Eq. 2.9.

New features emerge in the spectra when the nuclei are treated quantum mechanically [solid lines in Figs. 3.3 a) to g)] instead of classically by means of the BOA [dashed lines in Figs. 3.3 a) to g)]. The peaks are broadened, become asymmetric, and their amplitudes and energies change as a function of the initial configuration and charge of the molecule. In particular, I find that each classical BOA peak seems to split into a bonding and an antibonding contribution, lower and higher in energy, respectively. Depending on the energy shift and amplitude of each contribution, these can appear as separate peaks [we only clearly see this for the second BOA classical peak in Fig. 3.3 a) and c)] or shoulders in the spectra. The shoulders are giving rise to an asymmetry that can be visualised for almost every peak. With a classical description of the nuclei, I do not obtain these new quantum mechanical features in the optical spectra.

For internuclear potentials which are less repulsive and attractive for both small and larger X, respectively, [see Figs. 3.1 a) (blue PES) and b) (purple PES)], the line shape of the quantum nuclear peaks is narrowed, and their position approaches that of the BOA peaks at equilibrium distance X_{eq} [see Figs. 3.3 b) and e)]. For potentials which are repulsive for small X [see Fig. 3.1 a) (green PES)], all the quantum nuclear peaks are red shifted with respect to the BOA peaks at equilibrium distance X_{eq} [see Fig. 3.3 a)]. For potentials which are attractive for larger X [see Figs. 3.1 a) (orange PES) and b) (blue PES)], all the quantum nuclear peaks are blue shifted with respect to the BOA peaks at equilibrium distance X_{eq} [see Figs. 3.3 d) and f)]. In the case of Fig. 3.3 d), we see that the excitation energies of the peaks are much larger than for the other configurations (see energy scale of Fig. 3.3 d) and the explanation in Sec. 3.1.2.1).

In Figs. 3.3 a) to d), I clearly show for H_2^+ that only the classical peaks in the absorption spectra obtained from a BOA treatment (dashed lines) are clearly aligned with the energies of odd-parity unoccupied electronic levels ε_{2i+1} (odd-parity vertical dotted lines) independent of the configuration and charge of the molecule. This is because only the even to odd $\tilde{\xi}$ dipole allowed electronic Franck-Condon transitions are allowed by symmetry as explained in Sec. 2.2.5 and shown in Fig. 3.4. The occupied $\varphi_0(\xi)$ and first four unoccupied $\varphi_i(\xi)$ BOA electronic wavefunctions at X_{eq} are depicted in Fig. 3.4, ordered according to their energy. The electronic wavefunctions with even indices φ_{2i} are even functions of ξ, while the electronic wavefunctions with odd indices φ_{2i+1} are

odd functions of ξ. This parity of the electronic wavefunctions means that the transition dipole moment is zero for transitions from the ground state to even unoccupied states, i.e., $\langle\varphi_{2i+2}|\hat{\xi}|\varphi_0\rangle = 0$. Essentially, even-even optical transitions $\varphi_0 \rightarrow \varphi_{2i+2}$ are forbidden so long as φ_{2i+2} is an even function of ξ. This is what we observe when the nuclei are treated classically, as depicted in Fig. 3.4, and in Figs. 3.3 a) to d), where the classical BOA peaks (dashed lines) are aligned with the odd-parity vertical dotted lines ε_{2i+1}, i.e., the Franck-Condon transitions $\varphi_0 \rightarrow \varphi_{2i+1}$.

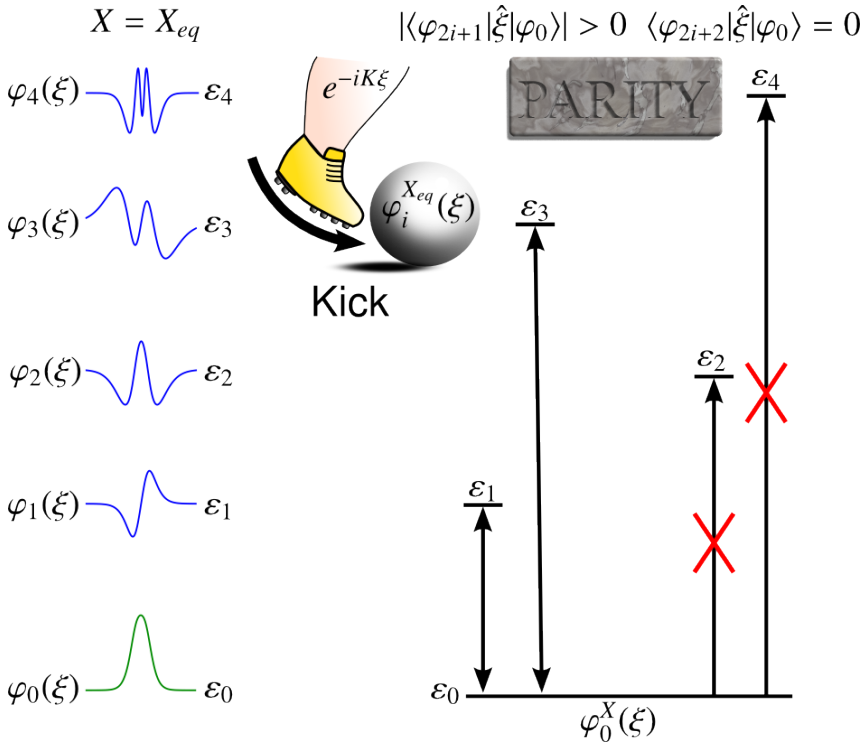

FIGURE 3.4. Schematic representation of the excitation process from the occupied $\varphi_0(\xi)$ to the first four unoccupied $\varphi_i(\xi)$ electronic levels at the equilibrium geometry ($X = X_{eq}$) after applying an impulsive perturbative "kick" $\sim e^{-iK\xi}$ for $K \ll 1$ (see Sec. 2.2.5 and Eqs. 2.48 and 2.52). On the right hand side of the figure, I show the allowed even to odd transitions from the even ground state electronic level to the two following first and third lowest excited electronic levels. The even to even transitions, i.e., to electronic levels which are even functions of ξ, are forbidden by parity. Figure reproduced with the permission of Duncan J. Mowbray.

However, for H_2 we find that the classical peaks in the absorption spectra obtained from a BOA treatment (dashed lines) are aligned with the second, sixth and tenth unoccupied BOA electronic transitions. To understand this, I plot in Fig. 3.5 the first eleven wavefunctions for the H_2 molecule as a function of both x and ξ.

As for H_2^+, only the even to odd ξ dipole allowed electronic Franck-Condon transitions are allowed by symmetry. However, for H_2 we also need to take into account the exchange symmetry with respect to x. In Fig. 3.5 the even-parity states are even from x to $-x$ and are therefore singlets. The odd-parity states are odd from x to $-x$ and are therefore triplets. Due to this exchange symmetry, only transitions from the ground state occupied singlet state to excited unoccupied singlet states are allowed. Moreover, only transitions from the occupied ground state even in ξ to unoccupied excited states odd in ξ are allowed by symmetry. Taking into account both the x and ξ factors, we see in Fig. 3.5 that only transitions from the ground state to the second, sixth and tenth excited states are allowed by symmetry.

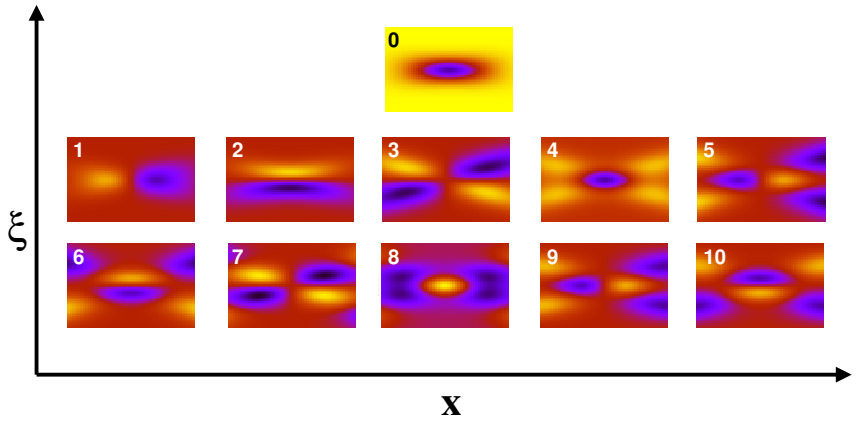

FIGURE 3.5. Electronic Born-Oppenheimer approximation wave functions $\varphi_i^{X_{eq}}(\xi, x)$ for $i = 0, \ldots, 10$ of an H_2 molecule in the configuration $\Delta_{II} = \frac{1}{3}; \Delta_{ee} = 1$.

New features arise in the quantum nuclear spectra in Figs. 3.3 a) to g) which cannot be described by their classical BOA corresponding spectra. This suggests that the quantum nature of the nuclei can play an important role when describing linear photoabsorption processes.

The quantum features are only noteworthy for H_2^+ in Figs. 3.3 a) and c) where the second even to odd allowed BOA Franck-Condon transition is split in red lower in energy and blue higher in energy shifted contributions. Moreover, for these two cases the overall shape of our 1D PES is closer the 3D PES as shown in Fig. 3.1 a) and b), respectively.

As these quantum features are not as strong for the other H_2^+ configurations and for the neutral H_2 homonuclear diatomic molecule, I will not analyse any of these cases further.

3.1.2.3. *Model.* The level splitting we observe for the second Born-Oppenheimer approximation (BOA) allowed energy transition in Figs. 3.3 a) and c) is reminiscent of level hybridisation. This motivates us to employ a simple two-level model to describe the energies and widths of the quantum nuclear peaks.

To quantify the validity of the classical approximations where $E_{vib}/E_{elec} \approx \sqrt{m_e/M}$ is small (see Appendix A), the two-level model I employ has a dependence on the electron nuclear mass ratio.

As I will show in Figs. 3.7 and 3.11, both the widths and positions of these peaks clearly depend on the electron-nuclear mass ratio $\frac{m_e}{M}$. Using this two-level model, I am going to quantitatively show how the observed quantum nuclear spectral peak energy shifts and widths are related to the BOA electronic energy levels ε_i at the equilibrium X_{eq} of the ground state through the electron-nuclear mass ratio $\frac{m_e}{M}$.

Within our two-level model, for each odd-parity excited electronic level φ_{2i+1} at ε_{2i+1}, I artificially introduce a level at $\widetilde{\varepsilon}_{2i+1}$ to which it couples. In particular, I am only going to focus on the first ε_1 and third ε_3 even to odd in ξ allowed excited electronic levels shown in Fig. 3.4 because these are the most intense in the spectra.

The resulting two-level system Hamiltonians $\hat{H}_{2\mathrm{LS}}$ for the first and third even to odd in ξ allowed transitions are given by

$$H_{2\mathrm{LS}}(\varepsilon_1) = \begin{bmatrix} \varepsilon_1 & \alpha\kappa \\ \alpha\kappa & \widetilde{\varepsilon}_1 \end{bmatrix}, \tag{3.3}$$

and

$$H_{2\mathrm{LS}}(\varepsilon_3) = \begin{bmatrix} \varepsilon_3 & \alpha\kappa \\ \alpha\kappa & \widetilde{\varepsilon}_3 \end{bmatrix}, \tag{3.4}$$

where $\alpha\kappa$ is the coupling term between the nuclei and electrons with a prefactor α which gives the strength of the coupling. Here I use the parameter $\kappa = (m_e/M)^{1/4}$ given in Appendix A [186] to introduce the electron-nuclear mass ratio.

All the peak energy positions in the quantum nuclear spectra can be fitted using only two parameters, the artificial level's energy $\widetilde{\varepsilon}_1$ or $\widetilde{\varepsilon}_3$, and the coupling constant α.

The determinant of the matrices $\hat{H}_{2\mathrm{LS}}$ can be used to calculate the first and third allowed transitions' energies ω_1 and ω_3 by

$$\det|H_{2\mathrm{LS}}(\varepsilon_1) - \omega_1\mathbb{1}| = 0 = \omega_1^2 - \omega_1(\widetilde{\varepsilon}_1 + \varepsilon_1) + \widetilde{\varepsilon}_1\varepsilon_1 - (\alpha\kappa)^2, \tag{3.5}$$

and

$$\det|H_{2\mathrm{LS}}(\varepsilon_3) - \omega_3\mathbb{1}| = 0 = \omega_3^2 - \omega_3(\widetilde{\varepsilon}_3 + \varepsilon_3) + \widetilde{\varepsilon}_3\varepsilon_3 - (\alpha\kappa)^2, \tag{3.6}$$

where $\mathbb{1}$ is the identity matrix of the same dimension as $\hat{H}_{2LS}(\varepsilon_1)$ and $\hat{H}_{2LS}(\varepsilon_3)$. As I will show in Sec. 3.1.2.4, for the first allowed transition I will only analyse the width and peak energy of the bonding − contribution. This is because I cannot fit the width and peak energy of the antibonding + contribution for the first allowed transition because it is coupled to the bonding contribution as a shoulder [see Figs. 3.3 a) and c)]. In this case I only analyse the bonding contribution in energy that arises from the coupling between ε_1 and $\widetilde{\varepsilon}_1$. This bonding contribution corresponds to the first separate peak we see in Figs. 3.3 a) and c). For the third allowed transition I will analyse both the bonding − and antibonding + contribution. As shown in Figs. 3.3 a) and c), the bonding and antibonding contribution correspond to the second and third separate peaks we can visualise in the quantum nuclear spectra (solid lines) which are positioned to the left and right of the BOA second odd allowed peak (dashed lines) in the spectra, respectively. In this case I analyse both the antibonding and bonding contribution peaks in energy that arise from the coupling between ε_3 and $\widetilde{\varepsilon}_3$.

Using the quadratic formula, the first allowed transition energy is given by

$$\omega_1 = \frac{\varepsilon_1 + \widetilde{\varepsilon}_1}{2} \pm \sqrt{\left(\frac{\varepsilon_1 - \widetilde{\varepsilon}_1}{2}\right)^2 + (\alpha\kappa)^2}, \tag{3.7}$$

where $\varepsilon_1 \approx 10$ eV, as shown in Fig. 3.3 a) and c).

The third allowed transition energy is given by

$$\omega_3 = \frac{\varepsilon_3 + \widetilde{\varepsilon}_3}{2} \pm \sqrt{\left(\frac{\varepsilon_3 - \widetilde{\varepsilon}_3}{2}\right)^2 + (\alpha\kappa)^2}, \tag{3.8}$$

where $\varepsilon_3 \approx 24$ eV as shown in Fig. 3.3 a) and c).

The coupling term between ε_{2i+1} and its corresponding $\widetilde{\varepsilon}_{2i+1}$, scales as the quantum nuclear displacement $\delta \sim \kappa$ (see Appendix A). The degree of coupling between ε_{2i+1} and its corresponding $\widetilde{\varepsilon}_{2i+1}$, which are coupled via the nuclear displacements, increases with the displacement of the nuclei. This coupling is therefore larger for smaller nuclear masses M, as these are lighter and can move more.

Therefore, I want to analyse the effect of the nuclear displacements $\delta \sim \kappa \sim (m_e/M)^{1/4}$ as a function of the nuclear mass M, as these displacements are causing the differences we see from a classical versus quantum nuclear treatment in the spectra. From Eqs. 3.7 and 3.8, we see that for larger couplings with a smaller nuclear mass M, the + and − contributions will be more separated in energy.

The width of the peaks in the absorption spectra is also related to the nuclear displacement. When the nuclei evolve quantum mechanically, the electrons can transfer part of their dipole moment to the nuclei. Depending on the speed of this transfer, the amplitude of the electronic dipole moment oscillations decreases in time at different time scales

depending on the mass of the nuclei. Since the widths of the absorption peaks are proportional to the decay of the dipole moment oscillations, we also expect the widths to scale as the electron-nuclear mass ratio to the one fourth. As heavy nuclei will displace less, damping the electronic dipole moment will take more time. The changes in the frequency of the oscillations of the dipole moment will not be abrupt, the peak energy will be more defined and the width of the peak narrower. For very large nuclear masses, the interaction with the electronic motion becomes nearly elastic because there will hardly be any energy transfer from the electrons to the nuclei. This allows the electrons to oscillate back and forth without the influence of any external nuclear displacements. As lighter nuclei will displace more, the decay of the electronic dipole moment will take less time. The changes in the frequency of the oscillations of the damped dipole moment will be more abrupt, the peak energy will be less defined and the width of the peak broader.

The simple two-level model I employ is able to quantitatively predict the widths and positions of the quantum peaks in the spectra, from the coupling between the electronic BOA classical allowed energy level to an artificial level, via the nuclear displacements $\delta \sim \kappa \sim (m_e/M_p)^{1/4}$ which are proportional to the electron-nuclear mass ratio.

3.1.2.4. *Analysis.* To provide a quantitative analysis of the differences between a classical Born-Oppenheimer approximation/Ehrenfest dynamics (BOA/ED) or quantum treatment of the nuclei, I will compare the total ground state energies and the peak positions and widths in the absorption spectra as I vary the nuclear mass.

The mass of every nuclei I have tested M_X with $X \in \mu, H, D, T, Li, Na, K$ is given by the nuclear-electron mass ratio $\frac{M_X}{m_e}$ where M_X corresponds to the mass of each nuclei X. For the nuclear mass case $M_p \times 10^4$, M_p is the proton mass. Note that even though I vary the nuclear mass M_X of our molecules, I fix their nuclear charge to that of a single proton $Z = 1$. This is because the repulsion between the nuclei of more massive homonuclear diatomic molecules with the correct charge would be so large that the molecules would be unstable [221]. Furthermore, this allows us to directly compare absorption spectra between these model systems for a fixed interaction potential with $Z = 1$ and different nuclear mass M. Most of the molecules used in this analysis are fictitious because I do not change the charge of the nuclei, except for H, D, and T, as these have a positive electric charge of $Z = 1$.

Analysis: Ground state accuracy

As explained in Appendix A, the accuracy of the static Born-Oppenheimer approximation (BOA) calculations can be understood from a perturbation theory argument in terms of the small parameter $\kappa = (m_e/M_p)^{1/4}$ [186]. There I show that the BOA ground state electron-nuclear eigenvalue for the H_2^+ and H_2 molecules in 1D is given by

$$\varepsilon_{gs}^{\mathrm{BOA/ED}} \approx \varepsilon^{(0)} + \varepsilon^{(2)}(\kappa^2) + \mathrm{O}(\kappa^4), \tag{3.9}$$

where $\varepsilon^{(0)}$ and $\varepsilon^{(2)}$ correspond to the electronic and nuclear motion eigenvalues, and, the first and third-order contribution to the eigenvalue, $\varepsilon^{(1)}$ and $\varepsilon^{(3)}$, vanish by symmetry. The first non-vanishing correction to the ground state energy for the full electron-nuclear problem using the BOA is the term of fourth order in κ.

To test the accuracy of the BOA approximations, I first compare the BOA ground state electron-nuclear eigenvalues to those obtained from quantum nuclei. We expect that the BOA should be accurate around the minimum of the ground state potential energy surface (PES), as the exact eigenvalues of the electron-nuclear problem can be interpreted in terms of the nuclear vibrational levels for the electronic ground state PES. As discussed in Sec. 3.1.2.1, the nuclear contribution comes from the ground state level of a quantum harmonic oscillator where the mass is included via ω.

To check the dependence of the static ground state eigenvalue accuracy of the BOA approach, on the electron-nuclear mass ratio, I use the following power law relation

$$\varepsilon_{gs}^{\mathrm{BOA}} - \varepsilon_{gs}^{\mathrm{QMI}} = a\kappa^{4b} = a\left(\frac{m_e}{M_X}\right)^b . \tag{3.10}$$

According to the above, we should obtain an exponent $b \approx 1$ for each molecule and different masses M_X, as the first non-vanishing term that the BOA does not include in 1D is the term of fourth order in κ.

Fitting the ground state error from Eq. 3.10 to the data in Tables 3.2 and 3.3, I obtain a power law of $b = 0.92(2)$ and $b = 1.05(2)$ for the BOA approach and H_2^+ and H_2, respectively, as shown in Fig. 3.6. Therefore, the BOA energy expression gives the correct total ground state energy of the full electron-nuclear problem up to fourth order in κ for both the H_2^+ and H_2 molecules.

M	$\varepsilon_{gs}^{\mathrm{QMI}}$(eV)	$\varepsilon_{gs}^{\mathrm{BOA}}$ (eV)	$\frac{m_e}{M_X}$
μ	-21.703395	-21.697297	0.004836
H	-21.970225	-21.969323	0.000545
D	-22.009642	-22.009272	0.000272
T	-22.027041	-22.026787	0.000182
Li	-22.053541	-22.053420	0.000079
Na	-22.076626	-22.076580	0.000023
K	-22.083189	-22.083160	0.000014

TABLE 3.2. M_2^+ ground state eigenvalues obtained from diagonalisation of the quantum nuclear approach $\varepsilon_{gs}^{\mathrm{QMI}}$, and ground state harmonic Born-Oppenheimer approximation $\varepsilon_{gs}^{\mathrm{BOA}}$ eigenvalues obtained from a harmonic fit around the minimum of the ground state potential energy surface. I show these results for different nuclear masses M_X, a fixed nuclear charge of a single electron $Z = 1$ and $\Delta_{II} = 1$ and $\Delta_{Ie} = 1$.

M	$\varepsilon_{gs}^{\mathrm{QMI}}$ (eV)	$\varepsilon_{gs}^{\mathrm{BOA}}$ (eV)	$\frac{m_e}{M_X}$
μ	-45.621166	-45.440564	0.004836
H	-45.739425	-45.722955	0.000545
D	-45.772460	-45.763130	0.000272
T	-45.786936	-45.779126	0.000182
Li	-45.810176	-45.807442	0.000079
Na	-45.831319	-45.830529	0.000023
K	-45.837552	-45.837070	0.000014

TABLE 3.3. M_2 ground state eigenvalues obtained by electron-nuclear quantum diagonalisation $\varepsilon_{gs}^{\mathrm{QMI}}$, and ground state harmonic Born-Oppenheimer approximation $\varepsilon_{gs}^{\mathrm{BOA}}$ vibration levels obtained from a harmonic fit around the minimum of the ground state potential energy surface. I show these results for different nuclear masses M_X, a fixed nuclear charge of a single electron $Z = 1$ and $\Delta_{II} = \sqrt{2}$ and $\Delta_{Ie} = 1$.

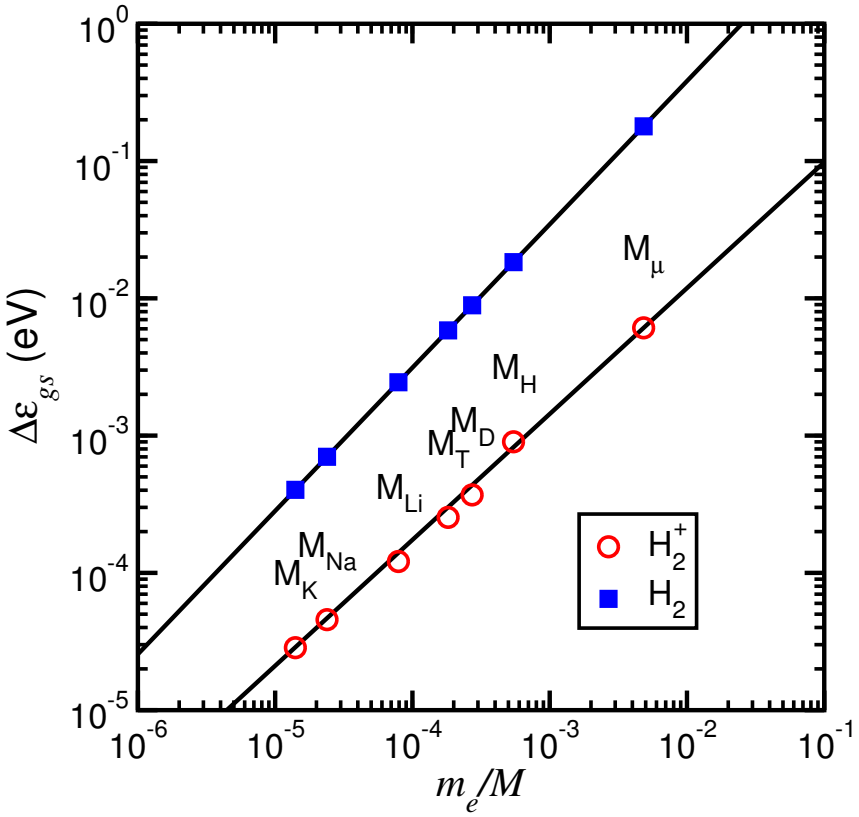

FIGURE 3.6. Difference in ground state total energy between the quantum and Born-Oppenheimer approximation classical nuclear approach $\Delta\varepsilon_{gs}$ in eV versus the electron-nuclear mass ratio m_e/M_X for H_2^+ ($\Delta_{II} = 1$ and $\Delta_{Ie} = 1$; ○) and H_2 ($\Delta_{II} = \Delta_{ee} = \sqrt{2}$ and $\Delta_{Ie} = 1$; ■). The solid lines correspond to a power law fit $a\,(m_e/M_X)^b$.

Analysis: Spectral energy shifts and widths

In Fig. 3.7 I show how the absorption spectra depends on the nuclear mass for the H_2^+ configurations, for which the overall potential energy surface (PES) shape is closest to that from the 3D treatment in Ref. [219]. Specifically, for H_2^+ I analyse in Figs. 3.7 a) and b), the configurations shown in Figs. 2.1 b) and c).

In Fig. 3.7 b) we see for H_2^+ that in the large mass limit ($M = 10^4 \times M_p$), the quantum nuclear spectra is aligned with the allowed even to odd vertical dotted Born-Oppenheimer approximation (BOA) transitions. The symmetry of the electronic wavefunctions $\varphi_i(\xi)$ is shown above the dotted vertical lines for the first four states in energy. As the nuclear mass decreases, we see in Figs. 3.7 a) and b) for H_2^+ that the second and third separate peaks in the spectra, ω_2 and ω_3, separate more in energy and get broader, as predicted from the two-level model. As explained in Sec. 3.1.2.3, these two peaks correspond to the bonding and antibonding contribution of the third allowed transition. As the mass increases, all peaks tend towards the fixed-nuclei at X_{eq} limit with respect to both the width and energy position. For H_2^+, the position of the first, second and fourth peaks in Fig. 3.7 a) and b) (ω_1, ω_2, and ω_4) are red-shifted and the third and fifth peaks (ω_3 and ω_5) are blue-shifted with respect to the fixed-nuclei at X_{eq}. Here ω_4 and ω_5 are the bonding and antibonding contributions of the fifth allowed transition in energy. As these peaks are not very intense in the spectra we will not analyse these contributions.

Overall, the width of all the peaks in Figs. 3.7 a) and b) decreases for all the peaks as the mass M increases, and they approach the classical limit centred at X_{eq}. The decay of the dipole moment shown in Fig. 3.8 presents this narrowing effect of the peaks in the time domain. As the nuclear mass increases, the decay of the dipole moment takes longer and the changes in the frequency are less abrupt. For a very large nuclear mass ($M_p \times 10^4$), the dipole becomes nearly elastic because it takes very long for it to decay as shown in the upper inset of Fig. 3.8. The dipole energy transfers are still present for very long times because the nuclei can transfer the energy back to the electrons. For very long times we can also clearly visualise beat frequencies for the muon mass case M_μ. These beat frequencies are oscillations which are overlaying the main one, as we can see that the dipole moment is composed of two minima and two maxima of different amplitude.

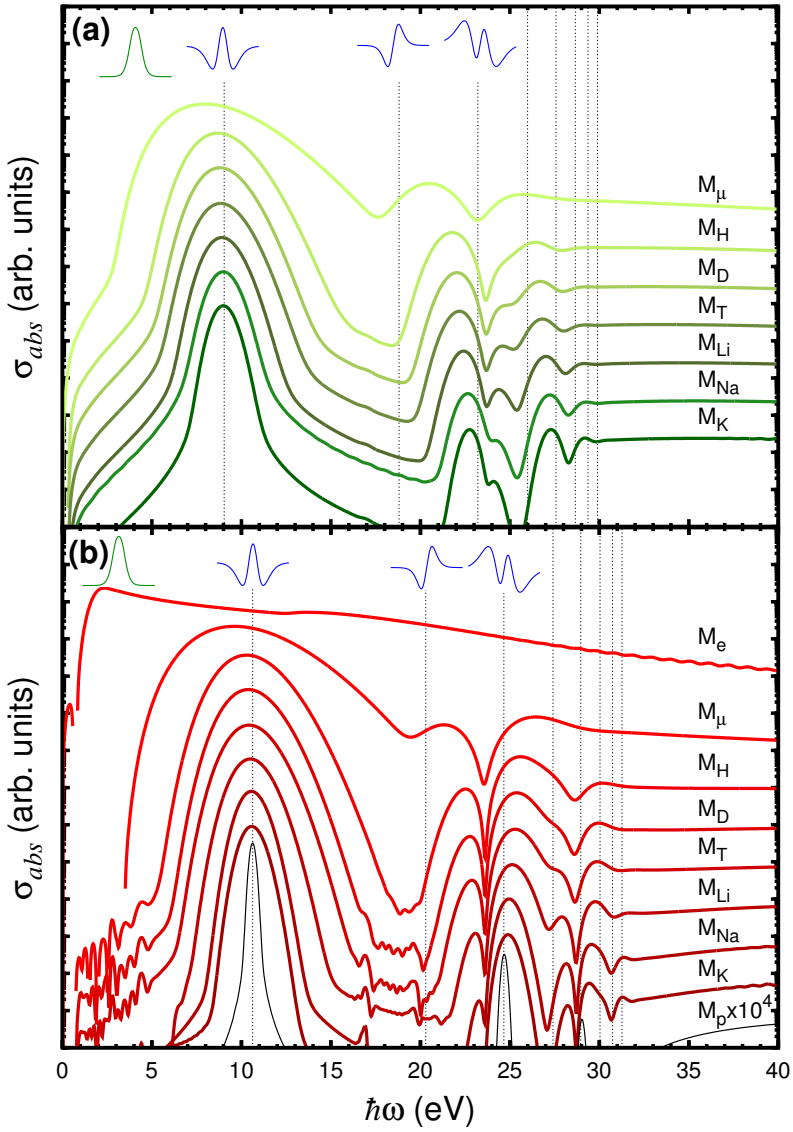

FIGURE 3.7. Quantum electron-nuclear absorption spectra for a positively charged homonuclear diatomic molecule with nuclear mass M of e, μ, H, D, T, Li, Na, K, or 10^4×p in the configuration (a) $\Delta_{II} = 0.5; \Delta_{Ie} = 1$ or (b) $\Delta_{II} = 1; \Delta_{Ie} = 1$. Dotted vertical lines denote the energies ε_i of the unoccupied electronic levels $\varphi_i^{X_{eq}}(\xi)$ (shown in blue as insets) relative to the energy ε_0 of the ground state electronic level $\varphi_0^{X_{eq}}(\xi)$ (shown in green as insets) for each configuration. Note that the spectra have been scaled with decreasing mass for clarity.

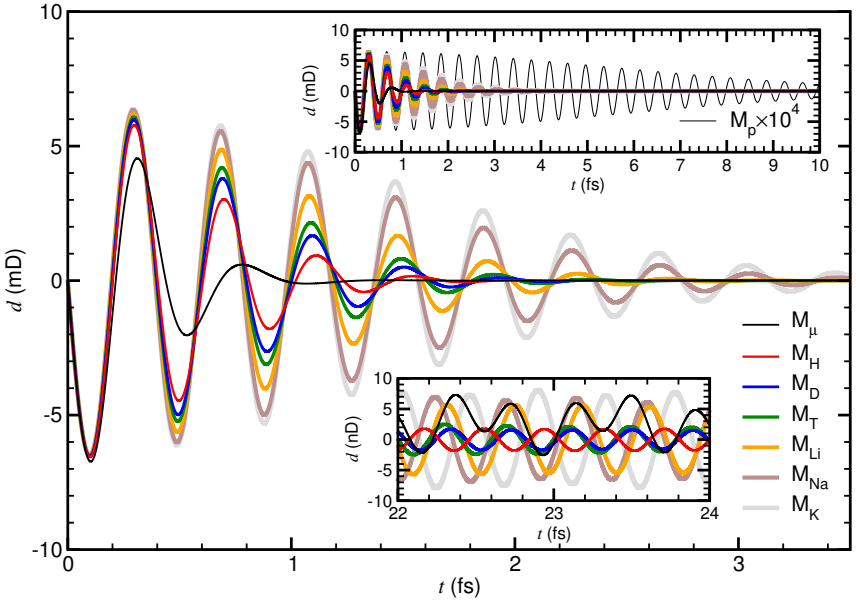

FIGURE 3.8. Evolution of the quantum electron-nuclear dipole moment d in milliDebye with time t after the initial "kick" in fs for nuclear masses M of μ, H, D, Ti, Li, Na, K, or (upper inset) 10^4×p of a positively charged homonuclear diatomic molecule in the configuration $\Delta_{II} = \Delta_{Ie} = a_0$. (lower inset) After 20 fs, the amplitude has decreased by a factor of one million.

To quantify the width and energy of the peaks in the spectra, I have fitted the peaks using both a Gaussian

$$\sum_{i=1}^{3} I_i \exp\left(-\frac{(\omega-\omega_i)^2}{2\sigma_i^2}\right), \tag{3.11}$$

and a Lorentzian

$$\sum_{i=1}^{3} I_i \frac{(\Gamma_i/2)^2}{(\omega-\omega_i)^2+(\Gamma_i/2)^2}, \tag{3.12}$$

function. Here $I_{i=1,2,3}$ corresponds to the intensities, $\omega_{i=1,2,3}$ to the energy positions of the peaks, $\sigma_{i=1,2,3}$ to the standard deviations, and $\Gamma_{i=1,2,3}$ to the full widths at half maximum of the first, second and third peak in energy of the QMI spectra.

One could think that the quantum coupling between electronic and nuclear vibrations could broaden the peaks, where peak values that lie many standard deviations away from the mean centred value could be noteworthy, giving rise to a Lorentzian line shape.

From Fig. 3.9, in which I show the quantum nuclear spectra for H_2^+, we clearly see that the tails of the peaks are Gaussian. Moreover, the three peaks can only be fitted simultaneously with Gaussian functions, as the Lorentzian fit to the first peak decays so slowly that the second and third peaks are completely obscured. Furthermore, the nuclear wave packet on the ground state PES is a solution of a harmonic eigenvalue problem and thus should have a Gaussian line shape. This means that the spectral line shape arises mainly from the shape of the PES, rather than the coupling between electronic and nuclear vibrations of the molecule. The electronic and nuclear levels are too far in energy for them to couple and give rise to a Lorentzian line shape.

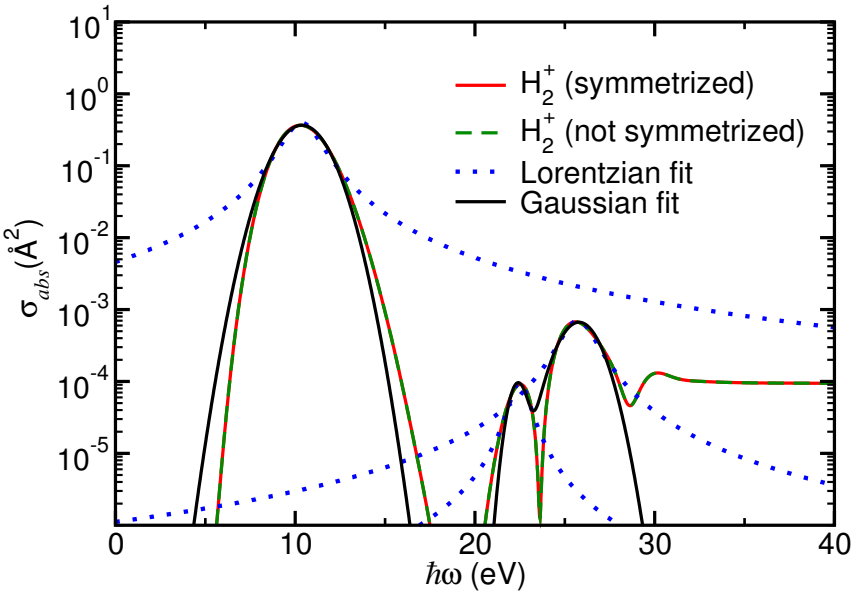

FIGURE 3.9. Quantum electron-nuclear absorption spectra for an H_2^+ molecule in the configuration $\Delta_{II} = 1$ and $\Delta_{Ie} = 1$ obtained with (red solid lines) and without (green dashed lines) imposing symmetry in X on the nuclear wave functions. Lorentzian (blue dotted lines) and Gaussian (black solid line) fits to the first three peaks of the spectra are also provided.

The width of the fixed-nuclei at X_{eq} spectrum in Fig. 3.2 is due to the artificial damping introduced in the spectra via Eq. 2.62. The electronic fixed-nuclei transitions should be delta-like functions, but are convoluted with a Gaussian function to plot the spectra (see Eqs. 2.61 and 2.62). However, the widths in the quantum nuclear spectra are physical, where the Gaussian line shape is due to the electron-electron ε_{2i+1} and $\widetilde{\varepsilon}_{2i+1}$ energy level coupling via the nuclear displacements $\delta \sim M^{-1/4}$. As explained at the end of Sec. 3.1.2.3,

the widths of the peaks will depend on the speed at which the electrons transfer their dipole moment to the nuclei, which in turn depends on the mass of the nuclei. As the mass decreases, all the peaks in Figs. 3.7 a) and b) get broader.

In Fig. 3.10 I use the two-level model discussed in Sec. 3.1.2.3 to fit the calculated quantum nuclear peak energies for various nuclear masses M.

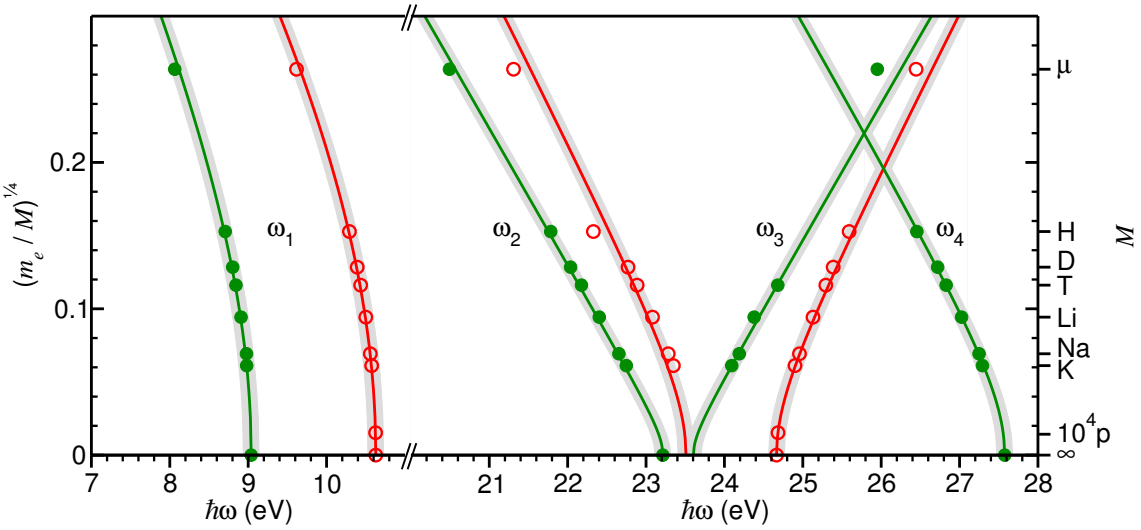

FIGURE 3.10. Two-level model fits to the first four peaks from Eqs. 3.13 and 3.14 in the quantum electron-nuclear absorption spectra ω_i for a positively charged diatomic molecule with nuclear mass M in the configuration $\Delta_{Ie} = 1$ and $\Delta_{II} = \frac{1}{2}$ (●) or $\Delta_{II} = 1$ (○). Level coupling has the form $\alpha(m_e/M)^{1/4}$, and the decoupled levels are obtained from the ground state electronic eigenenergies ε_n. Gray regions denote a ±0.1 eV estimated accuracy.

To plot Fig. 3.10 I invert Eqs. 3.7 and 3.8 to obtain the following for the first peak

$$\kappa = \left(\frac{m_e}{M}\right)^{1/4} = \frac{1}{\alpha}\sqrt{\left[\omega_1 - \left(\frac{\varepsilon_1 + \widetilde{\varepsilon}_1}{2}\right)\right]^2 - \left(\frac{\varepsilon_1 - \widetilde{\varepsilon}_1}{2}\right)^2}, \tag{3.13}$$

and for the second and third peak

$$\kappa = \left(\frac{m_e}{M}\right)^{1/4} = \frac{1}{\alpha}\sqrt{\left[\omega_3 - \left(\frac{\varepsilon_3 + \widetilde{\varepsilon}_3}{2}\right)\right]^2 - \left(\frac{\varepsilon_3 - \widetilde{\varepsilon}_3}{2}\right)^2}. \tag{3.14}$$

The energy of the first peak in the quantum nuclear spectra scales as κ^2, while the energy of the second and third peaks on κ. To understand this, I show for ω_1 that Eq. 3.7

$$\begin{aligned}\omega_1 &= \frac{\varepsilon_1+\widetilde{\varepsilon}_1}{2} \pm \frac{\widetilde{\varepsilon}_1-\varepsilon_1}{2}\sqrt{1+\frac{\left(\frac{\alpha}{M^{1/4}}\right)^2}{\left(\frac{\widetilde{\varepsilon}_1-\varepsilon_1}{2}\right)^2}} \\ &\approx \varepsilon_1 - \frac{\frac{\alpha^2}{M^{1/2}}}{\widetilde{\varepsilon}_1-\varepsilon_1},\end{aligned} \tag{3.15}$$

scales as κ^2 so long as $\alpha^2/M^{1/2} \ll \widetilde{\varepsilon}_1 - \varepsilon_1$. This is valid for ω_1 and every mass M shown in Fig. 3.10. Here I have used the Taylor expansion

$$\sqrt{1+\frac{\left(\frac{\alpha}{M^{1/4}}\right)^2}{\left(\frac{\varepsilon_1-\widetilde{\varepsilon}_1}{2}\right)^2}} \approx 1+\frac{1}{2}\frac{\left(\frac{\alpha}{M^{1/4}}\right)^2}{\left(\frac{\varepsilon_1-\widetilde{\varepsilon}_1}{2}\right)^2} - O\left[\frac{1}{8}\left(\frac{\left(\frac{\alpha}{M^{1/4}}\right)^2}{\left(\frac{\varepsilon_1-\widetilde{\varepsilon}_1}{2}\right)^2}\right)^2\right]. \tag{3.16}$$

For ω_3 I show that Eq. 3.8

$$\begin{aligned}\omega_3 &= \frac{\varepsilon_3+\widetilde{\varepsilon}_3}{2} \pm \frac{\alpha}{M^{1/4}}\sqrt{1+\frac{\left(\frac{\varepsilon_3-\widetilde{\varepsilon}_3}{2}\right)^2}{\left(\frac{\alpha}{M^{1/4}}\right)^2}} \\ &\approx \frac{\varepsilon_3+\widetilde{\varepsilon}_3}{2} \pm \left[\frac{\alpha}{M^{1/4}} + \frac{(\varepsilon_3-\widetilde{\varepsilon}_3)^2 M^{1/4}}{8\alpha}\right] \\ &\approx \frac{\varepsilon_3+\widetilde{\varepsilon}_3}{2} \pm \frac{\alpha}{M^{1/4}},\end{aligned} \tag{3.17}$$

scales as κ so long as $\varepsilon_3 - \widetilde{\varepsilon}_3 \ll 2\alpha/M^{1/4}$. This is valid for ω_3 and every mass M shown in Fig. 3.10. Here I have used the Taylor expansion

$$\sqrt{1+\frac{\left(\frac{\varepsilon_3-\widetilde{\varepsilon}_3}{2}\right)^2}{\left(\frac{\alpha}{M^{1/4}}\right)^2}} \approx 1+\frac{1}{2}\frac{\left(\frac{\varepsilon_3-\widetilde{\varepsilon}_3}{2}\right)^2}{\left(\frac{\alpha}{M^{1/4}}\right)^2} - O\left[\frac{1}{8}\left(\frac{\left(\frac{\varepsilon_3-\widetilde{\varepsilon}_3}{2}\right)^2}{\left(\frac{\alpha}{M^{1/4}}\right)^2}\right)^2\right]. \tag{3.18}$$

In general, the calculated peak positions are within 0.1 eV of the two-level model fit, which is also the expected accuracy of such calculations. I obtain a value of $\alpha \approx 11$ eV for the three main separate peak contributions ω_1, ω_2 and ω_3 in the spectra. For the first peak, $\widetilde{\varepsilon}_1 \approx 20$ eV and for the second and third peak $\widetilde{\varepsilon}_3 \approx 23.5$ eV.

I show that the separation between the two electronic final states ω_2 and ω_3 for H_2^+ in Figs. 3.10 and Figs. 3.7 a) and b) depends on the strength of the coupling between $\widetilde{\varepsilon}_3$ and ε_3. For smaller masses, the coupling is stronger with the nuclear displacement $\delta \sim M^{-1/4}$, leading to a larger energy separation between ω_2 and ω_3. For the largest mass case ($M_p \times 10^4$), the separation between ω_2 and ω_3 is of the order of 1 eV. However, we

cannot visualise both the bonding and antibonding contributions in the spectra in Figs. 3.7 a) and b), because these overlap due to their finite width.

In Fig. 3.11, I also show as expected from our model, that the width of the first and third peak scales as the electron-ion mass ratio to the one fourth, i.e. full width at half maximum FWHM $\approx (m_e/M)^{1/4}$, for the configurations shown in Fig. 2.1 b) and c) and H_2^+. Here I have obtained the FWHM from Eq. 3.11 for the configurations shown in Fig. 2.1 b) and c) and M_2^+ for different masses M. The FWHM for the first peak has a larger constant of proportionality than the third peak, but the widths for both configurations may be fit simultaneously.

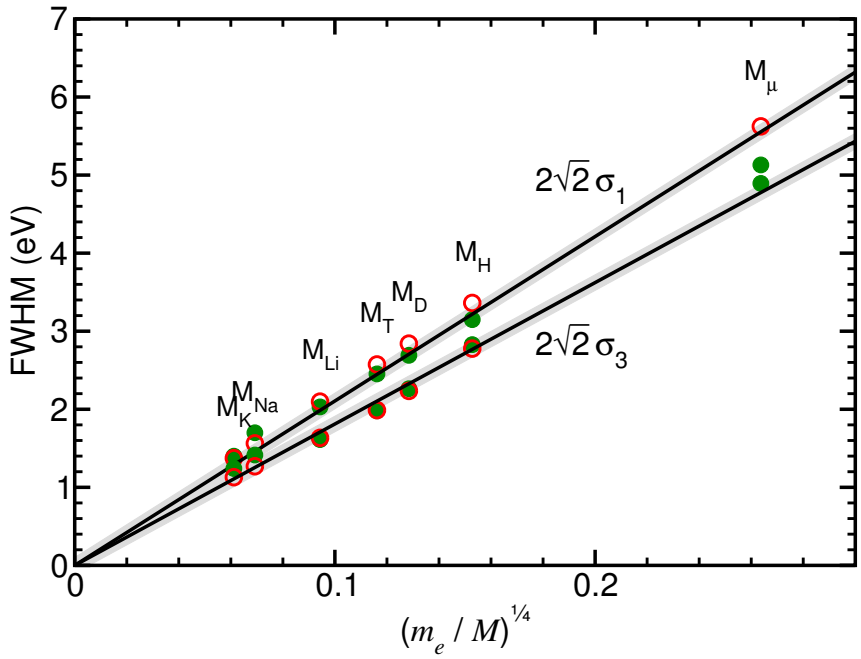

FIGURE 3.11. Full width at half maximum of the Gaussian fits (FWHM = $2\sqrt{2}\sigma_i$) to the first and third peaks of the absorption spectra for a positively charged homonuclear diatomic molecule with nuclear mass M of μ, H, D, T, Li, Na, or K versus the fourth root of the electron-nuclear mass ratio $(m_e/M)^{1/4}$ in the configuration $\Delta_{Ie} = 1$ and $\Delta_{II} = \frac{1}{2}$ (●) or $\Delta_{II} = 1$ (○). Black lines are linear fits to each peak for both configurations. Gray regions denote a ±0.1 eV estimated accuracy.

Altogether, this demonstrates the predictive power of our simple two-level model for describing the quantum nuclear spectral energies and widths as a function of the nuclear mass.

3.1.3. Conclusions. For the H_2^+ and H_2 molecules, the quantum electron-nuclear time dependent Schrödinger equation can be numerically solved due to the small number of electrons and nuclei they contain (these are three and four body systems). To simplify this numerical task, I have modelled these systems in 1D and in the centre of mass.

I have tested several initial configurations for both molecules, using several values for the Soft Coulomb parameters. These give rise to classical ground state potential energy surfaces (PES) with different behaviours for larger and small internuclear separations.

Having access to the quantum electron-nuclear solution has allowed me to test the validity of widely used classical nuclear approximations, both from a static and time dependent perspective. By varying the nuclear mass of the quantum electron-nuclear problem I have been able to check the validity of the classical approximations. For large nuclear masses the results obtained from a quantum electron-nuclear treatment should be consistent with the classical results.

I have found from the static calculation, that the quantum electron-nuclear ground state energies differ from those obtained from the classical approximations. From a perturbation theory argument in terms of $(\frac{m_e}{M_p})^{1/4}$, I have found that the classical approximations can only describe accurately the ground state energy up to the electronic and nuclear motion eigenvalues.

I have found from the time-dependent linear response spectra new features that are only present from a quantum electron-nuclear perspective. In particular, each classical allowed narrow peak splits into a wider bonding and antibonding contribution, lower and higher in energy, respectively. The amplitude and energy shift of these contributions strongly depends on the initial configuration. For initial configurations that give rise to PES that are strongly attractive for larger X, the antibonding blue shifted contribution dominates in the quantum electron-nuclear spectra. For initial configurations that give rise to PES that are strongly repulsive for small X, the bonding red shifted contribution dominates in the quantum electron-nuclear spectra. For initial configurations where the PES is not overall strongly repulsive and attractive, these quantum features will be weaker.

I have analysed both the position and width of these contributions as a function of the electron-nuclear mass ratio $\frac{m_e}{M_p}$ by means of a simple two level model. With this two-level model, the final coupling between the Born-Oppenheimer approximation (BOA) electronic energy levels via the quantum nuclear displacement $\delta \sim (\frac{m_e}{M_p})^{1/4}$, is analysed for different nuclear masses in terms of the mass ratio. Such a model accurately describes the energy and width dependence of every peak as a function of this mass ratio for both molecules and several configurations.

This work has shown that the magnitude of the final quantum electron-electron coupling, given by the mass ratio via the quantum nuclear displacements δ, can limit the domain of applicability of the classical approaches. For light atoms, the quantum nature of the nuclei may play an important role when describing absorption processes.

3.2. Photoionisation yields of neon and argon atoms[2]

In this section I study the photoionisation of neon and argon atoms subject to free electron sources by means of time-dependent density functional theory (TDDFT). With our TDDFT calculations based on the Kohn-Sham (KS) wavefunctions I have obtained both the total and individual contribution from each ionisation channel. This is done in the perturbative regime where a good agreement between experiment and a lowest-order perturbation theory (LOPT) perturbative theoretical method has already been obtained. It was thought that TDDFT was unable to describe non-perturbative phenomena such as the non-sequential double photoionisation knee found experimentally for helium. From a comparison between the total and individual yields obtained from LOPT and TDDFT we conclude that TDDFT can provide a very good description of the total and individual ionisation yields for neon and argon atoms exposed to strong laser pulses. As the performance of TDDFT depends on the asymptotic behaviour of the exchange-correlation functionals, I assess the reliability of different adiabatic density functionals and conclude that an accurate description of long-range interactions is crucial for obtaining the correct ionisation yield over a wide range of intensities.

3.2.1. Computational details and procedure. For the neon and argon atoms I discretise the three spatial Cartesian coordinates (x, y, z). Due to the spherical symmetry of these atoms, I use a spherical box. The spatial coordinates are equivalent in all three directions. These coordinates are discretised in the spherical box intervals $box_{int} \in [-b, b]$ with

$$b_j = -b + j\Delta b \text{ for } j= 0, 1, 2...N_b, \tag{3.19}$$

by using N_b equispaced points. The spacing between two adjacent points in the b direction is $\Delta b = \frac{2b}{N_b}$. The total simulation box size will be given by $2b$ from $-b$ to b.

Convergence is achieved when a decrease in Δb and an increase in b does not change the static and time propagation observables I analyse.

Within time-dependent density functional theory (TDDFT), I first solve the electronic ground state all-electron problem at the density functional theory (DFT) level from Eq. 2.76 using the functionals proposed in Sec. 2.4.2 for the atoms with charge $q = 0 \ldots (N_0 - 1)$. Note that we at least need one bound electron to perform this calculation. From this DFT problem the all electron eigenvalues and wavefunctions are obtained for each functional and each atom with charge $q = 0 \ldots (N_0 - 1)$. A ground

[2]This section is largely an adaptation of the work by A. Crawford-Uranga, U. De Giovannini, E. Räsänen, M. J. T. Oliveira, D. J. Mowbray, G. M. Nikolopoulos, E. T. Karamatskos, D. Markellos, P. Lambropoulos, S. Kurth and A. Rubio; *Time-dependent density-functional theory of strong-field ionization of atoms by soft x rays*; Phys. Rev. A **90**, 033412 (2014); DOI:10.1103/PhysRevA.90.033412. As such, the reported work includes collaboration with the rest of the authors of the article.

state parametrised pseudopotential is generated for each atom with charge $q = 0$ and each functional used according to the requirements shown at the end of Sec. 2.4.4. Once I have chosen the pseudopotential, I solve the DFT problem again using the $q = 0$ generated pseudopotentials for each functional and each atom with charge $q = 0 \ldots (N_0 - 1)$, to obtain the pseudo eigenvalues and wavefunctions.

In Table 3.4, I show the relative percentage errors introduced by the generated pseudopotential in the outermost valence energy levels of argon and neon, for increasingly ionised species and the different exchange-correlation functionals tested. The error is here evaluated relative to an all-electron calculation. Since our pseudopotentials have been generated from a neutral ground state configuration with $q = 0$, the errors increase linearly as a function of the charged state. Here the errors are larger for neon than for argon, because the neon pseudopotentials have been generated using a larger radial cutoff r_c (see Sec. 2.4.4).

LDA Rel. err. (%)	Ne^{+} / Ar^{+}	Ne^{2+} / Ar^{2+}	Ne^{3+} / Ar^{3+}	Ne^{4+} / Ar^{4+}	Ne^{5+} / Ar^{5+}	Ne^{6+} / Ar^{6+}	Ne^{7+} / Ar^{7+}
$2s$ / $3s$	-0.39 / 0.04	-0.41 / 0.10	-0.11 / 0.20	0.42 / 0.32	1.13 / 0.49	1.97 / 0.73	1.39 / 1.10
$2p$ / $3p$	0.18 / 0.06	0.99 / 0.14	2.20 / 0.25	3.68 / 0.41	5.31 / 0.61	7.05 / 0.91	7.18 / 1.35
$3d$ / $3d$	-0.07 / 0.08	0.33 / 0.21	1.93 / 0.37	4.12 / 0.59	6.47 / 0.89	8.82 / 1.33	10.10 / 2.02
PBE Rel. err. (%)							
$2s$ / $3s$	-0.42 / 0.03	-0.47 / 0.06	-0.18 / 0.12	0.35 / 0.18	1.05 / 0.27	1.91 / 0.40	1.21 / 0.72
$2p$ / $3p$	0.16 / 0.04	0.98 / 0.10	2.21 / 0.17	3.69 / 0.26	5.35 / 0.39	7.21 / 0.59	7.40 / 0.97
$3d$ / $3d$	-0.08 / 0.08	0.30 / 0.18	1.85 / 0.31	3.99 / 0.48	6.32 / 0.72	8.73 / 1.09	10.03 / 1.75
LB94 Rel. err. (%)							
$2s$ / $3s$	-0.19 / 0.10	-0.03 / 0.27	0.39 / 0.51	0.99 / 0.85	1.60 / 1.33	1.96 / 2.04	1.88 / 3.26
$2p$ / $3p$	0.34 / 0.12	1.22 / 0.30	2.48 / 0.58	3.99 / 0.96	5.61 / 1.49	7.16 / 2.28	8.11 / 3.63
$3d$ / $3d$	-0.10 / 0.08	0.47 / 0.35	1.79 / 0.74	3.58 / 1.28	5.56 / 2.04	7.58 / 3.11	8.87 / 4.93
CXD-LDA Rel. err. (%)							
$2s$ / $3s$	-0.21 / 0.07	-0.41 / 0.10	0.02 / 0.06	0.59 / 0.16	1.28 / 0.53	1.89 / 0.60	1.71 / 1.65
$2p$ / $3p$	0.35 / 0.09	0.84 / 0.14	2.15 / 0.09	3.61 / 0.22	5.19 / 0.65	6.67 / 0.75	7.33 / 1.91
$3d$ / $3d$	0.04 / 0.06	0.54 / 0.19	1.83 / 0.15	3.63 / 0.30	5.64 / 0.86	7.71 / 1.07	9.36 / 2.43

TABLE 3.4. Neon and argon pseudopotential vs all electron relative percentage errors for the outermost valence states for different exchange-correlation functionals.

Starting from this pseudo ground state calculation with $q = 0$, I then apply an external Gaussian strong laser pulse to our atoms, Eq. 2.111, and numerically propagate in real space in the interacting volume V the electronic time-dependent Kohn-Sham (TDKS), Eq. 2.109, using an enforced time-reversal symmetry based propagator, Eq. 2.51. Here I use a time-dependent adiabatic extension of the functionals in Sec. 2.4.2 with their associated pseudopotential generated for the ground state neutral configuration.

For the external Gaussian laser I use for neon a fixed photon energy of $\omega = 93$ eV and I consider the cases of a short 5 fs and a 30 fs full width at half maximum (FWHM) long laser pulse for several intensities from 10^{13} W/cm^2 to 5×10^{15} W/cm^2. In both cases I propagate the TDDFT equations for 25 fs and 153 fs, respectively. For argon, a

10 fs FWHM pulse of energy $\omega = 105$ eV, a full propagation time of 51 fs and several intensities from 10^{13} W/cm^2 to 5×10^{15} W/cm^2 have also been used.

To calculate the total yields from Eq. 2.127, $N(t)$ decreases with time due to the ionised electrons that are absorbed into the complex absorbing potential (CAP) region and $N_0 = 8$ are the total initial number of valence electrons that are not frozen in the pseudopotential for both atoms. Then I use an exponential fit near the end of the propagation times, given in the previous paragraph, to extrapolate $N(t)$. I follow this procedure for each atom and each intensity I have tested. To obtain the individual yields I calculate Eq. 2.127 for each q charged state at the end of the propagation times for each atom and each intensity without extrapolation.

I perform the Kohn-Sham (KS) and TDKS calculations in a R=16 Å radius spherical box and discretise the problem on a Cartesian grid with spacing ΔR=0.16 Å.

To solve the TDKS equation an R_{ab}=8 Å complex absorbing potential, Eq. 2.115, is introduced in our 16 Å radius total spherical box to account for electrons escaping from the interacting volume V during the time propagation. Within the CAP region the ionised electrons' reflections are damped via the propagation of Eq. 2.116. During the time propagation our 16 Å radius total spherical box has an interacting volume V of radius 8 Å and an absorbing CAP volume V_{CAP} of radius 8 Å. The interacting volume is big enough to hold the atom and its outgoing electrons that interact with the atom's electrons and nucleus. The absorbing CAP volume is a spherical shell that is big enough to trap the non-interacting outgoing electrons while avoiding reflections back to the interacting volume.

I find that for a 16 Å radius total spherical box and an 8 Å complex absorbing potential, using $\eta = 1$ is enough to guarantee good continuum properties for the outgoing electron's kinetic energy range that I consider in this work for neon and argon. To check this in Sec. 3.2.2 I have compared the experimental absorption spectra to the one obtained from TDDFT for different absorbing boxes, until reflections are negligible for this range.

I also find that the spacing of 0.16 Å I have used is small enough to describe accurately the steep Coulomb potential for the innermost valence state eigenvalues with charge +6 and +7. The errors in the eigenvalues for these innermost valence states for all the functionals are between 0.001 and 0.01 Ha.

3.2.2. Results. In this section I compare the time-dependent density functional theory (TDDFT) versus lowest-order perturbation theory (LOPT) photoionisation yields obtained for the neon and argon atoms. In particular, I compare the yields obtained from these two methods for the total as well as the individual photoionisation yields. The LOPT yields have been obtained by collaborators and compared separately to experimental results finding a good agreement. I have focused on the TDDFT results. In particular, I have mainly analysed the long range effect of the exchange-correlation (xc) potentials.

3.2.2.1. *Neon atom.* In Fig. 3.12 I compare TDDFT and LOPT total ionisation yields for neon as a function of the laser intensity.

The overall agreement is remarkably good for all the xc functionals in a wide range of intensities (plots are in log scale). However, as the intensity increases, the agreement gradually deteriorates with TDDFT tending towards lower ionisation yields. This behaviour is more pronounced in the 30 fs case in Fig. 3.12 (b), where the TDDFT ion yield flattens out for intensities $\gtrsim 10^{15}$ W/cm^2, while LOPT yields higher values.

As LOPT has shown itself to be in excellent agreement with experiment [**156**, **200**, **201**, **222**], we deduce that our TDDFT results have a tendency to slightly underestimate the total ionic yield. It must be added, however, that these differences are minor and are likely to fall within the present experimental accuracy of many FEL experiments. Therefore, we conclude that TDDFT has predictive power over a wide range of laser pulse intensities.

The high-lying unoccupied Kohn-Sham (KS) bound states, close to the ionisation threshold, are expected to be more accurately described by the LB94 and CXD-LDA functionals as explained in Sec. 2.4.2. This is reflected in a superior description of the ionisation process with LB94, as it provides the best agreement with LOPT. In this respect, the relatively poor accuracy of CXD-LDA compared to LB94 deserves further examination.

To discern the impact of the underlying ground state and the quality of the Hartree plus exchange-correlation (xc) functional, I compare in Fig. 3.13 the full solution of the time-dependent Kohn-Sham (TDKS) with one in which I keep V_{H} and V_{xc} frozen in the initial ground state configuration (the independent KS response).

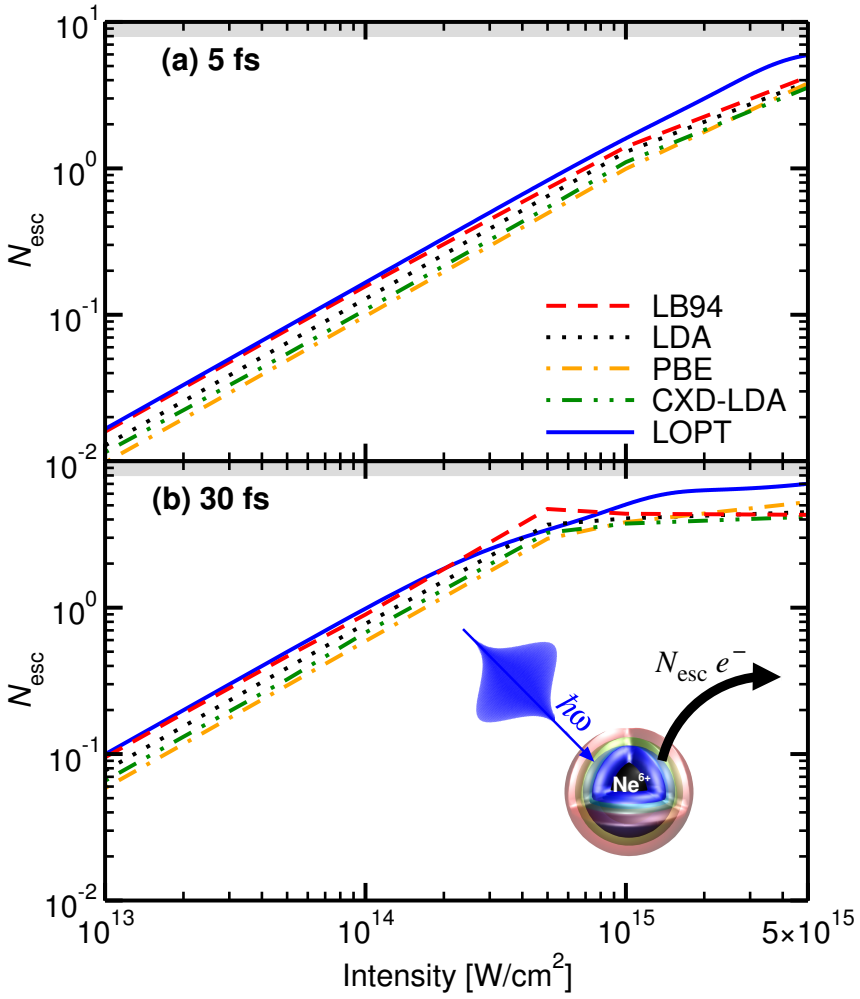

FIGURE 3.12. Neon total number of escaped electrons N_{esc} for different laser intensities and (a) 5 fs and (b) 30 fs full width at half maximum pulses of $\omega = 93$ eV. Different time-dependent density functional theory functionals are compared with lowest-order perturbation theory. The neon ionisation process is shown as an inset. Shaded regions indicate the electrons frozen in the pseudopotential.

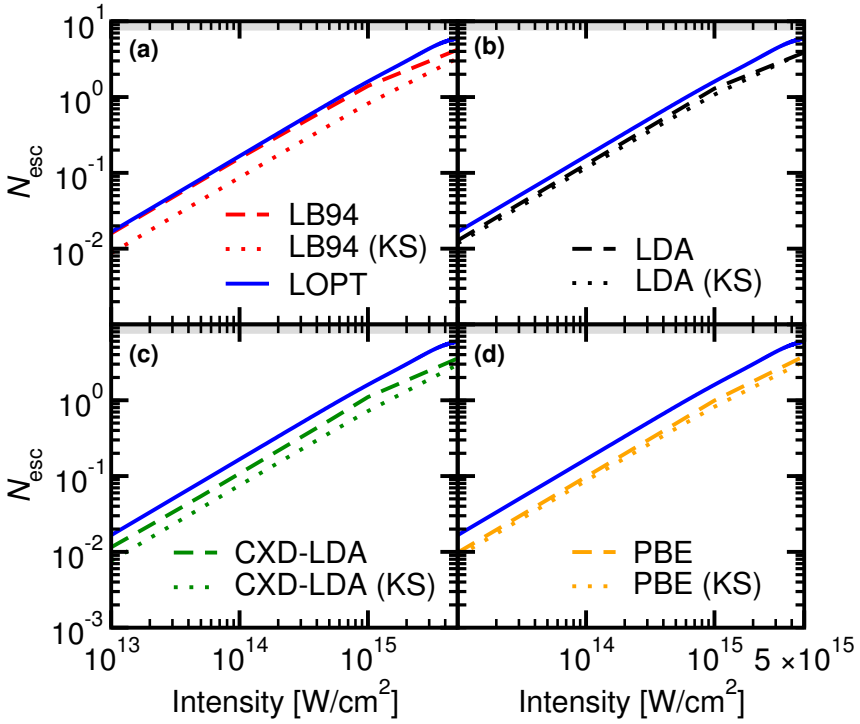

FIGURE 3.13. As in Fig. 3.12 for a 5 fs full width at half maximum pulse and different approximation levels: LB94 (a), LDA (b), CXD-LDA (c) and PBE (d). In each panel we compare lowest-order perturbation theory (solid), time-dependent density functional theory (dashed) and the independent Kohn-Sham response (dotted). Shaded regions indicate the electrons included in the pseudopotential.

Electrons are thus treated as non-interacting particles moving in a fixed external potential. The effects of such a crude approximation are almost indiscernible when the xc potential is short ranged, i.e., $V_{xc} \sim e^{-r}$, as for LDA and PBE (*cf.* Fig. 3.13 (b) and (d)). However, this is not the case when the xc potential is long-ranged, i.e., $V_{xc} \sim -1/r$, as for LB94 and CXD-LDA (*cf.* Fig. 3.13 (a) and (c)).

In an independent KS response picture, the total ionisation yields are directly related to the KS eigenvalues. For long-ranged xc potentials, the KS eigenvalues are more strongly bound, reducing total ionisation yields compared to short-ranged xc potentials. However, when the xc potential is propagated in time, the total ionisation yields only increase significantly for the long-ranged xc potentials (~100% increase for LB94 and ~33% for CXD-LDA at $I = 10^{14}$ W/cm^2). For long-ranged xc potentials, the ejected electrons in time may induce an attractive potential via redistribution of the electronic density on the

ion. Thus, the kinetic energy of the ejected electrons will be reduced due to this stabilisation of the electronic levels. To support this analysis I have employed linear response TDDFT [223] to calculate the cross sections shown in Fig. 3.14.

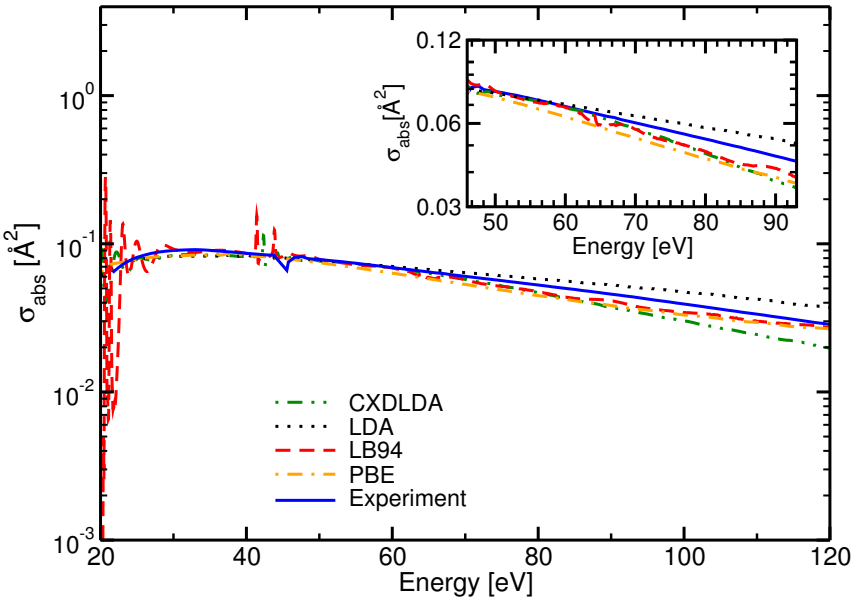

FIGURE 3.14. Neon absorption cross-section (logarithmic scale) above the first ionisation threshold. Result for different time-dependent density functional theory exchange-correlation functionals, LDA (black), PBE (orange), CXD-LDA (green), LB94 (red), compared with experimental data (blue) [224]. In the inset I focus on the range of energies relevant for ionisation from a ω = 93 eV laser pulse.

In Fig. 3.14 we see that the linear absorption cross section of electrons increases as the kinetic energies decrease below 93 eV [225]. The linear absorption cross section measures the probability of an absorption process as a function of the kinetic energy of the outgoing ionised electrons. For a larger absorption probability, the atoms absorb more energy from the incoming electromagnetic source and a larger number of electrons can be ionised from the atom. As the probability of the absorption process is larger for kinetic energies below 93 eV, we obtain a larger number of ionised electrons than for a kinetic energy of 93 eV. Therefore, we obtain a larger number of ionised electrons when the xc potential is propagated with time than when it is frozen. This effect becomes relevant mostly when the long-range electron-electron interaction is accurately described because the electronic levels are stabilised as explained in the previous paragraph.

Our complex absorbing potential (CAP) absorbs well as there are no spurious reflections and the cross-sections with different TDDFT xc functionals smoothly follow the experimental one [224] in the energy range associated to our pulses. The ionisation potential in TDDFT is given by the KS eigenvalue of each bound electron. A rough estimate of the TDDFT quality attained in the description of ionisation processes initiated by a laser of a given frequency ω, is therefore given by the behaviour of absorption spectra in an energy range identified by the lower- and higher-energy KS ionisation potentials of the non-frozen valence electrons as shown in the inset of Fig. 3.14.

In Fig. 3.15 I show neon individual TDDFT (thicker) and the independent KS response (thinner) ionisation yields obtained with LB94 and LDA using Eq. 2.127. We observe that TDDFT ionic yields up to Ne^{4+} are in good agreement with LOPT for a large range of laser intensities; $I \lesssim 10^{15}$ W/cm^2 for a 5 fs pulse, [Fig. 3.15 (a)], and $I \lesssim 5 \times 10^{14}$ W/cm^2 for a 30 fs one [Fig. 3.15 (b)]. For more strongly ionised species, Ne^{5+} through Ne^{8+}, the discrepancy is larger, especially for the 30 fs pulse. From Fig. 3.15 (a) we see that the individual ionisation yields for all channels are ordered as LB94(KS) < LDA(KS) ~ LDA < LB94, as was also the case for the total ionisation yields shown in Fig. 3.13 (a) and (b).

The total and partial ionisation yields are in good agreement with LOPT, as long as the channels with an associated charge $\geq Ne^{5+}$ play a negligible role in the ionisation process (*cf.* Figs. 3.12 and 3.15). Experimental ionisation channels up to Ne^{6+} present excellent agreement with LOPT [200, 156, 222, 201]. We can therefore conclude that TDDFT describes well the ionic yields up to Ne^{4+}, with the current state-of-the-art experimental data.

The trend observed in the TDDFT total yields for the different xc functionals, [Fig. 3.12], is reflected in the single ionisation channels for both pulse lengths: namely, the inclusion of a correct asymptotic decay systematically improves the description of each channel.

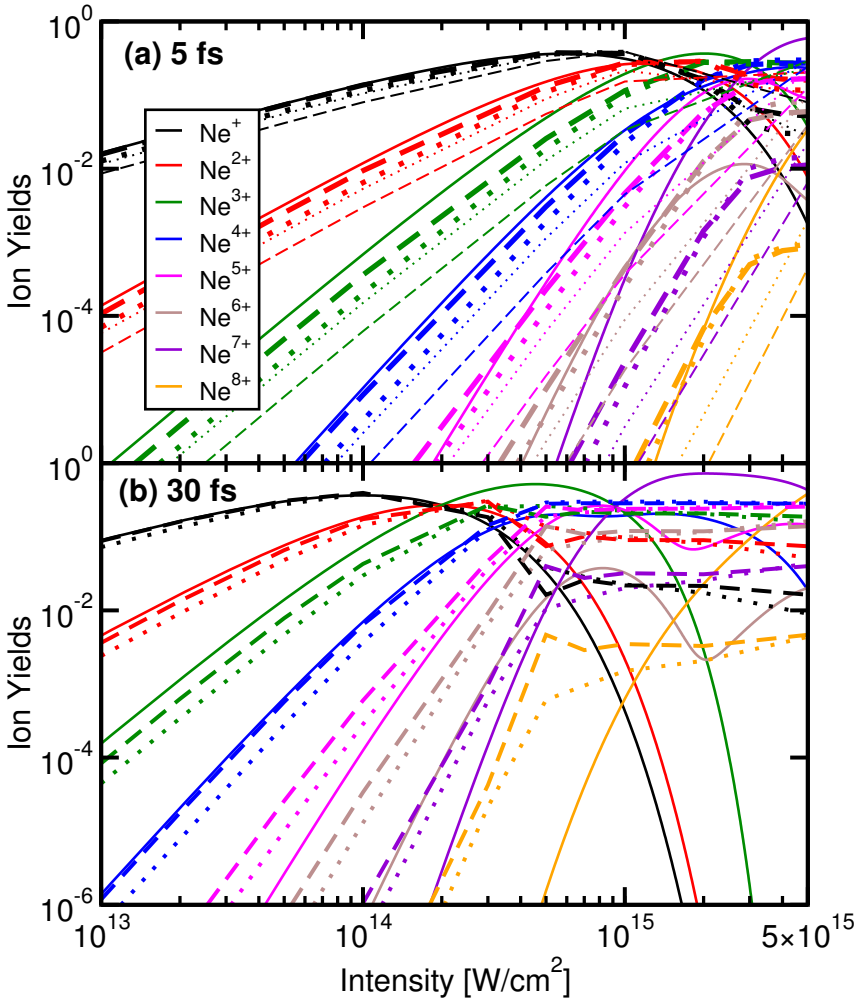

FIGURE 3.15. Neon individual ionisation yields as a function of the intensity for (a) 5 fs and (b) 30 fs full width at half maximum laser pulses of $\omega = 93$ eV. Time-dependent density functional theory (thicker) and the independent Kohn-Sham response (thinner) with LB94 (dashed) and LDA (dotted) functionals are compared to lowest-order perturbation theory (solid).

3.2.2.2. *Argon atom.* In Fig. 3.16 I present the results for total and individual ionisation yields of argon. The total ionisation yields for all the considered functionals except LB94, [Fig. 3.16 (a)], qualitatively follow LOPT but systematically predict lower values. LB94 remarkably reproduces LOPT up to $I \lesssim 5 \times 10^{14}$ W/cm^2. For higher intensities,

it departs towards lower ionisation values similarly to what was observed for neon in Fig. 3.12.

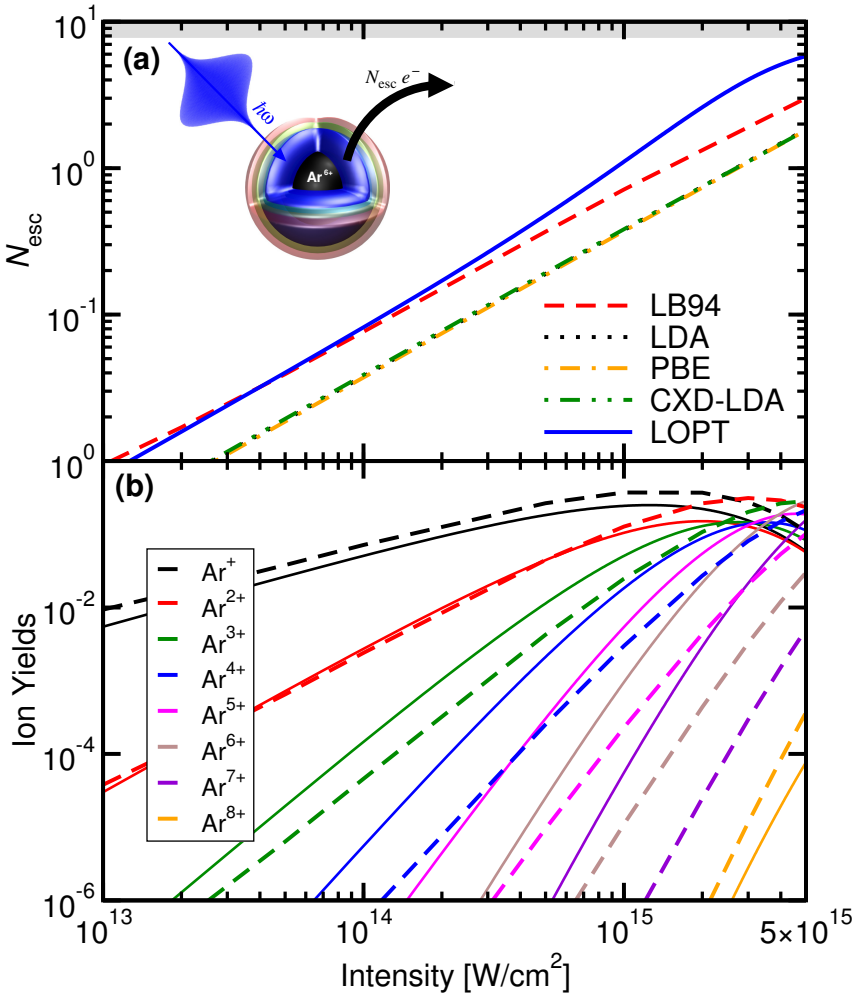

FIGURE 3.16. Argon total and individual ionic yields as a function of the laser intensity for a 10 fs full width at half maximum laser pulse of $\omega = 105$ eV. (a) Total ionisation yield for different time-dependent density functional theory exchange-correlation functionals and lowest-order perturbation theory. (b) Individual ionisation channels for LB94 (dashed) and lowest-order perturbation theory (solid). The argon ionisation process is shown as an inset. Shaded regions indicate electrons frozen in the pseudopotential.

The intensity dependence of single ionisation channels, as shown in Fig. 3.16 (b), is in good agreement up to Ar^{3+} for LB94 only. It then deteriorates for higher ionised species.

The cross sections for argon shown in Fig. 3.17, also demonstrate that our complex absorbing potential (CAP) absorbs well and that ionisation yields increase for decreasing outgoing kinetic energies.

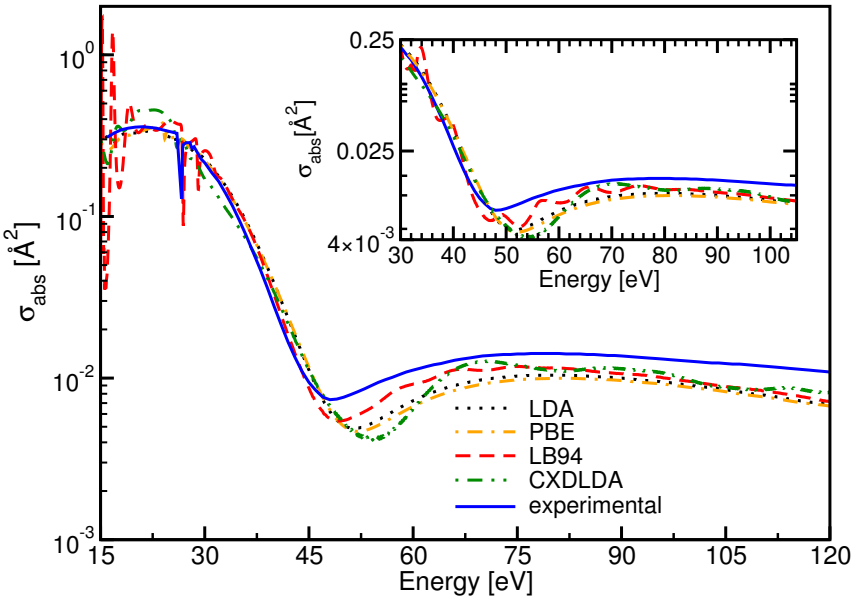

FIGURE 3.17. Argon absorption cross-section (logarithmic scale) above the first ionisation threshold. Result for different time-dependent density functional theory exchange-correlation functionals, LDA (black), PBE (orange), CXD-LDA (green), LB94 (red), compared with experimental data (blue) [224]. In the inset we focus on the range of energies relevant for ionisation from a ω = 105 eV laser pulse.

In general, I have shown that the agreement between LOPT and TDDFT is remarkably good for all the exchange-correlation (xc) functionals for both argon and neon and channels with an associated charge below 5+. However, the agreement is not as good for channels with an associated charge above 6+. TDDFT tends to underestimate the LOPT results for the Ne^{7+} (see Fig. 3.15 a)) and Ar^{7+} (see Fig. 3.16 b)) charged channels, whereas it overestimates LOPT for the Ne^{8+} (see Fig. 3.15 b)) and Ar^{8+} (see Fig. 3.16 b)) charged channels.

There are several sources of error within TDDFT which could lead to these effects. First, the pseudopotential transferability errors increase with the charge of the ionised contribution as they have been generated from the neutral configuration as shown in

Sec. 3.2.1. Second, it has been found that for argon there is an important experimental effect [202] which I do not include within TDDFT. From the analysis of photoelectron energy spectra for argon, an ionised plus excited contribution of the sixth species has been detected and quantified. The seventh species is sequentially produced from these two contributions of the sixth species. As shown experimentally, the sixth ionised contribution produced is much larger than the sixth excited contribution. Therefore it is reasonable to think that the seventh species will be mainly produced from the sixth ionised contribution. However, it has been found experimentally that the excited contribution strongly contributes to the production of the seventh species. Therefore the sixth excited contribution must be included to calculate the ionisation yields for the seventh species. Otherwise, within TDDFT the ionisation yields will be clearly underestimated with respect to the experimental results. Third, for Ne^{8+} and Ar^{8+}, the spurious correlation effects between the core electrons frozen in the pseudopotential and the escaped electrons in the absorbing boundary are included. Fourth, the observed deviation for highly ionised species may trace back to an improper spatial- and time-dependence of the adiabatic functionals. When we apply a periodic field to our atoms, a charge-transfer excitation takes place where the population of the initial and final state will oscillate with time. The non-local spatial dependence on the density can be partly treated with GGA functionals such as LB94 and CXD-LDA, as these take into account both the density and the gradient of the density at the coordinate where the functional is evaluated (see Sec. 2.3.1.1). This non-local dependence can only be partly treated with GGAs, because only the short range non-locality in the gradients of the density is included. The non-local time dependence on the density cannot be described with any of the adiabatic functionals used, as these neglect memory effects. As shown in Eq. 2.110, within the adiabatic approximation, we input the instantaneous density into a ground state xc functional at time t, neglecting the effect of the density at all previous times $t' < t$. The effect of using an adiabatic versus exact functional has been shown in 1D for He, a two electron system [226, 227, 228]. The correlation potential obtained for charge-transfer excitations over one Rabi cycle using an exact versus adiabatic functional has been compared. A time-dependent oscillating step structure in the correlation potential can only be described accurately using an exact functional. To describe the long-range charge-transfer from one state to another, or from different regions of space, a non-local spatial functional is necessary. To describe the time-dependence of the oscillating step due to the generation of a net acceleration across the atom, a non-local time-dependent functional is necessary.

These possible TDDFT sources of error have to be tested to check if the ionisation yields improve for these highly ionised species. This can be achieved for example by using harder, more transferable pseudopotentials as well as testing new functionals that can describe spatial and temporal non-localities and self interaction effects better. However, as we are mostly interested in the intensity regime where LOPT is expected to be valid, these issues are not so relevant for this study. Since the two approaches are built

on completely different bases, the resulting agreement for lower intensities indicates that both are able to provide a realistic picture of the underlying physics.

3.2.3. Conclusions. For the neon and argon atoms, I have studied their strong field ionisation (up to the X-ray regime) by means of a perturbative (lowest-order perturbation theory, LOPT) and a non-perturbative (time-dependent density functional theory, TDDFT) theoretical method. Studying the strong field ionisation of these atoms has become recently possible experimentally due to the advances and development of free electron lasers (FEL). Under strong fields, multiple ionisation processes where more than one electron is ejected simultaneously, become important to understand the ionisation of these atoms. These multiple ionisation processes are enhanced for high intensity and short duration laser pulses.

LOPT has shown to be an accurate theoretical method by comparison to experimental results for these two atoms. To obtain the ionisation results within LOPT a series of rate equations for each atom are formulated according to the experimental conditions used. LOPT is a perturbative method, which cannot handle non-perturbative effects such as electron correlation, and it is applicable only under certain intensities and pulse durations.

TDDFT can deal with all the limitations of LOPT, but was thought to fail to describe strong field ionisation when tested for helium. However, I have found that by comparing the TDDFT results to the LOPT ones (which have been previously compared to experimental results as mentioned above) for neon and argon atoms subject to strong fields, I obtain accurate ionisation yields, as long as the charge of the ion is not too high. Since the two theoretical approaches are built on completely different bases, the resulting agreement for lower intensities indicates that both are able to provide a realistic picture of the underlying physics.

Within TDDFT I obtain the best results when I use an LB94 functional, which describes better the levels close to the ionisation threshold due to its long range behaviour. To understand the effect of the long range behaviour, I have analysed the cross sections in the energy range identified by the deeper and higher KS ionisation potentials. There I show that the amount of ionisation increases when the kinetic energy of the ejected electrons decreases. For long-ranged potentials, the kinetic energy of the ejected electrons will be more reduced than for short-ranged potentials, due to a stronger stabilisation of the electronic levels induced by a stronger attractive potential via redistribution of the electronic density on the ion.

To simplify our TDDFT calculations I have used a pseudopotential (adapted to each long and short ranged exchange-correlation potential I have tested) to freeze the inner core electrons, as these are not strongly ionised under the laser conditions I employ. As we are numerically limited to a simulation box of a certain size and the ejected continuum electrons will be delocalised in space, I add a complex absorbing boundary region at the

edges of the box. This absorbing boundary region absorbs the ionised ejected electrons to avoid unphysical reflections.

I have shown that both the total as well as individual ionised contribution of the electrons that are not frozen in the pseudopotential can be accurately described by means of both LOPT and TDDFT. For highly charged species both the TDDFT and LOPT results are not as good. Several possible TDDFT sources of error have to be tested to check if the ionisation yields improve for these highly ionised species. One could test harder more transferable pseudopotentials as well as new functionals that can describe spatial and temporal non-localities and self interaction effects better.

3.3. Nuclear effects on the Time Resolved Photoemission Spectra of ethylene[3]

In this section I have studied the ionisation of an ethylene molecule subject to a pump probe setup with time-dependent density functional theory (TDDFT). The π_z-bond in the ethylene molecule is responsible for its useful reactivity. Due to this reactivity, ethylene is used to produce many products which are widely used. To investigate this reactivity I follow the dynamic evolution of the molecular orbitals of ethylene due to the π_z to π_z^* excitation triggered by the pump pulse which is then monitored by the time-dependent reaction of ethylene to a delayed strong extreme ultraviolet (XUV) probe laser. To visualise this evolution I have looked at the time-resolved photoemission spectra and photoangular distribution because they can be used to directly probe electron and nuclear dynamics in molecules. This analysis has been performed including the nuclear motion via the Ehrenfest dynamics (ED) approach and not including it via the Born-Oppenheimer approximation (BOA) approach to investigate the effects of nuclear motion. Due to ethylene's double bond between the two carbon atoms the molecule is relatively rigid and distortions as well as elongations of this bond require a lot of energy. However, the nuclear changes induced under strong non-perturbative sources can be large for its single C-H bonds due to their small mass and small force constant. I have found that nuclear motion can only be clearly observed if I artificially fix the occupation of the pumped π_z^* state and not use a pump. Otherwise, the pump causes the depopulation of the π_z^* state and the occupation of this state must be sufficient for changes in the nuclear positions to be resolved by the probe.

3.3.1. Computational details and procedure. For the ethylene molecule I also discretise the three spatial Cartesian coordinates (x, y, x), as I have done for the neon and

[3]This section is largely an adaptation of the work by A. Crawford-Uranga, U. De Giovannini, D. J. Mowbray, S. Kurth and A. Rubio; *Modelling the effect of nuclear motion on the attosecond time-resolved photoelectron spectra of ethylene*; J. Phys. B: At. Mol. Opt. Phys. **47**, 124018 (2014); DOI:10.1088/0953-4075/47/12/124018. As such, the reported work includes collaboration with the rest of the authors of the article.

argon atoms. The ethylene molecule is not spherically symmetric, but I use a spherically symmetric box to discretise its three spatial Cartesian coordinates. To discretise these coordinates, I use a spherical box of a finite set of values b in the box intervals $box_{int} \in [-b, b]$ which are discretised as:

$$b_j = -b + j\Delta b \text{ for } j = 0, 1, 2...N_b, \tag{3.20}$$

by using N_b equispaced points. The spacing between two adjacent points in the b direction is $\Delta b = \frac{2b}{N_b}$. The total simulation box size will be given by $2b$ from $-b$ to b.

Convergence is achieved when a decrease in Δb and an increase in b does not change the static and time propagation observables I analyse.

As I use a spherical box, the spatial coordinates are equivalent in all three directions.

The ground state density is first obtained by solving the Kohn-Sham (KS) equations self-consistently at the density functional theory (DFT) level using Eq. 2.76. To approximate the exchange-correlation (xc) term I use a local density approximation (LDA) functional coupled to an average density self interaction correction, Eq. 2.113. To freeze the Carbon 1s core electrons I use an LDA pseudopotential that is already included with the `Octopus` [213, 214, 215] code. I employ a spherical box of radius $R = 30\ a_0$ with a grid spacing of $\Delta R = 0.3\ a_0$. I first find for the ADSIC functional the minimum geometry by force minimisation using Eq. 2.114, to make sure that the molecule is initially in its ground state. The ground state geometry is given in Sec. 3.3.2.1.

Once I have found the relaxed molecular structure, I apply to our ground state a pump pulse followed by a probe pulse for different time delays, Eq. 2.112. The photoionisation process I consider is depicted schematically in Fig. 3.18, where the laser parameters have been adapted from Ref. [205]. First, a pump pulse is used to resonantly excite from the bound π_z to the π_z^* state. I employ an ultraviolet (UV) pump laser of energy $\omega_{Pu} = 0.326$ Ha, with a 15 cycle trapezoidal shape (3 cycle ramp), and an intensity $I = 1.67 \times 10^{11}$ W/cm^2 polarised along the x-axis. The frequency of the pump is tuned to excite this excitation of interest. The dynamic evolution of the electronic levels of ethylene due to the π_z to π_z^* excitation triggered by the pump pulse is then monitored by the time-dependent reaction of ethylene to a delayed strong probe laser. The probe is an extreme ultraviolet (XUV) laser of energy $\omega_{pr} = 1.8$ Ha, with a 40 cycle trapezoidal shape (8 cycle ramp), and an intensity of $I = 1.02 \times 10^{11}$ W/cm^2 polarised along the z-axis. This delayed strong probe pulse is used to eject the electrons of ethylene to a laser driven unbound continuum state. The time delay between the pump and the probe is measured from the onset of the pump to the centre of the probe so that negative delays correspond to cases where the probe precedes the pump, as shown in Fig. 3.19.

Alternatively, I also follow the procedure described in the previous paragraph by starting from an artificially π_z^* pumped state by fixing its occupation. In this case, as the initial state of our time-dependent density functional theory (TDDFT) time propagation, I use a KS Slater determinant which differs from the KS ground state in that the highest occupied

molecular orbital (HOMO) (π_z) is empty while the lowest unoccupied molecular orbital (LUMO) (π_z^*) is fully occupied. This corresponds to the situation where the pumped contribution from the HOMO to LUMO has been efficiently maximised. Therefore, for this case I omit the pump and use the same probe. Here, the time delay is measured as the difference from the centre of the probe to the starting point of the time evolution, as shown in Fig. 3.19.

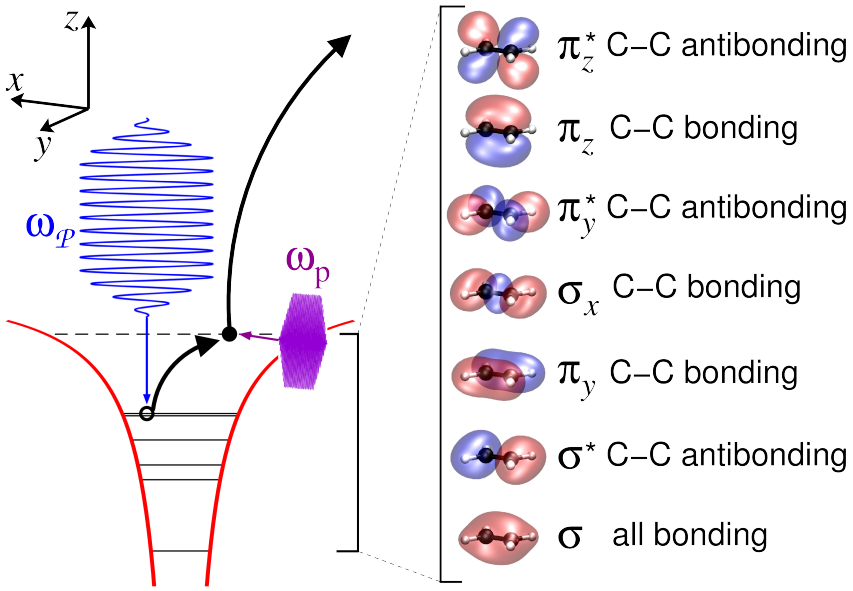

FIGURE 3.18. Schematic of the pump-probe setup employed to study the time-resolved photoemission spectra of ethylene. The pump (blue) is an ultraviolet laser pulse of energy $\omega_{Pu} = 0.326$ Ha, with a 15 cycle trapezoidal shape (3 cycle ramp), and an intensity $I = 1.67 \times 10^{11}$ W/cm^2. polarised along the C–C bond, i.e., x axis. The excited electron is probed using an extreme ultraviolet probe laser (violet) of energy $\omega_{pr} = 1.8$ Ha, with a 40 cycle trapezoidal shape (8 cycle ramp), and an intensity of $I = 1.02 \times 10^{11}$ W/cm^2 polarised along the z axis. The calculated Hartree potential (red) for the x coordinate along the yz plane, Kohn-Sham eigenvalues (black horizontal lines), structural schematics (C in black, H in white), and Kohn-Sham orbitals (isosurfaces of $\pm 0.05 e/a_0^{3/2}$) for ethylene are shown according to their energy. The π_z state is the highest occupied molecular orbital and the π_z^* state is the lowest unoccupied molecular orbital.

I model the time-resolved photoemission spectra (TRPES) and photoangular distributions (PAD) to obtain the kinetic energies and angular distributions of the outgoing electrons by solving the time evolution of ethylene according to the following. I partition the whole space as described in Sec. 2.4.7. In region A I solve in real space the discretised

coupled time-dependent Kohn-Sham (TDKS) equation (Eq. 2.109) either for fixed nuclei or for nuclei following the classical equations of motion (Eq. 2.123), in the presence of a mask boundary absorber function $M(\mathbf{r})$ of a given width $\mathbf{R}_{ab}$ (see Eq. 2.140). I introduce a 15 a_0 wide Mask Method boundary absorber to collect the photoelectrons and prevent electronic reflections inside the total 30 a_0 box. To propagate the TDKS Eq. 2.109 I use an enforced time-reversal symmetry operator (Eq. 2.51) and a time step of $\Delta t = 1.2$ as.

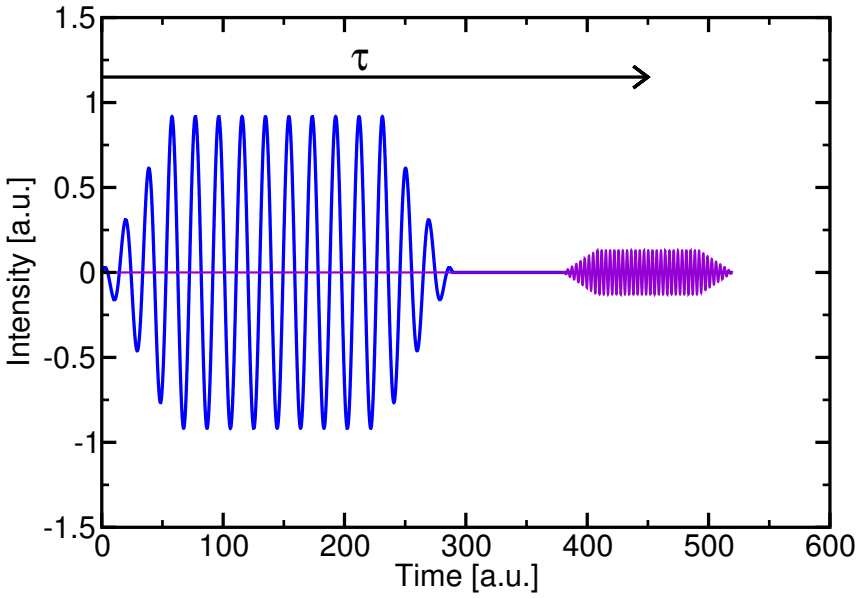

FIGURE 3.19. Schematic of the time delay between the pump in blue and the probe in violet. When the pump is not present, the time delay is measured from the starting point of the time evolution.

To propagate the Ehrenfest Eq. 2.123 I use a velocity Verlet algorithm (Eq. 2.124) with a random initial velocity (Eq. 2.125) introduced by an initial temperature of 300 K≈25°C to follow experimental ambient conditions. Otherwise the nuclei are left fixed. Absorbed electrons in A are collected via $M(\mathbf{r})$ and propagated in momentum space as free Volkov states within the ionisation region B. From the photoelectrons in region B the momentum-resolved photoelectron probability $\mathcal{P}(\mathbf{p})$ in Eq. 2.139 is obtained by Fourier transformation within the localised small absorbing boundary region of 15 a_0. From $\mathcal{P}(\mathbf{p})$ we can then extract and visualise the photoemission spectra $P(E)$ and photoangular distribution $P(E,\theta)$ given in Eqs. 2.130 and 2.131, respectively. These are calculated as a function of the delay time between the pump and probe and are measured only when the probe pulse is applied.

3.3.2. Results. In this section I compare the frozen Born-Oppenheimer approximation (BOA) versus moving Ehrenfest dynamics (ED) nuclei time-resolved photoemission spectra (TRPES) and photoangular distribution (PAD) I obtain for an ethylene molecule from two different approaches. In the first approach I apply a pump to excite from the $\pi_z \rightarrow \pi_z^*$, followed by a time delayed probe. In the second approach, I initially start from a pumped state by fixing the occupation of the π_z^*, followed by the application of a time delayed probe.

3.3.2.1. *Pump plus probe.* In Fig. 3.20 I show the geometry of the ethylene molecule. On the right hand side of Fig. 3.20, I show the first seven molecular orbitals for ethylene ordered according to their energy. These describe the regions of space in which there is a high probability of finding the molecules' electrons. These molecular orbitals are constructed by combining bonding and antibonding combinations of atomic orbitals, lower and higher in energy.

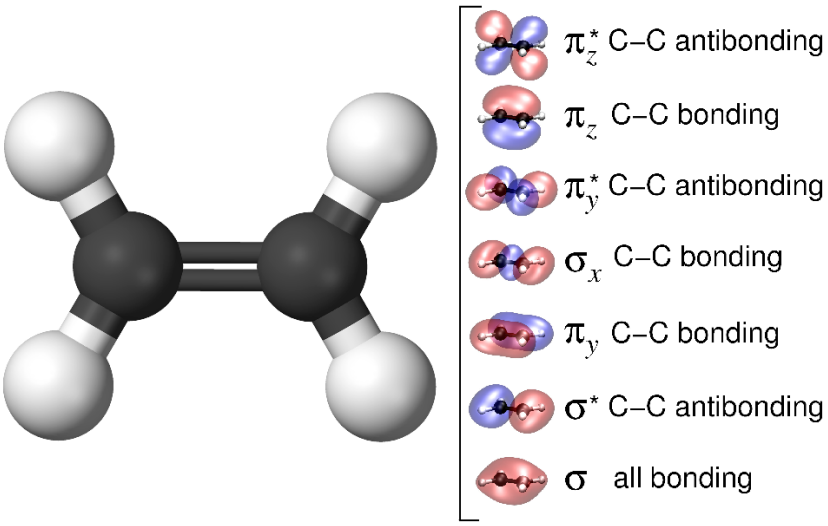

FIGURE 3.20. Schematic representation of the ethylene molecule's coplanar geometry and its first seven molecular orbitals ordered according to their energy. The two carbon atoms are shown black and the four hydrogen atoms white. The blue atomic orbital lobes are negative phases and the red atomic orbitals are positive phases. These are separated by nodal surfaces at which the electron density is zero.

The TRPES for ethylene with the nuclei frozen at their equilibrium positions is shown in Fig. 3.21 (a). The spectra presents similar features to those described in Ref. [205].

Brighter areas correspond to more ionisation with larger kinetic energies and darker areas to less.

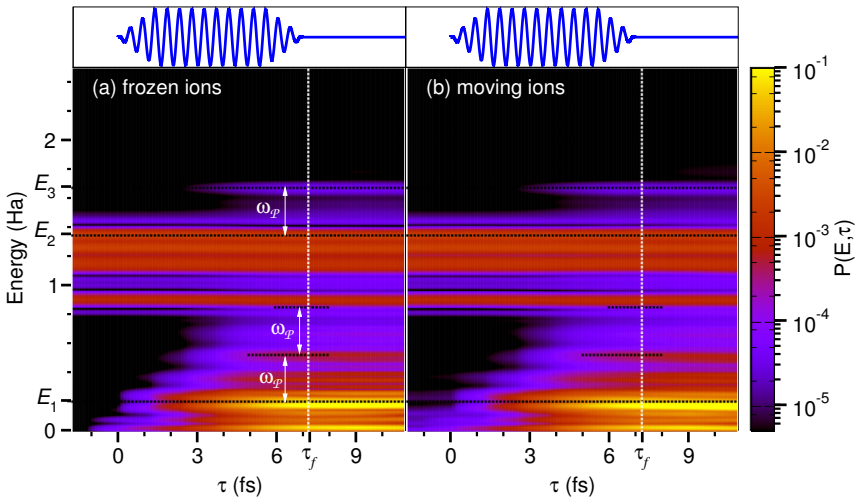

FIGURE 3.21. Time-resolved photoemission spectra $P(E,\tau)$ of ethylene as a function of the photoelectron's kinetic energy in Ha and the pump-probe time delay τ in fs with frozen (a), or moving (b) nuclei. Nuclear motion is modelled with an initial temperature of 300 K. Pump (blue) and probe (violet) pulses are polarised with laser parameters as described in Fig. 3.18. The pump is depicted in the upper panels of (a) and (b) as a function of τ. Here $E_1 = 2\omega_{Pu} - I_p$, $E_2 = \omega_{\rm pr} - I_p$, $E_3 = \omega_{Pu} + \omega_{\rm pr} - I_P$. The energies $E_1, E_1 + \omega_{Pu}, E_1 + 2\omega_{Pu}, E_2, E_3$ (black) and the time delay τ_f (white) are shown to guide the eye. White arrows correspond to the pump's energy ω_{Pu}.

The first ionisation potential obtained from LDA+ADSIC is $I_p = 0.447$ Ha, compared to the experimental value of 0.386 Ha [229]. Here, I_p has been evaluated within density functional theory (DFT) using the vacuum energy minus that of the highest occupied Kohn-Sham (KS) molecular orbital (HOMO), i.e., $I_p \approx E_{vac} - \varepsilon_{\rm HOMO}$. The carbon-carbon (C–C) bond-length obtained from LDA+ADSIC is 2.337 a_0, in fair agreement with the experimental one of 2.531 a_0 [230]. The (C–C) bond-length has been obtained by molecular force minimisation ($\leq 2.4\times10^{-5}\ \frac{\rm Ha}{a_0}$), with the two carbon atoms placed on the x-axis at $x = \pm 1.169\ a_0$ and hydrogens in the xy-plane at $(x,y) = (\pm 2.120, \pm 1.785)\ a_0$.

The peak at $E_1 = 2\omega_{Pu} - I_p = 0.205$ Ha constitutes the main ionisation channel and it is due to the pump alone. Here, the absorption of a pump photon leading to a $\pi_z \rightarrow \pi_z^*$ transition, is followed by a second pump photon which directly excites electrons from the π_z^* state into the continuum. Multiphoton replicas of this peak can be observed at energies separated by the two following integer multiples of ω_{Pu}.

The peak at $E_2 = \omega_{pr} - I_p = 1.353$ Ha corresponds to the direct emission from the highest occupied KS molecular π_z orbital into the continuum.

A similar mechanism, but with electrons ejected from deeper levels, is responsible for the peaks lying at energies lower than E_2. These peaks depend on molecular ground state properties and the probe laser only. For this reason they can be observed also for negative delays $\tau < 0$.

The population of the π_z^* state increases with the delay for $\tau > 0$. At about the same τ for which E_1 becomes visible, the peak at $E_3 = \omega_{Pu} + \omega_{pr} - I_P = 1.679$ Ha begins to emerge. This peak corresponds to electrons ejected into the continuum from the π_z^* state, which is transiently occupied via the pump pulse. This ionisation channel is the one we are interested in but for which I get the least ionisation. Here one integer multiple of ω_{Pu} is the difference between E_2 and E_3.

To further analyse the results, in Fig. 3.22 I plot a cut of the TRPES at $\tau_f = 7.26$ fs, after the pump has been switched off.

In the figure I introduce new peak labels in addition to E_1, E_2, E_3, which have been previously discussed. These labels identify the contribution to each peak from the ground state KS orbitals of ethylene shown in Fig. 3.18. We can identify the peak to the corresponding orbital from the KS eigenvalues, the symmetry of the orbitals and the PADs.

Supplementary information regarding the nature of PES peaks can be obtained from the PADs. $\mathcal{P}(\mathbf{p})$ can be evaluated by Fermi's golden rule as

$$\mathcal{P}(\mathbf{p}) \propto \sum_f |\langle \varphi_f | \mathbf{A}_0 \cdot \mathbf{p} | \varphi_i \rangle|^2 \delta(E_f - E_i - \omega), \tag{3.21}$$

where φ_i, φ_f, E_i and E_f are the electronic initial and final orbitals and energies, $\mathbf{A}_0$ the laser polarisation axis where $\mathbf{A}(t) = \int_0^t d\tau \mathbf{E}(\tau)$ is the vector potential in the velocity gauge, ω the frequency of the pump and $\mathbf{p}$ the momentum of the ejected electrons. In a momentum space approach, we can express $\mathcal{P}(\mathbf{p})$ for electrons ejected from orbitals with π-symmetry as

$$\mathcal{P}(\mathbf{p})^2 \propto |\mathbf{A}_0 \cdot \mathbf{p}|^2 |\tilde{\varphi}_i(\mathbf{p})|^2, \tag{3.22}$$

where $\tilde{\varphi}_i(\mathbf{p})$ is the Fourier transform of the initial orbital in momentum space [231]. The dot product between $\mathbf{A}_0 \cdot \mathbf{p}$ is a geometrical polarisation factor, so that ejected photoelectrons will have total momentum $\mathbf{p}$ along $\mathbf{A}_0$ and no momentum along perpendicular directions of $\mathbf{A}_0$. PADs for angles close to the laser polarisation direction, where the polarisation factor $|\mathbf{A} \cdot \mathbf{p}|$ is close to unity, reflect the nodal symmetry of the orbital from which the electron has been ejected.

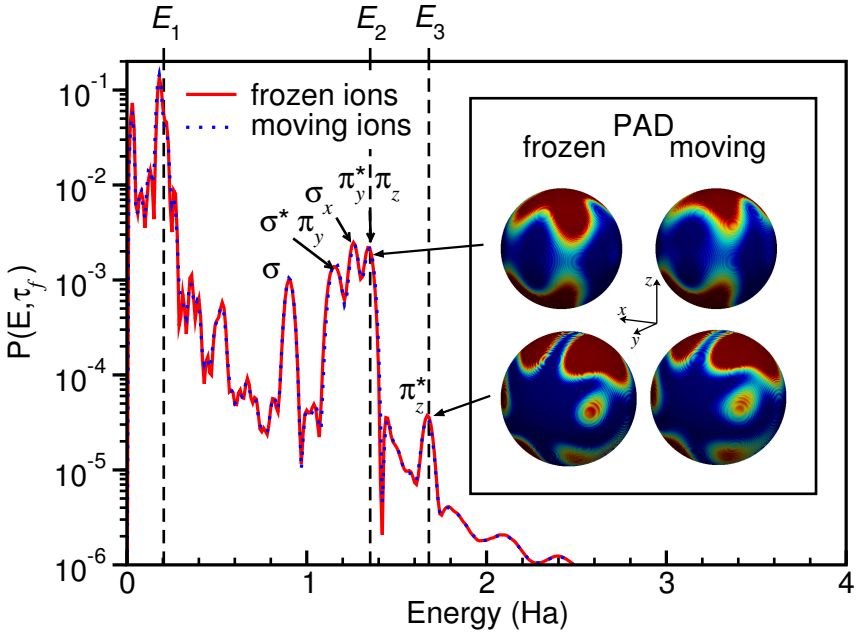

FIGURE 3.22. Photoemission spectra of ethylene versus the photoelectron's kinetic energy in Ha for a probe applied at the end of the pump (τ_f = 7.26 fs as shown in Fig. 3.21) $P(E,\tau_f)$. The nuclei are either frozen (red), or their motion is classically modelled at an initial temperature of 300 K (blue). Peaks at E_1, E_2 and E_3 correspond to the energy transitions described in Fig. 3.21, while those labelled σ, σ^*, π_y, σ_x and π_y^* correspond to direct excitations by the probe from the respective orbitals depicted in Fig. 3.18. Photoangular distributions for ethylene at the energies E_2 and E_3 when the pump has ended τ_f for frozen and moving nuclei are shown in the inset.

As it is reasonable that most photoelectrons are emitted along the laser polarisation direction, the pump is polarised along x because of the symmetry of the π_z orbital, so that no photoelectrons are ejected due to the pump. Due to the symmetry of the π_z^* orbital, photoelectron ejection will be enhanced along z, so that the probe we apply is polarised along z.

The inset of Fig. 3.22 shows how the frozen and moving nuclei's PADs correlate with the originating orbital symmetry. Photoelectrons emerging with kinetic energy E_2 are ejected from almost degenerate π_y^* and π_z orbitals. The PADs associated with E_2 coherently display a symmetry compatible with the superposition of these orbitals. On the other hand, the PADs for E_3 present a nodal structure clearly linked to a π_z^* orbital symmetry.

As shown in Fig. 3.21(b), the effect of nuclear motion on the electronic TRPES is negligible. Further, the PAD is minimally changed by the effect of moving the nuclei as shown in the inset of Fig. 3.22. These negligible effects are due mainly to the fact that the π_z^* orbital is depopulated through the direct ionisation channel observed at E_1 via a second pump. This process is very strong and the π_z^* is depleted by the pump so that the probe application process E_3 we are interested in is very weak. The applied pump does not induce a sufficient occupation of the antibonding π_z^* orbital for changes in the nuclear positions to be resolved by the probe.

As a result, the molecular geometry is minimally modified during the action of the probe pulse, with a maximum change in the C–C bond-length of less than 0.033 a_0. For the laser parameters depicted in Fig. 3.18, the photoelectron properties of the molecule are largely unaffected by the coupling with nuclear degrees of freedom.

I have tried to fix this problem by increasing and decreasing the intensity of the pump, as it causes the depopulation of the π_z^*. If I decrease its intensity, we reduce the depopulation of π_z^* due to a second pump but we also decrease the π_z^* population by excitation from the π_z due to a first pump from E_1. If I increase its intensity, we can trigger nonlinear effects such as a displacement of the peaks and the emergence of new peaks in Fig. 3.22. In the strong non-linear regime the TRPES and PAD will depend on the perturbation.

3.3.2.2. *Artificial pump plus probe.* A stronger nuclear response can be stimulated artificially by propagating an initially fully occupied electronic excited state π_z^* without the need of a pump. In the previous case, the pump laser was in charge of populating the π_z^* excited state, which was subsequently observed during its construction, by means of a delayed probe pulse. We now investigate the effect of the coupling between nuclear and electronic degrees of freedom while keeping the excited state π_z^* fully populated.

To this end, I artificially promote one electron from the highest occupied Kohn-Sham (KS) molecular orbital (HOMO) π_z to the first lowest unoccupied molecular orbital (LUMO) π_z^*, and propagate keeping this configuration fixed. The KS LUMO with π_z^* symmetry is of antibonding nature (see Fig. 3.18). We thus expect its occupation to have sizeable effects on the nuclei's motion, especially on the C–C bond. I employ the same probe pulse shown in Fig. 3.18, while the pump pulse has been omitted. Here, the time delay is measured as the difference from the centre of the probe to the starting point of the time evolution.

Changes in the bond length and the torsion of the molecule induced by the initial electronic excitation are shown on the left and right hand side of Fig. 3.23 (a), respectively. The same is shown in Fig. 3.24 for a longer time propagation. The C–C bond length displays an oscillatory behaviour. It initially increases up to 0.53 a_0 at $\tau_m = 10.8$ fs over its initial ground state equilibrium position, and then oscillates in time.

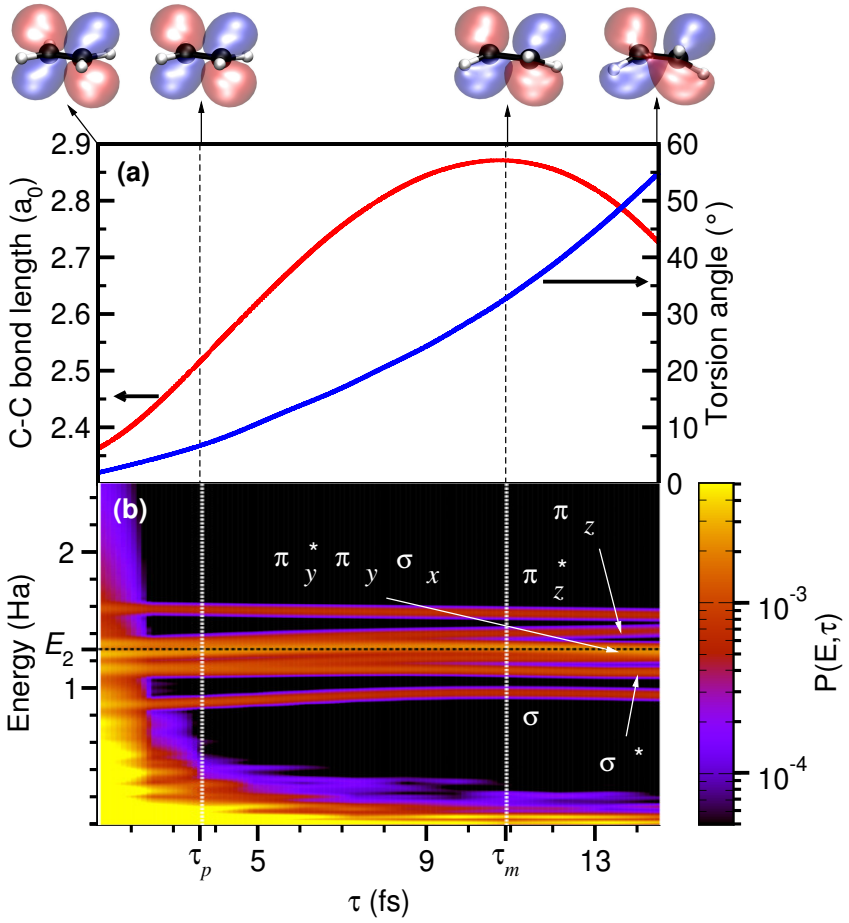

FIGURE 3.23. (a) Ethylene carbon-carbon bond length in a_0 (red) and torsion angle in ° (blue) versus the probe time delay τ in fs from an artificial $\pi_z \rightarrow \pi_z^*$ excited initial state. The nuclei's motion is classically modelled starting from 300 K and the ground state. The black vertical lines are the times at which the C–C bond length reaches its maximum $\tau_m = 10.8$ fs and a previous time $\tau_p = 3.6$ fs for comparison. The molecular structure and π_z^* orbital at the start, τ_p, τ_m and end of the simulation are shown above. (b) Probe time-resolved photoemission spectra $P(E, \tau)$ for all the labelled orbitals of ethylene in Fig. 3.18, as a function of the photoelectron's kinetic energy in Ha and the probe time delay τ in fs (see Fig. 3.18 for details of the probe) starting from the ground state. The nuclei's motion is classically modelled with an initial temperature of 300 K. The black vertical lines are the times at which the C–C bond length reaches its maximum $\tau_m = 10.8$ fs and a previous time $\tau_p = 3.6$ fs for comparison.

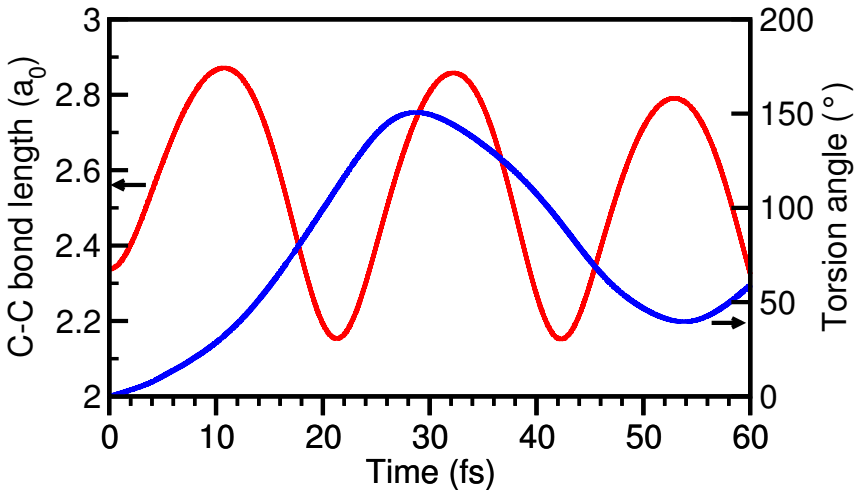

FIGURE 3.24. Ethylene carbon-carbon bond length in a_0 (red) and torsion angle in ° (blue) as a function of time in fs, with the nuclei's motion classically modelled starting from 300 K and a molecular excited state created by artificially promoting one electron from the Kohn-Sham highest occupied molecular orbital to the lowest unoccupied molecular orbital.

The molecule undergoes a twist along the C–C axis reaching a maximum torsion of 150.6°. This behaviour is at the core of cis-trans isomerisation processes happening in many photochemical reactions [232]. The vibrational stretching frequency along the C–C bond ($\omega_{CC} = 7.14 \times 10^{-3}$ Ha) and the torsional distortion ($\omega_{torsion} = 2.82 \times 10^{-3}$ Ha) are in qualitative agreement with the experimental data ($\omega_{CC} = 7.39 \times 10^{-3}$ Ha and $\omega_{torsion} = 4.67 \times 10^{-3}$ Ha) [232].

These modifications of the molecule's geometry are reflected in the TRPES shown in figure 3.23 (b). The initial spectrum changes in time, as the peaks shift in position and separate close to the maximum elongation time τ_m of the C–C bond.

The lowest energy peak is consistent with all-bonding σ orbital electrons (see Fig. 3.18), and is therefore sensitive to the molecule's bond-length and relatively insensitive to its torsion angle.

The following peak in energy splits into two new peaks. The peak that shifts and increases in energy, corresponds to the π_y state, whereas the one that does not, to the σ^* state. These two which were practically degenerate in Fig. 3.22, now separate. The π_y state energy shift is due to the fact that it connects hydrogens bound to different carbon atoms, and is therefore sensitive to the molecule's torsion and the C–C bond length.

The intermediate peak in energy corresponds to the σ_x, π_y^* and π_y states. Here the σ_x does not shift in energy, as it is only weakly affected by the molecule's bond stretching. The π_y^* shifts towards lower energies because it does not connect hydrogens bound to different carbon atoms. The π_y shifts towards higher energies because it does connect hydrogens bound to different carbon atoms.

The second to last peak in energy corresponds to the π_z state. The π_y^* and π_z states are not degenerate anymore as was the case in Fig. 3.22.

The highest and last peak in energy is consistent with the π_z^*.

The LUMO π_z^* orbital evolution is shown on top of Fig. 3.23. The π_z^* and π_z orbitals become degenerate when a torsion angle of 90° is reached. The former and latter build and deplete probability along the nodal plane, shifting towards lower and higher energies, respectively.

In order to support this analysis, in Fig. 3.25 (c) I present selected cuts of the TRPES at the specific time delays $\tau_p = 3.6$ fs, $\tau_m = 10.8$ fs and $\tau_e = 14.5$ fs. The time evolution of each photoelectron peak, can here be monitored identifying each peak with its PAD *fingerprint* in Fig. 3.25 (a) and (b). The peaks labelled **F**, **G**, **H**, which shift towards lower energies as time evolves, belong to the same state according to the PADs. This state can easily be associated to a π_z^* orbital due to its nodal structure. Similarly, the peaks **C**, **D**, **E**, which shift towards higher energies as time evolves, all originate from the same π_z orbital.

In comparison to the HOMO E_2 PADs we observed in the pump-probe case of Fig. 3.22, the π_z character is here more defined. This is because the occupation of the KS LUMO state is lifting the π_y^*, π_z degeneracy that we had previously.

When the C–C elongation is at its maximum value at τ_m, a new peak emerges at $E_{\mathbf{B}} = 1.22$ Ha, which disappears at τ_e and τ_p. In order to understand where this extra peak comes from, I have obtained the photoelectron spectrum of methylene with the same probe pulse used for ethylene as shown grey filled in Fig. 3.25 (c). The PADs and orbitals of the peaks labelled **B** (belonging to ethylene C_2H_2) and **A** (belonging to methylene C_2H_4) in Fig. 3.25 (a) display a π_y symmetry. We can therefore conclude, that this extra peak is related to the π_y ethylene state which becomes less stable as the C–C bond length increases. We cannot clearly associate it to the dissociation of the molecule because the C-C bond length oscillates for a long time as shown in Fig. 3.24.

The first main peak corresponds to a σ state, which increases in energy until τ_m and then decreases again until τ_e as shown in the PES in Fig. 3.25 (c). The second main peak shifts towards lower energies as time evolves. This corresponds to the σ^* and π_y states, which separate in energy at τ_m, as explained above. The third peak contains σ_x and π_y^*, as well as π_y for $\tau \neq \tau_m$. The following peaks correspond to the π_z and then the π_z^*. The order of the peaks I find for the PES in Fig. 3.25 (c) corresponds to the one I find for the TRPES in Fig. 3.23.

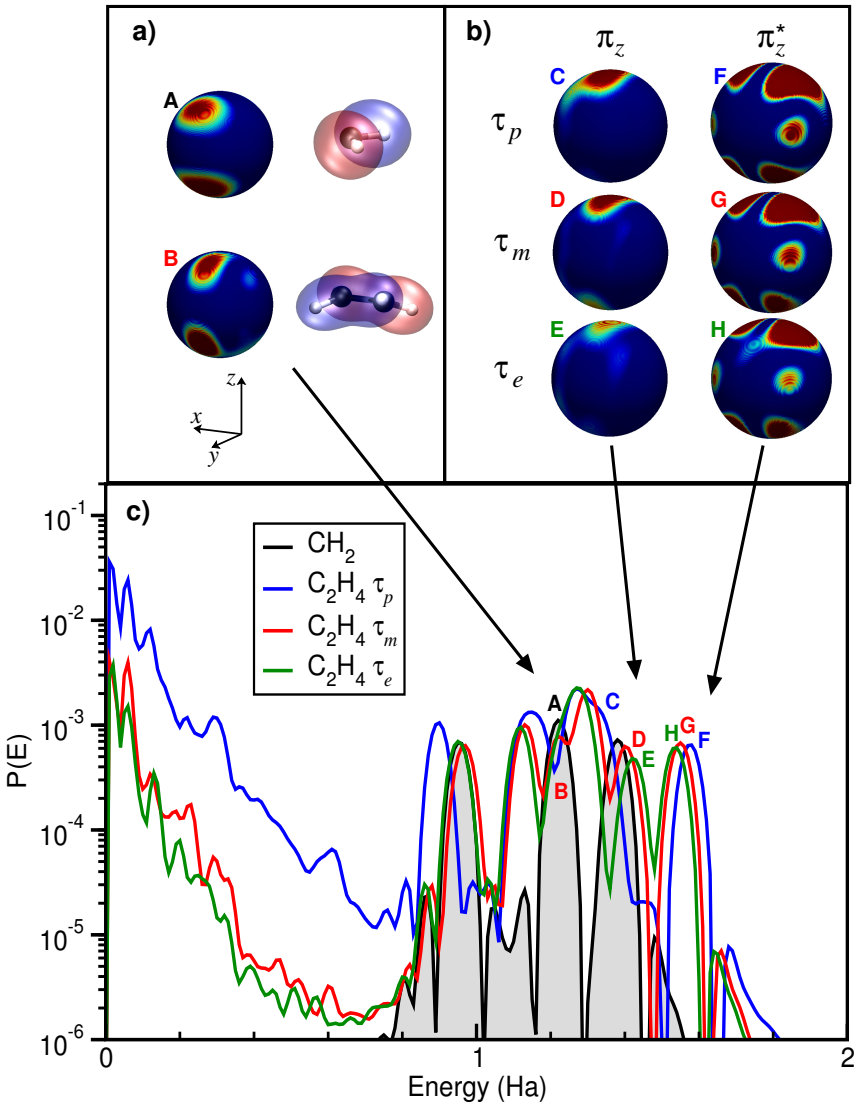

FIGURE 3.25. (a) Photoangular distributions and π_y orbitals for methylene C_2H_4 (A) and ethylene C_2H_2 (B). (b) Ethylene photoangular distributions for π_z/π_z^* orbitals at τ_p, τ_m and τ_e. (c) Photoemission spectra for a probe applied to the methylene molecule and to the ethylene molecule for the time at which the C–C bond length reaches its maximum $\tau_m = 10.8$ fs, an earlier time $\tau_p = 3.6 < \tau_m$ fs and at the end of the simulation $\tau_e = 14.5$ fs. The photoangular distribution for the peaks labelled in the photoemission spectra for both ethylene and methylene are shown in (a) and (b).

3.3.3. Conclusions. For the ethylene molecule, I have probed the electronic only and electronic plus nuclear effects of exciting the π_z to π_z^* transition. This is done to investigate the reactivity of such a transition because many useful products are obtained from ethylene due to this reactivity.

First, I have used an ultraviolet (UV) pump that is tuned to excite this π_z to π_z^* transition of interest. The dynamic evolution of the electronic levels of the molecule with or without including the nuclear motion is then monitored in time by means of a delayed strong and short extreme ultraviolet (XUV) probe laser. The probe ejects the molecule's electrons out to an evolving laser driven unbound continuum state. The outgoing electrons' kinetic energies and angular distributions are then calculated, during the application of the probe, as a function of the time delay between the pump and the probe.

To model the kinetic energies and angular distributions, I divide our space into two regions, an interacting and a noninteracting region which are connected by an absorbing boundary region. In the interacting localised region, I solve the electron plus nuclear equations using a real space grid basis. To model the electrons I use time-dependent density functional theory (TDDFT) and for the nuclei I either freeze them within the Born-Oppenheimer approximation (BOA) or I move them according to Ehrenfest dynamics (ED). In the non interacting region, where the electrons are freely driven by the laser field, I analytically propagate the outgoing electrons in momentum space using a plane wave basis. Most of the terms in both regions can be analysed within the small absorbing region simplifying the computational problem.

To evaluate these, we want the excitation by a pump followed by the ionisation by a probe sequence, to be the dominant process that takes place. However, I find that this pump plus probe sequential process is actually very weak. The dominant process is the pump π_z to π_z^* excitation process followed by a second pump π_z^* ionisation process which depopulates the π_z^*, leaving only a π_z^* small occupation for the second probe ionisation process which we are interested in. The induced occupation of the π_z^* due to the pump is not sufficient for changes in the nuclear positions to be resolved by the probe. In this case the kinetic energies and angular distributions hardly change by including the nuclear motion or not, and I find that the molecule hardly experiences any elongation or torsion.

To visualise the effects of nuclear motion, I have started from an initially pumped state by fixing the occupation of the π_z^* and I apply the same probe as when I use the pump too. By doing so, we avoid the depopulation of the π_z^* because we do not use a pump and because its population is fixed.

In this case I see that the kinetic energies change in time due to the nuclear motion, as the electronic peaks shift in position and separate into new contributions. I also find that the molecule experiences a large elongation and torsion.

I have analysed these nuclear effects on the molecular orbitals of ethylene in terms of the symmetry of the orbitals and the angular distributions.

This work has shown that it is possible to visualise large elongational and torsional effects of a double bonded rigid ethylene molecule. Therefore, it may even be possible to study more interesting processes such as the dissociation of molecules.

CHAPTER 4

General conclusions and future work

The experimental analysis of spectroscopic properties is a complex task, especially when one wants to understand the dynamic response of coupled electrons and nuclei to a strong external electromagnetic source. Due to the recent advances in optics, we can now follow the real time response of nuclei and electrons to very intense ultrashort lasers. When a molecule or an atom is exposed to an intense ultrashort laser, many non-linear effects can occur. This non-linear response becomes more complicated for molecules because we also have to take into account the induced vibrational changes. Computer simulations allow us to interpret with a reasonable degree of accuracy, many physical processes that occur for molecular and atomic systems when they are exposed to a strong external electromagnetic source.

Treating the coupled electron-nuclear many body problem quantum mechanically is only feasible for small benchmark systems such as the H_2^+ and H_2 molecules. In order to be able to theoretically interpret the experimental results for larger more complicated systems, approximations are employed for both the nuclei and electrons. To treat the nuclei I have used classical approximations such as the Born-Oppenheimer approximation (BOA) and Ehrenfest dynamics (ED). To treat the electrons I have used time-dependent density functional theory (TDDFT) because it is a simple and accurate method which can describe time-dependent non-perturbative phenomena.

In this thesis, I have obtained the linear response photoabsorption spectra for a 1D model of the H_2^+ and H_2 molecules. This problem can be solved quantum mechanically, allowing us to test the accuracy of approximations which treat nuclei classically. I have compared the linear response spectra that I obtain from a quantum and classical nuclear approach for different molecular masses. These approximations are only accurate as long as the mass M of the nuclei is large. I have found that quantum nuclear effects are important to describe the linear response spectra, especially for the H_2^+ molecule. These effects are gradually less intense as the mass of the molecule increases. This is something that one would expect because the classical and quantum approaches should be consistent for large masses. However, the most interesting effect is that the quantum nuclear effects can already be visualised in linear response. Using a simple two level system as a function of the mass of the molecules, I have been able to quantitatively interpret the widths and positions of the excitations peaks in the spectra. More work needs to be done to understand the physical origin that is behind the success of the two level system. Moreover, I

still need to understand why the nuclear effects are more important for the one electron molecule than the two electron molecule.

The strong field photoionisation of neon and argon atoms exposed to free electron lasers has been studied in this thesis using TDDFT. Lowest-order perturbation theory (LOPT) has been successfully used to interpret experimental photoionisation results for argon and neon in the perturbative regime. This perturbative method works very well as long as the laser used is not too intense and too short. For intense ultrashort pulses we need to have access to a non-perturbative approach such as TDDFT. However, it was thought that TDDFT was unable to describe the strong field photoionisation of atoms because it did not work for the helium "knee". Surprisingly, comparing our TDDFT results to the LOPT ones, I find that TDDFT can provide a very good description of the ionisation processes for neon and argon atoms. As the performance of TDDFT strongly depends on the locality and asymptotic behaviour of the exchange-correlation functional, I have tested the asymptotic behaviour effect with different exchange-correlation functionals. Long range potentials decay as a real atom whereas short range potentials decay too fast. Therefore, as expected, I have found that the performance of TDDFT improves using long-range potentials. The LOPT results are a bit better than the TDDFT ones, but we can still try to improve the performance of TDDFT. A possible option which I have not analysed here is to use functionals which can describe non-localities better than the ones employed here. I have compared the TDDFT and LOPT ionisation yields in the perturbative regime where LOPT can work. However, TDDFT turns out to be a non-perturbative method which can provide very good photoionisation results and can be used to interpret more complicated non-linear phenomena.

Finally, in this thesis I have also studied the strong pump probe ionisation of an ethylene molecule. For an ethylene molecule we also have to include the vibrational degrees of freedom which we do not have for the neon and argon atoms. Pump probe spectroscopy is an appropriate technique here because it can resolve both the vibrational and electronic degrees of freedom. The intense short probe that I have used triggers non-perturbative effects which we can analyse with TDDFT. Ethylene contains single C-H bonds and a double C=C bond. For these light atoms, nuclear changes should be large under strong non-perturbative sources. Due to the relatively strong force constant for the C=C double bond, distortions as well as elongations of this bond require a lot of energy. The intense ultrashort probe I use is strong enough to induce a huge rotation and elongation of the double bond of the ethylene molecule. We can only see the nuclear motion with the ED scheme because with the BOA scheme the nuclear positions are fixed. Extracting information from the orbitals obtained from the angular distributions and the time resolved spectra I have been able to see how these nuclear changes affect the photoemission of the molecule's orbitals. As we do not have to deal with the orientation of the molecule computationally, we can obtain the angular distributions for each orbital. It would be harder to observe these nuclear effects experimentally due to two reasons. First, the orientation

of the molecule cannot be fixed experimentally as can be done theoretically. Second, the occupation of the non-stationary state due to the pump has to be sufficient for changes in the nuclear positions to be resolved by the probe. This is also experimentally very hard to control because this non-stationary state can get ionised or relax before we can even apply the probe. Theoretically we can fix the orientation of the molecule and the occupation of the non-stationary state to apply the probe. With our TDDFT approach it may even be possible to observe the dissociation of molecules computationally, a process which may be very hard to control experimentally.

Bibliography

[1] W. Heisenberg. über den anschaulichen inhalt der quantentheoretischen kinematik und mechanik. *Zeitschrift für Physik*, 43(3-4):172–198, 1927. 1

[2] F. Kelkensberg, C. Lefebvre, W. Siu, O. Ghafur, T. T. Nguyen-Dang, O. Atabek, A. Keller, V. Serov, P. Johnsson, M. Swoboda, T. Remetter, A. L'Huillier, S. Zherebtsov, G. Sansone, E. Benedetti, F. Ferrari, M. Nisoli, F. Lépine, M. F. Kling, and M. J. J. Vrakking. Molecular dissociative ionization and wave-packet dynamics studied using two-color XUV and IR pump-probe spectroscopy. *Phys. Rev. Lett.*, 103:123005, Sep 2009. 1

[3] A. Föhlisch et al. Direct observation of electron dynamics in the attosecond domain. *Nature*, 436:373–376, 2005. 1

[4] H. S. Kato, M. Furukawa, M. Kawai, M. Taniguchi, T. Kawai, T. Hatsui, and N. Kosugi. Electronic structure of bases in dna duplexes characterized byresonant photoemission spectroscopy near the fermi level. *Phys. Rev. Lett.*, 93:086403, Aug 2004. 1

[5] Eylon Yavin, Amie K. Boal, Eric D. A. Stemp, Elizabeth M. Boon, Alison L. Livingston, Valerie L. O'Shea, Sheila S. David, and Jacqueline K. Barton. Proteindna charge transport: Redox activation of a dna repair protein by guanine radical. *Proceedings of the National Academy of Sciences of the United States of America*, 102(10):3546–3551, 2005. 1

[6] E. Goulielmakis, V. S. Yakovlev, A. L. Cavalieri, M. Uiberacker, V. Pervak, A. Apolonski, R. Kienberger, U. Kleineberg, and F. Krausz. Attosecond control and measurement: Lightwave electronics. *Science*, 317(5839):769–775, 2007. 1

[7] Ahmed H. Zewail. Femtochemistry: atomic-scale dynamics of the chemical bond. *The Journal of Physical Chemistry A*, 104(24):5660–5694, 2000. 1

[8] Markus Drescher, Michael Hentschel, Reinhard Kienberger, Gabriel Tempea, Christian Spielmann, Georg A. Reider, Paul B. Corkum, and Ferenc Krausz. X-ray pulses approaching the attosecond frontier. *Science*, 291(5510):1923–1927, 2001. 1

[9] M. Hentschel et al. Attosecond metrology. *Nature*, 414:509–513, 2001. 1

[10] P. M. Paul, E. S. Toma, P. Breger, G. Mullot, F. Augé, Ph. Balcou, H. G. Muller, and P. Agostini. Observation of a train of attosecond pulses from high harmonic generation. *Science*, 292(5522):1689–1692, 2001. 1

[11] M. DiDomenico. Smallsignal analysis of internal (couplingtype) modulation of lasers. *Journal of Applied Physics*, 35(10), 1964. 1

[12] T. Brabec, Ch. Spielmann, and F. Krausz. Mode locking in solitary lasers. *Opt. Lett.*, 16(24):1961–1963, Dec 1991. 1

[13] G. Steinmeyer, D. H. Sutter, L. Gallmann, N. Matuschek, and U. Keller. Frontiers in ultrashort pulse generation: Pushing the limits in linear and nonlinear optics. *Science*, 286(5444):1507–1512, 1999. 1

[14] D. E. Spence, P. N. Kean, and W. Sibbett. 60-fsec pulse generation from a self-mode-locked ti:sapphire laser. *Opt. Lett.*, 16(1):42–44, Jan 1991. 1

[15] M. Nisoli, S. De Silvestri, and O. Svelto. Generation of high energy 10 fs pulses by a new pulse compression technique. *Applied Physics Letters*, 68(20), 1996. 1

[16] Charles G. Durfee, Andy R. Rundquist, Sterling Backus, Catherine Herne, Margaret M. Murnane, and Henry C. Kapteyn. Phase matching of high-order harmonics in hollow waveguides. *Phys. Rev. Lett.*, 83:2187–2190, Sep 1999. 1

[17] E. Constant, D. Garzella, P. Breger, E. Mével, Ch. Dorrer, C. Le Blanc, F. Salin, and P. Agostini. Optimizing high harmonic generation in absorbing gases: Model and experiment. *Phys. Rev. Lett.*, 82:1668–1671, Feb 1999. 1

[18] Ximao Feng, Steve Gilbertson, Hiroki Mashiko, He Wang, Sabih D. Khan, Michael Chini, Yi Wu, Kun Zhao, and Zenghu Chang. Generation of isolated attosecond pulses with 20 to 28 femtosecond lasers. *Phys. Rev. Lett.*, 103:183901, Oct 2009. 1

[19] H. M. Milchberg, C. G. Durfee III, and T. J. McIlrath. High-order frequency conversion in the plasma waveguide. *Phys. Rev. Lett.*, 75:2494–2497, Sep 1995. 1

[20] Robert Szipöcs, Christian Spielmann, Ferenc Krausz, and Kárpát Ferencz. Chirped multilayer coatings for broadband dispersion control in femtosecond lasers. *Opt. Lett.*, 19(3):201–203, Feb 1994. 1

[21] R. L. Fork, C. H. Brito Cruz, P. C. Becker, and C. V. Shank. Compression of optical pulses to six femtoseconds by using cubic phase compensation. *Opt. Lett.*, 12(7):483–485, Jul 1987. 1

[22] Andrius Baltuška, Takao Fuji, and Takayoshi Kobayashi. Controlling the carrier-envelope phase of ultrashort light pulses with optical parametric amplifiers. *Phys. Rev. Lett.*, 88:133901, Mar 2002. 1

[23] J. Seres et al. Laser technology: Source of coherent kiloelectronvolt x-rays. *Nature*, 433:596, 2005. 1

[24] Zenghu Chang, Andy Rundquist, Haiwen Wang, Margaret M. Murnane, and Henry C. Kapteyn. Generation of coherent soft x rays at 2.7 nm using high harmonics. *Phys. Rev. Lett.*, 79:2967–2970, Oct 1997. 1

[25] Charles A. Brau. Free-electron lasers. *Science*, 239(4844):1115–1121, 1988. 1

[26] I. D. Williams, J. McKenna, J. Wood, M. Suresh, W. A. Bryan, S. L. Stebbings, E. M. L. English, C. R. Calvert, B. Srigengan, E. J. Divall, C. J. Hooker, A. J. Langley, and W. R. Newell. Excited ions in intense femtosecond laser pulses: Laser-induced recombination. *Phys. Rev. Lett.*, 99:173002, Oct 2007. 1

[27] Jeffrey L. Krause, Kenneth J. Schafer, and Kenneth C. Kulander. High-order harmonic generation from atoms and ions in the high intensity regime. *Phys. Rev. Lett.*, 68:3535–3538, Jun 1992. 1

[28] J. J. Macklin, J. D. Kmetec, and C. L. Gordon. High-order harmonic generation using intense femtosecond pulses. *Phys. Rev. Lett.*, 70:766–769, Feb 1993. 1

[29] M. Yu. Ivanov and P. B. Corkum. Generation of high-order harmonics from inertially confined molecular ions. *Phys. Rev. A*, 48:580–590, Jul 1993. 1

[30] Philippe Antoine, Anne L'Huillier, and Maciej Lewenstein. Attosecond pulse trains using high˘order harmonics. *Phys. Rev. Lett.*, 77:1234–1237, Aug 1996. 1

[31] E. Goulielmakis, M. Schultze, M. Hofstetter, V. S. Yakovlev, J. Gagnon, M. Uiberacker, A. L. Aquila, E. M. Gullikson, D. T. Attwood, R. Kienberger, F. Krausz, and U. Kleineberg. Single-cycle nonlinear optics. *Science*, 320(5883):1614–1617, 2008. 1

[32] M. Y. Shverdin, D. R. Walker, D. D. Yavuz, G. Y. Yin, and S. E. Harris. Generation of a single-cycle optical pulse. *Phys. Rev. Lett.*, 94:033904, Jan 2005. 1

[33] G. Sansone, E. Benedetti, F. Calegari, C. Vozzi, L. Avaldi, R. Flammini, L. Poletto, P. Villoresi, C. Altucci, R. Velotta, S. Stagira, S. De Silvestri, and M. Nisoli. Isolated single-cycle attosecond pulses. *Science*, 314(5798):443–446, 2006. 1

[34] Ivan P. Christov, Margaret M. Murnane, and Henry C. Kapteyn. High-harmonic generation of attosecond pulses in the "single-cycle" regime. *Phys. Rev. Lett.*, 78:1251–1254, Feb 1997. 1

[35] J. Seres et al. Coherent superposition of laser-driven soft-x-ray harmonics from successive sources. *Nature Physics*, 3:878–883, 2007. 1

[36] Andy Rundquist, Charles G. Durfee, Zenghu Chang, Catherine Herne, Sterling Backus, Margaret M. Murnane, and Henry C. Kapteyn. Phase-matched generation of coherent soft x-rays. *Science*, 280(5368):1412–1415, 1998. 1

[37] H. R. Lange, A. Chiron, J.-F. Ripoche, A. Mysyrowicz, P. Breger, and P. Agostini. High-order harmonic generation and quasiphase matching in xenon using self-guided femtosecond pulses. *Phys. Rev. Lett.*, 81:1611–1613, Aug 1998. 1

[38] Emily A. Gibson, Ariel Paul, Nick Wagner, Ra'anan Tobey, David Gaudiosi, Sterling Backus, Ivan P. Christov, Andy Aquila, Eric M. Gullikson, David T. Attwood, Margaret M. Murnane, and Henry C. Kapteyn. Coherent soft x-ray generation in the water window with quasi-phase matching. *Science*, 302(5642):95–98, 2003. 1

[39] W. C. Röntgen. On a new kind of rays. *Science*, 3(59):227–231, 1896. 1

[40] John M. J. Madey. Stimulated emission of bremsstrahlung in a periodic magnetic field. *Journal of Applied Physics*, 42(5), 1971. 1

[41] D. A. G. Deacon, L. R. Elias, J. M. J. Madey, G. J. Ramian, H. A. Schwettman, and T. I. Smith. First operation of a free-electron laser. *Phys. Rev. Lett.*, 38:892–894, Apr 1977. 1

[42] S. V. Milton, E. Gluskin, N. D. Arnold, C. Benson, W. Berg, S. G. Biedron, M. Borland, Y.-C. Chae, R. J. Dejus, P. K. Den Hartog, B. Deriy, M. Erdmann, Y. I. Eidelman, M. W. Hahne, Z. Huang, K.-J. Kim, J. W. Lewellen, Y. Li, A. H. Lumpkin, O. Makarov, E. R. Moog, A. Nassiri, V. Sajaev, R. Soliday, B. J. Tieman, E. M. Trakhtenberg, G. Travish, I. B. Vasserman, N. A. Vinokurov, X. J. Wang, G. Wiemerslage, and B. X. Yang. Exponential gain and saturation of a self-amplified spontaneous emission free-electron laser. *Science*, 292(5524):2037–2041, 2001. 1

[43] J. Andruszkow, B. Aune, V. Ayvazyan, N. Baboi, R. Bakker, V. Balakin, D. Barni, A. Bazhan, M. Bernard, A. Bosotti, J. C. Bourdon, W. Brefeld, R. Brinkmann, S. Buhler, J.-P. Carneiro, M. Castellano, P. Castro, L. Catani, S. Chel, Y. Cho, S. Choroba, E. R. Colby, W. Decking, P. Den Hartog, M. Desmons, M. Dohlus, D. Edwards, H. T. Edwards, B. Faatz, J. Feldhaus, M. Ferrario, M. J. Fitch, K. Flöttmann, M. Fouaidy, A. Gamp, T. Garvey, C. Gerth, M. Geitz, E. Gluskin, V. Gretchko, U. Hahn, W. H. Hartung, D. Hubert, M. Hüning, R. Ischebek, M. Jablonka, J. M. Joly, M. Juillard, T. Junquera, P. Jurkiewicz, A. Kabel, J. Kahl, H. Kaiser, T. Kamps, V. V. Katelev, J. L. Kirchgessner, M. Körfer, L. Kravchuk, G. Kreps, J. Krzywinski, T. Lokajczyk, R. Lange, B. Leblond, M. Leenen, J. Lesrel, M. Liepe, A. Liero, T. Limberg, R. Lorenz, Lu Hui Hua, Lu Fu Hai, C. Magne, M. Maslov, G. Materlik, A. Matheisen, J. Menzel, P. Michelato, W.-D. Möller, A. Mosnier, U.-C. Müller, O. Napoly, A. Novokhatski, M. Omeich, H. S. Padamsee, C. Pagani, F. Peters, B. Petersen, P. Pierini, J. Pflüger, P. Piot, B. Phung Ngoc, L. Plucinski, D. Proch, K. Rehlich, S. Reiche, D. Reschke, I. Reyzl, J. Rosenzweig, J. Rossbach, S. Roth, E. L. Saldin, W. Sandner, Z. Sanok, H. Schlarb, G. Schmidt, P. Schmüser, J. R. Schneider, E. A. Schneidmiller, H.-J. Schreiber, S. Schreiber, P. Schütt, J. Sekutowicz, L. Serafini, D. Sertore, S. Setzer, S. Simrock, B. Sonntag, B. Sparr, F. Stephan, V. A. Sytchev, S. Tazzari, F. Tazzioli, M. Tigner, M. Timm, M. Tonutti, E. Trakhtenberg, R. Treusch, D. Trines, V. Verzilov, T. Vielitz, V. Vogel, G. v. Walter, R. Wanzenberg, T. Weiland, H. Weise, J. Weisend, M. Wendt, M. Werner, M. M. White, I. Will, S. Wolff, M. V. Yurkov, K. Zapfe, P. Zhogolev, and F. Zhou. First observation of self-amplified spontaneous emission in a free-electron laser at 109 nm wavelength. *Phys. Rev. Lett.*, 85:3825–3829, Oct 2000. 1

[44] A. Tremaine, X. J. Wang, M. Babzien, I. Ben-Zvi, M. Cornacchia, H.-D. Nuhn, R. Malone, A. Murokh, C. Pellegrini, S. Reiche, J. Rosenzweig, and V. Yakimenko. Experimental characterization of nonlinear harmonic radiation from a visible self-amplified spontaneous emission free-electron laser at saturation. *Phys. Rev. Lett.*, 88:204801, May 2002. 1

[45] V. Ayvazyan, N. Baboi, I. Bohnet, R. Brinkmann, M. Castellano, P. Castro, L. Catani, S. Choroba, A. Cianchi, M. Dohlus, H. T. Edwards, B. Faatz, A. A. Fateev, J. Feldhaus, K. Flöttmann, A. Gamp, T. Garvey, H. Genz, Ch. Gerth, V. Gretchko, B. Grigoryan, U. Hahn, C. Hessler, K. Honkavaara, M. Hüning, R. Ischebeck, M. Jablonka, T. Kamps, M. Körfer, M. Krassilnikov, J. Krzywinski, M. Liepe, A. Liero, T. Limberg, H. Loos, M. Luong, C. Magne, J. Menzel, P. Michelato, M. Minty, U.-C. Müller, D. Nölle, A. Novokhatski, C. Pagani, F. Peters, J. Pflüger, P. Piot, L. Plucinski, K. Rehlich, I. Reyzl, A. Richter, J. Rossbach, E. L. Saldin, W. Sandner, H. Schlarb, G. Schmidt, P. Schmüser, J. R. Schneider, E. A. Schneidmiller, H.-J. Schreiber, S. Schreiber, D. Sertore, S. Setzer, S. Simrock, R. Sobierajski, B. Sonntag, B. Steeg, F. Stephan, K. P. Sytchev, K. Tiedtke, M. Tonutti, R. Treusch, D. Trines, D. Türke, V. Verzilov, R. Wanzenberg, T. Weiland, H. Weise, M. Wendt, I. Will, S. Wolff, K. Wittenburg, M. V. Yurkov, and K. Zapfe. Generation of gw radiation pulses from a vuv free-electron laser operating in the femtosecond regime. *Phys. Rev. Lett.*, 88:104802, Feb 2002. 1

[46] W.B. Colson. One-body electron dynamics in a free electron laser. *Physics Letters A*, 64(2):190 – 192, 1977. 1

[47] E.T. Scharlemann. Wiggle plane focusing in linear wigglers. *Journal of Applied Physics*, 58(6), 1985. 1

[48] R. Bonifacio, C. Pellegrini, and L.M. Narducci. Collective instabilities and high-gain regime in a free electron laser. *Optics Communications*, 50(6):373 – 378, 1984. 1

[49] Kwang-Je Kim. Three-dimensional analysis of coherent amplification and self-amplified spontaneous emission in free-electron lasers. *Phys. Rev. Lett.*, 57:1871–1874, Oct 1986. 1

[50] E. T. Scharlemann, A. M. Sessler, and J. S. Wurtele. Optical guiding in a free-electron laser. *Phys. Rev. Lett.*, 54:1925–1928, Apr 1985. 1

[51] L. H. Yu, S. Krinsky, and R. L. Gluckstern. Calculation of universal scaling function for free-electron-laser gain. *Phys. Rev. Lett.*, 64:3011–3014, Jun 1990. 1

[52] W. Ackermann et al. Operation of a free-electron laser from the extreme ultraviolet to the water window. *Nature Photonics*, 1:336–342, 2007. 1

[53] T. Shintake et al. A compact free-electron laser for generating coherent radiation in the extreme ultraviolet region. *Nature Photonics*, 2:555–559, 2008. 1

[54] P. Emma et al. First lasing and operation of an angstrom-wavelength free-electron laser. *Nature Photonics*, 4:641–647, 2010. 1

[55] T. Ishikawa et al. A compact x-ray free-electron laser emitting in the sub-angstrom region. *Nature Photonics*, 6:540–544, 2012. 1

[56] L. Young et al. Femtosecond electronic response of atoms to ultra-intense x-rays. *Nature*, 466:56–61, 2010. 1

[57] Y. Hikosaka, M. Fushitani, A. Matsuda, C.-M. Tseng, A. Hishikawa, E. Shigemasa, M. Nagasono, K. Tono, T. Togashi, H. Ohashi, H. Kimura, Y. Senba, M. Yabashi, and T. Ishikawa. Multiphoton double ionization of ar in intense extreme ultraviolet laser fields studied by shot-by-shot photoelectron spectroscopy. *Phys. Rev. Lett.*, 105:133001, Sep 2010. 1

[58] A. A. Sorokin, S. V. Bobashev, T. Feigl, K. Tiedtke, H. Wabnitz, and M. Richter. Photoelectric effect at ultrahigh intensities. *Phys. Rev. Lett.*, 99:213002, Nov 2007. 1

[59] M. G. Makris, P. Lambropoulos, and A. Mihelič. Theory of multiphoton multielectron ionization of xenon under strong 93-ev radiation. *Phys. Rev. Lett.*, 102:033002, Jan 2009. 1

[60] T. S. Luk, H. Pummer, K. Boyer, M. Shahidi, H. Egger, and C. K. Rhodes. Anomalous collision-free multiple ionization of atoms with intense picosecond ultraviolet radiation. *Phys. Rev. Lett.*, 51:110–113, Jul 1983. 1

[61] D. J. Bradley, P. Ewart, J. V. Nicholas, J. R. D. Shaw, and D. G. Thompson. Photoionization from the selectively excited $3s3p^1P_1 \circ statetothe 3p^21s_0$ autoionization level of mg i. *Phys. Rev. Lett.*, 31:263–266, Jul 1973. 1

[62] M. Uiberacker et al. Attosecond real-time observation of electron tunnelling in atoms. *Nature*, 446:627–632, 2007. 1

[63] P. B. Corkum. Plasma perspective on strong field multiphoton ionization. *Phys. Rev. Lett.*, 71:1994–1997, Sep 1993. 1

[64] M. Lewenstein, Ph. Balcou, M. Yu. Ivanov, Anne L'Huillier, and P. B. Corkum. Theory of high-harmonic generation by low-frequency laser fields. *Phys. Rev. A*, 49:2117–2132, Mar 1994. 1

[65] P. Salières, B. Carré, L. Le Déroff, F. Grasbon, G. G. Paulus, H. Walther, R. Kopold, W. Becker, D. B. Milošević, A. Sanpera, and M. Lewenstein. Feynman's path-integral approach for intense-laser-atom interactions. *Science*, 292(5518):902–905, 2001. 1

[66] B. Walker, B. Sheehy, K. C. Kulander, and L. F. DiMauro. Elastic rescattering in the strong field tunneling limit. *Phys. Rev. Lett.*, 77:5031–5034, Dec 1996. 1

[67] P. B. Corkum, N. H. Burnett, and F. Brunel. Above-threshold ionization in the long-wavelength limit. *Phys. Rev. Lett.*, 62:1259–1262, Mar 1989. 1

[68] P. Agostini, F. Fabre, G. Mainfray, G. Petite, and N. K. Rahman. Free-free transitions following six-photon ionization of xenon atoms. *Phys. Rev. Lett.*, 42:1127–1130, Apr 1979. 1

[69] G. G. Paulus, W. Nicklich, Huale Xu, P. Lambropoulos, and H. Walther. Plateau in above threshold ionization spectra. *Phys. Rev. Lett.*, 72:2851–2854, May 1994. 1

[70] Baorui Yang, K. J. Schafer, B. Walker, K. C. Kulander, P. Agostini, and L. F. DiMauro. Intensity-dependent scattering rings in high order above-threshold ionization. *Phys. Rev. Lett.*, 71:3770–3773, Dec 1993. 1

[71] Naoki Miyamoto, Masato Kamei, Dai Yoshitomi, Teruto Kanai, Taro Sekikawa, Takashi Nakajima, and Shuntaro Watanabe. Observation of two-photon above-threshold ionization of rare gases by xuv harmonic photons. *Phys. Rev. Lett.*, 93:083903, Aug 2004. 1

[72] E. P. Wigner and L. Eisenbud. Higher angular momenta and long range interaction in resonance reactions. *Phys. Rev.*, 72:29–41, Jul 1947. 1

[73] D. N. Fittinghoff, P. R. Bolton, B. Chang, and K. C. Kulander. Observation of nonsequential double ionization of helium with optical tunneling. *Phys. Rev. Lett.*, 69:2642–2645, Nov 1992. 1

[74] J. B. Watson, A. Sanpera, D. G. Lappas, P. L. Knight, and K. Burnett. Nonsequential double ionization of helium. *Phys. Rev. Lett.*, 78:1884–1887, Mar 1997. 1

[75] A. Rudenko, K. Zrost, B. Feuerstein, V. L. B. de Jesus, C. D. Schröter, R. Moshammer, and J. Ullrich. Correlated multielectron dynamics in ultrafast laser pulse interactions with atoms. *Phys. Rev. Lett.*, 93:253001, Dec 2004. 1

[76] Stefanie Gräfe and Misha Yu. Ivanov. Effective fields in laser-driven electron recollision and charge localization. *Phys. Rev. Lett.*, 99:163603, Oct 2007. 1

[77] Toru Morishita, Shinichi Watanabe, and C. D. Lin. Attosecond light pulses for probing two-electron dynamics of helium in the time domain. *Phys. Rev. Lett.*, 98:083003, Feb 2007. 1

[78] Nam A. Nguyen and André D. Bandrauk. Electron correlation of one-dimensional h_2 in intense laser fields: Time-dependent extended hartree-fock and time-dependent density-functional-theory approaches. *Phys. Rev. A*, 73:032708, Mar 2006. 1

[79] Robert C. Forrey, Zong-Chao Yan, H. R. Sadeghpour, and A. Dalgarno. Single and double photoionization from dipole response function. *Phys. Rev. Lett.*, 78:3662–3664, May 1997. 1

[80] Camilo Ruiz, Luis Plaja, Luis Roso, and Andreas Becker. *Ab initio* calculation of the double ionization of helium in a few-cycle laser pulse beyond the one-dimensional approximation. *Phys. Rev. Lett.*, 96:053001, Feb 2006. 1

[81] Kurt W. Meyer, Chris H. Greene, and Brett D. Esry. Two-electron photoejection of he and H^-. *Phys. Rev. Lett.*, 78:4902–4905, Jun 1997. 1

[82] F. W. Byron and Charles J. Joachain. Multiple ionization processes in helium. *Phys. Rev.*, 164:1–9, Dec 1967. 1

[83] R. Moshammer, B. Feuerstein, W. Schmitt, A. Dorn, C. D. Schröter, J. Ullrich, H. Rottke, C. Trump, M. Wittmann, G. Korn, K. Hoffmann, and W. Sandner. Momentum distributions of ne^{n+} ions created by an intense ultrashort laser pulse. *Phys. Rev. Lett.*, 84:447–450, Jan 2000. 1

[84] M. Weckenbrock, D. Zeidler, A. Staudte, Th. Weber, M. Schöffler, M. Meckel, S. Kammer, M. Smolarski, O. Jagutzki, V. R. Bhardwaj, D. M. Rayner, D. M. Villeneuve, P. B. Corkum, and R. Dörner. Fully differential rates for femtosecond multiphoton double ionization of neon. *Phys. Rev. Lett.*, 92:213002, May 2004. 1

[85] M. Weckenbrock, A. Becker, A. Staudte, S. Kammer, M. Smolarski, V. R. Bhardwaj, D. M. Rayner, D. M. Villeneuve, P. B. Corkum, and R. Dörner. Electron-electron momentum exchange in strong field double ionization. *Phys. Rev. Lett.*, 91:123004, Sep 2003. 1

[86] X. Liu, H. Rottke, E. Eremina, W. Sandner, E. Goulielmakis, K. O. Keeffe, M. Lezius, F. Krausz, F. Lindner, M. G. Schätzel, G. G. Paulus, and H. Walther. Nonsequential double ionization at the single-optical-cycle limit. *Phys. Rev. Lett.*, 93:263001, Dec 2004. 1

[87] A. D. Shiner et al. Probing collective multi-electron dynamics in xenon with high-harmonic spectroscopy. *Nature Physics*, 7:464–467, 2011. 1

[88] A. L'Huillier, L. A. Lompre, G. Mainfray, and C. Manus. Multiply charged ions formed by multiphoton absorption processes in the continuum. *Phys. Rev. Lett.*, 48:1814–1817, Jun 1982. 1

[89] H. Rottke, C. Trump, M. Wittmann, G. Korn, W. Sandner, R. Moshammer, A. Dorn, C. D. Schröter, D. Fischer, J. R. Crespo Lopez-Urrutia, P. Neumayer, J. Deipenwisch, C. Höhr, B. Feuerstein, and J. Ullrich. Coincident fragment detection in strong field photoionization and dissociation of H_2. *Phys. Rev. Lett.*, 89:013001, Jun 2002. 1

[90] M. F. Kling, Ch. Siedschlag, A. J. Verhoef, J. I. Khan, M. Schultze, Th. Uphues, Y. Ni, M. Uiberacker, M. Drescher, F. Krausz, and M. J. J. Vrakking. Control of electron localization in molecular dissociation. *Science*, 312(5771):246–248, 2006. 1

[91] A. S. Alnaser, S. Voss, X. M. Tong, C. M. Maharjan, P. Ranitovic, B. Ulrich, T. Osipov, B. Shan, Z. Chang, and C. L. Cocke. Effects of molecular structure on ion disintegration patterns in ionization of o_2 and n_2 by short laser pulses. *Phys. Rev. Lett.*, 93:113003, Sep 2004. 1

[92] Valérie Blanchet, Marek Z. Zgierski, Tamar Seideman, and Albert Stolow. Discerning vibronic molecular dynamics using time-resolved photoelectron spectroscopy. *Nature*, 401:52–54, 1999. 1

[93] H. Hertz. Ueber einen einfluss des ultravioletten lichtes auf die electrische entladung. *Annalen der Physik*, 267(8):983–1000, 1887. 1

[94] A. Einstein. über einen die erzeugung und verwandlung des lichtes betreffenden heuristischen gesichtspunkt. *Annalen der Physik*, 322(6):132–148, 1905. 1

[95] CarloMaria Bertoni. Quantum description of the matter-radiation interaction. In Settimio Mobilio, Federico Boscherini, and Carlo Meneghini, editors, *Synchrotron Radiation*, pages 145–178. Springer Berlin Heidelberg, 2015. 1

[96] M. L. Goldberger and K. M. Watson. In *Collision Theory*, page 944. Dover Publications, 2004. 1

[97] D. W. Turner and M. I. Al Jobory. Determination of ionization potentials by photoelectron energy measurement. *The Journal of Chemical Physics*, 37(12), 1962. 1

[98] André T. J. B. Eppink and David H. Parker. Velocity map imaging of ions and electrons using electrostatic lenses: Application in photoelectron and photofragment ion imaging of molecular oxygen. *Review of Scientific Instruments*, 68(9), 1997. 1

[99] G. Westmacott, M. Frank, S. E. Labov, and W. H. Benner. Using a superconducting tunnel junction detector to measure the secondary electron emission efficiency for a microchannel plate detector bombarded by large molecular ions. *Rapid Communications in Mass Spectrometry*, 14(19):1854–1861, 2000. 1

[100] J. K. Freericks, H. R. Krishnamurthy, and Th. Pruschke. Theoretical description of time-resolved photoemission spectroscopy: Application to pump-probe experiments. *Phys. Rev. Lett.*, 102:136401, Mar 2009. 1

[101] S. X. Hu and L. A. Collins. Attosecond pump probe: Exploring ultrafast electron motion inside an atom. *Phys. Rev. Lett.*, 96:073004, Feb 2006. 1

[102] R. Kienberger et al. Atomic transient recorder. *Nature*, 427:817–821, 2004. 1

[103] J. Itatani, F. Quéré, G. L. Yudin, M. Yu. Ivanov, F. Krausz, and P. B. Corkum. Attosecond streak camera. *Phys. Rev. Lett.*, 88:173903, Apr 2002. 1

[104] P. Krehl and S. Engemann. August toepler the first who visualized shock waves. *Shock Waves*, 5(1-2):1–18, 1995. 1

[105] A. Assion, M. Geisler, J. Helbing, V. Seyfried, and T. Baumert. Femtosecond pump-probe photoelectron spectroscopy: Mapping of vibrational wave-packet motion. *Phys. Rev. A*, 54:R4605–R4608, Dec 1996. 1

[106] Ingo Fischer, D. M. Villeneuve, Marc J. J. Vrakking, and Albert Stolow. Femtosecond wavepacket dynamics studied by timeresolved zerokinetic energy photoelectron spectroscopy. *The Journal of Chemical Physics*, 102(13), 1995. 1

[107] T. Baumert, R. Thalweiser, and G. Gerber. Femtosecond two-photon ionization spectroscopy of the b state of na_3 clusters. *Chemical Physics Letters*, 209(12):29 – 34, 1993. 1

[108] Douglas R. Cyr and Carl C. Hayden. Femtosecond timeresolved photoionization and photoelectron spectroscopy studies of ultrafast internal conversion in 1,3,5hexatriene. *The Journal of Chemical Physics*, 104(2), 1996. 1

[109] M. Drescher et al. Time-resolved atomic inner-shell spectroscopy. *Nature*, 419:803–807, 2002. 1

[110] J. Breidbach and L. S. Cederbaum. Universal attosecond response to the removal of an electron. *Phys. Rev. Lett.*, 94:033901, Jan 2005. 1

[111] Marlene Wickenhauser, Joachim Burgdörfer, Ferenc Krausz, and Markus Drescher. Time resolved fano resonances. *Phys. Rev. Lett.*, 94:023002, Jan 2005. 1

[112] Joan B. Pallix and Steven D. Colson. Time-resolved photoelectron studies of the relaxation of the s1(1e') excited state of sym-triazine. *Chemical Physics Letters*, 119(1):38 – 41, 1985. 1

[113] Ellen Sekreta and James P. Reilly. Direct observation of intersystem crossing in benzene by laser photoelectron spectroscopy. *Chemical Physics Letters*, 149(56):482 – 486, 1988. 1

[114] Xinbei Song, Charles W. Wilkerson Jr., John Lucia, Steven Pauls, and James P. Reilly. Direct observation of time-dependent intramolecular vibrational relaxation in jet-cooled p-n-alkylanilines by laser photoelectron spectroscopy. *Chemical Physics Letters*, 174(5):377 – 384, 1990. 1

[115] A. Mühlpfordt and U. Even and N.P. Ernsting. Zero-kinetic-energy photoelectron spectroscopy and excited-state intramolecular proton transfer in a double benzoxazole. *Chemical Physics Letters*, 263(12):178 – 184, 1996. 1

[116] K. A. Hanold, M. C. Garner, and R. E. Continetti. Photoelectron-photofragment angular correlation and energy partitioning in dissociative photodetachment. *Phys. Rev. Lett.*, 77:3335–3338, Oct 1996. 1

[117] J. A. Davies, R. E. Continetti, D. W. Chandler, and C. C. Hayden. Femtosecond time-resolved photoelectron angular distributions probed during photodissociation of no_2. *Phys. Rev. Lett.*, 84:5983–5986, Jun 2000. 1

[118] Lora Nugent-Glandorf, Michael Scheer, David A. Samuels, Anneliese M. Mulhisen, Edward R. Grant, Xueming Yang, Veronica M. Bierbaum, and Stephen R. Leone. Ultrafast time-resolved soft x-ray photoelectron spectroscopy of dissociating br_2. *Phys. Rev. Lett.*, 87:193002, Oct 2001. 1

[119] Sorensen, S. L. and Björneholm, O. and Hjelte, I. and Kihlgren, T. and Öhrwall, G. and Sundin, S. and Svensson, S. and Buil, S. and Descamps, D. and LHuillier, A. and Norin, J. and Wahlström, C.-G. Femtosecond pumpprobe photoelectron spectroscopy of predissociative rydberg states in acetylene. *The Journal of Chemical Physics*, 112(18), 2000. 1

[120] Etienne Gagnon, Predrag Ranitovic, Xiao-Min Tong, C. L. Cocke, Margaret M. Murnane, Henry C. Kapteyn, and Arvinder S. Sandhu. Soft x-ray-driven femtosecond molecular dynamics. *Science*, 317(5843):1374–1378, 2007. 1

[121] O. Geßner, A. M. D. Lee, J. P. Shaffer, H. Reisler, S. V. Levchenko, A. I. Krylov, Jonathan G. Underwood, H. Shi, A. L. L. East, D. M. Wardlaw, E. t. H. Chrysostom, C. C. Hayden, and Albert Stolow. Femtosecond multidimensional imaging of a molecular dissociation. *Science*, 311(5758):219–222, 2006. 1

[122] T. Weber et al. Complete photo-fragmentation of the deuterium molecule. *Nature*, 431:437–440, 2004. 1

[123] M. Schultze, M. Fieß, N. Karpowicz, J. Gagnon, M. Korbman, M. Hofstetter, S. Neppl, A. L. Cavalieri, Y. Komninos, Th. Mercouris, C. A. Nicolaides, R. Pazourek, S. Nagele, J. Feist, J. Burgdörfer, A. M. Azzeer, R. Ernstorfer, R. Kienberger, U. Kleineberg, E. Goulielmakis, F. Krausz, and V. S. Yakovlev. Delay in photoemission. *Science*, 328(5986):1658–1662, 2010. 1

[124] K. Klünder, J. M. Dahlström, M. Gisselbrecht, T. Fordell, M. Swoboda, D. Guénot, P. Johnsson, J. Caillat, J. Mauritsson, A. Maquet, R. Ta¨, and A. L'Huillier. Probing single-photon ionization on the attosecond time scale. *Phys. Rev. Lett.*, 106:143002, Apr 2011. 1

[125] P. Eckle, A. N. Pfeiffer, C. Cirelli, A. Staudte, R. Dörner, H. G. Muller, M. Büttiker, and U. Keller. Attosecond ionization and tunneling delay time measurements in helium. *Science*, 322(5907):1525–1529, 2008. 1

[126] A. N. Pfeiffer et al. Timing the release in sequential double ionization. *Nature Physics*, 7:428–433, 2011. 1

[127] A. Knapp, A. Kheifets, I. Bray, Th. Weber, A. L. Landers, S. Schössler, T. Jahnke, J. Nickles, S. Kammer, O. Jagutzki, L. Ph. H. Schmidt, T. Osipov, J. Rösch, M. H. Prior, H. Schmidt-Böcking, C. L. Cocke, and R. Dörner. Mechanisms of photo double ionization of helium by 530 ev photons. *Phys. Rev. Lett.*, 89:033004, Jun 2002. 1

[128] U. Becker, R. Hölzel, H. G. Kerkhoff, B. Langer, D. Szostak, and R. Wehlitz. Electron-ejection asymmetries by molecular orientation following *k*-shell excitation of co. *Phys. Rev. Lett.*, 56:1455–1458, Apr 1986. 1

[129] I. V. Litvinyuk, Kevin F. Lee, P. W. Dooley, D. M. Rayner, D. M. Villeneuve, and P. B. Corkum. Alignment-dependent strong field ionization of molecules. *Phys. Rev. Lett.*, 90:233003, Jun 2003. 1

[130] F. Heiser, O. Geßner, J. Viefhaus, K. Wieliczek, R. Hentges, and U. Becker. Demonstration of strong forward-backward asymmetry in the $c1s$ photoelectron angular distribution from oriented co molecules. *Phys. Rev. Lett.*, 79:2435–2437, Sep 1997. 1

[131] Hideki Ohmura, Naoaki Saito, and M. Tachiya. Selective ionization of oriented nonpolar molecules with asymmetric structure by phase-controlled two-color laser fields. *Phys. Rev. Lett.*, 96:173001, May 2006. 1

[132] L. Holmegaard et al. Photoelectron angular distributions from strong-field ionization of oriented molecules. *Nature Physics*, 6:428–432, 2010. 1

[133] Vinod Kumarappan, Lotte Holmegaard, Christian Martiny, Christian B. Madsen, Thomas K. Kjeldsen, Simon S. Viftrup, Lars Bojer Madsen, and Henrik Stapelfeldt. Multiphoton electron angular distributions from laser-aligned cs_2 molecules. *Phys. Rev. Lett.*, 100:093006, Mar 2008. 1

[134] E. Shigemasa, J. Adachi, M. Oura, and A. Yagishita. Angular distributions of $1s\sigma$ photoelectrons from fixed-in-space n_2 molecules. *Phys. Rev. Lett.*, 74:359–362, Jan 1995. 1

[135] Christer Z. Bisgaard, Owen J. Clarkin, Guorong Wu, Anthony M. D. Lee, Oliver Gener, Carl C. Hayden, and Albert Stolow. Time-resolved molecular frame dynamics of fixed-in-space cs2 molecules. *Science*, 323(5920):1464–1468, 2009. 1

[136] J. Itatani et al. Tomographic imaging of molecular orbitals. *Nature*, 432:867–871, 2004. 1

[137] Serguei Patchkovskii, Zengxiu Zhao, Thomas Brabec, and D. M. Villeneuve. High harmonic generation and molecular orbital tomography in multielectron systems: Beyond the single active electron approximation. *Phys. Rev. Lett.*, 97:123003, Sep 2006. 1

[138] M. Meckel, D. Comtois, D. Zeidler, A. Staudte, D. Pavičić, H. C. Bandulet, H. Pépin, J. C. Kieffer, R. Dörner, D. M. Villeneuve, and P. B. Corkum. Laser-induced electron tunneling and diffraction. *Science*, 320(5882):1478–1482, 2008. 1

[139] Hyotcherl Ihee, Vladimir A. Lobastov, Udo M. Gomez, Boyd M. Goodson, Ramesh Srinivasan, Chong-Yu Ruan, and Ahmed H. Zewail. Direct imaging of transient molecular structures with ultrafast diffraction. *Science*, 291(5503):458–462, 2001. 1

[140] André D. Bandrauk and Szczepan Chelkowski. Dynamic imaging of nuclear wave functions with ultrashort uv laser pulses. *Phys. Rev. Lett.*, 87:273004, Dec 2001. 1

[141] T. Zuo, A.D. Bandrauk, and P.B. Corkum. Laser-induced electron diffraction: a new tool for probing ultrafast molecular dynamics. *Chemical Physics Letters*, 259(34):313 – 320, 1996. 1

[142] S. N. Yurchenko, S. Patchkovskii, I. V. Litvinyuk, P. B. Corkum, and G. L. Yudin. Laser-induced interference, focusing, and diffraction of rescattering molecular photoelectrons. *Phys. Rev. Lett.*, 93:223003, Nov 2004. 1

[143] T. Remetter et al. Attosecond electron wave packet interferometry. *Nature Physics*, 2:323–326, 2006. 1

[144] Kenneth C. Kulander. Multiphoton ionization of hydrogen: A time-dependent theory. *Phys. Rev. A*, 35:445–447, Jan 1987. 1

[145] André D. Bandrauk, S. Chelkowski, and Isao Kawata. Molecular above-threshold-ionization spectra: The effect of moving nuclei. *Phys. Rev. A*, 67:013407, Jan 2003. 1

[146] M. Lein, E. K. U. Gross, and V. Engel. Intense-field double ionization of helium: Identifying the mechanism. *Phys. Rev. Lett.*, 85:4707–4710, Nov 2000. 1

[147] D. Bauer. Two-dimensional, two-electron model atom in a laser pulse: Exact treatment, single-active-electron analysis, time-dependent density-functional theory, classical calculations, and nonsequential ionization. *Phys. Rev. A*, 56:3028–3039, Oct 1997. 1

[148] Jonathan Parker, K T Taylor, Charles W Clark, and Sayoko Blodgett-Ford. Intense-field multiphoton ionization of a two-electron atom. *Journal of Physics B: Atomic, Molecular and Optical Physics*, 29(2):L33, 1996. 1

[149] J. D. D. Martin and J. W. Hepburn. Electric field induced dissociation of molecules in rydberg-like highly vibrationally excited ion-pair states. *Phys. Rev. Lett.*, 79:3154–3157, Oct 1997. 1

[150] Isao Kawata, Hirohiko Kono, Yuichi Fujimura, and André D. Bandrauk. Intense-laser-field-enhanced ionization of two-electron molecules: Role of ionic states as doorway states. *Phys. Rev. A*, 62:031401, Aug 2000. 1

[151] M. Born and J. R. Oppenheimer. On the quantum theory of molecules. *Ann. Physik*, 84(458):1–32, 1927. 1, 2.1.1, A

[152] P. Ehrenfest. Bemerkung ber die angenherte gltigkeit der klassischen mechanik innerhalb der quantenmechanik. *Zeitschrift für Physik*, 45(7-8):455–457, 1927. 1

[153] Graham A. Worth and Lorenz S. Cederbaum. Beyond born-oppenheimer: Molecular dynamics through a conical intersection. *Annual Review of Physical Chemistry*, 55(1):127–158, 2004. PMID: 15117250. 1

[154] Nikos L. Doltsinis and Dominik Marx. First pinciples molecular dynamics involving excited states and nonadiabatic transitions. *Journal of Theoretical and Computational Chemistry*, 01(02):319–349, 2002. 1

[155] L. V. Keldysh. Ionization in the field of a strong electromagnetic wave. *JETP*, 20(5):1307, 1965. 1

[156] P. Lambropoulos and G. M. Nikolopoulos. Multiple ionization under strong xuv to x-ray radiation. *Eur. Phys. J. Special Topics*, 222:2067, 2013. 1, 3.2.2.1, 3.2.2.1

[157] P. Lambropoulos. Mechanisms for multiple ionization of atoms by strong pulsed lasers. *Phys. Rev. Lett.*, 55:2141–2144, Nov 1985. 1

[158] K. Boyer and C. K. Rhodes. Atomic inner-shell excitation induced by coherent motion of outer-shell electrons. *Phys. Rev. Lett.*, 54:1490–1493, Apr 1985. 1

[159] Sydney Geltman. Multiple ionization of a hartree atom by intense laser pulses. *Phys. Rev. Lett.*, 54:1909–1912, Apr 1985. 1

[160] W. E. Cooke, T. F. Gallagher, S. A. Edelstein, and R. M. Hill. Doubly excited autoionizing rydberg states of sr. *Phys. Rev. Lett.*, 40:178–181, Jan 1978. 1

[161] W. E. Cooke and T. F. Gallagher. Observation of pair splittings in the autoionization spectrum of ba. *Phys. Rev. Lett.*, 41:1648–1652, Dec 1978. 1

[162] C. J. Joachain, N. J. Kylstra, and R. M. Potvliege. *Atoms in Intense Laser Fields*. Cambridge University Press, 2011. Cambridge Books Online. 1

[163] Ch. Spielmann, N. H. Burnett, S. Sartania, R. Koppitsch, M. Schnürer, C. Kan, M. Lenzner, P. Wobrauschek, and F. Krausz. Generation of coherent x-rays in the water window using 5-femtosecond laser pulses. *Science*, 278(5338):661–664, 1997. 1

[164] M. Schnürer, Ch. Spielmann, P. Wobrauschek, C. Streli, N. H. Burnett, C. Kan, K. Ferencz, R. Koppitsch, Z. Cheng, T. Brabec, and F. Krausz. Coherent 0.5-kev x-ray emission from helium driven by a sub-10-fs laser. *Phys. Rev. Lett.*, 80:3236–3239, Apr 1998. 1

[165] Kenneth C. Kulander. Time-dependent hartree-fock theory of multiphoton ionization: Helium. *Phys. Rev. A*, 36:2726–2738, Sep 1987. 1

[166] M. J. Nandor, M. A. Walker, L. D. Van Woerkom, and H. G. Muller. Detailed comparison of above-threshold-ionization spectra from accurate numerical integrations and high-resolution measurements. *Phys. Rev. A*, 60:R1771–R1774, Sep 1999. 1

[167] Armin Scrinzi, Michael Geissler, and Thomas Brabec. Ionization above the coulomb barrier. *Phys. Rev. Lett.*, 83:706–709, Jul 1999. 1

[168] M. Lezius, V. Blanchet, D. M. Rayner, D. M. Villeneuve, Albert Stolow, and Misha Yu. Ivanov. Nonadiabatic multielectron dynamics in strong field molecular ionization. *Phys. Rev. Lett.*, 86:51–54, Jan 2001. 1

[169] E. Runge and E. K. U. Gross. Density functional theory for time-dependent systems. *Phys. Rev. Lett*, 52:997, 1984. 1, 2.3.2

[170] C. A. Ullrich, U. J. Gossmann, and E. K. U. Gross. Time-dependent optimized effective potential. *Phys. Rev. Lett.*, 74:872–875, Feb 1995. 1

[171] Benjamin G. Levine, Chaehyuk Ko, Jason Quenneville, and Todd J. Martínez. Conical intersections and double excitations in time-dependent density functional theory. *Molecular Physics*, 104(5-7):1039–1051, 2006. 1

[172] T. Kreibich and E. K. U. Gross. Multicomponent density-functional theory for electrons and nuclei. *Phys. Rev. Lett.*, 86:2984–2987, Apr 2001. 1

[173] Benjamin Kaduk and Troy Van Voorhis. Communication: Conical intersections using constrained density functional theoryconfiguration interaction. *The Journal of Chemical Physics*, 133(6), 2010. 1

[174] P. Romaniello, D. Sangalli, J. A. Berger, F. Sottile, L. G. Molinari, L. Reining, and G. Onida. Double excitations in finite systems. *The Journal of Chemical Physics*, 130(4), 2009. 1

[175] Michael J. G. Peach, Peter Benfield, Trygve Helgaker, and David J. Tozer. Excitation energies in density functional theory: An evaluation and a diagnostic test. *The Journal of Chemical Physics*, 128(4), 2008. 1

[176] Andreas Dreuw, Jennifer L. Weisman, and Martin Head-Gordon. Long-range charge-transfer excited states in time-dependent density functional theory require non-local exchange. *The Journal of Chemical Physics*, 119(6):2943–2946, 2003. 1

[177] R. J. Magyar and S. Tretiak. Dependence of spurious charge-transfer excited states on orbital exchange in tddft: large molecules and clusters. *Journal of Chemical Theory and Computation*, 3(3):976–987, 2007. 1

[178] M. Petersilka and E. K. U. Gross. Strong-field double ionization of helium: A density-functional perspective. *Laser Physics*, 9(1):1–10, 1999. 1

[179] B. Walker, B. Sheehy, L. F. DiMauro, P. Agostini, K. J. Schafer, and K. C. Kulander. Precision measurement of strong field double ionization of helium. *Phys. Rev. Lett.*, 73:1227–1230, Aug 1994. 1

[180] Manfred Lein and Stephan Kümmel. Exact time-dependent exchange-correlation potentials for strong-field electron dynamics. *Phys. Rev. Lett.*, 94:143003, Apr 2005. 1

[181] F. Wilken and D. Bauer. Adiabatic approximation of the correlation function in the density-functional treatment of ionization processes. *Phys. Rev. Lett.*, 97:203001, Nov 2006. 1

[182] David J. Tozer and Nicholas C. Handy. Improving virtual kohnsham orbitals and eigenvalues: Application to excitation energies and static polarizabilities. *The Journal of Chemical Physics*, 109(23):10180–10189, 1998. 1

[183] Oleg A. Vydrov and Gustavo E. Scuseria. Assessment of a long-range corrected hybrid functional. *The Journal of Chemical Physics*, 125(23):–, 2006. 1

[184] G. Hunter. Conditional probability amplitudes in wave mechanics. *International Journal of Quantum Chemistry*, 9(2), 1975. 2.1.1

[185] Ali Abedi, Neepa T. Maitra, and E. K. U. Gross. Exact factorization of the time-dependent electron-nuclear wave function. *Phys. Rev. Lett.*, 105(123002):1–4, 2010. 2.1.1

[186] S. Takahashi and K. Takatsuka. On the validity range of the born-oppenheimer approximation: A semiclassical study for all particle quantization of three-body coulomb systems. *J. Chem. Phys.*, 124(144101):1–14, 2006. 2.2, 3.1.2.3, 3.1.2.4, A

[187] J. R. Hiskes. Dissociation of molecular ions by electric and magnetic fields. *Phys. Rev.*, 122(4):1207–1217, 1961. 2.2

[188] R. Loudon. One-dimensional hydrogen atom. *Am. J. Phys.*, 27:649–655, 1959. 2.2

[189] M. Lein, T. Kreibich, E. K. U. Gross, and V. Engel. Strong-field ionization dynamics of a model H_2 molecule. *Phys. Rev. A*, 65(033403):8, 2002. 2.2.1

[190] K. Yabana and G.F. Bertsch. Time-dependent local-density approximation in real time. *Phys. Rev. B*, 54(7):4484–4487, 1996. 2.2.5

[191] Alberto Castro, Miguel A L Marques, and Angel Rubio. Propagators for the time-dependent Kohn–Sham equations. *J Chem. Phys.*, 121(8):3425–3433, 2004. 2.2.5

[192] G. Onida, L. Reining, and A. Rubio. Electronic excitations: density-functional versus many-body green's-function approaches. *Rev. Mod. Phys.*, 74(2):601–659, 2002. 2.2.5

[193] P. Hohenberg and W. Kohn. Inhomogeneous electron gas. *Phys. Rev.*, 136(3B):B864–B871, 1964. 2.3.1

[194] W. Kohn and L. J. Sham. Self-consistent equations including exchange and correlation effects. *Physical Review*, 140:A4: A1133, 1965. 2.3.1

[195] J. P. Perdew and Y. Wang. Accurate and simple analytic representation of the electron-gas correlation energy. *Phys. Rev. B*, 45:13244, 1992. 2.3.1.1, 2.4.2

[196] X. Andrade and A. Aspuru-Guzik. Prediction of the derivative discontinuity in density functional theory from an electrostatic description of the exchange and correlation potential. *Phys. Rev. Lett.*, 107:183002, 2011. 2.3.1.1, 2.4.2

[197] J. P. Perdew, K. Burke and M. Ernzerhof. Generalised gradient approximation made simple. *Phys. Rev. Lett.*, 77:3865, 1996. 2.3.1.1, 2.4.2

[198] R. van Leeuwen and E. J. Baerends. Exchange-correlation potential with correct asymptotic behaviour. *Phys. Rev. A*, 49:2421, 1994. 2.3.1.1, 2.4.2

[199] M.A.L. Marques, N.T. Maitra, F.M.S. Nogueira, E.K.U. Gross, and A. Rubio, editors. *Fundamentals of Time-Dependent Density Functional Theory*, volume 837 of *Lecture Notes in Physics*. Springer, Berlin, 2012. 2.3.2

[200] P. Lambropoulos and K. G. Papamihail and P. Decleva. Theory of multiple ionization of xenon under strong xuv radiation and the role of the giant resonance. *J. Phys. B: At. Mol. Opt. Phys.*, 44:175402, 2011. 2.4, 3.2.2.1, 3.2.2.1

[201] G. M. Nikolopoulos and P. Lambropoulos. Multiple ionization of neon under soft x-rays: Theory vs experiment. *J. Phys. B: At. Mol. Opt. Phys.*, 47:115001, 2014. 2.4, 3.2.2.1, 3.2.2.1

[202] M. Ilchen and T. Mazza and E. T. Karamatskos and D. Markellos and S. Bakhtiarzadeh and A. J. Rafipoor and T. J. Kelly and N. Walsh and J. T. Costello and P. O'Keeffe and N. Gerken and M. Martins and P. Lambropoulos and M. Meyer. private communication to be published, 2014. 2.4, 3.2.2.2

[203] C.A. Ullrich. Time-dependent kohnsham approach to multiple ionization. *Journal of Molecular Structure: {THEOCHEM}*, 501502(0):315 – 325, 2000. 2.4, 2.4.6

[204] U. De Giovannini, D. Varsano, M. A. L. Marques, H. Appel, E. K. U. Gross, and A. Rubio. *Ab initio* angle- and energy-resolved photoelectron spectroscopy with time-dependent density-functional theory. *Phys. Rev. A*, 85:062515, Jun 2012. 2.4, 2.4.7

[205] U. De Giovannini, G. Brunetto, A. Castro, J. Walkenhorst, and A. Rubio. Simulating pump-probe photo-electron and absorption spectroscopy on the attosecond time-scale with time-dependent density-functional theory. *Chemphyschem*, 14:1363–1376, 2013. 2.4.1, 3.3.1, 3.3.2.1

[206] J P Perdew and Alex Zunger. Self-interaction correction to density-functional approximations for many-electron systems. *Phys Rev B*, 23(10):5048–5079, May 1981. 2.4.2

[207] C Legrand, E Suraud, and P G Reinhard. Comparison of self-interaction-corrections for metal clusters. *Journal of Physics B: Atomic, Molecular and Optical Physics*, 35(4):1115–1128, February 2002. 2.4.2

[208] Wang Zhi-Ping, Wang Jing, and Zhang Feng-Shou. Excitation and Ionization of Ethylene by Charged Projectiles. *Chinese Phys. Lett.*, 27(1):013101, January 2010. 2.4.2

[209] Z P Wang, P M Dinh, P G Reinhard, E Suraud, and F S Zhang. Nonadiabatic effects in the irradiation of ethylene. *Int. J. Quantum Chem.*, pages 480–486, 2011. 2.4.2

[210] Claude Leforestier and Robert E Wyatt. Optical potential for laser induced dissociation. *J. Chem. Phys.*, 78(5):2334–2344, 1983. 2.4.3

[211] R Kosloff and D Kosloff. Absorbing boundaries for wave propagation problems. *J. Comput. Phys.*, 63(2):363–376, 1986. 2.4.3

[212] Umberto De Giovannini, AskHjorth Larsen, and Angel Rubio. Modeling electron dynamics coupled to continuum states in finite volumes with absorbing boundaries. *The European Physical Journal B*, 88(3), 2015. 2.4.3

[213] A. Castro, M. A. L. Marques, H. Appel, M. Oliveira, C. A. Rozzi, X. Andrade, F. Lorenzen, E. K. U. Gross, and A. Rubio. Octopus: a tool for the application of time-dependent density functional theory. *Phys. Stat. Sol. B*, 243(11):2465–2488, 2006. 2.4.4, 3.1.1, 3.3.1

[214] X. Andrade, J. Alberdi-Rodriguez, D. A Strubbe, M.J T Oliveira, F. Nogueira, A. Castro, J. Muguerza, A. Arruabarrena, S.G Louie, A. Aspuru-Guzik, A. Rubio, and M.A.L. Marques. Time-dependent density-functional theory in massively parallel computer architectures: the octopus project. *J. Phys.: Condens. Matter*, 24(233202):12, 2012. 2.4.4, 3.1.1, 3.3.1

[215] M.A.L. Marques, A. Castro, G.F. Bertsch, and A. Rubio. Octopus: a first-principles tool for excited electron-ion dynamics. *Computer Physics Communications*, 151:60–78, 2003. 2.4.4, 3.1.1, 3.3.1

[216] N. Troullier and J. L. Martins. Efficient pseudopotentials for plane-wave calculations. *Phys. Rev. B*, 43:1993, 1991. 2.4.4

[217] M. Oliveira and F. Nogueira. Generating relativistic pseudo-potentials with explicit incorporation of semi-core states using ape, the atomic pseudo-potentials engine. *Comput. Phys. Commun.*, 178:524, 2008. 2.4.4

[218] D. R. Hamann, M. Schlter, and C. Chiang. Norm conserving pseudopotentials. *Phys. Rev. Lett.*, 43(20):1494, 1979. 2.4.4

[219] Hiromichi Niikura, F. Légaré, R. Hasbani, A. D. Bandrauk, Misha Yu. Ivanov, D. M. Villeneuve, and P. B. Corkum. Sub-laser-cycle electron pulses for probing molecular dynamics. *Nature*, 417:917–922, June 2002. 3.1, 3.1.2.1, 3.1.2.4

[220] L. J. Schaad and W. V. Hicks. Equilibrium bond length in H_2^+. *J. Chem. Phys.*, 53:851, 1970. 3.1.2.1

[221] H. F. Beyer and V. P. Shevelko. *Atomic physics with heavy ions*. Springer, 1999. 3.1.2.4

[222] P. Lambropoulos, G. M. Nikolopoulos, and K. G. Papamihail. Route to direct multiphoton multiple ionisation. *Phys. Rev. A*, 83:021407(R), 2011. 3.2.2.1, 3.2.2.1

[223] M A L Marques, N T Maitra, F Nogueira, E K U Gross, and Angel Rubio. *Fundamentals of Time-Dependent Density Functional Theory, Lecture Notes in Physics, Vol. 837*. Springer, 2011. 3.2.2.1

[224] J A R Samson and W C Stolte. Precision measurements of the total photoionization cross-sections of He, Ne, Ar, Kr, and Xe. *J. Electron Spectrosc.*, 123(2-3):265–276, 2002. 3.14, 3.2.2.1, 3.17

[225] Xiao-Min Tong and Shih-I Chu. Density-functional theory with optimized effective potential and self-interaction correction for ground states and autoionizing resonances. *Phys. Rev. A*, 55:3406–3416, May 1997. 3.2.2.1

[226] J. I. Fuks, N Helbig, I. V. Tokatly, and Angel Rubio. Nonlinear phenomena in time-dependent density-functional theory: What Rabi oscillations can teach us. *Phys. Rev. B*, 84(7):075107, 2011. 3.2.2.2

[227] J I Fuks, P Elliott, A Rubio, and N T Maitra. Dynamics of Charge-Transfer Processes with Time-Dependent Density Functional Theory. *J. Phys. Chem. Lett.*, 4(5):735–739, February 2013. 3.2.2.2

[228] P. Elliott, J. I. Fuks, A. Rubio, and N. T. Maitra. Universal Dynamical Steps in the Exact Time-Dependent Exchange-Correlation Potential. *Phys. Rev. Lett.*, 109:266404, 2012. 3.2.2.2

[229] D. W. Turner, C. Baker, A. D. Baker, , and C. R. Brundle, editors. *Molecular Photoelectron Spectroscopy*. Wiley, London, 1970. 3.3.2.1

[230] Norman C. Craig, Peter Groner, and Donald C. McKean. Equilibrium structures for butadiene and ethylene: Compelling evidence for pi-electron delocalization in butadiene. *J. Phys. Chem. A*, 110:7461–7469, 2006. 3.3.2.1

[231] P Puschnig, S Berkebile, A J Fleming, G Koller, K Emtsev, T Seyller, J D Riley, C Ambrosch-Draxl, F P Netzer, and M G Ramsey. Reconstruction of Molecular Orbital Densities from Photoemission Data. *Science*, 326(5953):702–706, October 2009. 3.3.2.1

[232] Thomas Kunert, Frank Grossmann, and Rüdiger Schmidt. Nonadiabatic dynamics of ethylene in femtosecond laser pulses. *Phys. Rev. A*, 72(2):023422, August 2005. 3.3.2.2

[233] B.H. Bransden and C. J. Joachain, editors. *Physics of atoms and molecules*. Addison-Wesley, 2003. A

APPENDIX A

Static accuracy of the Born-Oppenheimer approximation for the H_2^+ and H_2 molecules

The accuracy of the static Born-Oppenheimer approximation (BOA) calculations can be understood from a perturbation theory argument in terms of the small parameter $\kappa = (\frac{m_e}{m_I})^{\frac{1}{4}}$ [151, 186]. The ratio of vibrational to electronic energies, E_{vib} to E_{elec} depends on the electron-nuclear mass ratio m_e/M_p as [233]

$$\frac{E_{vib}}{E_{elec}} \approx \sqrt{\frac{m_e}{M}} \approx \frac{\delta^2}{a_0^2}, \tag{A.1}$$

where δ is the length scale of vibrational motion, and a_0 is the length scale of electronic motion, i.e., the Bohr radius. This means the ratio of nuclear to electronic motion is of the order $\delta/a_0 \approx (m_e/M)^{1/4}$. With this in mind, we may expand the Hamiltonian in Eq. 2.24 for the neutral H_2 molecule as a function of the small parameter κ to third order as follows

$$\begin{aligned}\hat{H}(X_{eq}+\kappa\zeta, x, \xi) \approx & -\frac{\partial^2}{\partial x^2} - \frac{1+M}{4M}\frac{\partial^2}{\partial \xi^2} + V(X_{eq}, x, \xi) \\ & + \kappa \frac{\partial}{\partial X} V(X, x, \xi)\Big|_{X=X_{eq}} \zeta \\ & - \kappa^2 \frac{\partial^2}{\partial \zeta^2} + \frac{1}{2!}\kappa^2 \frac{\partial^2}{\partial X^2} V(X, x, \xi)\Big|_{X=X_{eq}} \zeta^2 \\ & + \frac{1}{3!}\kappa^3 \frac{\partial^3}{\partial X^3} V(X, x, \xi)\Big|_{X=X_{eq}} \zeta^3 + \mathrm{O}(\kappa^4),\end{aligned} \tag{A.2}$$

where we have used $X = X_{eq}+\kappa\zeta$ and the potential V contains the last six terms in Eq. 2.24. Here μ_e and μ_{ep} are given in Eqs. B.29 and B.39, respectively.

Sorting the Hamiltonian in different powers of κ, i.e.,

$$\hat{H}(X_{eq}+\kappa\zeta, x, \xi) \approx \hat{H}^{(0)} + \kappa\hat{H}^{(1)} + \kappa^2\hat{H}^{(2)} + \kappa^3\hat{H}^{(3)}, \tag{A.3}$$

we obtain

$$\begin{aligned}
\hat{H}^{(0)} &= -\frac{1}{2\widetilde{\mu}_e}\frac{\partial^2}{\partial x^2} - \frac{1}{2\mu_{ep}}\frac{\partial^2}{\partial \xi^2} + V(X_{eq}, x, \xi),\\
\hat{H}^{(1)} &= \frac{\partial}{\partial X}V(X, x, \xi)\Big|_{X=X_{eq}}\zeta,\\
\hat{H}^{(2)} &= -\frac{\partial^2}{\partial \zeta^2} + \frac{1}{2!}\frac{\partial^2}{\partial X^2}V(X, x, \xi)\Big|_{X=X_{eq}}\zeta^2,\\
\hat{H}^{(3)} &= \frac{1}{3!}\frac{\partial^3}{\partial X^3}V(X, x, \xi)\Big|_{X=X_{eq}}\zeta^3.
\end{aligned} \tag{A.4}$$

Expanding the time-independent Schrödinger Eq. 2.9 in powers of κ to the third order, we obtain

$$\sum_{n=0}^{3}(\kappa^n\hat{H}^{(n)})[\kappa^n\psi^{(n)}] = \sum_{n=0}^{3}(\kappa^n\varepsilon^{(n)})[\kappa^n\psi^{(n)}]. \tag{A.5}$$

Decomposing Eq. A.5 in terms of κ, we find

$$\mathrm{O}(\kappa^0): \quad \hat{H}^{(0)}|\psi^{(0)}\rangle = \varepsilon^{(0)}|\psi^{(0)}\rangle, \tag{A.6}$$

$$\mathrm{O}(\kappa^1): \quad \hat{H}^{(0)}|\psi^{(1)}\rangle + \hat{H}^{(1)}|\psi^{(0)}\rangle = \varepsilon^{(0)}|\psi^{(1)}\rangle + \varepsilon^{(1)}|\psi^{(0)}\rangle, \tag{A.7}$$

$$\begin{aligned}\mathrm{O}(\kappa^2): \quad & \hat{H}^{(0)}|\psi^{(2)}\rangle + \hat{H}^{(1)}|\psi^{(1)}\rangle + \hat{H}^{(2)}|\psi^{(0)}\rangle\\ & = \varepsilon^{(0)}|\psi^{(2)}\rangle + \varepsilon^{(1)}|\psi^{(1)}\rangle + \varepsilon^{(2)}|\psi^{(0)}\rangle,\end{aligned} \tag{A.8}$$

$$\begin{aligned}\mathrm{O}(\kappa^3): \quad & \hat{H}^{(0)}|\psi^{(3)}\rangle + \hat{H}^{(1)}|\psi^{(2)}\rangle + \hat{H}^{(2)}|\psi^{(1)}\rangle + \hat{H}^{(3)}|\psi^{(0)}\rangle\\ & = \varepsilon^{(0)}|\psi^{(3)}\rangle + \varepsilon^{(1)}|\psi^{(2)}\rangle + \varepsilon^{(2)}|\psi^{(1)}\rangle + \varepsilon^{(3)}|\psi^{(0)}\rangle.\end{aligned} \tag{A.9}$$

$\hat{H}^{(0)}$ is the electronic frozen nuclear Hamiltonian at X_{eq} and $\varepsilon^{(0)}$ is the zeroth-order eigenvalue which corresponds to the electronic motion. Therefore, we choose the zeroth-order wavefunction as

$$\psi^{(0)}(X_{eq}, \xi, \zeta) = \chi(\zeta)\varphi^{(0)}(X_{eq}, \xi), \tag{A.10}$$

where $\varphi^{(0)}$ is the electronic eigenstate of $\hat{H}^{(0)}$ and $\chi(\zeta)$ is the nuclear wavefunction which will be specified later.

Based on Eqs. A.7, A.10 and the Hellmann-Feynman theorem (see Appendix D), $\varepsilon^{(1)}$ vanishes. This is because the first derivative with respect to the eigenvalue $\varepsilon^{(0)}$ at X_{eq} is zero. More explicitly,

$$\begin{aligned}
\varepsilon^{(1)} &= \langle\psi^{(0)}|\hat{H}^{(1)}|\psi^{(0)}\rangle\\
&= \left\langle\varphi^{(0)}\left|\frac{\partial}{\partial X}\hat{H}^{(0)}(X)\Big|_{X=X_{eq}}\right|\varphi^{(0)}\right\rangle\langle\chi\,|\zeta|\,\chi\rangle\\
&= \frac{\partial}{\partial X}\varepsilon^{(0)}(X)\Big|_{X=X_{eq}}\langle\chi|\zeta|\chi\rangle = 0.
\end{aligned} \tag{A.11}$$

From Eq. A.8 we obtain the second-order correction to the energy

$$\begin{aligned}\varepsilon^{(2)} =& \langle\psi^{(0)}|\hat{H}^{(2)}|\psi^{(0)}\rangle + \langle\psi^{(0)}|\hat{H}^{(1)}|\psi^{(1)}\rangle \\ =& \left\langle\chi\left|-\frac{\partial^2}{\partial\zeta^2}\right|\chi\right\rangle \\ &+ \left\langle\varphi^{(0)}\left|\frac{1}{2!}\,\frac{\partial^2}{\partial X^2}V(X,x,\xi)\Big|_{X=X_{eq}}\right|\varphi^{(0)}\right\rangle\left\langle\chi\left|\zeta^2\right|\chi\right\rangle \\ &- \sum_{n>0}\frac{\left|\left\langle\varphi_n^{(0)}\left|\frac{\partial}{\partial X}V(X,x,\xi)\right|_{X=X_{eq}}\right|\varphi_0^{(0)}\right\rangle\right|^2}{\varepsilon_n^{(0)}-\varepsilon_0^{(0)}}\langle\chi|\zeta^2|\chi\rangle,\end{aligned} \tag{A.12}$$

where the first order correction to the wavefunction is obtained from Eqs. A.7 and A.10

$$\begin{aligned}|\psi^{(1)}\rangle =& -\sum_{n>0}\frac{\left\langle\psi_n^{(0)}\left|\hat{H}^{(1)}\left|\psi_0^{(0)}\right\rangle\right|\psi_n^{(0)}\right\rangle}{\varepsilon_n^{(0)}-\varepsilon_0^{(0)}} \\ =& -\sum_{n>0}\frac{\left\langle\psi_n^{(0)}\left|\frac{\partial}{\partial X}V(X,x,\xi)\right|_{X=X_{eq}}\right|\varphi^{(0)}\right\rangle|\psi_n^{(0)}\rangle}{\varepsilon_n^{(0)}-\varepsilon_0^{(0)}}\zeta|\chi\rangle.\end{aligned} \tag{A.13}$$

Here $\varepsilon_n^{(0)}$ and $|\psi_n^{(0)}\rangle$ are the n^{th} electronic eigenvalue and eigenstate of the Hamiltonian $\hat{H}^{(0)}$.

We now choose $\chi(\zeta)$ (see Eq. A.10) to be the lowest eigenfunction of the harmonic oscillator problem. We can then express $\varepsilon^{(2)}$ in the form

$$\varepsilon^{(2)} = \left\langle\chi\left|-\frac{\partial^2}{\partial\zeta^2}\right|\chi\right\rangle + \frac{1}{2!}k_1\left\langle\chi\left|\zeta^2\right|\chi\right\rangle = \frac{1}{2}\omega_I, \tag{A.14}$$

where

$$\begin{aligned}k_1 =& \left\langle\varphi^{(0)}\left|\frac{\partial^2}{\partial X^2}V(X,x,\xi)\Big|_{X=X_{eq}}\right|\varphi^{(0)}\right\rangle \\ &- 2\sum_{n>0}\frac{\left|\left\langle\varphi_n^{(0)}\left|\frac{\partial}{\partial X}V(X,x,\xi)\right|_{X=X_{eq}}\right|\varphi_0^{(0)}\right\rangle\right|^2}{\varepsilon_n^{(0)}-\varepsilon_0^{(0)}},\end{aligned} \tag{A.15}$$

is the harmonic oscillator constant. Second order corrections to the energy thus correspond to the nuclear vibrations.

Finally, from Eqs. A.9, A.10 and A.13 we obtain for the third-order correction to the energy

$$\begin{aligned}\varepsilon^{(3)} =&\langle\psi^{(0)}|\hat{H}^{(1)}|\psi^{(2)}\rangle + \langle\psi^{(0)}|\hat{H}^{(2)}|\psi^{(1)}\rangle + \langle\psi^{(0)}|\hat{H}^{(3)}|\psi^{(0)}\rangle \\ =&\left\langle\varphi^{(0)}\left|\frac{\partial}{\partial X}V(X,x,\xi)\right|_{X=X_{eq}}\right|\varphi^{(2)}\right\rangle\langle\chi|\zeta^2|\chi\rangle \\ &+\left\langle\chi\left|-\frac{\partial^2}{\partial\zeta^2}\right|\chi\right\rangle \\ &+\left\langle\varphi^{(0)}\left|\frac{1}{2!}\frac{\partial^2}{\partial X^2}V(X,x,\xi)\right|_{X=X_{eq}}\right|\varphi^{(1)}\right\rangle\langle\chi|\zeta^2|\chi\rangle \\ &+\left\langle\varphi^{(0)}\left|\frac{1}{3!}\frac{\partial^3}{\partial X^3}V(X,x,\xi)\right|_{X=X_{eq}}\right|\varphi^{(0)}\right\rangle\langle\chi|\zeta^3|\chi\rangle,\end{aligned} \tag{A.16}$$

where the second-order correction to the wavefunction is from Eqs. A.8, and A.13

$$\begin{aligned}|\psi_0^{(2)}\rangle = &\sum_{n>0}\left(\frac{\left\langle\psi_n^{(0)}\left|\hat{H}^{(1)}\right|\psi_0^{(0)}\right\rangle}{\varepsilon_n^{(0)}-\varepsilon_0^{(0)}}\right)^2|\psi_n^{(0)}\rangle|\psi_n^{(0)}\rangle \\ &+\sum_{n>0}\frac{\left\langle\psi_n^{(0)}\left|\varepsilon^{(2)}-\hat{H}^{(2)}\right|\psi_0^{(0)}\right\rangle}{\varepsilon_n^{(0)}-\varepsilon_0^{(0)}}|\psi_n^{(0)}\rangle|\psi_0^{(0)}\rangle.\end{aligned} \tag{A.17}$$

All the terms from Eq. A.16 using Eqs. A.13 and A.17 vanish by parity. This is because they are all proportional to $\langle\psi^{(0)}|\hat{H}^{(3)}|\psi^{(0)}\rangle$ which is zero by parity since $\hat{H}^{(3)}$ is odd in ζ and $\psi^{(0)}$ is even in ζ. For this reason $\varepsilon^{(3)} = 0$.

Therefore the total energy in 1-D is given by

$$\varepsilon^{BOA} = \varepsilon^{(0)} + \varepsilon^{(2)}(\kappa^2) + O(\kappa^4), \tag{A.18}$$

i.e., the BOA energy expression gives the correct total ground state energy of the full electron-nuclear problem up to the fourth order in κ, as shown in Fig. 3.6.

For the H_2^+ homonuclear diatomic molecule we follow the same procedure as above using Eq. 2.23, so that expanded in terms of κ gives the Hamiltonian

$$\begin{aligned}\hat{H}(X_{eq}+\kappa\zeta,\tilde{\xi}) \approx & -\frac{1}{2\mu_e}\frac{\partial^2}{\partial\tilde{\xi}^2} + V(X_{eq},\tilde{\xi}) \\ & + \kappa\,\frac{\partial}{\partial X}V(X,\tilde{\xi})\Big|_{X=X_{eq}}\zeta \\ & - \kappa^2\frac{\partial^2}{\partial\zeta^2} + \frac{1}{2!}\kappa^2\,\frac{\partial^2}{\partial X^2}V(X,\tilde{\xi})\Big|_{X=X_{eq}}\zeta^2 \\ & + \frac{1}{3!}\kappa^3\,\frac{\partial^3}{\partial X^3}V(X,\tilde{\xi})\Big|_{X=X_{eq}}\zeta^3 + \mathrm{O}(\kappa^4),\end{aligned} \tag{A.19}$$

where μ_e is given in Eq. B.16.

Again, after including zero-point energy corrections, the error in the BOA ground state energy is $\mathrm{O}(\kappa^4) \sim m_e/M$, as shown in Fig. 3.6.

APPENDIX B

Centre of mass transformation for the H_2^+ and H_2 molecules

B.1. The H_2^+ molecule

1st step: Partial centre-of-mass transformation for the protons (*x* fixed)

We define the following partially transformed coordinates from the two coordinates X_1 and X_2 and their time-derivatives

$$X_{\mathrm{CM}(1)} = \frac{X_1 + X_2}{2} \quad \Rightarrow \quad V_{\mathrm{CM}(1)} = \frac{V_1 + V_2}{2}, \tag{B.1}$$

$$X = X_2 - X_1 \quad \Rightarrow \quad V = V_2 - V_1, \tag{B.2}$$

$$\tilde{x} = \tilde{x} \quad \Rightarrow \quad \tilde{v} = \tilde{v}, \tag{B.3}$$

where $X_{\mathrm{CM}(1)}$ is the centre of mass coordinate of the protons and X is the distance between the protons. Here, the velocities in each case correspond to the time derivatives of the corresponding positions.

In matrix form this partial transformation reads

$$\begin{pmatrix} X_{\mathrm{CM}(1)} \\ X \\ \tilde{x} \end{pmatrix} = A_1 \begin{pmatrix} X_1 \\ X_2 \\ \tilde{x} \end{pmatrix} = \begin{pmatrix} \frac{1}{2} & \frac{1}{2} & 0 \\ -1 & 1 & 0 \\ 0 & 0 & 1 \end{pmatrix} \begin{pmatrix} X_1 \\ X_2 \\ \tilde{x} \end{pmatrix}. \tag{B.4}$$

The inverse transformation is

$$\begin{pmatrix} X_1 \\ X_2 \\ \tilde{x} \end{pmatrix} = A_1^{-1} \begin{pmatrix} X_{\mathrm{CM}(1)} \\ X \\ \tilde{x} \end{pmatrix} = \begin{pmatrix} 1 & -\frac{1}{2} & 0 \\ 1 & \frac{1}{2} & 0 \\ 0 & 0 & 1 \end{pmatrix} \begin{pmatrix} X_{\mathrm{CM}(1)} \\ X \\ \tilde{x} \end{pmatrix}, \tag{B.5}$$

so that $A_1 A_1^{-1} = A_1^{-1} A_1 = \mathbb{1}$.

By substituting Eqs. B.5 in Eq. 2.21 we obtain

$$\begin{aligned} E = & \frac{1}{2} 2 M V_{\mathrm{CM}(1)}^2 + \frac{1}{2} \mu_p V^2 + \frac{1}{2} \tilde{v}^2 - \frac{1}{\sqrt{\left(\tilde{x} - X_{\mathrm{CM}(1)} + \frac{X}{2}\right)^2 + \Delta_{Ie}^2}} \\ & - \frac{1}{\sqrt{\left(X_{\mathrm{CM}(1)} + \frac{X}{2} - \tilde{x}\right)^2 + \Delta_{Ie}^2}} + \frac{1}{\sqrt{X^2 + \Delta_{II}^2}}, \end{aligned} \tag{B.6}$$

where the reduced mass of the two protons is

$$\mu_p = \frac{M}{2}. \tag{B.7}$$

2nd step: Centre-of-mass transformation for the electron (X fixed)

We define the following transformed coordinates from the two previous coordinates $X_{\mathrm{CM}(1)}$ and $\tilde{x}$ and their time-derivatives

$$\tilde{X}_{\mathrm{CM}(2)} = \frac{2MX_{\mathrm{CM}(1)} + \tilde{x}}{2M+1} \quad \Rightarrow \quad \tilde{V}_{\mathrm{CM}(2)} = \frac{2MV_{\mathrm{CM}(1)} + \tilde{v}}{2M+1}, \tag{B.8}$$

$$X = X \quad \Rightarrow \quad V = V, \tag{B.9}$$

$$\tilde{\xi} = \tilde{x} - X_{\mathrm{CM}(1)} \quad \Rightarrow \quad V_{\tilde{\xi}} = \tilde{v} - V_{\mathrm{CM}(1)}, \tag{B.10}$$

where $\tilde{X}_{\mathrm{CM}(2)}$ is the global centre of mass coordinate and $\tilde{\xi}$ is the distance between $X_{\mathrm{CM}(1)}$ and the electron. The internal degrees of freedom coordinates are X and $\tilde{\xi}$. Here, the velocities in each case correspond to the time derivatives of the corresponding positions.

In matrix form this transformation reads

$$\begin{pmatrix} \tilde{X}_{\mathrm{CM}(2)} \\ X \\ \tilde{\xi} \end{pmatrix} = A_2 \begin{pmatrix} X_{\mathrm{CM}(1)} \\ X \\ \tilde{x} \end{pmatrix} = \begin{pmatrix} \frac{2M}{2M+1} & 0 & \frac{1}{2M+1} \\ 0 & 1 & 0 \\ -1 & 0 & 1 \end{pmatrix} \begin{pmatrix} X_{\mathrm{CM}(1)} \\ X \\ \tilde{x} \end{pmatrix}. \tag{B.11}$$

The inverse transformation is

$$\begin{pmatrix} X_{\mathrm{CM}(1)} \\ X \\ \tilde{x} \end{pmatrix} = A_2^{-1} \begin{pmatrix} \tilde{X}_{\mathrm{CM}(2)} \\ X \\ \tilde{\xi} \end{pmatrix} = \begin{pmatrix} 1 & 0 & -\frac{1}{2M+1} \\ 0 & 1 & 0 \\ 1 & 0 & \frac{2M}{2M+1} \end{pmatrix} \begin{pmatrix} \tilde{X}_{\mathrm{CM}(2)} \\ X \\ \tilde{\xi} \end{pmatrix}, \tag{B.12}$$

so that $A_2 A_2^{-2} = A_2^{-2} A_2 = \mathbb{1}$.

The final two-step transformation is given by

$$\begin{aligned} \begin{pmatrix} \tilde{X}_{\mathrm{CM}(2)} \\ X \\ \tilde{\xi} \end{pmatrix} &= A_2 A_1 \begin{pmatrix} X_1 \\ X_2 \\ \tilde{x} \end{pmatrix} \\ &= \begin{pmatrix} \frac{2M}{2M+1} & 0 & \frac{1}{2M+1} \\ 0 & 1 & 0 \\ -1 & 0 & 1 \end{pmatrix} \begin{pmatrix} \frac{1}{2} & \frac{1}{2} & 0 \\ -1 & 1 & 0 \\ 0 & 0 & 1 \end{pmatrix} \begin{pmatrix} X_1 \\ X_2 \\ \tilde{x} \end{pmatrix} \\ &= \begin{pmatrix} \frac{M}{2M+1} & \frac{M}{2M+1} & \frac{1}{2M+1} \\ -1 & 1 & 0 \\ -\frac{1}{2} & -\frac{1}{2} & 1 \end{pmatrix} \begin{pmatrix} X_1 \\ X_2 \\ \tilde{x} \end{pmatrix}. \end{aligned} \tag{B.13}$$

The two-step inverse transformation of Eq. B.13 is given by

$$\begin{aligned}\begin{pmatrix} X_1 \\ X_2 \\ \tilde{x} \end{pmatrix} &= A_1^{-1}A_2^{-1}\begin{pmatrix} \tilde{X}_{\mathrm{CM}(2)} \\ X \\ \tilde{\xi} \end{pmatrix} \\ &= \begin{pmatrix} 1 & -\frac{1}{2} & 0 \\ 1 & \frac{1}{2} & 0 \\ 0 & 0 & 1 \end{pmatrix}\begin{pmatrix} 1 & 0 & -\frac{1}{2M+1} \\ 0 & 1 & 0 \\ 1 & 0 & \frac{2M}{2M+1} \end{pmatrix}\begin{pmatrix} \tilde{X}_{\mathrm{CM}(2)} \\ X \\ \tilde{\xi} \end{pmatrix} \\ &= \begin{pmatrix} 1 & -\frac{1}{2} & -\frac{1}{2M+1} \\ 1 & \frac{1}{2} & -\frac{1}{2M+1} \\ 1 & 0 & \frac{2M}{2M+1} \end{pmatrix}\begin{pmatrix} \tilde{X}_{\mathrm{CM}(2)} \\ X \\ \tilde{\xi} \end{pmatrix},\end{aligned} \tag{B.14}$$

so that $A_2A_1A_1^{-1}A_2^{-2} = A_1^{-1}A_2^{-2}A_2A_1 = \mathbb{1}$.

By substituting Eqs. B.12 in Eq. B.6 we finally obtain

$$\begin{aligned}E =& \frac{1}{2}(2M+1)\tilde{V}^2_{\mathrm{CM}(2)} + \frac{1}{2}\mu_p V^2 + \frac{1}{2}\tilde{\mu}_e V^2_{\tilde{\xi}} \\ &- \frac{1}{\sqrt{\left(\frac{X}{2}+\tilde{\xi}\right)^2 + \Delta^2_{Ie}}} - \frac{1}{\sqrt{\left(\frac{X}{2}-\tilde{\xi}\right)^2 + \Delta^2_{Ie}}} + \frac{1}{\sqrt{X^2+\Delta^2_{II}}},\end{aligned} \tag{B.15}$$

where the reduced mass of the two protons and the electron system is

$$\tilde{\mu}_e = \frac{2M}{2M+1}. \tag{B.16}$$

If we rewrite Eq. B.15 in terms of the classical momenta given by

$$P_{\tilde{X}_{\mathrm{CM}(2)}} = (2M+1)\tilde{V}_{\mathrm{CM}(2)}; P_X = \mu_p V; P_{\tilde{\xi}} = \tilde{\mu}_e V_{\tilde{\xi}}, \tag{B.17}$$

we obtain the following energy

$$\begin{aligned}E =& \frac{1}{2}\frac{P^2{}_{\tilde{X}_{\mathrm{CM}(2)}}}{2M+1} + \frac{1}{2}\frac{P_X^2}{\mu_p} + \frac{1}{2}\frac{P^2_{\tilde{\xi}}}{\tilde{\mu}_e} \\ &- \frac{1}{\sqrt{\left(\frac{X}{2}+\tilde{\xi}\right)^2 + \Delta^2_{Ie}}} - \frac{1}{\sqrt{\left(\frac{X}{2}-\tilde{\xi}\right)^2 + \Delta^2_{Ie}}} + \frac{1}{\sqrt{X^2+\Delta^2_{II}}}.\end{aligned} \tag{B.18}$$

The quantum momentum operators in 1-D are canonically defined as

$$\hat{P}_{\tilde{X}_{\mathrm{CM}(2)}} = -i\frac{\partial}{\partial \tilde{X}_{\mathrm{CM}(2)}}, \hat{P}_X = -i\frac{\partial}{\partial X}, \hat{P}_{\tilde{\xi}} = -i\frac{\partial}{\partial \tilde{\xi}}, \tag{B.19}$$

which are then substituted in Eq. B.18 instead of the correspondent classical momenta to obtain the following Hamiltonian

$$\begin{aligned}\hat{H} =& -\frac{1}{2(2M+1)}\frac{\partial^2}{\partial\tilde{X}^2_{\mathrm{CM}(2)}} - \frac{1}{2\mu_p}\frac{\partial^2}{\partial X^2} - \frac{1}{2\tilde{\mu}_e}\frac{\partial^2}{\partial\tilde{\xi}^2} \\ & - \frac{1}{\sqrt{\left(\frac{X}{2}+\tilde{\xi}\right)^2+\Delta^2_{Ie}}} - \frac{1}{\sqrt{\left(\frac{X}{2}-\tilde{\xi}\right)^2+\Delta^2_{Ie}}} + \frac{1}{\sqrt{X^2+\Delta^2_{II}}} \\ =& -\frac{1}{4M+2}\frac{\partial^2}{\partial\tilde{X}^2_{\mathrm{CM}(2)}} + \hat{H}_{int}(X,\tilde{\xi}),\end{aligned} \tag{B.20}$$

where $\hat{H}_{int}(X,\tilde{\xi})$ is the internal Hamiltonian, which depends only on the internal coordinates X and $\tilde{\xi}$

$$\begin{aligned}\hat{H}_{int}(X,\tilde{\xi}) =& -\frac{1}{2\mu_p}\frac{\partial^2}{\partial X^2} - \frac{1}{2\tilde{\mu}_e}\frac{\partial^2}{\partial\tilde{\xi}^2} \\ & - \frac{1}{\sqrt{\left(\frac{X}{2}+\tilde{\xi}\right)^2+\Delta^2_{Ie}}} - \frac{1}{\sqrt{\left(\frac{X}{2}-\tilde{\xi}\right)^2+\Delta^2_{Ie}}} + \frac{1}{\sqrt{X^2+\Delta^2_{II}}}.\end{aligned} \tag{B.21}$$

B.2. The H_2 molecule

1st step: Partial centre-of-mass transformation for the protons and the electrons

We define the following partially transformed coordinates from the four coordinates X_1, x_1, x_2, X_2 and their time-derivatives

$$X_{\mathrm{CM}(1)} = \frac{X_1+X_2}{2} \quad\Rightarrow\quad V_{\mathrm{CM}(1)} = \frac{V_1+V_2}{2}, \tag{B.22}$$

$$x_{\mathrm{CM}(1)} = \frac{x_1+x_2}{2} \quad\Rightarrow\quad v_{\mathrm{CM}(1)} = \frac{v_1+v_2}{2}, \tag{B.23}$$

$$X = X_2 - X_1 \quad\Rightarrow\quad V = V_2 - V_1, \tag{B.24}$$

$$x = x_2 - x_1 \quad\Rightarrow\quad v = v_2 - v_1, \tag{B.25}$$

where $X_{\mathrm{CM}(1)}$ is the centre of mass coordinate of the protons, $x_{\mathrm{CM}(1)}$ is the centre of mass coordinate of the electrons, X is the distance between the protons and x is the distance between the electrons. Here, the velocities in each case correspond to the time derivatives of the corresponding positions.

In matrix form this partial transformation reads

$$\begin{pmatrix} X_{\mathrm{CM}(1)} \\ X \\ x \\ x_{\mathrm{CM}(1)} \end{pmatrix} = B_1 \begin{pmatrix} X_1 \\ X_2 \\ x_1 \\ x_2 \end{pmatrix} = \begin{pmatrix} \frac{1}{2} & \frac{1}{2} & 0 & 0 \\ -1 & 1 & 0 & 0 \\ 0 & 0 & -1 & 1 \\ 0 & 0 & \frac{1}{2} & \frac{1}{2} \end{pmatrix} \begin{pmatrix} X_1 \\ X_2 \\ x_1 \\ x_2 \end{pmatrix}. \tag{B.26}$$

The inverse transformation is

$$\begin{pmatrix} X_1 \\ X_2 \\ x_1 \\ x_2 \end{pmatrix} = B_1^{-1} \begin{pmatrix} X_{\mathrm{CM}(1)} \\ X \\ x \\ x_{\mathrm{CM}(1)} \end{pmatrix} = \begin{pmatrix} 1 & -\frac{1}{2} & 0 & 0 \\ 1 & \frac{1}{2} & 0 & 0 \\ 0 & 0 & -\frac{1}{2} & 1 \\ 0 & 0 & \frac{1}{2} & 1 \end{pmatrix} \begin{pmatrix} X_{\mathrm{CM}(1)} \\ X \\ x \\ x_{\mathrm{CM}(1)} \end{pmatrix}, \tag{B.27}$$

so that $B_1 B_1^{-1} = B_1^{-1} B_1 = \mathbb{1}$.

By substituting Eqs. B.27 into Eq. 2.22 one obtains

$$\begin{aligned} E =& \frac{1}{2} 2M V_{\mathrm{CM}(1)}^2 + \frac{1}{2}\mu_p V^2 + \frac{1}{2} 2 v_{\mathrm{CM}(1)}^2 + \frac{1}{2}\mu_e v^2 \\ & - \frac{1}{\sqrt{\left(x_{\mathrm{CM}(1)} - \frac{x}{2} - X_{\mathrm{CM}(1)} + \frac{X}{2}\right)^2 + \Delta_{Ie}^2}} \\ & - \frac{1}{\sqrt{\left(X_{\mathrm{CM}(1)} + \frac{X}{2} - x_{\mathrm{CM}(1)} - \frac{x}{2}\right)^2 + \Delta_{Ie}^2}} \\ & - \frac{1}{\sqrt{\left(x_{\mathrm{CM}(1)} + \frac{x}{2} - X_{\mathrm{CM}(1)} + \frac{X}{2}\right)^2 + \Delta_{Ie}^2}} \\ & - \frac{1}{\sqrt{\left(X_{\mathrm{CM}(1)} + \frac{X}{2} - x_{\mathrm{CM}(1)} + \frac{x}{2}\right)^2 + \Delta_{Ie}^2}} \\ & + \frac{1}{\sqrt{X^2 + \Delta_{II}^2}} + \frac{1}{\sqrt{x^2 + \Delta_{ee}^2}}, \end{aligned} \tag{B.28}$$

where μ_p was defined in Eq. B.7 and the reduced mass of the two electrons is

$$\mu_e = \frac{1}{2}. \tag{B.29}$$

2nd step: Global centre-of-mass transformation for the molecule (X and x fixed)

We define the following transformed coordinates from the four previous coordinates $X_{\mathrm{CM}(1)}$, $x_{\mathrm{CM}(1)}$, X, x and their time-derivatives

$$X_{\mathrm{CM}(2)} = \frac{2MX_{\mathrm{CM}(1)} + 2x_{\mathrm{CM}(1)}}{2M+2} \quad \Rightarrow \quad V_{\mathrm{CM}(2)} = \frac{2MV_{\mathrm{CM}(1)} + 2v_{\mathrm{CM}(1)}}{2M+2}, \tag{B.30}$$

$$X = X \quad \Rightarrow \quad V = V, \tag{B.31}$$

$$x = x \quad \Rightarrow \quad v = v, \tag{B.32}$$

$$\xi = x_{\mathrm{CM}(1)} - X_{\mathrm{CM}(1)} \quad \Rightarrow \quad V_\xi = v_{\mathrm{CM}(1)} - V_{\mathrm{CM}(1)}, \tag{B.33}$$

where $X_{\mathrm{CM}(2)}$ is the global centre of mass coordinate and ξ is the distance between $x_{\mathrm{CM}(1)}$ and $X_{\mathrm{CM}(1)}$. The internal degrees of freedom coordinates are X, x and ξ. Here, the velocities in each case correspond to the time derivatives of the corresponding positions.

In matrix form this transformation reads

$$\begin{aligned}\begin{pmatrix} X_{\mathrm{CM}(2)} \\ X \\ x \\ \xi \end{pmatrix} &= B_2 \begin{pmatrix} X_{\mathrm{CM}(1)} \\ X \\ x \\ x_{\mathrm{CM}(1)} \end{pmatrix} \\ &= \begin{pmatrix} \frac{2M}{2M+2} & 0 & 0 & \frac{2}{2M+2} \\ 0 & 1 & 0 & 0 \\ 0 & 0 & 1 & 0 \\ -1 & 0 & 0 & 1 \end{pmatrix} \begin{pmatrix} X_{\mathrm{CM}(1)} \\ X \\ x \\ x_{\mathrm{CM}(1)} \end{pmatrix}.\end{aligned} \tag{B.34}$$

The inverse transformation is

$$\begin{aligned}\begin{pmatrix} X_{\mathrm{CM}(1)} \\ X \\ x \\ x_{\mathrm{CM}(1)} \end{pmatrix} &= B_2^{-1} \begin{pmatrix} X_{\mathrm{CM}(2)} \\ X \\ x \\ \xi \end{pmatrix} \\ &= \begin{pmatrix} 1 & 0 & 0 & -\frac{1}{M+1} \\ 0 & 1 & 0 & 0 \\ 0 & 0 & 1 & 0 \\ 1 & 0 & 0 & \frac{M}{M+1} \end{pmatrix} \begin{pmatrix} X_{\mathrm{CM}(2)} \\ X \\ x \\ \xi \end{pmatrix},\end{aligned} \tag{B.35}$$

so that $B_2 B_2^{-2} = B_2^{-2} B_2 = \mathbb{1}$.

The final two-step transformation is given by

$$\begin{aligned}
\begin{pmatrix} X_{\mathrm{CM}(2)} \\ X \\ x \\ \xi \end{pmatrix} &= B_2 B_1 \begin{pmatrix} X_1 \\ X_2 \\ x_1 \\ x_2 \end{pmatrix} \\
&= \begin{pmatrix} \frac{2M}{2M+2} & 0 & 0 & \frac{2}{2M+2} \\ 0 & 1 & 0 & 0 \\ 0 & 0 & 1 & 0 \\ -1 & 0 & 0 & 1 \end{pmatrix} \begin{pmatrix} \frac{1}{2} & \frac{1}{2} & 0 & 0 \\ -1 & 1 & 0 & 0 \\ 0 & 0 & -1 & 1 \\ 0 & 0 & \frac{1}{2} & \frac{1}{2} \end{pmatrix} \begin{pmatrix} X_1 \\ X_2 \\ x_1 \\ x_2 \end{pmatrix} \\
&= \begin{pmatrix} \frac{M}{2M+2} & \frac{M}{2M+2} & \frac{1}{2M+2} & \frac{1}{2M+2} \\ -1 & 1 & 0 & 0 \\ 0 & 0 & -1 & 1 \\ -\frac{1}{2} & -\frac{1}{2} & \frac{1}{2} & \frac{1}{2} \end{pmatrix} \begin{pmatrix} X_1 \\ X_2 \\ x_1 \\ x_2 \end{pmatrix}.
\end{aligned} \tag{B.36}$$

The final two-step inversion of Eq. B.36 is given by

$$\begin{aligned}
\begin{pmatrix} X_1 \\ X_2 \\ x_1 \\ x_2 \end{pmatrix} &= B_1^{-1} B_2^{-1} \begin{pmatrix} X_{\mathrm{CM}(2)} \\ X \\ x \\ \xi \end{pmatrix} \\
&= \begin{pmatrix} 1 & -\frac{1}{2} & 0 & 0 \\ 1 & \frac{1}{2} & 0 & 0 \\ 0 & 0 & -\frac{1}{2} & 1 \\ 0 & 0 & \frac{1}{2} & 1 \end{pmatrix} \begin{pmatrix} 1 & 0 & 0 & -\frac{1}{M+1} \\ 0 & 1 & 0 & 0 \\ 0 & 0 & 1 & 0 \\ 1 & 0 & 0 & \frac{M}{M+1} \end{pmatrix} \begin{pmatrix} X_{\mathrm{CM}(2)} \\ X \\ x \\ \xi \end{pmatrix} \\
&= \begin{pmatrix} 1 & -\frac{1}{2} & 0 & -\frac{1}{M+1} \\ 1 & \frac{1}{2} & 0 & -\frac{1}{M+1} \\ 1 & 0 & -\frac{1}{2} & \frac{M}{M+1} \\ 1 & 0 & \frac{1}{2} & \frac{M}{M+1} \end{pmatrix} \begin{pmatrix} X_{\mathrm{CM}(2)} \\ X \\ x \\ \xi \end{pmatrix},
\end{aligned} \tag{B.37}$$

so that $B_2 B_1 B_1^{-1} B_2^{-2} = B_1^{-1} B_2^{-2} B_2 B_1 = \mathbb{1}$.

By substituting Eqs. B.35 into Eq. B.28 we obtain

$$\begin{aligned} E =& \frac{1}{2}(2M+2)V_{\mathrm{CM}(2)}^2 + \frac{1}{2}\mu_p V^2 + \frac{1}{2}\mu_{ep}V_\xi^2 + \frac{1}{2}\mu_e v^2 \\ & - \frac{1}{\sqrt{\left(\frac{X}{2} - \frac{x}{2} + \xi\right)^2 + \Delta_{Ie}^2}} - \frac{1}{\sqrt{\left(\frac{X}{2} - \frac{x}{2} - \xi\right)^2 + \Delta_{Ie}^2}} \\ & - \frac{1}{\sqrt{\left(\frac{X}{2} + \frac{x}{2} + \xi\right)^2 + \Delta_{Ie}^2}} - \frac{1}{\sqrt{\left(\frac{X}{2} + \frac{x}{2} - \xi\right)^2 + \Delta_{Ie}^2}} \\ & + \frac{1}{\sqrt{X^2 + \Delta_{II}^2}} + \frac{1}{\sqrt{x^2 + \Delta_{ee}^2}}, \end{aligned} \tag{B.38}$$

where the reduced mass of the two electron two proton system is

$$\mu_{ep} = \frac{2M}{1+M}. \tag{B.39}$$

If we rewrite Eq. B.38 in terms of the classical momenta given by

$$P_{X_{\mathrm{CM}(2)}} = (2M+2)V_{\mathrm{CM}(2)}; P_X = \mu_p V; P_\xi = \mu_{ep}V_\xi; P_x = \mu_e v, \tag{B.40}$$

we obtain the following energy

$$\begin{aligned} E =& \frac{1}{2}\frac{P_{X_{\mathrm{CM}(2)}}^2}{2M+2} + \frac{1}{2}\frac{P_X^2}{\mu_p} + \frac{1}{2}\frac{P_\xi^2}{\mu_{ep}} + \frac{1}{2}\frac{P_x^2}{\mu_e} \\ & - \frac{1}{\sqrt{\left(\frac{X}{2} - \frac{x}{2} + \xi\right)^2 + \Delta_{Ie}^2}} - \frac{1}{\sqrt{\left(\frac{X}{2} - \frac{x}{2} - \xi\right)^2 + \Delta_{Ie}^2}} \\ & - \frac{1}{\sqrt{\left(\frac{X}{2} + \frac{x}{2} + \xi\right)^2 + \Delta_{Ie}^2}} - \frac{1}{\sqrt{\left(\frac{X}{2} + \frac{x}{2} - \xi\right)^2 + \Delta_{Ie}^2}} \\ & + \frac{1}{\sqrt{X^2 + \Delta_{II}^2}} + \frac{1}{\sqrt{x^2 + \Delta_{ee}^2}}. \end{aligned} \tag{B.41}$$

The quantum momentum operators in 1-D are canonically defined as

$$\hat{P}_{X_{\mathrm{CM}(2)}} = -i\frac{\partial}{\partial X_{\mathrm{CM}(2)}}, \hat{P}_X = -i\frac{\partial}{\partial X}, \hat{P}_x = -i\frac{\partial}{\partial x}, \hat{P}_\xi = -i\frac{\partial}{\partial \xi}, \tag{B.42}$$

which are then substituted in Eq. B.41 instead of the correspondent classical momenta to obtain the following Hamiltonian

$$\begin{aligned}\hat{H} = &-\frac{1}{2(2M+2)}\frac{\partial^2}{\partial {X_{\mathrm{CM}(2)}}^2} - \frac{1}{2\mu_p}\frac{\partial^2}{\partial X^2} - \frac{1}{2\mu_e}\frac{\partial^2}{\partial x^2} - \frac{1}{2\mu_{ep}}\frac{\partial^2}{\partial \xi^2} \\ &- \frac{1}{\sqrt{\left(\frac{X}{2} - \frac{x}{2} + \xi\right)^2 + \Delta_{Ie}^2}} - \frac{1}{\sqrt{\left(\frac{X}{2} - \frac{x}{2} - \xi\right)^2 + \Delta_{Ie}^2}} \\ &- \frac{1}{\sqrt{\left(\frac{X}{2} + \frac{x}{2} + \xi\right)^2 + \Delta_{Ie}^2}} - \frac{1}{\sqrt{\left(\frac{X}{2} + \frac{x}{2} - \xi\right)^2 + \Delta_{Ie}^2}} \\ &+ \frac{1}{\sqrt{X^2 + \Delta_{II}^2}} + \frac{1}{\sqrt{x^2 + \Delta_{ee}^2}} \\ = &-\frac{1}{4M+4}\frac{\partial^2}{\partial {X_{\mathrm{CM}(2)}}^2} + \hat{H}_{int}(X, x, \xi),\end{aligned} \tag{B.43}$$

where $\hat{H}_{int}(X, x, \xi)$ is the internal Hamiltonian, which depends only on the internal coordinates X, x and ξ

$$\begin{aligned}\hat{H}_{int}(X, x, \xi) = &-\frac{1}{2\mu_p}\frac{\partial^2}{\partial X^2} - \frac{1}{2\mu_e}\frac{\partial^2}{\partial x^2} - \frac{1}{2\mu_{ep}}\frac{\partial^2}{\partial \xi^2} \\ &- \frac{1}{\sqrt{\left(\frac{X}{2} - \frac{x}{2} + \xi\right)^2 + \Delta_{Ie}^2}} - \frac{1}{\sqrt{\left(\frac{X}{2} - \frac{x}{2} - \xi\right)^2 + \Delta_{Ie}^2}} \\ &- \frac{1}{\sqrt{\left(\frac{X}{2} + \frac{x}{2} + \xi\right)^2 + \Delta_{Ie}^2}} - \frac{1}{\sqrt{\left(\frac{X}{2} + \frac{x}{2} - \xi\right)^2 + \Delta_{Ie}^2}} \\ &+ \frac{1}{\sqrt{X^2 + \Delta_{II}^2}} + \frac{1}{\sqrt{x^2 + \Delta_{ee}^2}}.\end{aligned} \tag{B.44}$$

APPENDIX C

Modelling the Ehrenfest dynamics Hamiltonians for the H_2^+ and H_2 molecules

Here I describe how I model the Ehrenfest dynamics (ED) Hamiltonians. These Hamiltonians differ from the Born-Oppenheimer approximation (BOA) Hamiltonians by a factor of two. This difference with respect to the BOA is due to the different kicking effect that we apply. As the linear response absorption spectra does not depend on uniform translations of the nuclei and electrons, this effect can be disregarded.

For the H_2^+ molecule we use the following form

$$\hat{H}(x) = -\frac{\partial^2}{\partial \tilde{x}^2} - \frac{1}{\sqrt{\tilde{x}^2 + \Delta_{Ie}^2}}, \tag{C.1}$$

where the nuclear coordinates are defined as $X_2 = \frac{X_0}{2}$ and $X_1 = -\frac{X_0}{2}$ along the $\tilde{x}$ direction. Here, $X_0 = X_2 - X_1$ and Δ_{Ie} will change as shown in Fig. 2.1. The nuclear repulsion term is obtained from the interaction between the coordinates X_1 and X_2, where the charge of the interaction $Z_i Z_j$ from Eq. 2.20 is set to one and the Δ_{II} will change as shown in Sec. 2.1. By doing this, we end up with the following Hamiltonian

$$\begin{aligned}\hat{H}(X_0, \tilde{x}) = &- \frac{\partial^2}{\partial {X_1}^2} - \frac{\partial^2}{\partial {X_2}^2} - \frac{\partial^2}{\partial \tilde{x}^2} - \frac{1}{\sqrt{\left(\tilde{x} + \frac{X_0}{2}\right)^2 + \Delta_{Ie}^2}} \\ &- \frac{1}{\sqrt{\left(\tilde{x} - \frac{X_0}{2}\right)^2 + \Delta_{Ie}^2}} + \frac{1}{\sqrt{\left(\frac{X_0}{2} + \frac{X_0}{2}\right)^2 + \Delta_{II}^2}},\end{aligned} \tag{C.2}$$

where we have reduced X_0 by a factor of two with respect to the BOA, by comparison to Eq. 2.21.

For the H_2 molecule we solve the following Hamiltonian

$$\hat{H}(x_1, x_2) = -\frac{\partial^2}{\partial {x_1}^2} - \frac{\partial^2}{\partial {x_2}^2} - \frac{1}{\sqrt{x_1^2 + \Delta_{Ie}^2}} - \frac{1}{\sqrt{x_2^2 + \Delta_{Ie}^2}} + \frac{1}{2}\frac{1}{\sqrt{(x_2 - x_1)^2 + \Delta_{ee}^2}}, \tag{C.3}$$

where the coordinates are defined as $\frac{X_0}{2}$ and $\frac{X_0}{2}$ along both the x_1 and x_2 directions and where Δ_{Ie} will change as shown in Fig. 2.1. The charge of the nuclear interaction Z_iZ_j from Eq. 2.20 is set to $\sqrt{2}$ and the Δ_{II} will change as shown in Fig. 2.1.

By doing this, we end up with the following Hamiltonian

$$\begin{aligned}\hat{H}(X_0, x_1, x_2) = &-\frac{\partial^2}{\partial {X_1}^2} - \frac{\partial^2}{\partial {X_2}^2} - \frac{\partial^2}{\partial {x_1}^2} - \frac{\partial^2}{\partial {x_2}^2} - \frac{1}{\sqrt{\left(x_1 + \frac{X_0}{2}\right)^2 + \Delta_{Ie}^2}} \\ &- \frac{1}{\sqrt{\left(x_1 - \frac{X_0}{2}\right)^2 + \Delta_{Ie}^2}} - \frac{1}{\sqrt{\left(x_2 + \frac{X_0}{2}\right)^2 + \Delta_{Ie}^2}} - \frac{1}{\sqrt{\left(x_2 - \frac{X_0}{2}\right)^2 + \Delta_{Ie}^2}} \\ &+ \frac{1}{\sqrt{(x_2 - x_1)^2 + \Delta_{ee}^2}} + \frac{\sqrt{2}}{\sqrt{\left(\frac{X_0}{2} + \frac{X_0}{2}\right)^2 + \left(\frac{X_0}{2} + \frac{X_0}{2}\right)^2 + \Delta_{II}^2}},\end{aligned} \tag{C.4}$$

where we have reduced X_0 by a factor of two with respect to the BOA, by comparison to Eq. 2.22.

APPENDIX D

The Hellmann-Feynman theorem

Consider a 1D Hamiltonian $\hat{H}(X)$ which depends on some parameter X and let $|\psi\rangle$ be an eigenstate of that Hamiltonian:

$$\hat{H}(X)|\psi\rangle = \varepsilon|\psi\rangle \tag{D.1}$$

The Hellmann-Feynman theorem then relates the derivative of an eigenvalue of the Hamiltonian $\hat{H}(X)$ with respect to X, to the expectation value of the derivative of the eigenstate of the Hamiltonian $\hat{H}(X)$ with respect to that same parameter. This can be seen as follows:

$$\begin{aligned}
\frac{\partial}{\partial X}\varepsilon &= \frac{\partial}{\partial X}\langle\psi|\hat{H}(X)|\psi\rangle \\
&= \langle\frac{\partial}{\partial X}\psi|\hat{H}(X)|\psi\rangle + \langle\psi|\hat{H}(X)|\frac{\partial}{\partial X}\psi\rangle + \langle\psi|\frac{\partial}{\partial X}\hat{H}(X)|\psi\rangle \\
&= \varepsilon\langle\frac{\partial}{\partial X}\psi|\psi\rangle + \varepsilon\langle\psi|\frac{\partial}{\partial X}\psi\rangle + \langle\psi|\frac{\partial}{\partial X}\hat{H}(X)|\psi\rangle \\
&= \varepsilon\frac{\partial}{\partial X}\langle\psi|\psi\rangle + \langle\psi|\frac{\partial}{\partial X}\hat{H}(X)|\psi\rangle \\
&= \langle\psi|\frac{\partial}{\partial X}\hat{H}(X)|\psi\rangle = \frac{\partial}{\partial X}\varepsilon
\end{aligned} \tag{D.2}$$

where we have used:

$$\langle\psi|\psi\rangle = 1 \Rightarrow \frac{\partial}{\partial X}\langle\psi|\psi\rangle = 0. \tag{D.3}$$

Publications

(1) A. Crawford-Uranga, U. De Giovannini, E. Räsänen, M. J. T. Oliveira, D. J. Mowbray, G. M. Nikolopoulos, E. T. Karamatskos, D. Markellos, P. Lambropoulos, S. Kurth, A. Rubio; *Time-dependent density-functional theory of strong-field ionization of atoms by soft x rays*; Phys. Rev. A **90**, 033412 (2014); DOI:10.1103/PhysRevA.90.033412

(2) A. Crawford-Uranga, U. De Giovannini, D. J. Mowbray, S. Kurth, A. Rubio; *Modelling the effect of nuclear motion on the attosecond time-resolved photoelectron spectra of ethylene*; J. Phys. B: At. Mol. Opt. Phys. **47**, 124018 (2014); DOI:10.1088/0953-4075/47/12/124018

(3) A. Crawford-Uranga, D. J. Mowbray, D. M. Cardamone; *Quantum-ionic features in the absorption spectra of homonuclear diatomic molecules*; Phys. Rev. A **91**, 033410 (2015); DOI:10.1103/PhysRevA.91.033410

Research abroad

(1) King's College London Department of Theory and Simulation of Condensed Matter (01/09/2014-01/11/2014)

(2) Queen's University Belfast Atomistic Simulation Centre (01/02/2014 - 01/03/2014)

Conferences

(1) Young Researchers' Meeting : Naples, Italy (16 - 20/05/2011) Talk

(2) Time-Dependent Density-Functional Theory: Prospects and Applications : Benasque, Spain (school + workshop; 03 - 17/01/2012)

(3) Young Researchers' Meeting : Brussels, Belgium (21 - 25/05/2012) Talk

(4) Young Researchers' Meeting : Budapest, Hungary (20 - 24/05/2013) Talk

(5) Cronos M12 Meeting : San Sebastian, Spain (3 - 4/06/2013) Poster (using slides)

(6) Queen's University Belfast, Atomistic Simulation Centre: Belfast, Northern Ireland, United Kingdom (18/02/2014) Talk1 Talk2
(7) Spanish Scientific Research Council, Material Physics Center: San Sebastian, Spain (26/03/2014) Talk
(8) Free Electron Lasers and Attosecond Light Sources: portals to ultrafast dynamics in AMO systems: London, England, United Kingdom (Atto-FEL 2014 conference + COST XLIC WG1 meeting ; 30/06/2014-04/07/2014) Invited Talk
(9) ICAMM 2014, 3rd edition of the International Conference on Advanced Materials Modelling : Nantes, France (ICAMM 2014 conference only; 07/07/2014-09/07/2014) Talk
(10) Science at FELs : Villigen, Switzerland (15-17/09/2014) Talk
(11) Nano-Bio Spectroscopy Group meeting Seminar Talks

For more information check my Nano-Bio Spectroscopy Group web page